Evolutionary Design of Controlled Structures

Brett P. Masters and Edward F. Crawley

April 1997 SERC#1-97

(Under the sponsorship of NASA)

This report is based on the unaltered thesis of Brett P. Masters submitted to the Department of Aeronautics and Astronautics in partial fulfillment of the requirements for the degree of Science Doctorate at the Massachusetts Institute of Technology.

Abstract

Basic physical concepts of structural delay and transmissibility are provided for simple rod and beam structures. Investigations show the sensitivity of these concepts to differing controlled-structures variables, and to rational system modeling effects.

An evolutionary controls/structures design method is developed. The basis of the method is an accurate model formulation for dynamic compensator optimization and Genetic Algorithm based updating of sensor/actuator placement and structural attributes. One and three dimensional examples from the literature are used to validate the method. Frequency domain interpretation of these controlled structure systems provide physical insight as to how the objective is optimized and consequently what is important in the objective. Several disturbance rejection type controls-structures systems are optimized for a stellar interferometer spacecraft application. The interferometric designs include closed loop tracking optics. Designs are generated for differing structural aspect ratios, differing disturbance attributes, and differing sensor selections. Physical limitations in achieving performance are given in terms of average system transfer function gains and system phase loss.

A spacecraft-like optical interferometry system is investigated experimentally over several different optimized controlled structures configurations. Configurations represent common and not-so-common approaches to mitigating pathlength errors induced by disturbances of two different spectra. Results show that an optimized controlled structure for low frequency broadband disturbances achieves modest performance gains over a mass equivalent regular structure, while an optimized structure for high frequency narrow band disturbances is four times better in terms of root-mean-square pathlength. These results are predictable given the nature of the physical system and the optimization design variables. Fundamental limits on controlled performance are discussed based on the measured and fit average system transfer function gains and system phase loss.

Acknowledgments

This work was supported by the NASA Headquarters Grant No. NAGW-2014 for the purpose of Space Engineering with Dana Brewer as NASA contract administrator and Sharon Leah-Brown as the MIT contract administrator.

Contents

List of Figures

List of Tables

Chapter 1

Introduction

By the year 2000 software will perform nearly 80 percent of aerospace systems functions. Sensors and actuators that are integral to such systems have already enabled performance beyond the mundane tasks routinely performed by passive systems. As the reliability of such elements increases more complex algorithms are developed, employing millions of operations per second. The speed of such algorithms enable tasks previously not possible. Such a task is the real-time control of structural flexibility where actuator inputs to a system are amplified and phased in order to cancel unwanted motion or stress levels. The unwanted effects are disturbed by external or internal sources and are inferred from sensed measurements. These controlled structures can provide improved life cycle costs through, for example, improved resource usage. They may also enable scientific goals not previously achievable.

Space based structures that are characterized and compensated to sub micron motion levels have found utility in the stellar observation sciences. In such structures, control, other than that used in maintaining attitude, is typically introduced in the preliminary and detailed design stages, after the system is found to fail specifications passively. At this stage the structure is fixed in topology and member geometry leaving the control designer to accept the given plant dynamics. In some cases the actuator/sensor design is also fixed further limiting the achievable performance.

Consideration of structural control technology early in the design process of controlled structures leads to possible benefit, but also to numerous design variables and, subsequently, many criterion making the combined optimization problem very difficult. The payoff is that that the actuators/sensors are designed into the system and subsequently render the controls with greater influence over improving the performance. The drawback is that the combined optimization problem is plagued by large dimension in both the controls and structural eigen problems, and furthermore becomes combinatorial with the addition of discrete choices such as sensor/actuator location (distribution) and type (*e.g.* inertial or relative).

1.1 Objectives

The general objective of this thesis is to provide a method by which to investigate the impact of topological design on eventual closed loop performance in controlled structures. Using this method fundamental insight into optimizing motion error objective functions for controlled structures will be developed. Connections will be made to the basic physical principles by which controlled structural systems behave.

Other design objectives such as structural mass and control effort are explored in terms of validation examples from the literature. Such objectives exemplify typical spacecraft design goals. Besides validating the method, the solutions to these examples show the importance of cost and modeling formulations.

Specifically, the method is used to provide designs for a controlled stellar interferometer spacecraft. The purpose of this application example is to show the possible benefits of considering structural controls integrated into irregular structural designs. The designs provide key information regarding the design of the actuators and sensors with respect to the disturbances and performances.

Another objective of this thesis is to present optically and structurally compensated spacecraft-like interferometry experiments. The experiments are scaled realizations of the one dimensional application example. The experimental results reiterate where the combined system optimization is worth while in terms of improving performance.

1.2 Previously Published Work

In the past 20 years various investigators have tackled the dynamic controlled-structures optimization problem yielding a myriad of results and sparse implementation. Generally, in the 80's investigators proposed continuous methods that employed nonlinear programming or gradient search techniques. At issue was the choice of partial and directional derivatives, and the form of the cost functionals. The results were generally presented as follows: an optimization method, an example, and observations how the cost function improved with some interpretation of the spatial nature of the results. The optimization method was central to most papers and subsequently modeling accuracy in the examples was foregone. Topological controlled-structures optimization problems became more popular in the late 80's and early 90's. Implementations of discrete methods such simulated annealing, genetic algorithms and branch bound techniques have enabled topological searches that trade discrete variables.

In the published literature Rao, Maghami and Miller, *etc.* [1, 2, 3, 4] provide approaches where controls and structures topologies are fixed and the control gains, control bandwidth, and member cross-section variables optimized with respect to either mass, motion error or control effort costs. For the most part the above use nonlinear programming techniques and cover a variety of control techniques (LQR, H_2/H_∞ and positive real techniques respectively). They do not consider topological variations such as actuator/sensor placement simultaneously with structural variation. Onoda [5] does consider both simultaneously in the framework of a continuous problem, but the feedback is constant gains (LQR) and the actuation is coupled to rigid body control while the objective is mass minimization. This published result will serve as a validation example.

Another published example that does consider actuator/sensor placement concurrently with structural variations is provided by Sepulveda [6]. Sepulveda developed a method that uses branch and bound techniques that places collocated actuators and sensors in a truss structure while optimizing the member cross sections. The control method is local position and rate output feedback. Using a branch and bound technique allows the integer placement problem to be solved using continuous problems at each branch. While Sepulveda's work does consider structural and actuator/sensor placement variations simultaneously, the optimization uses suboptimal (but robust) output feedback and uses an intermediate variable formulation for the model. The model formulation allows simple calculations of gradients but foregoes the accuracy required for control.

Redesign optimization is achieved by Hanks, Smith and Skelton [7, 8, 9] by fixing the closed loop system and minimizing the control power. This method effectively redistributes the local position and rate feedback into the passive elements of the system. This, again, fixes the controls/structures topology but has the advantage of simplifying the optimization at the expense of dealing with relatively simple systems. Further developments of the method by Skelton [10] redistribute based on minimizing mixed H_2 and H_∞ objectives with one acting as a constraint while the other is optimized in convex fashion.

Results from the literature are various (see Table 1.1 for a summary) and are difficult to compare due to numerous factors;

- dimensionality of the structure (*e.g.* spring mass, beams and trusses) and structural discretization (whether structural member dynamics are observable)
- differing disturbances and performances
- sensor/actuator choice, differing in type, *e.g.*. internal relative versus external inertial, and location (only sometimes variable)
- differing control techniques

The question still remains, how does one design a structure to accept control, *i.e.* what are the necessary considerations, besides choosing an optimizer, and how well can we do in practice? The answers require a uniform investigation, in terms of modeling effort and choice of optimizer, over typical controlled structures, and an experimental verification.

Table 1.1: Examples from controls structures optimization literature. Motion metrics are denoted by z, strain by ϵ, control effort by u and structural mass by m. CL stands for Closed Loop and OL stands for Open Loop.

Invest.	metric	structure	control	sensors/actuators	opt. engine	Expmt.
Miller [5]	CL z^2	beam x-sec.	pos. + rate	fixed	NL prog.	No
Rao [4]	CL z^2	beam x-sec.	LQR	fixed	NL prog.	No
Maghami [6]	CL u^2	truss x-sec.	positive real	fixed	NL prog.	YES
Onoda [1]	CL z^2	beam x-sec.	LQR	fixed	NL prog.	No
Smith [7]	CL fixed	spring-mass-dashpot	covariance	fixed	quad. prog.	No
Sepulveda [2]	CL $\|z\|$, $\|u\|$, m	beam/truss x-sec.	pos. + rate	variable	Branch and Bound/ NL prog	No
Khot [3]	CL z^2	truss x-sec.	robust H_2/H_∞	fixed	NL prog.	No
Furuya [9]	OL ϵ^2	truss	-	variable	reduced stochastic search	No
Skelton [8]	CL fixed	spring-mass-dashpot	covariance	fixed	Linear Matrix Ineq.	No
Jacques [10, 11]	CL z^2	spring-mass	LQR	fixed	exact	No
Keane [12, 13, 14]	OL ϵ^2	truss	-	-	stochastic search	YES

Two published experimental results are considered here. The first is the result of a NASA program at the Langley Research Center, published by Maghami *et al.* [2]. In this case the cost function was control effort with constrained motion errors. Actuators and sensors topology was fixed, *i.e.* cold gas thruster inputs with collocated velocity measurements, and grouped cross-sectional variables and control gains optimized. Control design was essentially dissipative with broadband inertial disturbances entering at one end of the structure. Overall the optimal design was to stiffen the main structural sections, with primary flexible modes increasing in frequency by $\approx$ 40%. This globally added stiffness attenuates the flexible response for the same rigid body response, resulting in the actuators operating at less power to achieve a given performance. Overall the control power was reduced by just 3 dB rms.

The second experimental result reviewed is optimization of an open loop structural topology, performed and experimentally implemented by Keane [11] with remarkable narrow band disturbance rejection results. Here a genetic algorithm search is performed over structural topology (geometric location of truss joints) to minimize energy levels in a structural member at the end of a cantilevered two dimensional truss. The disturbance enters as a point force on a structural member near the cantilever root. Good performance, nearly 30 dB attenuation in energy at a given frequency (15 dB in generalized displacement), is achieved by adjustment of the local dynamics of the individual members. In this work it is unclear whether broadband performance is compromised in obtaining such narrow band performance.

1.3 Outline

The terminology in this thesis is based on interpretation of system transfer functions from disturbances and actuated controls to performances and measurements. The underlying modeling and physical interpretations of these transfer functions are described in Chapter 2.

The method used in this thesis will be developed in Chapter 3 from a modeling perspective, not the usual mathematical optimization perspective. An optimization/search method is selected that enables the propagation of accurate control models. In topological design of controlled structures there are many discrete choices available resulting in a large combinatorial design space. The method provided efficiently sorts these types of design spaces.

Before application of the method to a current aerospace systems problem, extensive validation against the literature is provided in Chapter 4. Published one and three dimensional controlled structures examples are encoded and investigated. These examples explore mass, motion error and control effort type objectives and constraints.

Space-based interferometric instruments are designed with respect to structural control in Chapter 5. The examples are based on conceptual designs performed at MIT for the Jet Propulsion Laboratory. They investigate two types of structural aspect ratio, beam-like versus box truss, and two types of system disturbance, residual attitude control forces versus prescribed interface motions.

To further validate the approach taken, experiments were designed that verify the results from the one dimensional application example. The experiments are scaled versions of the example. Many configurations are investigated to explore the physical limitations of the design examples.

Conclusions are drawn based on the physical limitations realized in the design and implementation of controlled structures. The conclusions are categorized into general systems conclusions and specific systems conclusions.

Chapter 2

Controlled Structures Systems Background

The primary purpose of this chapter is to outline the basic terminology, and discuss simple examples in the language that will be used throughout the thesis. Key physical concepts will be described in the discussion of the simple example. Transfer functions from inputs to outputs are presented for optimized structural systems throughout this thesis. Where possible, the Multiple-Input Multiple-Output transfer function matrix representing systems are parsed into critical Single-Input Single-Output transfer functions. Nominal and optimized structural systems transfer functions and system spatial topologies will be interpreted in terms of underlying fundamental physics. Classically, investigators either the transfer functions or the spatial representation of the system. Here, both will be connected. General physical descriptions are given in this chapter. For further details see the book by Crawley [12], publications by Miller [13] and von Flotow [14], and the theses by MacMartin [15] and McCain [16].

Another purpose of this chapter is to show that controlled structural systems are in fact limited by irrational structural behavior where the average system transfer function gain stays high while the occurrence of poles with increasing frequency causes phase loss. Nonminimum phase zeros occur but are not always primary contributors to this effect.

The first section gives systems definitions. With these in hand fundamental structural modeling is discussed. More specific examples are next investigated to show the second purpose of this chapter. A non dimensional parameter is introduced that is used to describe the evolutionary design objective for noncollocated disturbances and performances. Simple system sensitivities are given to illustrate how strongly the basic structural parameters couple into the design objectives. Exact asymptotic results for a few collocated beam systems are provided and some numerical studies are performed on a noncollocated beam example. Closed form single dof Linear Quadratic Control solutions are next recited from the literature to show the sensitivity of motion type performance to closed loop dampening and stiffness control. Finally, zero perturbations are given to highlight the effectual parameters for manipulating system pole-zero structure.

2.1 Systems Definitions

The objective of this section is to provide some background in the fundamental terminology and characterizations made throughout this thesis. Descriptions are given in the context of controlled structures where, in this thesis, high authority control is necessary to meet performance requirements. For the most part this section follows material in a conceptual design paper by Crawley *et. al.* [17] and a pending book by Crawley *et. al.* [12], "High Performance Structures: Dynamics and Control."

Figure 2.1 is an overview of controls-structures design. In the figure and in this thesis in general, w are the disturbances, z are the performances, u are the control forces and y are the measurements. Measurements and controls used in the isolation stages are denoted within those subsystems. The figure is misleading in that it represents various subsystems as independent block entities connected by signal flow, however, note the distinctive arrows to *and* from various entities. These arrow directions indicate coupled influence in terms of overall system impedances and are necessary in an accurate control design model. The various variables and block interactions are described in the following with some simple illustrative examples.

In this systems approach, illustrated by Figure 2.1, the disturbances and perfor-

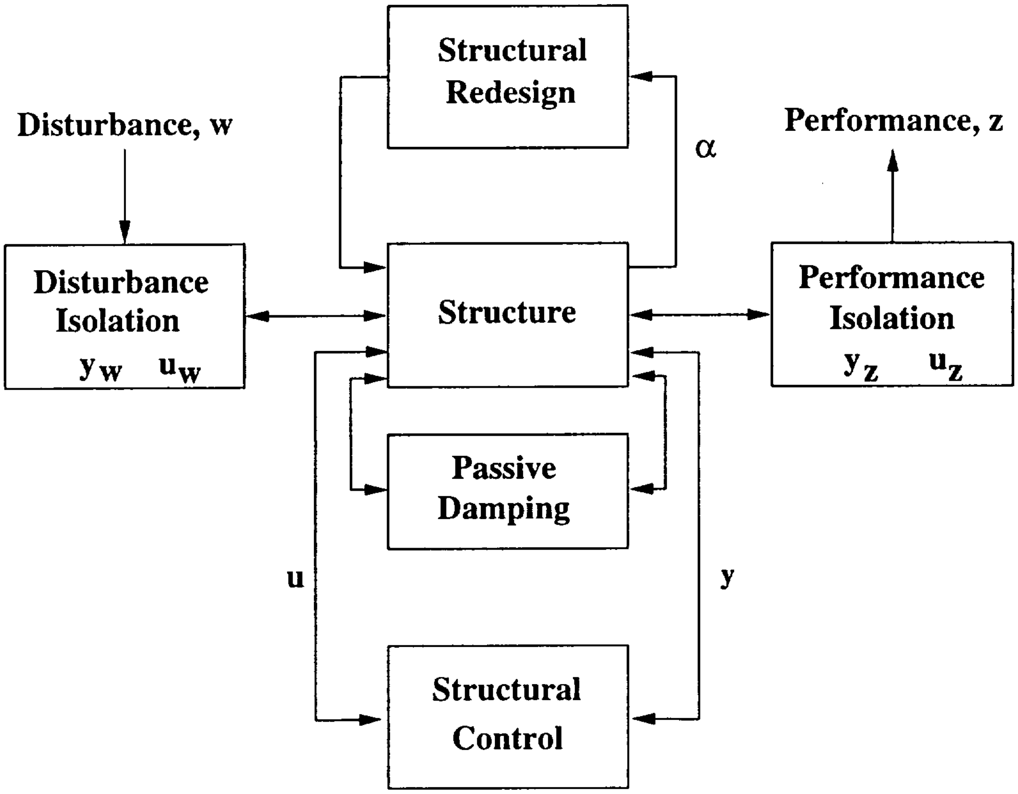

Figure 2.1: Overview of controls-structures design.

mances are modeled. The functional requirements on the dynamic performance of the structure are set by the user, and may evolve during the design process. They can be quantified in terms of structural performance outputs or metrics, *e.g.* the bending strains at a wing root, tip displacement of a flexible robot, or jitter of a telescope mirror. Attributes which must be defined include the location, type and frequency bandwidth of importance of the structural outputs. The location addresses where the structural system influences the performance and whether in a distributed or localized fashion. Types of structural performance include strain, and inertial and/or relative displacements and angles, and their rates and accelerations. Another type of performance variable that is often neglected is control effort, which derives from meeting a structural performance constraint. In this case z in Fig. 2.1 is a direct measure of u. Implicit performance variables such as flutter speed (an aeroelastic stability based measure) may also be measured directly.

Structural performance outputs, z, are written as linear combinations of the states in order to be compatible with linear control analysis,

$$z = C_{zx}x = [C_{zq}\, C_{z\dot{q}}] \left\{ \begin{array}{c} q \\ \dot{q} \end{array} \right\} \tag{2.1}$$

where x are the vectorized structural states, q the degrees of freedom of the structure as a whole, and the elements of matrix C_{zx} are geometric coefficients.

An example of geometric coefficients arises when the performance requires a spatial integral over some discrete representation of the domain. Discretely defined structural states must be weighted with integration weights before they are summed. Combining the performance variable z in the frequency domain through a square root Power Spectral Density (evaluated pointwise in frequency) function evaluated on the $j\omega$ axis, $\Phi_z(\omega)$, and integrating over frequency yields a scalar mean square cost, J_z,

$$J_{z_\omega}(\omega) = \Phi_z^H(\omega) R_{zz} \Phi_z(\omega) \tag{2.2}$$

$$J_z = 2 \int_0^\infty J_{z_\omega}(\omega) d\omega \tag{2.3}$$

where R_{zz} is a matrix of weights (positive semi-definite to be sufficient for modern control purposes) which express the relative importance of the various outputs. Note that frequency weights, which select the bandwidths of interest, can be included by filtering the structural outputs. Adding such weights increases states of the system model since for every weighting pole an extra state is needed.

When the performance is induced a characterization of the disturbance(s) , w, acting on the system is necessary. Disturbances are accounted for in two basic ways: either as forces emanating from energy/momenta sources that act on and in the system as body forces, or as prescribed motions occurring at an interface to a host body, or both. An example of a host driving prescribed motion in a system is seismic induced motion in a building. Shuttle vibrations originating from such things as vernier attitude control and crew motions cause the base of the antennae to follow a prescribed motion since the antennae is light weight and flexible with respect to the massive host and rigid mounting interface. External disturbances arise due to operational environment such as temperature, acoustics, aerodynamics, noisey host-body vibrations etc. Internal disturbances come about when functioning. Examples include motor imbalances, pumps and temperature control elements.

Disturbances may be described in terms of three attributes, *type*, *location* and *temporal distribution*. The type attribute is further delineated into action, reference and direction. Action may be force or displacement while reference may be relative or inertial. Location refers to the spatial occurrence of the disturbance and temporal distribution refers to its spectrum, *e.g.* deterministic periodic, stochastic broadband or band limited. Type and location are captured in a disturbance influence matrix,

$$F = \beta_w w \tag{2.4}$$

where β_w are the disturbability influence coefficients and w the disturbances. Temporal distribution can be implemented by filtering the input w so that w can be considered unit intensity white noise. Deterministic inputs can be bounded by filters or simply used as time domain inputs to linear systems. The filtering approach is less computationally intensive and will be used for optimization purposes in this thesis.

An example of how the disturbance influence matrix may couple to the system modeling can be seen in the expression for a prescribed interface motion where the equation of motion is partitioned,

$$\begin{bmatrix} M_{ss} & M_{si} \\ M_{is} & M_{ii} \end{bmatrix} \begin{bmatrix} \ddot{x}_s \\ \ddot{x}_i \end{bmatrix} + \begin{bmatrix} K_{ss} & K_{si} \\ K_{is} & K_{ii} \end{bmatrix} \begin{bmatrix} x_s \\ x_i \end{bmatrix} = \begin{bmatrix} \beta_{w_s} w_s \\ \beta_{w_i} w_i \end{bmatrix}, \tag{2.5}$$

into the interface, i, and disturbed system, s, dof. Rearranging the top equation gives,

$$M_{ss}\ddot{x}_s + K_{ss}x_s = -M_{si}\ddot{x}_i - K_{si}x_i + \beta_{w_s} w_s\,, \tag{2.6}$$

which yields the disturbed system driven by the interface motion $\{\ddot{x}_i,\ x_i\}$ through the coupled mass and stiffness matrix. Disturbances that act on the system dof directly, w_s, are also present.

Structural actuators are also categorized by type and location. Examples of actuators that act on angle are reaction wheels and gimbals. The reaction wheel is inertial while the the gimbal is relative. Examples of internal actuators that act on relative

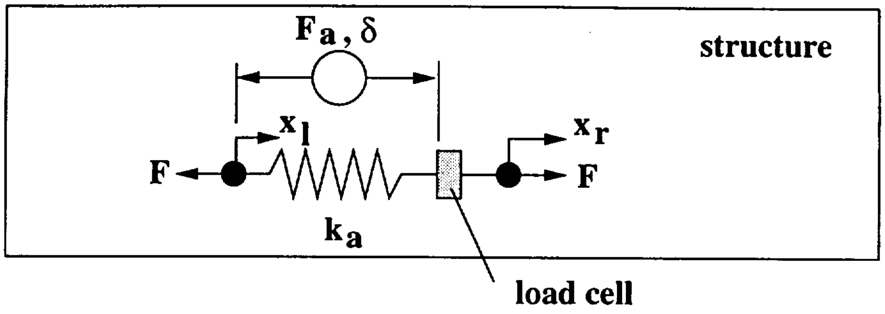

Figure 2.2: Simple spring strut actuator as an internal member to a structure.

displacements or strain are those fashioned out of piezo ceramic and electrostrictive active materials. These may be arranged as stacks of wafers, levered stacks, plain wafers or even fibers in a matrix. Active materials can be integrated into a structure with desired spatial distribution. For actuators the terminology "temporal distribution" is replaced with internal dynamics. All actuators have dynamics that affect their bandwidth to differing degrees. When in the bandwidth of structural control these dynamics must be modeled and appended to the system model [18]. Piezo ceramic actuators are high bandwidth as is evidenced by their usage in ultrasonic applications so their internal dynamics are ignored.

An example of modeling and categorizing an active strut structural actuator is shown in Fig. 2.2. The strut is assumed to have no internal dynamics therefore it is just a spring. In the figure F_a and δ are commands and F and x are resultants.

The resultant force F is simply,

$$F = F_a - k_a(x_r - x_l)\,, \tag{2.7}$$

which is reacted by the internal forces of the structure, $M_{ss}\ddot{x}_s + K_{ss}x_s$.

If using piezoelectric ceramic struts, **and** the electrode voltage is being commanded, then F_a is $k_a\delta$. The displacement δ is desired and the displacement x realized. Here, the control influence coefficients would include the actuator stiffness k_a. The type of actuator is relative displacement. For piezo-ceramics this k_a is stiff (on the order of an equal geometry aluminum strut) and it is for this reason that they couple well to structural problems. If a voice coil strut arrangement is used, then F_a is a force proportional to the commanded current. Since a voltage amplification is usually used, the electrical resistance and inductance of the voice coil is needed in the model since current is not commanded. For a voice coil the actuation stiffness k_a is that of soft flexures or may be tuned [19]. Their mass can not be neglected because they rely on a high density magnet for reaction, nor can their internal dynamics due to power amplifier limitations and eddy current losses be neglected.

In the evolutionary designs of the application examples in this thesis active members are modeled as an applied force (or moment) pair, a generalized force F_a. The active member stiffness is therefore lumped into the plant and the optimization will, for a given force choose the actuator stiffness (which will sometimes loosely be called impedance in this thesis). The effect of this modeling choice is important when considering internal relative sensors such as load measurements.

Similarly to disturbances and actuators, structural sensors have type and location attributes. As with actuators their internal dynamics must also be considered for control purposes when they are in the bandwidth of interest. Examples of widely used structural sensors are accelerometers, strain gages and load cells. Examples of high end structural sensors are laser metrology systems, electron tunneling devices, rate-gyros and angle encoders. Type specification for accelerometers would be extensive inertial as would be for rate-gyros. Rate-gyros have limited bandwidth and drift at a very slow rate whereas accelerometers can measure to very high frequencies but usually not below 1 Hz. A strain gage is an intensive relative measure. It is intended as a point measure, but like most sensors they are susceptible to sensitivity to secondary variables. Adaptation of active materials such as piezo ceramic wafers and PVDF film as strain sensors allows spatially distributed measurements of the second order tensor quantities.

As an example the internal relative load cell sensor used in this thesis is as pictured in Fig. 2.2. Here, the measurement is,

$$y_{LC} = -(k_a + k_p)(x_r - x_l) + Du \,, \tag{2.8}$$

where if $u = \delta$, then $D = k_a$, and if $u = k_a\delta = F_a$ then $D = 1$. In either case the low frequency measure of y_{LC} is $\approx k_p(x_r - x_l)$ where k_p is the surrounding structural stiffness. For higher frequencies of inputs from the actuator u, the response $x_r - x_l$ decreases and the measure is dominated by the Du term. This is good for control because the flexible response becomes less observable in the sensor at high frequencies where it is often desirable to roll off control gains.

Another example is measuring extensive inertial acceleration where,

$$y_{acc} = M_{ss}^{-1} K_{ss} x_s + M_{ss}^{-1} C_{ss} \dot{x}_s + M_{ss}^{-1} u \,. \tag{2.9}$$

Here, the inverse of the mass matrix comes into the measurement coefficients. Again the presence of the feed through term is concerning but this is not the inhibiting factor for this sensor's usage as a control sensor. The problem is that the displacement response of distributed structures does not roll off like $1/\omega^2$ in the frequency domain at high frequencies. The roll off rate is usually less, meaning more sensitivity at high frequencies. Correspondingly the acceleration, which is proportional to the displacement by a factor of $-\omega^2$, continues to increase in average transfer function gain at high frequencies. The implementation issue is the ability to roll off loop control gain using system weights.

Understanding the relationship between the actuation inputs and sensed outputs is necessary for visualizing the effect a controller can have on performance. An important definition is that of **collocation** when an actuator and sensor are in the same location and act/measure in the same sense. When a sensor actuator pair is truly collocated the transfer function from input to output is phase bounded. Mathematically this has been proved to lead to interlaced complex poles and minimum phase complex zeros [20]. Examples of simple collocated input output pairs on simple structures will be shown in the following section. The significance of this pole-zero structure is that, with simple feedback of the correct derivative/integral of the measurement near loop gain cross-over, the controller will be phase stable. Pure collocation is a mathematical abstraction. It can, however, be quantified over a bandwidth by the nature of the complex zeros with respect to the structural poles. Usually at high enough frequencies, or small enough wave numbers, the sensor is not measuring the exact mathematical variable and the actuator is not perfectly actuating as desired.

This is a concern when placing a structural actuator/sensor pair in a highly internally indeterminant configuration and desiring broad band damping. For example, placing an active strut-load cell pair in an indeterminant mounting configuration leads to actuated and sensed shear stresses and bending moments. The sensed variable is not collocated with that actuated for all frequencies of input because of the nonuniformity in the local stress fields due to the indeterminacy.

Collocation is necessary but not sufficient for achieving good control action over a broad band of important flexible modes. Collocation with good modal residues (or even pole-zero spacing near the important modes) and a transfer function that rolls off at high frequencies, is sufficient for good control action over these modes. Neither of the above statements mention performance, because a collocated structural actuator sensor pair may achieve high gain feedback at an amenable location in the structure, yet stiffness control and dampening of this location does not stop disturbances from propagating through all the structural states to the performance. Modern control techniques use knowledge of disturbance and performance directions to apply a collocated actuator sensor to reducing the performance. When the sensor is the performance and the actuator is collocated (output isolation), or when the sensor measures the disturbance and the actuator is collocated (input isolation) impressive performance improvements are realized.

Input-output modification refers to the class of actions which serve to reduce the energy passed into the structure, and or reduce the impact of structural motion on the performance metric. The options include input shaping of commands, disturbance reduction or cancellation, and isolation. Command shaping seeks to filter the input at the frequencies of structural resonance while minimizing impact on the tracking performance. Disturbance reduction or cancellation minimizes the disturbance by redesign of the device, using techniques such as reactuation (ie inertially uncoupling device motion from mount reactions) and adaptive balancing of rotating machinery. The most common form of input output modification is passive or active isolation, either at the site of the disturbance or the performance output. By modifying the supporting structure or using sensors and actuators, isolation takes advantage of the energy flow "bottleneck" present in some systems. These systems are by far the easiest to improve because the disturbance and performance are localized on the structure, not distributed. When localized, disturbance isolation is used to reduce the transmission of disturbances above a low pass corner frequency or within a narrowband frequency notch.

When completely collocated with the disturbance or performance, input/output isolation can be modeled as a frequency weight on the input/output, *i.e.* if a true control loop sensitivity is used. This will be described further in Chapter 3.

2.2 Simple Structural Modeling and Terminology

Simple structural models for specific inputs and outputs are parameterized in this section. By comparison with exact continuum models of simple structures it is proposed by Crawley [12] that the shape of the structural transmissibility be established by a relatively small number of parameters. The structural transmissibility from an input w to an output z is the transfer function,

$$G_{zw}(\omega) = \frac{z(\omega)}{w(\omega)}. \tag{2.10}$$

Exact wave domain expressions can be found for undamped simple structures. An example of finding these solutions for a free-free beam is given in Appendix A. The exact models are irrational transcendental functions.

In order to establish the parametric terminology a SISO collocated example is first detailed in terms of conventional methods. Figure 2.3 shows the exact irrational transfer function magnitude, dashdot, for an inertial force-displacement pair at the center of an undamped free-free beam. The frequency axis has been normalized by the fundamental flexible mode frequency. The exact transfer function appears to be damped, albeit lightly, due to the fact that the continuous transfer function is plotted over a finite number of frequency points.

Poles and zeros of the transfer function are parameterized by normalized natural frequency and damping, and plotted underneath the magnitude plot. They are calculated from a 52 element finite element model of the beam. This plot helps envision

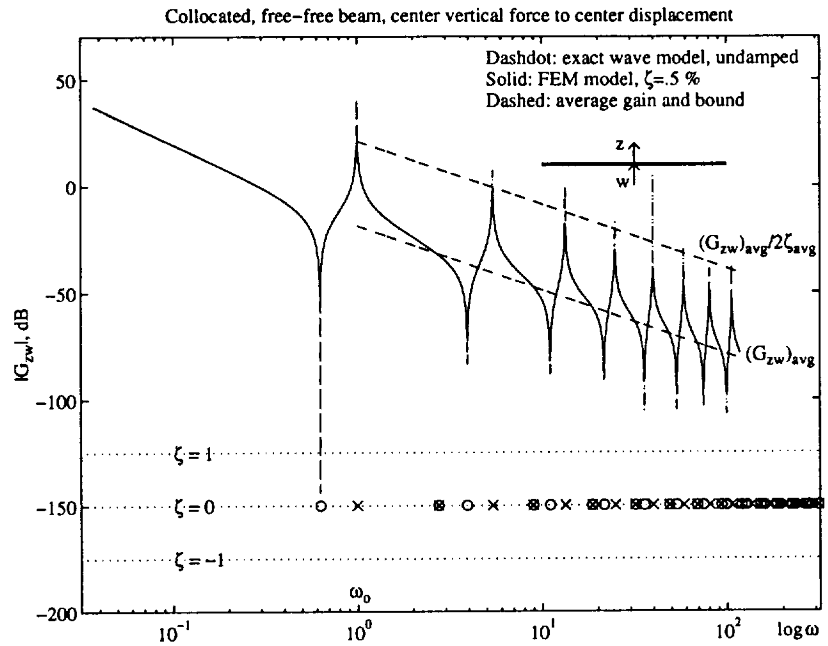

Figure 2.3: A structural transfer function magnitude with pole-zero-ζ plot. Poles are x's and zeros are o's.

the phase effects of the lightly damped structural poles and zeros, where nonminimum phase zeros would have negative damping. Viewing the compressed pole-zero map under the transfer function is an aid in understanding control limitations and hidden model intricacies. For example, the symmetry of the structural system in Fig. 2.3 greatly reduces the visible transfer function modal density via the $j\omega$ axis pole-zero cancellations (shown) of the antisymmetric modes.

Conventionally, a detailed finite element model is constructed, some estimate of modal damping made, and the solid lined transfer function of Fig. 2.3 computed from first or second order truncated modal forms. Mathematically, modal information from the discretized system may be represented as a summation of independent modal responses. The infinite sum depends on three modal parameters for each flexible mode; the natural frequency, ω_i, the damping ratio, ζ_i, and the modal residue, R_i,

$$G_{zw}(s) = (s^h)\left\{\sum_{i=0}^{i=n_{mod}} \frac{R_i}{s^2+2\zeta_i\omega_i s+\omega_i^2} + D_{zw}\right\}. \tag{2.11}$$

The order of s that premultiplies the transfer function, h, determines the temporal nature of the output, *e.g.* displacement, $h = 0$, rate, $h = 1$, or acceleration, $h = 2$. When the structural measurements are relative, they may be insensitive to rigid body motion resulting in $R_0 = 0$ for $\omega_0 = 0$. The D_{zw} term is not zero for a truncated model. It represents a static correction term for all the high frequency truncated modes. To ensure a finite energy norm from unit intensity white noise input to output the D_{zw} term is often folded into the structural plant. When necessary, for one disturbance,

$$R_{n_{mod}+1} = \omega^2_{n_{mod}+1} D_{zw} , \tag{2.12}$$

for a mode of arbitrary frequency, $\omega_{n_{mod}+1} > \omega_{n_{mod}}$, and arbitrary damping ratio. If the model disturbances roll off in frequency, then appending a correction mode is unnecessary, since augmenting the structural plant with disturbance weights will ensure a finite output energy.

Another form of the s-plane SISO structural response is pole, p, zero, z, gain, g form where,

$$G_{zw}(s) = \frac{g s^h \prod_{k=1}^{k=k_{zeros}} (s - z_k)}{\prod_{i=1}^{i=i_{poles}} (s - p_i)} . \tag{2.13}$$

In this form the transfer function denominator is the product of complex pole factors, $p_i = -\zeta_i \omega_i \pm j\omega_i \sqrt{1 - \zeta_i^2}$, and the numerator is the product of complex zero factors. It is the absolute value of p and z that is plotted in the pole-zero-ζ plots. The zeros are often investigated as an indication the achievable performance. Freudenburg and Looze [21] provide fundamental limitations based on nonminimum phase zeros in rational systems. Boyd and Desoer [22] extend these notions to the multivariable case. One of the purposes of this chapter is to show that controlled structural systems are in fact limited by irrational structural behavior, not the occurrence of nonminimum phase zeros explicitly.

A more reasonable method of determining the underlying physics of the transfer function is to smooth the response. In order to understand this, it is useful to introduce the average transfer function (sometimes called the dereverberated transfer function for collocated inputs and outputs) [16]. The average transfer function "smoothes" out the modal characteristics by taking local averages on the Bode plot. Alternatively, for a collocated transfer function, it can be obtained by setting the damping ratio to critical or by assuming asymptotic frequency domain mass and stiffness properties for each mode.

The average transfer function shown in Fig. 2.3 has an asymptotic log-log scale slope below the fundamental frequency (ω_o), set at -2 by the presence of a rigid body mode, or 0 for a constrained structure. For a rigid body mode, the system mass ($\int_L mdx$) sets the magnitude of low frequency transmissibility, while for a constrained structure, the stiffness (EI) influences the magnitude of the quasistatic transmissibility. The average transfer function at high frequencies also has an asymptotic slope. This is determined by the attributes of the inputs and outputs and the nature of the simple structural element. For a beam the log-log slope commonly ranges from $-3/2$ for a force input to a displacement output, to $-1/2$ for a moment in to an angle out. If the output is rate or acceleration, the slope will increase by one or two depending on the number of differentiators needed. Physically the collocated average transfer function captures the direct displacement field response of the structure, independent of far field boundaries.

The resonant aspect of the transfer function, however, is a result of standing wave motion or modes within the structure and is thus dependent on the nature of the structural boundary conditions as well as the properties of the structure itself. It can be coarsely characterized by the modal density, ρ_{ω_i}, and the average damping ratio, ζ_{avg}. A line drawn by a factor of $1/2\zeta_{avg}$ above average transfer function bounds the magnitude of the resonant response. Clearly this bound is conservative for the finite element model with constant modal damping. The reason is that for this model the modal residues are monotonically decreasing with increasing modal frequency. In realistic truss structures the damping ratio decreases at high frequencies [23], an effect due to roughly stiffness proportional structural damping and the spatial localization of the modes. This effect counters the reducing residues and the modal peaks rise to gains that are bounded by the general amplification factor $1/\zeta_{avg}$.

Thus with six parameters, the degree of constraint and nature of the inputs and output (which set the slopes of the asymptotes), the frequency and mass (which set the intercept of the asymptotes) and the damping ratio and modal density (which bound the resonant behavior), the transfer function can be quantitatively characterized. This insight can be used to estimate the transfer function, without any other modeling, or to interpret the results of a coarse finite element model, and make conceptual decisions on subsequent structural modifications.

2.3 Fundamentals of Noncollocated Simple Structures

As stated in the introduction this thesis intends to provide a method for preliminary design of controlled structures. In preliminary design a more detailed knowledge of system properties is required to ascertain, for example, stability. Now that a general physical interpretation of structural transfer functions has been given, a more detailed investigation of some simple examples is needed to define some ideas that are central to interpretations in the thesis. It is proposed that two necessary considerations for controls-structures optimization are average transfer function gain and structural phase loss. These two attributes are detailed in this section for a simple rod and a beam. These two simple elements make up the complicated truss structures studied in this thesis and are fundamental building blocks of all complex structures.

First, an axial force u to displacement y, input-output pair is examined on a free-free rod. The rod motion is governed by a non-dispersive second order partial differential equation. Exact, finite element and modal residual interpretations of resulting transfer functions are given. The exact, Laplace solution for a free-free rod is so simple it is given here,

$$G_{yu}(x_y) = \frac{c}{EAs} \frac{cosh(\frac{s}{c}(L - x_y))}{sinh(\frac{sL}{c})}, \tag{2.14}$$

where c is the speed of sound in the rod, $\sqrt{E/\rho}$, s is the Laplace variable, L is the length of the rod, and x_y is the placement of the displacement sensor from the left end. There are a few key characteristics of the exact definition of Eqn. 2.14 that carry over to the complicated exact expressions for beams. The first characteristic is that the high frequency average transfer function asymptote is defined to be $\frac{c}{EAs}$, having slope of -1 when plotted on a log magnitude versus log frequency scale. The remaining irrational transcendental function involves exponentially growing functions that fluctuate with increasing log frequency density.

To define the usage of modal residuals before studying the noncollocated case the collocated rod pair transfer function is plotted in Fig. 2.4. In this case the finite element model and the exact model are compared over a much higher modal density than the previous collocated beam example. The finite element model uses 62 elements and begins to show discrepancies with the exact modal frequencies at about the tenth mode. The important notion is that of cumulative residual,

$$R_{cum} = \sum_{i}^{i\geq p} \frac{R_i}{\omega_i^2}, \tag{2.15}$$

where the static terms for all the modes above and including the ordinate ω_p are summed and the magnitude of the resultant plotted. The cumulative residuals, R_{cum} are plotted as *'s in Fig. 2.4. Conceptually, for a collocated input/output pair, the complex zeros are found near the intersection of this static asymptote and the cumulative inertial terms of the lower modes,

$$\sum_{i}^{i<p} -\frac{R_i}{\omega^2}, \tag{2.16}$$

to the left of each plotted point. Modal mass is included in the R_i. For a collocated system the intersections result in complex zeros because of the sign of the cumulative residuals with respect to the cumulative inertias.

Below the tenth mode the cumulative residuals track the high frequency average transfer function gain. Above the tenth mode discretization and high modal density cause the residuals to depart from the average gain. The important conclusion is that asymptotic residual modal stiffness holds the average transfer function gain high.

The free-free rod represents an interesting case in that under a certain noncollocated condition, $x_y = L$, there are no finite frequency transmission zeros in the exact transfer function. One use of this example is to study the effects of discretization on

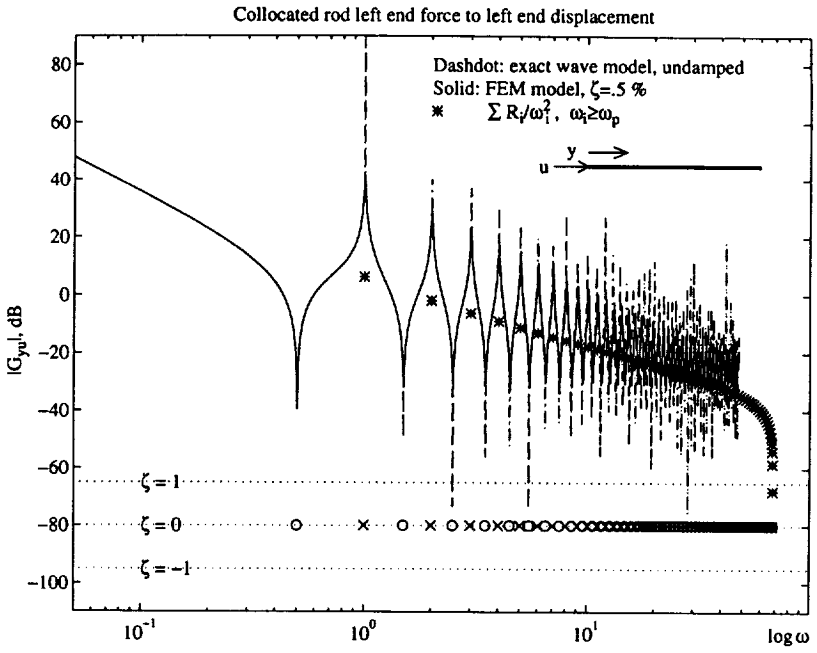

Figure 2.4: Rod collocated transfer function magnitude where a 62 element FEM is compared to the exact solution.

zeros. The example will also be used to study the average transfer function gain of a simple nondispersive noncollocated system. Figure 2.5 shows the example, comparing the undamped exact model with a .5 % damped FEM. Again cumulative residuals are shown. The pole-zero-ζ plot is shown with discretization zeros plotted for two levels of damping assumed in the finite element model.

All the pole-zero structure apparent in the collocated example appears to have fallen apart. However, the average transfer function has not changed. The exact asymptote is unchanged, fixed with log-log slope of -1. Only the numerator of the transcendental function has changed. The poles do not change with sensor position.

Zeros have appeared due purely to FEM discretization. When the FEM is uniformly damped to .5 % the zeros occur in minimum phase, and nonminimum phase, complex pairs with decreasing damping as frequency increases. They are plotted as o's. These nonminimum phase and minimum phase pairs do not form quadrantal symmetry in the s plane. The nonminimum phase zeros are offset from the minimum phase in frequency. When the FEM model damping is reduced to zero, the occur-

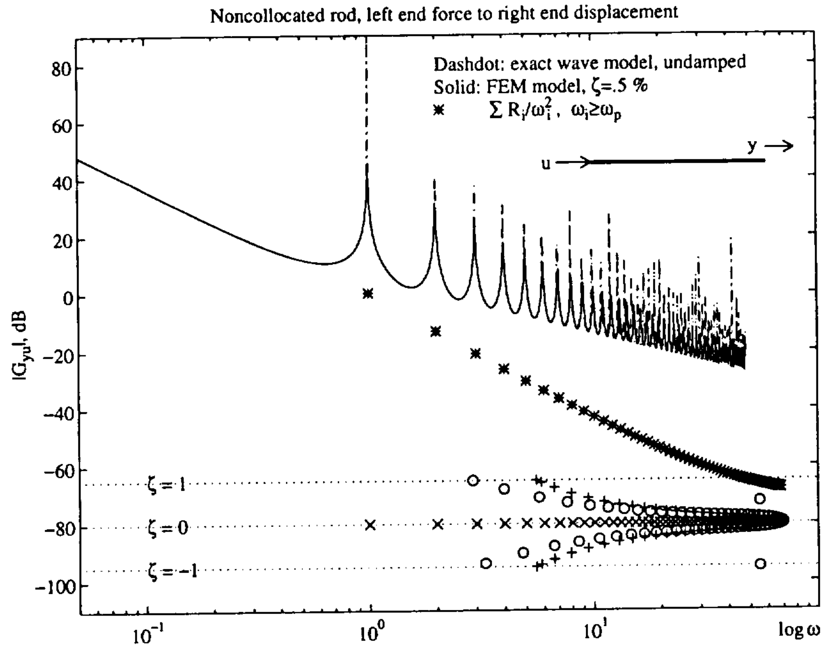

Figure 2.5: Rod noncollocated transfer function magnitude where a 62 element FEM is compared to the exact solution. Zeros, o, are computed from the FEM with .5 % damping, +'s are computed from the FEM with no damping.

rence of the discretization zeros is delayed in frequency and quadrantal symmetry is realized, shown by the +'s. Again, they decrease in damping with increased frequency. The significance of quadrantal symmetry is that the net effect of a complex zero quartet is purely magnitude increase with no corresponding phase. They pass high frequencies with increasing gain.

Since these zeros are due to pure discretization effects it is natural to assume that their location in frequency will be sensitive to spatial discretization. For the undamped FEM the onset of the zeros was found to occur at 52, 54 and 60 Hz for 31, 62 and 124 element discretizations respectively. Apparently,

> *"discretization zeros are more sensitive to assumed modal damping than to spatial refinement."*

This is depicted by the o's starting near 30 Hz for the .5 % damped model compared to 54 Hz for the undamped model.

The nature of the discretized zeros is to provide gain increase with no average phase change. They do not, however, have a large effect on the average transfer

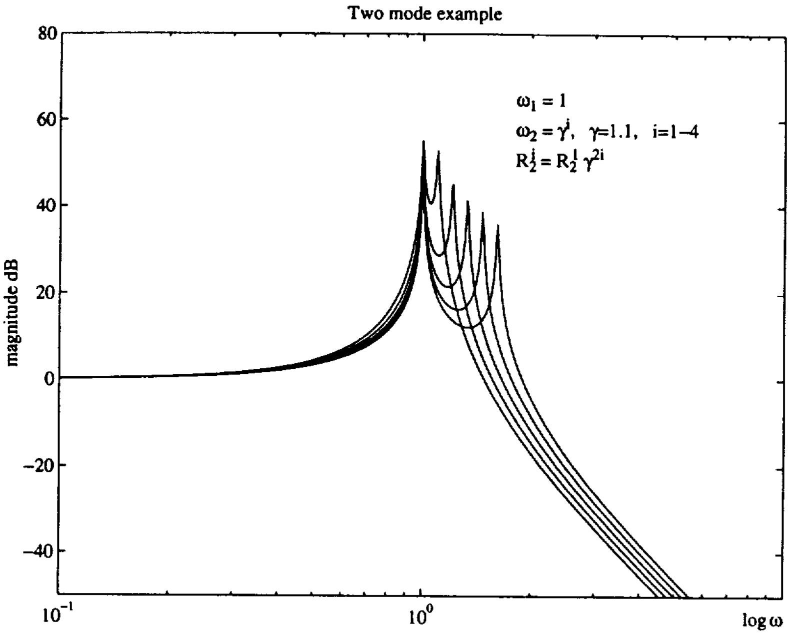

Figure 2.6: Fictitious two mode example that shows the effect of closely spaced resonance peaks with alternating residue sign.

function gain in this case. To see this note the cumulative residuals. The residual structural stiffness no longer holds the gain high. Physically, the average gain is high because of summing neighboring resonant peaks. This effect is illustrated for two fictitiously generated modes in the transfer function magnitude in Fig. 2.6. In the figure mode two has opposite sign residue to mode one. Mode two is shifted in frequency while the summed low frequency residual for the system is maintained as a constant. Note that when closely spaced the resonant curves interact to bolster the average gain. This is the effect seen in the noncollocated rod example.

The important nondimensional parameter to consider, for these closely spaced modes with opposite sign residues, is defined as,

$$\gamma_{\omega_{ij}} \equiv \frac{(|R_i - R_j|)}{(\zeta_i + \zeta_j)\omega_j(\omega_i - \omega_j)} / \left(\sum R_k/\omega_k^2\right), \tag{2.17}$$

This parameter, $\gamma_{\omega_{ij}}$, is discretely defined for neighboring modes i and j, $i > j$, of strong residue, $|R_i| \sim |R_j|$. It is derived by summing two closely spaced second order modal responses. The magnitude of expression is expanded, in terms of a point on the resonance curve at the algebraic mean of the two modal frequencies. The locus of the chosen point is investigated with damping terms set to zero as the modes are brought together. This results in the factor,

$$\frac{(|R_i - R_j|)}{\omega_j(\omega_i - \omega_j)} . \tag{2.18}$$

Simple inspection of a resonance curve close to resonance shows that the response is dominated by the inverse of the damping ratio. This factor is included in terms of the average damping ratio. Residual stiffness of the appropriate nominal transfer function is used to nondimensionalize the quotient. The objective is to reduce the parameter over a bandwidth of modes in order to bring down the average transfer gain. For example, large average ζ reduces the average gain since inputs propagating from the disturbance may never make it to the performance sensitive locations, or at least are sufficiently attenuated by the lossy medium while traveling. Another simple observation is that increased modal spacing separates the resonance peaks allowing the response in between to drop in magnitude, thus dropping the average gain. However, if this modal separation requires general softening then the effect of the factor $1/\omega_j$ competes with the factor $1/(\omega_i - \omega_j)$. Note that, since R_i and R_j are opposite in sign their individual magnitudes are summed in $|R_i - R_j|$. Reducing the magnitude of the residues also reduces the average gain.

Structural delay is evident in the phase of the system shown in Fig. 2.5 as the phase-loss due to occurrence of the poles. The nearly quadrantal zeros contribute no average net phase. Structural delay is manifested in the rate of occurrence of poles, or once again modal density. Equation 2.14 shows how the speed of sound in the structure and the dimension of the structure determine the rate in which the poles occur with increased frequency. The fundamental dilemma in controlling structures is,

> *"the average gain stays high while the phase rolls off."*

The difficulty arises in rolling off the control and maintaining stability.

A free-free beam noncollocated example is now investigated. No new insights would be gained from looking at the collocated case. The input is an inertial moment

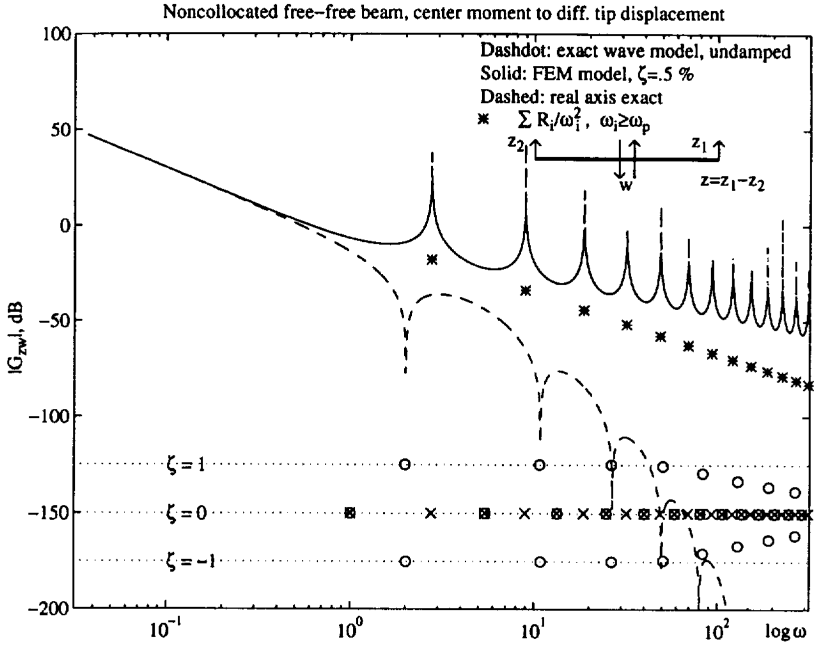
Noncollocated free–free beam, center moment to diff. tip displacement

Figure 2.7: Beam noncollocated transfer function magnitude where a 52 element FEM is compared to the exact solution.

acting at the center of the beam span and the output is the differenced vertical motion of the left and right beam tips. Since the response of a beam to distributed vertical loading is governed by a fourth order dispersive partial differential equation, the underlying physical transmission of the noncollocated structural transfer functions is different than that of a rod as shown in Fig. 2.7.

There are two properties of this transfer function worth noting. The first is that there are no apparent zeros in the solid and dashdot curves which are evaluated on the $j\omega$ axis. In the rod example it was sufficient to check the exact transfer function. Since, the exact expression for the beam is complicated the whole complex plane must be investigated for zeros. This is done by equating the wave number with the Laplace variable through dispersion. Effectively a quadrant of the complex plane is spanned on radial lines from the origin. Zeros are found on the real axis as shown by the dashed curve in Fig. 2.7. They must occur in pairs due to the fact that the transfer function evaluated on the $j\omega$ axis is a real function. Zeros found from the FEM model of the beam confirm this. Eventually discretization effects are inevitable as depicted by the decrease in damping of the zeros near 100 Hz. In the FEM complex pole-zero cancellations arise due to the unobservable/undisturbable symmetric modes.

Even though the exact expression for the beam is complicated, see Appendix A, there still exists a simple factor representing the average transfer function gain. The average gain has slope of -1 in the log-log plot. Again, the cumulative residuals lie underneath the transfer function gain, showing the importance of the modal spacing in the average gain. In this case there is help keeping the transfer gain high from the real zero pairs, but as before it is not significant on a log scale. These zero pairs contribute no phase loss to the system.

> *"The structural delay phase loss is, once again, realized by the rate at which poles occur with increasing frequency."*

The free-free beam example closely mimics the first application design example. In the application example there are lumped masses in the center and at the tips representing spacecraft bus and payload respectively. The lack of complex zeros in the simple beam shows how hard this example will be to control with relative structural actuators.

2.4 Fundamental Sensitivities

In this section simple systems are investigated to show the sensitivities to fundamental parameters. The sensitivities are not used in the evolutionary design in this thesis. They are given to show the returns-to-scale from performing structural optimization on an assumed structurally controlled system.

The sensitives are broken into two objectives. The first objective is to reduce the average transfer function gain from disturbance to performance. This objective assumes that control action serves only to dampen the flexible modes. The second objective is to improve pole-zero spacing in a collocated control loop. Here, the desire is to improve the ability of a controller to dampen and, under certain conditions, stiffen or destiffen the plant.

First analytical expressions for the average transfer function gain of simple collocated systems are integrated to yield displacement based performance costs, J_z of

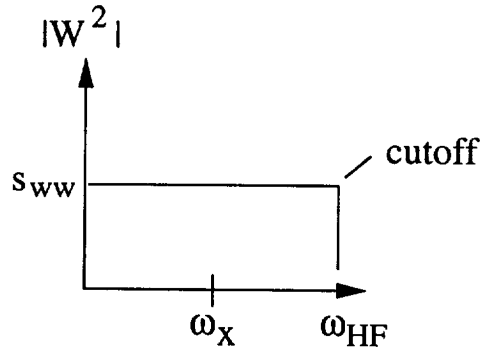

Figure 2.8: Ideal input spectrum for average transfer.

Eqn. 2.3. These costs are investigated for their sensitivity to fundamental parameters. Numerics are next used to show the average transfer gain sensitivity of the noncollocated beam example from the previous section. A specific expression for structural system zero perturbations is given which is by no means general, but is sufficient to illustrate the important sensitivities for improving pole-zero spacing for a given input/output pair.

Assuming dampening via control in the collocated disturbance to performance case renders the mean square performance as the square of the area under the average transfer function gain curve. The strategy here is to use asymptotic expressions for the average transfer function gain computed from wave domain solutions, see Appendix A and Ref. [16]. The squares of these asymptotic transfer functions are integrated assuming an input disturbance with fixed intensity s_{ww}. Assuming an ideal broadband input with high cutoff frequency, ω_{HF}, as shown in Fig. 2.8, allows exact computation of the upper limit in the integral of Eqn. 2.3.

Certain systems may be indefinite at the lower limit of Eqn. 2.3, *i.e.* systems with observable and disturbable rigid body modes. When considered, these systems are corrected to have finite rigid body mode frequency, ω_{RB}. The resulting performance can be interpreted in the limit as this frequency approaches zero. Case two of Fig. 2.9 shows such a case.

Cases are shown in Fig. 2.9 that span an inertial input/output pair acting in a single dof system to a relative input/output pair acting in a distributed system. For

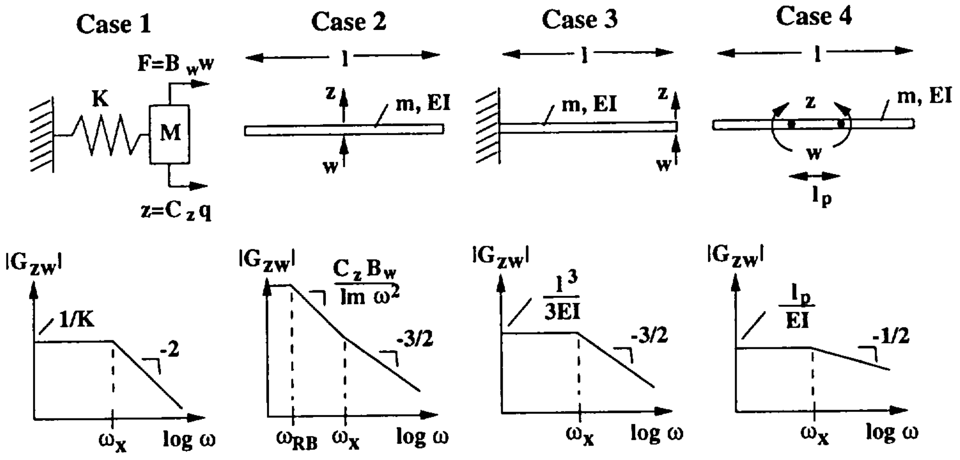

Figure 2.9: Collocated input/output cases for exact computation of J_z from average transfer function asymptotes.

each case, an asymptote and slope are given on schematics of the system transfer functions. Input influence coefficients are denoted as B_w while output influence coefficients are denoted C_z and are shown explicitly in case 1. The asymptotes intersect at frequency ω_x. Specifically, the performance is integrated as,

$$J_z = 2\int_0^\infty G_{zw}^H S_{ww} G_{zw} d\omega\,, \tag{2.19}$$

where S_{ww} is the general disturbance intensity, which was denoted as s_{ww} for a single input. Results for each case are listed in Table 2.1. Case three lists the performance in two different forms. The first in terms of the intersection frequency ω_x. The second in terms of the low frequency asymptote. For each case an explicit expression is shown for the intersection frequency, ω_x, and the fundamental structural mode ω_o. In case one the two frequencies are equal, in cases two and three they are close to equal and in case four they are similar if l_p, the separation between the moment pair is approximately equal to $l/5.6$.

The performance expressions listed in Table 2.1 show several interesting trends. The first three cases have a term proportional to $1/\omega_x^3$. The second case includes the singular term $1/\omega_{RB}^3$ which tends to infinity as the rigid body frequency nears zero. Take case one, for example. Stiffening the spring by a factor of two improves the mean square performance by a factor of $1/(2\sqrt{2})$. In case two the mean square performance is dominated by the first term in the bracketed expression. Assuming a uniform

Table 2.1: Exact expression for performance integrals of asymptotic collocated systems. For the first three cases $\omega_{HF} = \infty$.

Variable	Case 1	Case 2	Case 3	Case 4
J_z	$\frac{s_{ww}(C_z B_w)^2}{M^2} \frac{8}{3\omega_x^3}$	$\frac{s_{ww}(C_z B_w)^2}{(lm)^2}(\frac{8}{3\omega_{RB}^3} + \frac{1}{3\omega_x^3})$	$\frac{s_{ww}(C_z B_w)^2}{(lm)^2} \frac{3}{\omega_x^3}$	$\frac{2s_{ww}(C_z B_w)^2 l_p^2}{(EI)^2}\omega_x(1 + \ln \frac{\omega_{HF}}{\omega_x})$
J_z			$s_{ww}(\frac{l^3}{3EI})^2 \frac{3}{2}\omega_x$	
ω_x	$\sqrt{\frac{K}{M}}$	$\frac{16}{l^2}\sqrt{\frac{EI}{m}}$	$\frac{3}{l^2}\sqrt{\frac{EI}{m}}$	$\frac{1}{2l_p^2}\sqrt{\frac{EI}{m}}$
ω_o	$\sqrt{\frac{K}{M}}$	$\frac{(4.73)^2}{l^2}\sqrt{\frac{EI}{m}}$	$\frac{(1.875)^2}{l^2}\sqrt{\frac{EI}{m}}$	$\frac{(4.73)^2}{l^2}\sqrt{\frac{EI}{m}}$

beam rectangular cross-section, a simple doubling of the thickness, t, decreases the performance by a factor of 1/4 since $m \sim t$. This is purely an inertia effect. In the constrained case, case three, the performance is strongly influenced by inertia and flexibility. Increasing cross-section thickness (again assuming rectangular) by a factor of two improves the performance by a factor of $1/2^5$ since $\omega_x \sim t$ and, as before, $m \sim t$. Now consider the beam in case three to be a cantilevered uniform truss where, $EI \sim r_g^2 A$ with A being the longeron strut cross-section area and r_g is half the truss cross-section depth. In this case $m \sim A$ also, so that ω_x does not, to first order, depend on changes in A. Increasing the member wall thickness by a factor of two will now only improve the performance by a factor of 1/4 through the inertia term $(lm)^2$.

> *"This shows the reduced effectiveness of a truss optimization that changes member sizes only."*

Considering topological changes such as r_g improves the performance sensitivity, as in this case $\omega_x \sim r_g$, so that the performance $\sim 1/r_g^3$.

The last case in the table is an interesting one because its upper limit of integration is undefined. A higher bandwidth of disturbance ω_{HF} results in worse performance by the factor $\ln \omega_{HF}/\omega_x$. This is because the average gain does not roll off fast enough at high frequencies. Increasing the uniform thickness of this beam improves the performance by a factor of 1/4, again a reduced sensitivity when compared to the cantilevered case. The performance is dependent on the square of the separation length of the moment pair, l_p. Reducing this parameter by a factor of two improves the performance by a factor of 1/4. Note as $l_p \rightarrow 0$ the performance is driven to zero and the natural logarithm diminishes. This is simply the input and output sensitivities cancelling.

All of the above cases depend on the square of the disturbance intensity and the square of the input influence coefficient. The power of disturbance isolation is realized in this dependency, where for a given s_{ww} the objective is to reduce B_w for modes above the isolation resonance. Similarly performance isolation reduces C_z for modes above the isolation resonance. When the disturbance and performance act and measure at a point, as in the cases shown, these coefficients can easily be halved with active control systems that incur less structural mass penalty than incurred by doubling the beam thickness.

Exact wave domain expressions for noncollocated average transfer function gains can be calculated and are presented in Ref. [16] and [12]. Expressions like those presented in Table 2.1 can be computed and similar sensitivities to fundamental structural parameters found. The results show the same trends as those in Table 2.1. However, it was stated earlier in the chapter, that these average transfers depend on closely spaced resonance effects. Since the wave models are undamped the FEM model of the beam in Fig. 2.7 will be used to investigate the effect of damping on the high frequency average gain.

Figure 2.10 shows the effect of changing the FEM damping from $\zeta = .5$ to $\zeta = 10$. At high frequencies the dashed curve asymptotes to the same slope as the cumulative residuals that are plotted as *'s. This effect shows that for uniform damping treatment (such as that obtained from cabling and thermal blanketing) the high frequency disturbances are attenuated by the lossy medium in which they travel around the structure.

> *"When poles of appropriately signed residues are closely spaced, adding damping attenuates the average transfer function response."*

The attenuation confirms the resonance effects hidden in the average gain.

Another goal for a noncollocated disturbance to performance topology might be to reduce the cumulative residual in a bandwidth emphasized by disturbances. For example, target the bandwidth of near the third mode in the above system. The

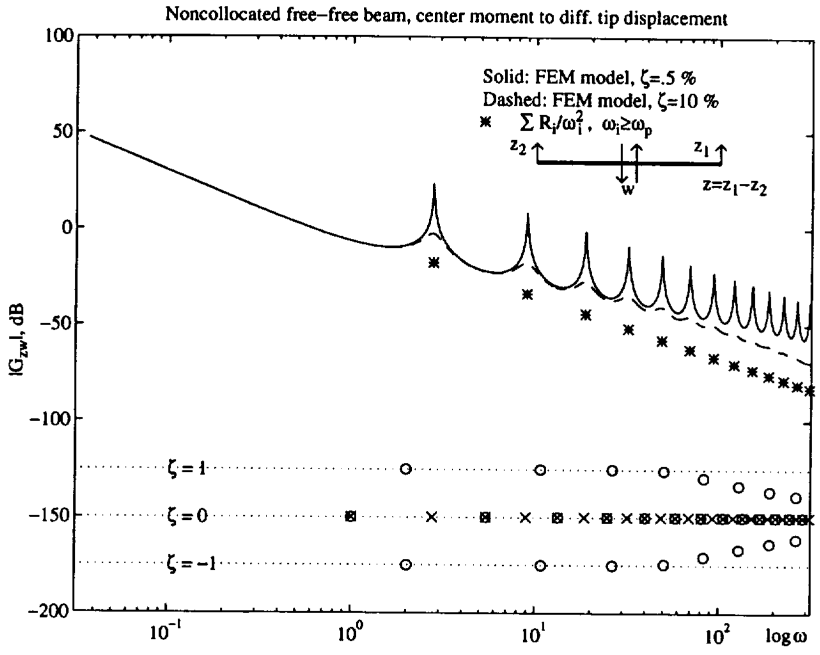

Figure 2.10: Beam noncollocated transfer function magnitude where a FEM with $\zeta = .5$ % is compared with the same FEM with $\zeta = 10$ %.

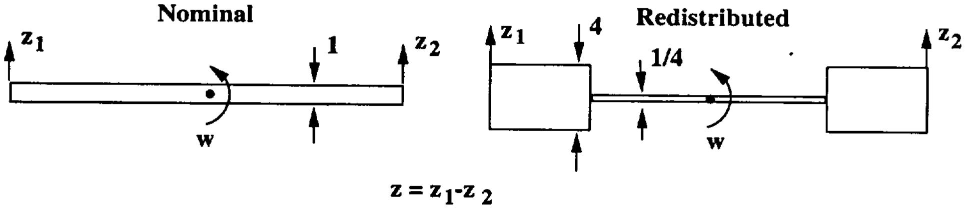

Figure 2.11: Postulated stiffness change for reducing noncollocated average gain.

difference between the average transfer gain and the cumulative residuals appears to be $\approx$ 10 dB. At this point a structural distribution that is physically motivated by results presented later in this thesis is used. The distribution is shown in Fig. 2.11.

The transfer function for the redistributed system, dashed, is compared to that of the nominal beam, solid, in Fig. 2.12. As evidenced by the figure the objective has been achieved. The average transfer function gain has been reduced near the nominal third mode. Cumulative residuals for the redistributed system are plotted as +'s. The cumulative residuals have been reduced in the region local to the third mode. In the proposed parameter of Eqn. 2.17 the residues are included in the numerator. The

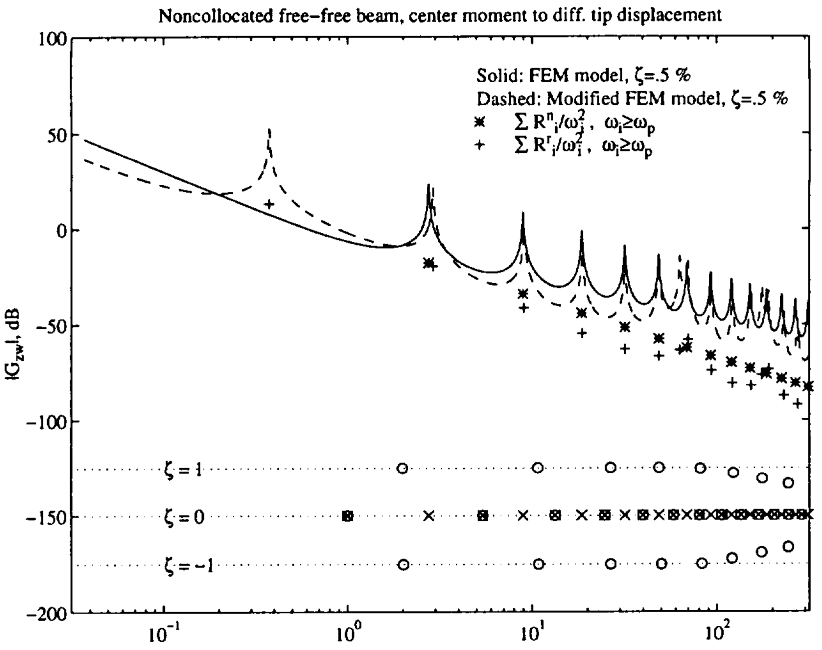

Figure 2.12: Beam noncollocated transfer function magnitude where the nominal FEM with $\zeta = .5$ % is compared with the redistributed FEM with $\zeta = .5$ %.

modal spacing has indeed been increased between respective pairs, but the general softening of the modes has compromised these improvements in the average gain. Results like this one are expected to scale well to truss and fuselage like structures which often exhibit pass bands and stop bands in their transfer functions due to the regularity with which they were built.

> *"Manipulation of topological variables in truss structures, such as node locations and member connectivities, is expected to do extremely well in reducing transmissions from high frequency narrow band disturbances to sensitive performance locations."*

A good study that shows this effect for open loop two dimensional truss structures is provided by Keane [24, 25, 11].

The task remains to provide dampening of the high frequency modes so that the performance gains of reducing the average transfer gain can be realized.

Assumptions such as uniform damping increase are clearly an overstatement of the ability of a structural control system to act on a complicated structure. There are many good examples in the literature to support this assertion [26, 27, 28, 29,

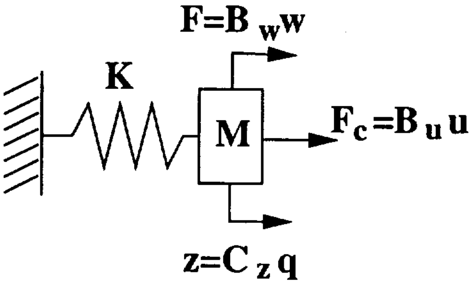

Figure 2.13: Single degree of freedom example for analytical LQR performance computations.

30, 31]. However complicated, there is a simple example in the published literature that enumerates the effect of closed loop parameters on the performance of a simple single mode system. Exact analytical closed loop Linear Quadratic Regulator costs were computed for a collocated single mode system by Jacques [32] and worked into a more concise form by Crawley in both publications [17] and [12]. Figure 2.13 shows the system under consideration. In the figure influence coefficients B_u map the controls u onto the mass. The solution requires the exact solution of the standard regulator Riccati equation for a two state system. Tabulated results from Ref. [12] are repeated here in Table 2.2. It is not possible to do justice to this table in just a few short paragraphs. However, there are some important characteristics worth noting. This simple LQR result will show the sensitivity of the performance to limited gain (intermediate control penalty, ρ) and high gain (small control penalty) closed loop control. In Table 2.2 further parameters such as control power are represented as,

$$J_u = \int_0^{\infty} u^T u d\tau \,, \tag{2.20}$$

and subscripts CL placed on ζ and ω_o refers to closed loop parameters. In the first column limits of ρ are given that describe the ranges of control action.

Compare the open loop J_z and the closed loop J_z when considered as a function of ζ_{CL} and ω_{CL} with the integrated performance in case one of Table 2.1. The difference is that the damping ratio is integrated into the constant in the asymptotic calculation. For expensive control $\lim \rho \rightarrow \infty$ the compensation gains serve to dampen the system. The closed loop performance is inversely proportional to the closed loop damping

Table 2.2: Optimal linear quadratic regulator performance contribution from single mode

Asymptote	$J_z(\rho)$	$J_z(J_u)$	ζ_{CL}	ω_{CL}^2
open loop	$\frac{C_z^2 B_w^2 s_{ww}}{4M^2\zeta\omega_o^3}$	$\frac{C_z^2 B_w^2 s_{ww}}{4M^2\zeta\omega_o^3}$	ζ	ω_o^2
damps mode ($\lim\rho \to \infty$)	$\frac{\rho^{\frac{1}{2}} C_z B_w^2 s_{ww}}{2M\omega_o B_u}$	$\frac{C_z^2 B_w^4 s_{ww}^2}{4M^2\omega_o^2 B_u^2 J_u}$	$\frac{C_z B_u}{\rho^{\frac{1}{2}} M\omega_o^2} + \zeta$	$\approx \omega_o^2$
stiffens mode ($\lim\rho \to 0$)	$\frac{\rho^{\frac{3}{4}} C_z^{\frac{1}{2}} B_w^2 s_{ww}}{2^{\frac{3}{2}} M^{\frac{1}{2}} B_u^{\frac{3}{2}}}$	$\frac{27 C_z^2 B_w^8 s_{ww}^3}{64 M^2 B_u^6 J_u^3}$	$\approx .707$	$\frac{C_z B_u}{\rho^{\frac{1}{2}} M} + \omega_o^2$

ratio ζ_{CL}. Improving ζ_{CL} by an order of magnitude is not uncommon in controlled structures, resulting in an order of magnitude improvement in the mean square J_z. High levels of control, $\lim\rho \to 0$, result in stiffening of the single dof system, the damping ratio being fixed at the order two Butterworth pattern (.707). The point here is that the performance goes like $1/\omega_{CL}^3$.

> *"Stiffness control has a large effect on the closed loop performance, but at a price, the control power required is also large."*

A classic example of this result is attitude control. Structural control of realistic systems has yet to realize good stiffness control results. The postulate is that combined controlled structures optimization will yield better results for the same, or less, control power by allowing stiffness variations to enable control.

An objective in enabling structural control of distributed systems is even pole-transmission zero spacing over the important bandwidth in the transfer functions from controls to sensors. It is also desirable that the transfer function be collocated over that particular bandwidth and beyond where the control must be rolled off or up. To study this sensitivity a simple first order sensitivity of system transmission zeros is given. This is by no means a general expression because of the implicit sensitivities required in order to compute that of the zeros.

There are many definitions for MIMO system zeros, one will be given here, for others see the Control Handbook published by CRC [33]. Open loop system transmission zeros of a particular MIMO transfer function, for example G_{zw}, are found by solving the generalized eigenvalue problem,

$$\begin{bmatrix} z_i I - A & -B_w \\ -C_z & -D_{zw} \end{bmatrix} \eta_i \;=\; 0\,, \tag{2.21}$$

where the subscript i stands for the ith zero. Zero sensitivities can be found in similar fashion to a structural eigen problem. The problem is generally no longer symmetric, requiring the left eigenvectors, ψ, where

$$\begin{bmatrix} (\psi_i^s)^H & (\psi_i^o)^H \end{bmatrix} \begin{bmatrix} \eta_i^s \\ \eta_i^i \end{bmatrix} \;=\; 1.0\ . \tag{2.22}$$

Note that here the hermitian is used since the eigenvectors are generally complex. Taking perturbations of Eqn. 2.21 and premultiplying by the left eigenvalues yields,

$$\begin{aligned} &\begin{bmatrix} (\psi_i^s)^H & (\psi_i^o)^H \end{bmatrix} \begin{bmatrix} \frac{\Delta z_i}{\Delta \alpha_k} I - \frac{\Delta A}{\Delta \alpha_k} & -\frac{\Delta B_w}{\Delta \alpha_k} \\ -\frac{\Delta C_z}{\Delta \alpha_k} & -\frac{\Delta D_{zw}}{\Delta \alpha_k} \end{bmatrix} \begin{bmatrix} \eta_i^s \\ \eta_i^i \end{bmatrix} \; + \\ &\begin{bmatrix} (\psi_i^s)^H & (\psi_i^o)^H \end{bmatrix} \begin{bmatrix} z_i I - A & B_w \\ C_z & D_{zw} \end{bmatrix} \begin{bmatrix} \frac{\Delta \eta_i^s}{\Delta \alpha_k} \\ \frac{\Delta \eta_i^i}{\Delta \alpha_k} \end{bmatrix} \;=\; 0\,. \end{aligned} \tag{2.23}$$

Since the second term in Eqn. 2.23 is zero by vector identity, the first matrix term may be expanded (dropping the subscript i) to give,

$$\frac{\Delta z}{\Delta \alpha_k} \;=\; \frac{1}{(\psi^s)^H \eta^s} \left[(\psi^s)^H \frac{\Delta A}{\Delta \alpha_k} \eta^s + (\psi^o)^H \frac{\Delta C_z}{\Delta \alpha_k} \eta^s + (\psi^s)^H \frac{\Delta B_w}{\Delta \alpha_k} \eta^i + (\psi^o)^H \frac{\Delta D_{zw}}{\Delta \alpha_k} \eta^i \right]. \tag{2.24}$$

Terms in this last equation depend implicitly on derivatives of open loop structural system eigenvectors. These derivatives are easy to find for distinct eigenvalues, for example by Nelson's method [34]. Problems arise when there are multiplicity of eigenvalues. Many good references exist which cover these cases [35, 36, 37]. Recently even algorithms for nearly defective systems (multiplicity of eigenvectors) have become available in the literature [37].

The reason for developing the expression in Eqn. 2.24 is the relative importance of the terms. The first term shows how the zero sensitivities are directly related to the sensitivities of the poles, $\Delta A/\Delta \alpha_k$. The last term, $\Delta D_{zw}/\Delta \alpha_k$ shows that model truncation effects should not be ignored when taking the sensitivities. Terms two and three show the importance of considering the mode shapes. Generally, for a global stiffness change the first term dominates terms two and three and the zero perturbations track that of the poles, of course they do so in differing directions, ψ^s and η^s. For relative inputs and outputs that act through a stiffness, like that of the piezoelectric strut actuator shown in Eqn. 2.7, a local change in stiffness brings terms two and three on par with the first term. By far the largest sensitivity in Eqn. 2.24 occurs when considering $\Delta\alpha_k$ to loosely represent an actuator/sensor location change. In this case the first term is negligible (accept when the input/output pair is massive or excessively stiff) and the second and third terms relatively large. That is the zeros perturbations do not track that of the poles.

> *"Input output location changes therefore provide the largest sensitivity for changing pole-zero separation in a bandwidth."*

2.5 Summary

In this chapter systems definitions are presented from the perspective of controlled structures interconnections of Fig. 2.1. A basic overview of inputs and outputs is given in terms of performance, disturbance, actuators and sensors. Simple examples of modeling relative and motion prescribed inputs and outputs are given that are relevant to modeling needed for the examples in the thesis. Fundamental terminology in structural modeling is given for a simple beam example. The terminology encompasses a physical parameterization of structural transfer functions based on wave model notions.

Further investigation of noncollocated systems showed the importance of the resonant peaks in the average flexible response. A simple rod showed the effects of FEM discretization on model zeros. These zeros are shown to be very sensitive to the assumed modal damping and weakly sensitive to spatial discretization. A simple beam showed the occurrence of physical real zero pairs. Although the tendency of all the zeros found was to increase the average gain while having no effect on the phase, they do not contribute strongly to the overall average transfer gain at high frequencies. Closely spaced resonances were found to hold the average transfer function gain high.

A nondimensional parameter was proposed which details this effect. Structural phase loss was shown to occur because of the onset of poles in both dispersive and non dispersive examples.

Exact expressions for the mean square performance under simple average transfer function asymptotes were given. The expressions showed the sensitivity of the performance to changes in basic structural parameters. A numerical investigation of the sensitivity of a noncollocated beam system average gain showed that, as expected, increasing average damping improved the performance. The improved performance is due to the fact that emanating waves from the disturbance are attenuated by loss before reaching the performance. Sensitivity of the average gain was also shown to a stiffness redistribution strategy. Where the poles are separated the average gain is seen to be reduced showing that the proposed nondimensional parameter adequately describes the performance objective.

Closed form analytical expressions for a single dof LQR control example were recited from the literature. From these expressions sensitivities of performance were given to closed loop damping and stiffness control. The ability to achieve these levels of control in realistic distributed systems was noted.

Perturbations for system transmission zeros was given. The equation was used to point out the relative effects of structural changes on the ability to change the pole-zero structure. Input/output location changes were shown to strongly affect the pole-zero separations.

With these insights a method is now developed that evolves a general controlled structural system with all the necessary considerations for model based control.

Chapter 3

Method Formulation

A method was developed that can handle controlled structures with many dof, topological variations, and dynamic compensation techniques. The method originated from a modeling for control perspective. Only zeroth order objective/fitness evaluations are used with a Genetic Algorithm (G.A.) search. The search is performed over possible structural components, which may include internal member properties, nodal locations and member connectivities, and actuator/sensor locations. Dynamic controllers are solved for as an inner, closed form, solution for each design. Figure 3.1 outlines the method flow.

The method can be separated into two procedures. The first is objective function, or cost, evaluation. This occurs for every model in each generation of designs. The second procedure is the propagation of information from one generation to the next. In the following two sections the first addresses modeling and cost evaluation and the second presents design propagation. Several discrete processes arise when modeling a realistically dimensioned structural system for control. These discrete processes require that only zeroth order information be used to compare designs.

3.1 Objective Function Evaluations

Since only zeroth order information is necessary for the genetic search, full attention may be devoted to an accurate representation of the system response. Within each

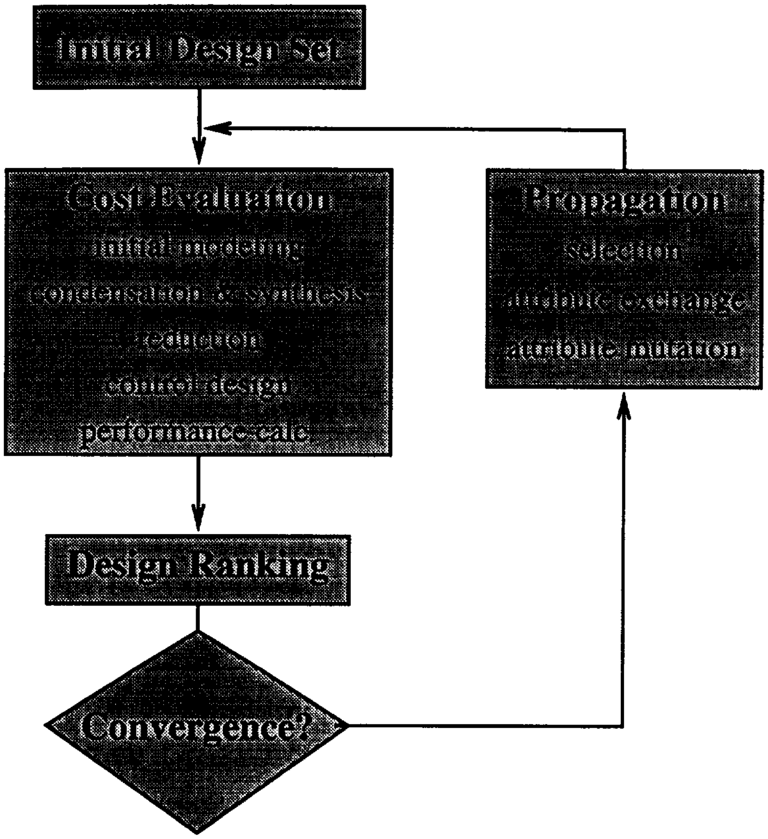

Figure 3.1: Method overview

cost evaluation a process of condensation, model reduction and weighting is performed to ready the model for dynamic controller computation. Taking derivatives of such a process is a very difficult task, since in fact they may not exist, *e.g.* differing modes may enter and leave the model basis or the model order may naturally vary based on a singular value threshold.

In the following section modeling and cost evaluation are first addressed. The discussion on modeling begins with structural models generated from component formulation, condensation and synthesis. Eigen solutions are then found for the synthesized models and state-space models formed for control design. In the application examples the proposed method for finding dynamic controllers is H_2 optimal design. A brief mention is made of the validation example control techniques which differ from H_2 design. The motion error part of the Linear Quadratic H_2 cost serves as the performance used for design ranking in the application design examples. A solution procedure for the motion error part is given as well as explicit derivatives with respect to structural parameters. The derivatives are shown to be too expensive to use during G.A. runs.

3.1.1 Modeling for control

For most structures, of realistic dimension, a full model would be too large to compute during each evaluation step. To address this problem the structure is first discretized into component models. These discretized component models are condensed and synthesized into a global model of much lower order. Typically for realistic G.A. run times, global models on the order of 200 dof were sought. An example of component wise discretization is selecting repeated structural units consisting of an integer number of bays in a truss boom.

Given each new set of structural parameters (attributes), component models, enumerated by subscript i, are assembled using finite elements [38],

$$M_i\ddot{p}_i + C_i\dot{p}_i + K_i p_i = \beta_{w_i} w_i + \beta_{u_i} u_i \tag{3.1}$$

$$y_i = c_{yp_i} p_i + c_{y\dot{p}_i}\dot{p}_i \tag{3.2}$$

$$z_i = c_{zp_i} p_i + c_{z\dot{p}_i}\dot{p}_i \tag{3.3}$$

where p are the component structural dof, w are the disturbances, u the actuation, z the local performances and y the measurements. Within the components enough fidelity is included to capture variation in local dynamics with changes in grid point location, member cross-section and actuator/sensor location. If the component doesn't include active variables (disturbances,performances,sensors or actuators) and if the internal dynamics are above the bandwidth of important performance, then quasistatic information is enough.

To reduce and synthesize component models into a manageable global model Component Mode Synthesis is used [39]. Active locations within the components, *i.e.* those actuated, disturbed, sensed and performing, are treated as interface dof. This extends an observability/controlability notion proposed by Triller and Kammer [40]. Constraint modes are used for integral structural actuators such as piezo-electric struts in a truss where as attachment modes are better suited to inertial force actuators. It is necessary to treat the active dof with care in order to preserve the integrity of the system transfer functions which in turn will determine the ability of the system to be controlled. Treatment of active dof as interface dof preserves their static response which is important for preserving the system zero locations, that enable or inhibit control.

The CMS routine (given for constraint modes only) is as follows:

- Partition ith component matrices into interior ”p_o”, and interface “p_a”, dof
- Fix interface dof and solve interior eigenvalue problem for normal modes, ϕ_i^N, ignoring local damping elements
- Find constraint modes, ϕ_i^C, via static solutions to normalized loads
- Assemble and use transformation matrix , T_i, to reduce component system

$$\begin{aligned}
T_i &= \begin{bmatrix} I & 0 \\ \phi_i^C & \phi_i^N \end{bmatrix}, \\
\overline{K_i} &= T_i^T \begin{bmatrix} k_{aa} & k_{ao} \\ k_{oa} & k_{oo} \end{bmatrix}_i T_i\,, \\
\overline{M_i} &= T_i^T \begin{bmatrix} m_{aa} & m_{ao} \\ m_{oa} & m_{oo} \end{bmatrix}_i T_i\,, \\
\overline{\beta}_{u \text{ or } w_i} &= T_i^T \beta_{u \text{ or } w_i}\,, \\
\overline{c}_{z \text{ or } y_i} &= c_{z \text{ or } y_i} T_i\,.
\end{aligned} \tag{3.4}$$

- Synthesize $i = 1, \ldots, n$ system using constraint equations that govern the interface/active dynamics. Note that the active dof may simply include concentrated dampers.

To incorporate attachment modes for the active dof appropriate interface dof would be left free during the computation of Φ_i^A, and the transformation matrix built accordingly. The component wise condensations are ideally suited to parallel computation.

Ideally each component would be condensed by dedicated floating point processors, and the global model synthesized by a master processor.

An eigen solution is now found for the synthesized high fidelity model (we have local flexibility in the form of the kept internal modes),

$$(K_{syn} - \omega^2 M_{syn})\,\psi_d \;=\; 0 \tag{3.5}$$

with mass normalization

$$\psi_d^T M_{syn} \psi_d \;=\; I \tag{3.6}$$

For control purposes the model is now further reduced using only modal information. This is accomplished using approximate balanced singular value reduction developed by Gregory [41]. In this work approximate solutions to the appropriate products of performance, observability, disturbance and controllability grammians are found. The basic assumption is that two modes are decoupled (for the purposes of balancing) if their settling times are long compared to the time it takes for the motion of the modes to move in and out of phase. This will be true if

$$\frac{\max(\zeta_i, \zeta_j)\max(\omega_i, \omega_j)}{|\omega_i - \omega_j|} \;\cong\; \frac{T_{beat}}{T_{settling}} \;\ll\; 1 \tag{3.7}$$

Given that the above is approximately true the ensuing relations are used for the approximate singular values,

$$\begin{aligned}
\sigma^2_{zw_i} &\cong \frac{\beta_{w_i}\Sigma_{ww}\beta^T_{w_i}}{(4\zeta_i\omega_i)^2}\left\{\frac{c^T_{z_i}R_{zz}c_{z_i}}{\omega_i^2} + c^T_{\dot{z}_i}R_{zz}c_{\dot{z}_i}\right\}, \\
\sigma^2_{zu_i} &\cong \frac{\beta_{u_i}\Sigma_{uu}\beta^T_{u_i}}{(4\zeta_i\omega_i)^2}\left\{\frac{c^T_{z_i}R_{zz}c_{z_i}}{\omega_i^2} + c^T_{\dot{z}_i}R_{zz}c_{\dot{z}_i}\right\}, \\
\sigma^2_{yw_i} &\cong \frac{\beta_{w_i}\Sigma_{ww}\beta^T_{w_i}}{(4\zeta_i\omega_i)^2}\left\{\frac{c^T_{y_i}R_{yy}c_{y_i}}{\omega_i^2} + c^T_{\dot{y}_i}R_{yy}c_{\dot{y}_i}\right\}, \\
\sigma^2_{yu_i} &\cong \frac{\beta_{u_i}\Sigma_{uu}\beta^T_{u_i}}{(4\zeta_i\omega_i)^2}\left\{\frac{c^T_{y_i}R_{yy}c_{y_i}}{\omega_i^2} + c^T_{\dot{y}_i}R_{yy}c_{\dot{y}_i}\right\}.
\end{aligned} \tag{3.8}$$

$$\sigma_i^2 \;=\; \alpha_{zw_i}\sigma^2_{zw_i} + \alpha_{zu_i}\sigma^2_{zu_i} + \alpha_{yw_i}\sigma^2_{yw_i} + \alpha_{yu_i}\sigma^2_{yu_i}\,. \tag{3.9}$$

where the subscript i refers to the mode number or corresponding row and column of the β and c matrices respectively. The matrices R and Σ have been included to weight the disturbances, controls, performances and sensors relatively. Weighting of these inputs and outputs with respect to each other is included in the α's. Here, system transfer function weights, evaluated at every modal frequency, as well as maximum singular value normalizations are used. The σ's are ranked and the highest modes kept, or a threshold may be set and the model order may naturally vary.

The assumption is that removing small residue modes will not degrade the ability to do control on a given plant (matrix of transfer functions),

$$\left\{ \begin{array}{c} z(s) \\ y(s) \end{array} \right\} = \left[\begin{array}{cc} G_{zw}(s) & G_{zu}(s) \\ G_{yw}(s) & G_{yu}(s) \end{array} \right] \left\{ \begin{array}{c} w(s) \\ u(s) \end{array} \right\}, \tag{3.10}$$

$$u(s) = -K(s)y(s), \tag{3.11}$$

where K is the dynamic compensation and (s) represents the Laplace variable. If there were a destabilizing mode with small residue, the optimal dynamic compensator would, generally speaking, invert this pole, limiting the stability robustness of the controller design to this pole. This leads to the conclusion that this mode should be more disturbable and observable in the performance, *i.e.* have larger σ_{zw_i}, which is exactly what most robust techniques will do for a given sensor/actuator suite.

There is still work to do to retain the integrity of the plant model for the purposes of control. When accurately predicting the ability to damp a mode, or invert a plant, in closed loop it is necessary to preserve the system transmission zeros [21]. To do this static modes are found for every disturbance and actuator,

$$\psi_s = K_{syn}^{-1} \left[\begin{array}{cc} \beta_w & \beta_u \end{array} \right], \tag{3.12}$$

and are orthogonalized with respect to the kept dynamic modes,

$$\tilde{\psi}_s = \psi_s - \psi_{d_{kept}} \psi_{d_{kept}}^T M_{syn} \psi_s . \tag{3.13}$$

The static modes are then decoupled using eigen solution decomposition,

$$\left(\tilde{\psi}_s^T M_{syn} \tilde{\psi}_s - \lambda^2 I \right) \theta = 0, \tag{3.14}$$

yielding correction modes, $\Lambda = diag(\lambda)$ and $\Theta = column(\theta)$, that are appended when forming the state space system:

$$\begin{aligned} \dot{x} &= Ax + B_w w + B_u u \\ z &= C_z x + D_{zw} w + D_{zu} u \\ y &= C_y x + D_{yw} w + D_{yu} u\,, \end{aligned} \tag{3.15}$$

where x represents the combined dynamic and static correction mode states of the system. Initially, the system can be formed in Hessenberg form with appended correction modes,

$$\begin{aligned} A &= \begin{bmatrix} 0 & I \\ -\Omega^2 & -2\zeta\Omega \end{bmatrix}, \\ \begin{bmatrix} B_w & B_u \end{bmatrix} &= \begin{bmatrix} 0 & 0 \\ \phi_d^T \beta_w & \phi_d^T \beta_u \\ \multicolumn{2}{c}{\Omega_s^{-2} \Lambda^{\frac{1}{2}} \Theta^T} \end{bmatrix}, \\ \begin{bmatrix} C_z \\ C_y \end{bmatrix} &= \begin{bmatrix} c_z \\ c_y \end{bmatrix} \begin{bmatrix} \phi_d & \tilde{\phi}_s \Theta \Lambda^{-\frac{1}{2}} \end{bmatrix}, \end{aligned} \tag{3.16}$$

where incorporated in Ω are the correction mode frequencies, Ω_s, which are chosen to be higher than the bandwidth of interest. Approximate modal damping is used, $\zeta = .5\%$, and concentrated dampers are added through rate feedback. Rigid body control is now incorporated, if needed, by feeding back the appropriate position, integral (appended integrator) and rate sensors.

Weights are incorporated in the system that emulate disturbance frequency content and possible disturbance/performance isolation. Further weights provide loop shaping capability, on u and y, that must reflect realistic capability of the actuator/sensor topology. The complete system in the notation of Doyle [42] is

$$sys = \begin{bmatrix} A & B_d C_{\tilde{d}} & 0 & 0 & 0 & B_d D_{\tilde{d}} & B_u \\ 0 & A_{\tilde{d}} & 0 & 0 & 0 & B_{\tilde{d}} & 0 \\ 0 & 0 & A_{\tilde{u}} & 0 & 0 & 0 & B_{\tilde{u}} \\ B_{\tilde{z}} C_z & B_{\tilde{z}} D_{zd} C_{\tilde{d}} & 0 & A_{\tilde{z}} & 0 & B_{\tilde{z}} D_{zd} D_{\tilde{d}} & B_{\tilde{z}} D_{zu} \\ B_{\tilde{y}} C_y & B_{\tilde{y}} D_{yd} C_{\tilde{d}} & 0 & 0 & A_{\tilde{y}} & B_{\tilde{y}} D_{yd} D_{\tilde{d}} & B_{\tilde{y}} D_{yu} \\ D_{\tilde{z}} C_z & D_{\tilde{z}} D_{zd} C_{\tilde{d}} & 0 & C_{\tilde{z}} & 0 & D_{\tilde{z}} D_{zd} D_{\tilde{d}} & D_{\tilde{z}} D_{zu} \\ 0 & 0 & D_{z_a} C_{\tilde{u}} & 0 & 0 & 0 & D_{z_a} D_{\tilde{u}} \\ D_{\tilde{y}} C_y & D_{\tilde{y}} D_{yd} C_{\tilde{d}} & 0 & 0 & C_{\tilde{y}} & D_{\tilde{y}} D_{yd} D_{\tilde{d}} & D_{\tilde{y}} D_{yu} \end{bmatrix}, \tag{3.17}$$

where the $(\tilde{\ })$ variables represent the respective weighting dynamics, and an auxiliary performance row z_a is appended for the control penalty. The corresponding system state vector is,

$$x_{sys} = \begin{bmatrix} x & x_{\tilde{d}} & x_{\tilde{u}} & x_{\tilde{z}} & x_{\tilde{y}} \end{bmatrix}, \tag{3.18}$$

which includes all the weighting states augmented to the original state vector x. For H_2 performance calculations $D_{zd} = 0$. Typically disturbances roll off as do sensors dynamics $D_{\tilde{d}\,\text{or}\,\tilde{y}} = 0$ whereas performance and control weights do not, $D_{\tilde{z}\,\text{or}\,\tilde{u}} \neq 0$. For conditioning purposes the system is next transformed to real modal form, with block second order terms as follows,

$$\begin{aligned} A_i &= \begin{bmatrix} -\zeta_i\omega_i & \omega_i\sqrt{1-\zeta_i^2} \\ -\omega_i\sqrt{1-\zeta_i^2} & -\zeta_i\omega_i \end{bmatrix}, \\ B_i &= \begin{bmatrix} \zeta_i\sqrt{\frac{R_i}{\omega_i}} \\ \sqrt{\frac{R_i}{\omega_i}} \end{bmatrix}, \\ C_i &= \begin{bmatrix} \sqrt{\frac{R_i}{\omega_i}} & \zeta_i\sqrt{\frac{R_i}{\omega_i}} \end{bmatrix}, \end{aligned} \tag{3.19}$$

where R_i is the complex modal residue for the ith mode and the B and C are formed assuming forcing input and displacement measurement with the system originally in Hessenberg form.

3.1.2 Control design and objective computation

In the application examples presented in this thesis standard H_2 control design is implemented to minimize the Linear Quadratic cost,

$$\begin{aligned} J_{LQ} &= \lim_{T\to\infty} \tfrac{1}{T}\,\mathbb{E}\left\{ \int_0^T \bar{z}^T\,\bar{z}\,\mathrm{dt} \right\} \\ &= (\|G_{\bar{z}\,\bar{w}}\|_2)^2 \,. \end{aligned} \tag{3.20}$$

subject to constraints

$$V = \begin{bmatrix} B_w \\ D_{yw} \end{bmatrix} \begin{bmatrix} B_w^T & D_{yw}^T \end{bmatrix} = \begin{bmatrix} V_{xx} & V_{xy} \\ V_{xy}^T & V_{yy} \end{bmatrix} \geq 0 \ , \ V_{yy} > 0 \,, \tag{3.21}$$

$$R = \begin{bmatrix} C_z^T \\ D_{zu}^T \end{bmatrix} \begin{bmatrix} C_z & D_{zu} \end{bmatrix} = \begin{bmatrix} R_{xx} & R_{xu} \\ R_{xu}^T & R_{uu} \end{bmatrix} \geq 0 \ , \ R_{uu} > 0 \,, \tag{3.22}$$

where $\mathbb{E}$ is the expectation operator and $\overline{()}$ is used to denote performances that are augmented with penalized controls and disturbances that are augmented with sensor noise as shown in the constraint Eqn.s 3.21 and 3.22. The solution for the dynamic compensator (K) is,

$$\begin{aligned} \dot{x_c} &= A_c x_c + B_c y \\ u &= -C_c x_c \ , \end{aligned} \tag{3.23}$$

with

$$\begin{aligned} A_c &= A - B_u F - H C_y + B_u D_{yu} C_y \\ B_c &= H \\ C_c &= F \,, \end{aligned} \tag{3.24}$$

where

$$F = R_{uu}^{-1}\left[R_{xu}^T + B_u^T P\right] \tag{3.25}$$

$$H = \left[Q C_y^T + V_{xy}\right] V_{yy}^{-1} \,, \tag{3.26}$$

and P and Q solve the following Riccati equations [43]

$$0 = PA + A^T P + R_{xx} - [PB_u + R_{xu}] R_{uu}^{-1} [R_{xu}^T + B_u^T P] \tag{3.27}$$

$$0 = AQ + QA^T + V_{xx} - [QC_y^T + V_{xy}] V_{yy}^{-1} [V_{xy}^T + C_y Q] \,. \tag{3.28}$$

These Riccati equations are solved using eigen decomposition of the Hamiltonian matrices, which are randomly perturbed if non distinct eigenvalues exist.

The controller is only guaranteed stable on the model it is given. Resulting closed loop performance is consistently limited by phase loss in the modeled system. In-the-bandwidth unmodeled (truncated or poorly discretized) dynamics may still limit actual implementation and it is this threat that requires the method be validated on a design model experiment.

Use of the H_2 control design technique allows consideration of parameter robustness through noise modeling [29, 44, 45] and unmodeled dynamics via frequency weights. At this stage in a design it is unnecessary to deal with absolute guarantees of stability or performance robustness. For the application examples in Chapter 5 extra performances and disturbances were added to the system that penalize and disturb distributed structural motion. In the actual implementations in Chapter 6 sensitivity weighted designs were used to robustify the controllers.

A good account of sensitivity weighting is given by Grocott [29]. When sensitivity weighting, derivatives of the state trajectories are taken (shown for regulation),

$$\frac{\partial \dot{x}}{\partial \alpha_i} = A\frac{\partial x}{\partial \alpha_i} + \frac{\partial A}{\partial \alpha_i}x + B_u\frac{\partial u}{\partial \alpha_i} + \frac{\partial B_u}{\partial \alpha_i}u \,. \tag{3.29}$$

with respect to certain parameters, α_i. Static condensation, $\frac{\partial \dot{x}}{\partial \alpha_i} = 0$, and assumptions on dimension, $\frac{\partial u}{\partial \alpha_i} = 0$, render an expression that is substituted in the regulator part of the cost to give,

$$\begin{aligned} R'_{xx} &= R_{xx} + \sum_{i=1}^{n_\alpha} \frac{\partial A}{\partial \alpha_i}^T A^{-T} R_{\alpha\alpha_i} A^{-1} \frac{\partial A}{\partial \alpha_i}, \\ R'_{xu} &= R_{xu} + \sum_{i=1}^{n_\alpha} \frac{\partial A}{\partial \alpha_i}^T A^{-T} R_{\alpha\alpha_i} A^{-1} \frac{\partial B_u}{\partial \alpha_i}, \\ R'_{uu} &= R_{uu} + \sum_{i=1}^{n_\alpha} \frac{\partial B_u}{\partial \alpha_i}^T A^{-T} R_{\alpha\alpha_i} A^{-1} \frac{\partial B_u}{\partial \alpha_i}, \end{aligned} \tag{3.30}$$

which implicitly requires that A be invertible. These are weighting matrices for a modified LQR problem. A dual derivation results in modified estimator noises.

Control techniques for the validation examples in Chapter 4 differ from the H_2 method presented here. In the first validation example [5](1-D beam) LQR was used for control design (the optimization cost is discussed later) assuming full state feedback. The static feedback gains, $u = -Fx_s$, required for implementation were computed using Eqn. 3.25. For the second validation example (3-D truss) the control was static gain output feedback with constraints on closed loop damping. Since vibration control was desired only at a single frequency the inner loop controls solution was obtained using gradient search. The closed loop system is simply

$$A_{cl} = A_s - B_u L C_y \,, \tag{3.31}$$

where L are the control gains.

Performances in the application examples are not considered the LQ cost J_{LQ}, but rather the integral of the modified disturbance to the motion error performance transfer function.

$$G^{cl}_{z\overline{w}}(s) = G^{ol}_{z\overline{w}}(s) - G_{zu}(s)K(s)(I + G_{yu}(s)K(s))^{-1}G_{y\overline{w}}(s)\,. \tag{3.32}$$

The superscript *cl* refers to the closed loop transfer function and superscript *ol* refers to the open loop transfer function. The subscript $z\overline{w}$ refers to the effect on the motion error structural performance from both the structural disturbance and the sensor noise. Computation of this fitness/cost only requires the solution of one more Lyapunov equation of $\mathcal{O}(A_s)$ (as opposed to the complete LQ cost which requires the solution of an $2 \times \mathcal{O}(A_s)$ Lyapunov equation). With

$$Q_s = \left[QC_y^T + V_{xy}\right] V_{yy}^{-1} \left[V_{xy}^T + C_y Q\right] \,, \tag{3.33}$$

and

$$A_{reg} = A - B_u F \,, \tag{3.34}$$

solve

$$0 = A_{reg}\hat{Q} + \hat{Q}A_{reg}^T + Q_s \,, \tag{3.35}$$

for $\hat{Q}$, giving the desired performance measure as

$$J_z \;=\; \mathrm{tr}\left\{C_z(Q+\hat{Q})C_z^T\right\}. \tag{3.36}$$

Sensitivities of this objective with respect to structural perturbations are given here. These are not used in the examples in this thesis. The reason for showing the sensitivity derivation is to show the computational cost involved with using them. Sensitivities to structural perturbation may be scaled and incorporated in the objective function and are computed for fixed actuator and sensor locations. Following a Lagrangian approach yields,

$$\begin{aligned} J_z^* \;=\;& \mathrm{tr}\left\{C_z^T C_z(Q+\hat{Q})\right\} \\ +\;& \mathrm{tr}\left\{H_1(AQ+QA^T+V_{xx}-\left[QC_y^T+V_{xy}\right]V_{yy}^{-1}\left[V_{xy}^T+C_yQ\right])\right\} \\ +\;& \mathrm{tr}\left\{H_2(A_{reg}\hat{Q}+\hat{Q}A_{reg}^T+V_{xx}-\left[QC_y^T+V_{xy}\right]V_{yy}^{-1}\left[V_{xy}^T+C_yQ\right])\right\}, \end{aligned} \tag{3.37}$$

where H_1 and H_2 are matrix Lagrange multipliers, and J represents the Lagrangian. Note that the regulator solution is implicit in A_{reg}. Taking derivatives with respect to Q and $\hat{Q}$ yields equations for H_1 and H_2,

$$\begin{aligned} \tfrac{\partial J_z}{\partial Q} \;&=\; H_1A_{est}^T+A_{est}H_1+C_z^TC_z+H_2\left[QC_y^T+V_{xy}\right]V_{yy}^{-1}\left[V_{xy}^T+C_yQ\right] &&= 0\,, \\ \tfrac{\partial J_z}{\partial \hat{Q}} \;&=\; H_2A_{reg}+A_{reg}^TH_2+C_z^TC_z &&= 0\,, \end{aligned} \tag{3.38}$$

where,

$$A_{est} \;\equiv\; A-\left[QC_y^T+V_{xy}\right]V_{yy}^{-1}C_y\,. \tag{3.39}$$

The solutions of these simply coupled Lyapunov equations are then used to compute the sensitivity of the objective function,

$$\begin{aligned} \tfrac{\partial J_z}{\partial \alpha_i} \;=\;& \mathrm{tr}\left\{\tfrac{\partial C_z^TC_z}{\partial \alpha_i}(Q+\hat{Q})\right\} \\ +\;& \mathrm{tr}\left\{H_1(\tfrac{\partial A}{\partial \alpha_i}Q+Q\tfrac{\partial A^T}{\partial \alpha_i}+\tfrac{\partial V_{xx}}{\partial \alpha_i}-\tfrac{\partial}{\partial \alpha_i}(\left[QC_y^T+V_{xy}\right]V_{yy}^{-1}\left[V_{xy}^T+C_yQ\right]))\right\} \\ +\;& \mathrm{tr}\left\{H_2(\tfrac{\partial A_{reg}}{\partial \alpha_i}\hat{Q}+\hat{Q}\tfrac{\partial A_{reg}^T}{\partial \alpha_i}-\tfrac{\partial}{\partial \alpha_i}(\left[QC_y^T+V_{xy}\right]V_{yy}^{-1}\left[V_{xy}^T+C_yQ\right]))\right\} \end{aligned} \tag{3.40}$$

The major expense of using the above expression appears to be the computational cost of the two Lyapunov equations. Fortunately, both the regulator and estimator systems are already decomposed when Eqn.s 3.27 and 3.28 are solved using Hamiltonian decomposition. However, inverses of the closed loop regulator and estimator eigenvectors are also required for solutions to the Lyapunov equations. The inverse of the regulator closed loop eigenvectors is generated when solving Eqn. 3.35, so only one extra inverse of $\mathcal{O}(n)$ is required. The real expense of computing these sensitives occurs in the computation of the derivatives such as $\frac{\partial A}{\partial \alpha_i}$ and $\frac{\partial}{\partial \alpha_i}(C_y^T V_{yy}^{-1} C_y)$ which involves structural eigenvalue and eigenvector derivatives [35, 36, 37].

Loosely speaking, the α's in the above expressions may in fact represent local actuator and sensor location changes. Since these are usually discrete changes (*e.g.* for struts in trusses) we may replace the partial derivatives with neighborhood operators. That is, define a sensitivity as a change in objective function divided by a local change in location, say centroid of a strut location to centroid of a neighboring location. In some sense, near optima, these neighborhood derivatives should be small.

The exorbitant expense of computing these derivatives precluded their usage. Sensitivities of the design solutions in Chapter 5 are explored numerically.

3.2 Outer Loop Model Propagation

For the outer loop optimization, or search, the G.A. appeals [46, 47, 48] because of its robust handling of systems that change order and its ability to handle topological changes easily. The method also has the advantage of being inherently parallel in that many independent function evaluations are required. In his experiences with optimizers and open loop structural topology problems, Keane [24], finds the G.A. to work best. The key to the G.A. is effective encoding of the system properties in the design space, *eg.* nodal locations, member cross-sections, connectivity arrangements, sensor/actuator placement. In this thesis a non simple implementation of a G.A. is used.

The method proceeds by a propagation of a discrete sample space of systems.

Initial sets of designs are usually chosen randomly, so as to *populate* the design space, and may require some projection in order to be feasible. Bounding the design space is often necessary as a multitude of options exist in the larger domain of topological variation. A simple representation of the design space is,

$$\Omega = \left\{ X^P, Y^Q, \ldots \right\} , \tag{3.41}$$

$$\begin{array}{l} \left\{ \begin{array}{cccc} x_j^1 & x_j^2 & \ldots & x_j^l \end{array} \right\} \in X , \\ \left\{ \begin{array}{cccc} y_j^1 & y_j^2 & \ldots & y_j^m \end{array} \right\} \in Y , \end{array}$$

where X and Y represent particular attribute types, *e.g.* nodal locations and member cross sections, with superscripts, $()^P$ and $()^Q$, that represent the order of variation within the type. For example, for 50 structural members each with 3 bit representation for cross section yields a variation order of 8^{50}. A particular element of an attribute of the jth design is denoted x_j^i, where x^i represents the phenotypical values of this selection. For example, x^i may represent beam properties that are the result of static condensation of particular arrangements of trusswork.

Propagation follows selection according to *fitness* (or scaled cost), f_j, whereby the best designs are given higher chance of proceeding. This is usually performed by implementing a biased roulette wheel approach [46]. Let η be a generated random variable with uniform distribution between 0 and 1. To run the roulette wheel,

$$\begin{array}{lrcl} \text{initialize} & C & = & \eta \displaystyle\sum_{j=1}^{j=n_{gen}} f_j \\ & P & = & 0 \\ & j_s & = & 1 , \end{array} \tag{3.42}$$

then run a while loop,

$$\begin{array}{lrcl} \text{while} & P & \leq & C \\ & j_s & = & j_s + 1 \\ & P & = & P + f_{j_s} \\ \text{end} & & & \end{array} \tag{3.43}$$

the end of which yields the selected parent as the j_s design.

Attributes from the randomly selected designs are transposed to yield new designs in a process called *crossover.* A standard crossover operation for attributes of type x is

$$\left(c^1 \;\ldots\; c^l \right) \in \{0,1\} \ , \tag{3.44}$$

$$\begin{array}{ccc} x_j^1 & \ldots & x_j^l \\ x_k^1 & \ldots & x_k^l \end{array} \rightarrow \begin{array}{ccc} \hat{x}_n^1 & \ldots & \hat{x}_n^l \\ \hat{x}_{n+1}^1 & \ldots & \hat{x}_{n+1}^l \end{array} \ , \tag{3.45}$$

$$\hat{x}_n^p = \begin{cases} x_j^p & \text{if } c^p = 1 \\ x_k^p & \text{otherwise} \end{cases} \ ,$$

$$\hat{x}_{n+1}^p = \begin{cases} x_k^p & \text{if } c^p = 1 \\ x_j^p & \text{otherwise} \end{cases} \ .$$

The crossover mask c is typically two uniform concatenated strings of ones and zeros, *e.g.* $c = (1,1,1,1,\ldots,1,1,0,0,0,\ldots,0,0,0)$. In more complex G.A.'s rules are applied during crossover to emulate biological functions such as *dominance* and *learning* by altering the regularity of c. In this thesis crossover is performed in each individual chromosome. It is proposed but not shown in this thesis that this encoding allows faster convergence of the solutions. This crossover is not considered simple since it is information exchange in multiple chromosomes. Before the new *children* designs are evaluated, a small amount of *mutation* introduces random allowable changes to the system attributes.

In the motion error performance based G.A.'s implemented in this thesis, fitness for each design is logarithmically scaled as,

$$f_j = M - 10 \log J_{z_j} \ , \tag{3.46}$$

where M ensures that f_j is positive. Calculated fitness values of the new designs generated from propagating attributes are compared to the population from which they came and the best half of the total pool propagated. Identical designs are eliminated from the best half in favor of the next best performers so that the next generation designs maintain some diversity.

Constraints are usually dealt with using penalty functions and projection methods that find the closest design in the feasible design space [49].

Operation of the G.A. can be understood by a growth equation for good *schemes* of attributes. Let a scheme of good attributes be H where

$$H = \left\{ z_j^p, z_j^{p+1}, \ldots, z_j^{p+n} \right\} , \tag{3.47}$$

then let $m(H,j)$ be the number of this scheme present in generation j. Growth of this number can be represented as,

$$m(H,j+1) \geq m(H,j)\frac{f(H)}{\overline{f}} \left[1 - p_c \frac{\delta(H)}{l-1} - \mathcal{O}(H) p_m \right] , \tag{3.48}$$

where $f(H)$ is the average fitness of designs representing H at generation j, $\overline{f}$ is the average fitness of the entire generation, p_c is the probability of crossover, $\delta(H)$ is the string length of scheme H, l is the total string length of the attribute string z, $\mathcal{O}(H)$ is the order or number of important attributes in H (*e.g.* if z_j^{p+4} and z_j^{p+5} do not effect the influence of H then $\mathcal{O}(H) = n - 1$), and p_m is the probability of mutation. The equation shows the number m grows with the improvement, from being H inclusive, to the average fitness, and deteriorates with finite probability of the scheme string being broken by a crossover operation. The number m also deteriorates with finite probability of the important attributes within the scheme mutating. A conclusion is that short, low-order, above average schema propagate exponentially and increase in number.

The growth equation shows that the G.A. is inefficient and converges slowly, like a power law, yet it is the inefficiency that allows a number of diverse solvable options to result when the design space is combinatorially hard. Typically the G.A. will appear to converge quickly in the early generations. This is because the underlying population is generated from a random seed, the average fitness of which is easy to improve upon. It is the very foundation of random information that allows the final designs to surpass common solutions in performance.

3.3 Summary

A simple modular method has been presented which allows search over many topological variants. The method involves current techniques for condensation, model reduction, Ritz mode correction and control computation. A modification of component mode synthesis is made to include active degrees of freedom in the interface set. Disturbance and performance weights are added to the reduction process.

The novelty in the method is that, in the frame-work of the zeroth order search technique, discrete choices can be made that allow formulation of accurate low order models for control. This frame-work allows sensor actuator placement and structural optimization to occur simultaneously while not compromising the basis of the model. Structural topology choices such as truss work arrangement and variations in nodal location may also be incorporated. Traditional sensitivities do not exist for these quantities.

The Genetic Algorithm has been adapted for topological controlled structures search using phenotype encoding of system attributes into multiple chromosomes per design. A non simple crossover operation is employed that accelerates the model mixing process. The method relies on slow exponential growth. Success of the method requires that good schemes of attributes propagate. Results from the method are not intended to be the "global optimum", that would require a tighter definition of some of the design variables and runs that take too long. The solutions are used to bring about fundamental physical insights into the best designs.

Before making use of the method to solve an application example validation against published results in the literature is required. Examples were found that test the modeling accuracy and algorithmic optimization capability of the method.

Chapter 4

Validation

Validation examples were sought to test the capability of the method against published results. The first example given in this chapter was published by Onoda [5] and represents a one dimensional high aspect ratio, low model dimension, structure with relatively simple control and useful design metric. The second example, published by Sepulveda [6], tests the ability to deal with three-dimensional structures (one of the few examples in the current literature because of the complicated nature of the results) with simplified output feedback control. Sepulveda covers motion error, control effort and structural weight design metrics. When considered together the validation examples cover two different structural dimensions, four different types of design metric and two differing control techniques.

Both validation examples will begin with statements of the optimization problem. Published results for each problem are directly compared with results from Genetic searches. Where published models are available they are compared, otherwise the models used by the G.A.'s are presented to illustrate the objectives. Presenting only the optimized costs, as is often done in the literature, gives no indication of the model accuracy of the solutions.

In both cases the proposed H_2 control design method described in Chapter 3 is replaced by the control method used by the respective authors. This shows the versatility of the proposed method in that modular blocks such as the control design technique can be replaced easily.

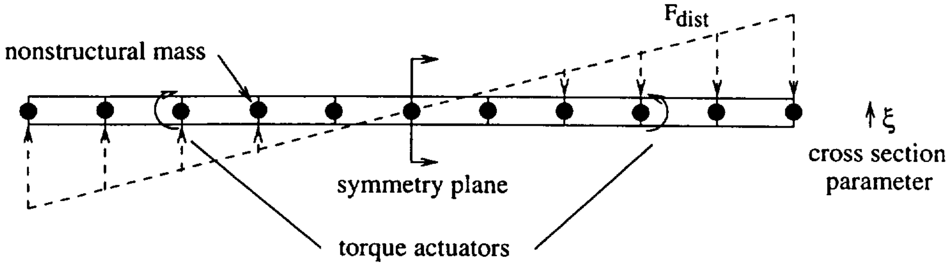

Figure 4.1: Onoda's beam example

4.1 One Dimensional Flexible Spacecraft

Onoda [5] poses a flexible spacecraft problem as a ten element beam. The beam is subject to an external distributed disturbance force where the applied forces are independent of the local mass density, as shown in Fig. 4.1. The designs are constrained to be symmetric and optimized over the cross section variable ξ and a paired actuator location. In this case the actuator provides rigid body control as well as being capable of controlling the flexible dynamics.

The optimization problem is posed as,

$$\min\ J_{design} = \frac{(m_s + \alpha\sigma_u)}{m_N} \tag{4.1}$$

where m_s is the structural mass,

$$\sigma_u = \int_0^\infty u^T u \,\mathrm{dt} \tag{4.2}$$

is the LQR control power, which is converted to units of mass via $\alpha \approx 10$ [kg/(N.m)^2], and m_N is a normalized mass set to twice the structural mass of the nominal system (there is nonstructural distributed mass). The optimization is subject to,

$$J_z \leq \mathrm{VAL\ m}^2\,, \tag{4.3}$$

where,

$$J_z = \frac{1}{L}\int_0^{\mathrm{L}}\int_0^\infty z^T z \,\mathrm{dtdx}\,. \tag{4.4}$$

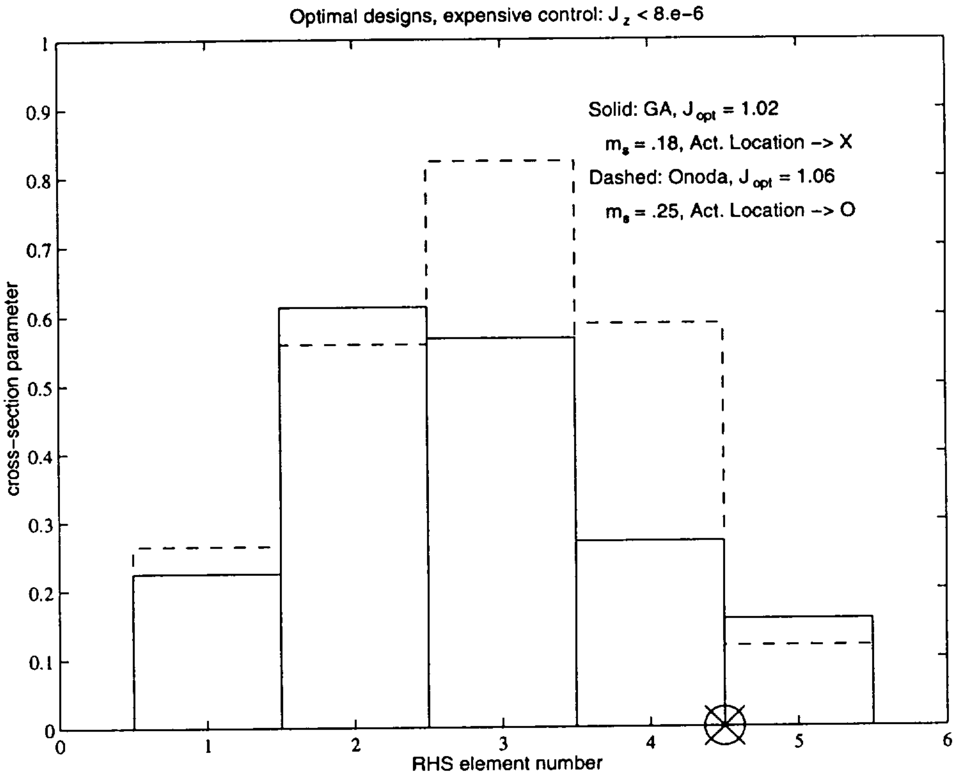

Figure 4.2: Material distribution for expensive control optimization

Note that in this case J_{design} is not J_z, the later being constrained. The chosen VAL depends on whether a cheap or expensive control solution is sought. The regulator variable z is the integrated lateral displacements along the beam. In order to meet the constraint of Eqn. 4.3 bisection of the control penalty is used. This is possible because the regulator state cost decreases monotonically as control penalty is reduced. There exists an implicit problem in the design of the regulator,

$$u = -R_{uu}^{-1} B_u^T P x \,,$$

but,

$$P = P(M(\alpha\sigma_u)) \,, \tag{4.5}$$

where P is the regulator Ricatti solution and M is the system mass. This implicit dependence is solved by adapting the G.A. with a continuation method in the initial generations, starting with an initial guess for $\alpha\sigma_u$ and improving it as the design con-

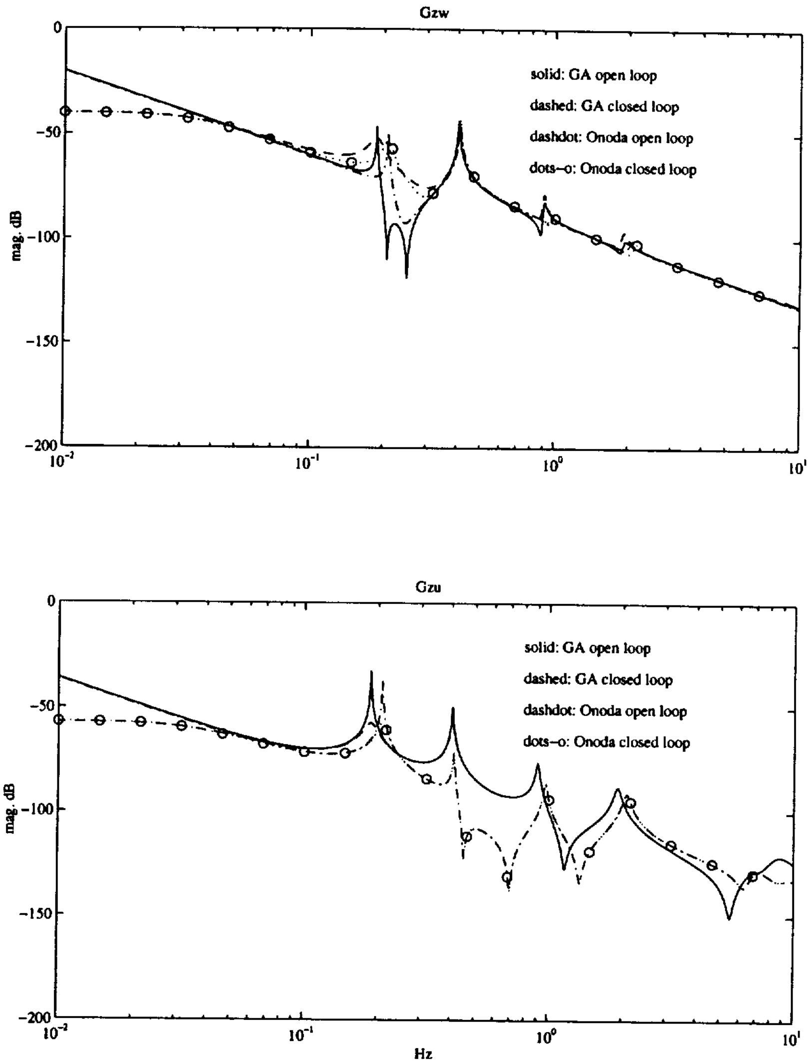

Figure 4.3: Disturbance to performance and control to performance (regulator) transfer functions for the expensive control optimization

verged (N.B. convergence was achieved). This particular implicit statement poses a problem for Onoda in that there exists implicit derivatives of the structural eigenvalues with respect to the control gains. These gradients are often not well conditioned, especially when poles and zeros cross in the regulator transfer functions. In his work, Onoda does not mention how this problem was overcome.

The G.A. ran with 50 designs propagated over 100 generations with crossover probability 0.8 and mutation probability 0.05. These parameters were found to work best over several trial initial populations.

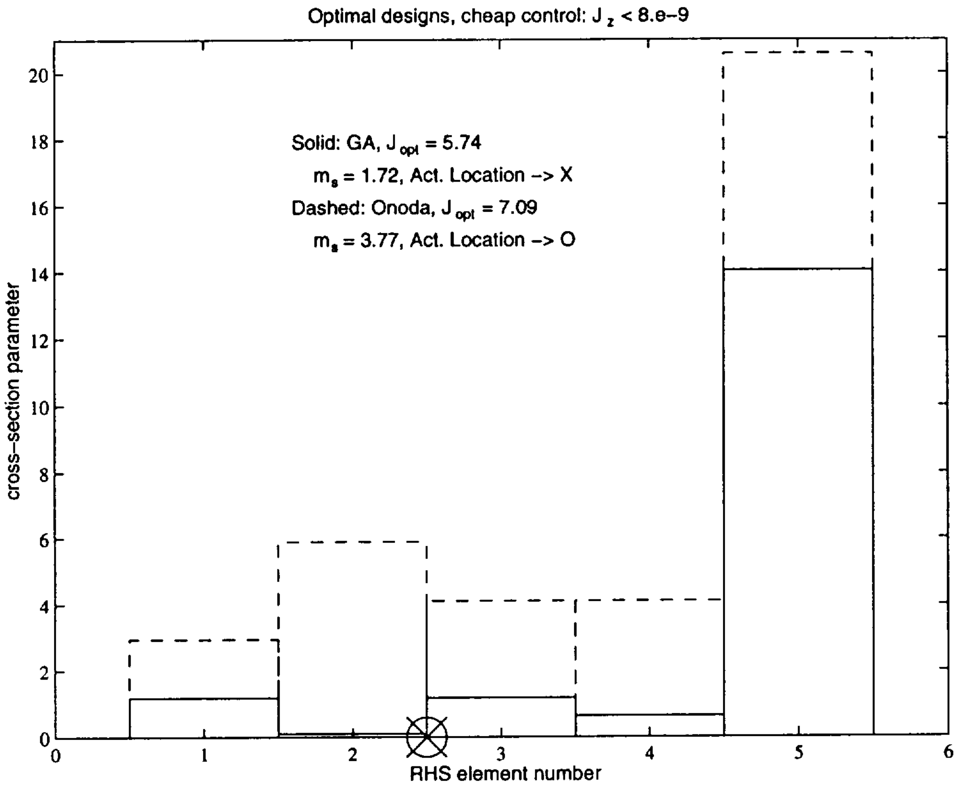

Figure 4.4: Material distribution for cheap control optimization

Results for expensive control are shown in Fig. 4.2. For this design VAL $= 8\times10^{-6}$ or approximately 3 mm rms. The results are clearly similar in shape with the same actuator location. The G.A. design is somewhat lighter weight (seen by comparing m_s) and more control is exerted to achieve the required vibration constraint. Resulting cost, J_{opt}, which is the optimized design cost, is marginally less than that of Onoda's. Note that Onoda's objective function value for the published optimal design was returned by the proposed cost evaluation code.

Results in transfer function form, see Fig. 4.3, show that the expensive control is predominantly rigid body control with some dampening of the fundamental structural mode. The dashed dot line rides just below the solid showing that Onoda's design is slightly more massive. The extra mass in Onoda's structure results in flexible modes than are stiffer than the G.A. design. For a fixed desired performance, J_z, a stiffer system generally means less control effort is required to meet a given performance. There is notable difference in the dynamics shown in G_{zw} and G_{zu} for the competing

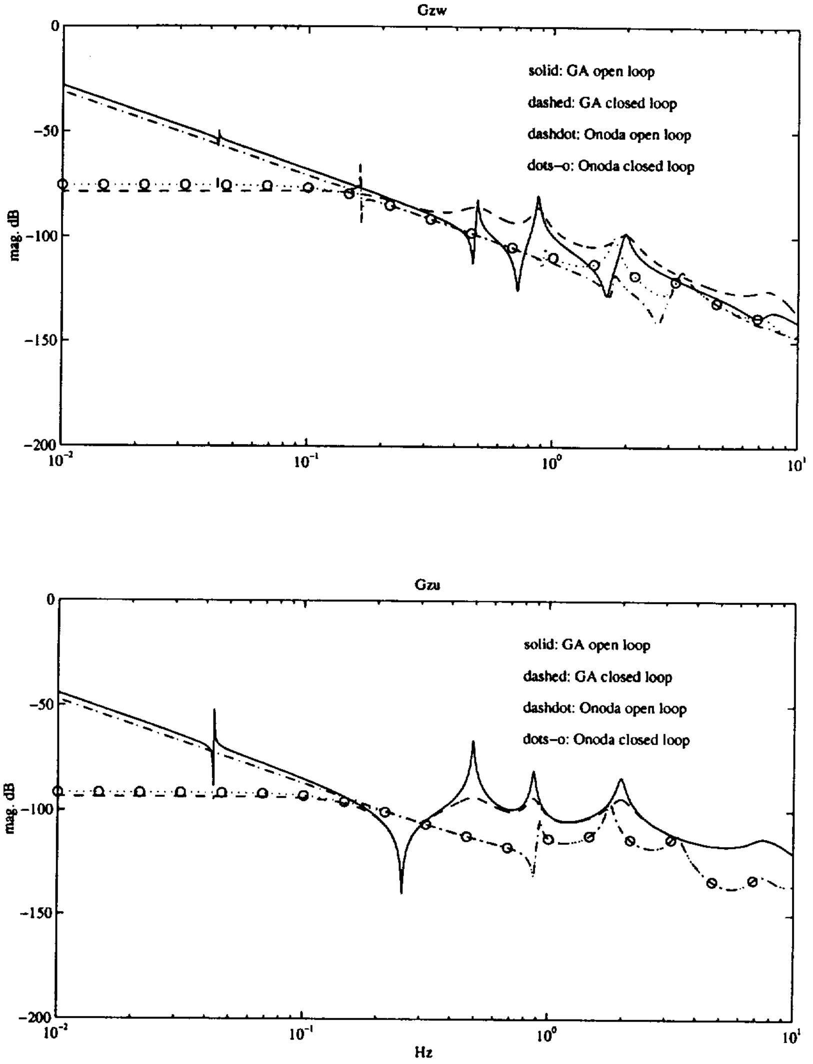

Figure 4.5: Disturbance to performance and control to performance (regulator) transfer functions for the cheap control optimization

designs, *e.g.* double lightly damped zeros in contrasting designs and loops. For the most part the solution remains relatively independent of these variations since they contribute little to the constrained performance.

In the cheap control optimization VAL $= 8 \times 10^{-9}$, or approximately 0.1 mm rms. The compared designs are shown in Fig. 4.4 and again the G.A. result exhibits similar shape, the same actuator location, and is lighter weight. Comparing to the expensive control designs, the system is 5 and 7 times as heavy respectively. The mass of the structure has increased aiding in achieving the desired performance constraint.

The transfer functions of Fig. 4.5 show similar trends to the expensive control with a few notable differences. The first difference is that some of the dynamics has been localized as seen by a small residue pole at relatively low frequencies. The second difference is that the G.A. design now includes control over an increased bandwidth, dampening several modes and therefore requiring more control power, but yet again with improved cost because of the gains in structural weight. Note that the modes of the regulator transfer are clearly dampened by the actuator u but the performance when excited by the disturbance source is worse near the flexible modes.

In general the expensive control trend was to design a less massive structure than nominal, and in the G.A. design trade some structural weight for less expensive control authority. The cheap control trend was to design a more massive structure than nominal, and, again, in the G.A. design, trade structural weight for control authority. Here we can see how the results were dominated by the somewhat arbitrary parametric weighting in the design cost function, α. This shows the value of choosing the coefficients in a scalar multi-objective optimization, see the paper by Rao [1] that details game thoeretic approaches to optimizing structures.

4.2 Precision Truss

Further validation was sought against a three-dimensional example presented by Sepulveda [6], shown in Fig. 4.6. This example is one that tests the ability of the method to handle three dimensional structures. The objective is to place a number piezoelectric actuators, that have local displacement and rate feedback to minimize several cases of objective function. Objective functions in this work include motion error, control effort and structural weight minimizations. Specifically they are,

(i) summed y and z dynamic displacements of the outriggers subject to:

  fixed member cross sections

  compression constraints on the actuators: $F_a \leq 0$

  voltage constraints on the actuators: $-V_o \geq V_a \geq V_o$

feedback gain constraints: $-2 \times 10^5 \geq h_{disp} \geq 10^6$ V/in, $0 \geq h_{vel} \geq 10^6$ V.s/in

first and second mode damping constraints: $11\% \geq \zeta_1 \geq 90\%$, $4\% \geq \zeta_2 \geq 90\%$

(ii) control effort subject to similar constraints as above and:

dynamic displacements of the outriggers ≤ 1.0 in

(iii) structural weight with similar actuator constraints as in 1) and:

member cross sections bounded: $0.001 \geq A_p \geq 0.8\,\text{in}^2$

dynamic displacements bounded: $|q_y| \leq 0.01$ in. and $|q_z| \leq 0.03$ in.

relaxed damping constraints: $\zeta_1 \geq 11\%$, $\zeta_2 \geq 4\%$, and $\zeta_3 \geq 1\%$

control effort ≤ 20 lb.

Responses are optimized under a 7.07 lb., 12 Hz, sinusoidal disturbance from the shown location. Piezo-electric strut actuators were constrained to be in locations below the mid plate (around twenty possible) with further constraints that no two actuators could adjoin. Each actuator weighed 0.556 lb. adding significantly to the 2.13 lb. passive nominal structural weight of the truss. The nominal truss exhibited three global modes below the disturbance frequency, ≈ 7.6 Hz bending in z axis, ≈ 9.9 Hz bending in y axis, and ≈ 11.2 Hz torsion about x axis. Higher modes occurred at 35 Hz and above and were truncated and replaced with a static feed thru mode.

Sepulveda's method used branch and bound techniques to solve a $\{0, 1\}$ problem for screened actuator placement. With the screened actuators fixed a gradient search on intermediate response quantities and feed back gains was used to hone the design.

When using the proposed method of this thesis, the G.A. searched over actuator placement and structural member variation while control gains were optimized simultaneously using standard constrained optimization gradient search code. Actuator stiffness and mass was included in each design in appropriate locations. Genetic Algorithm crossover and mutation probabilities were set as in the first validation example with 30 designs propagated over 50 generations found to be sufficient. Dynamic

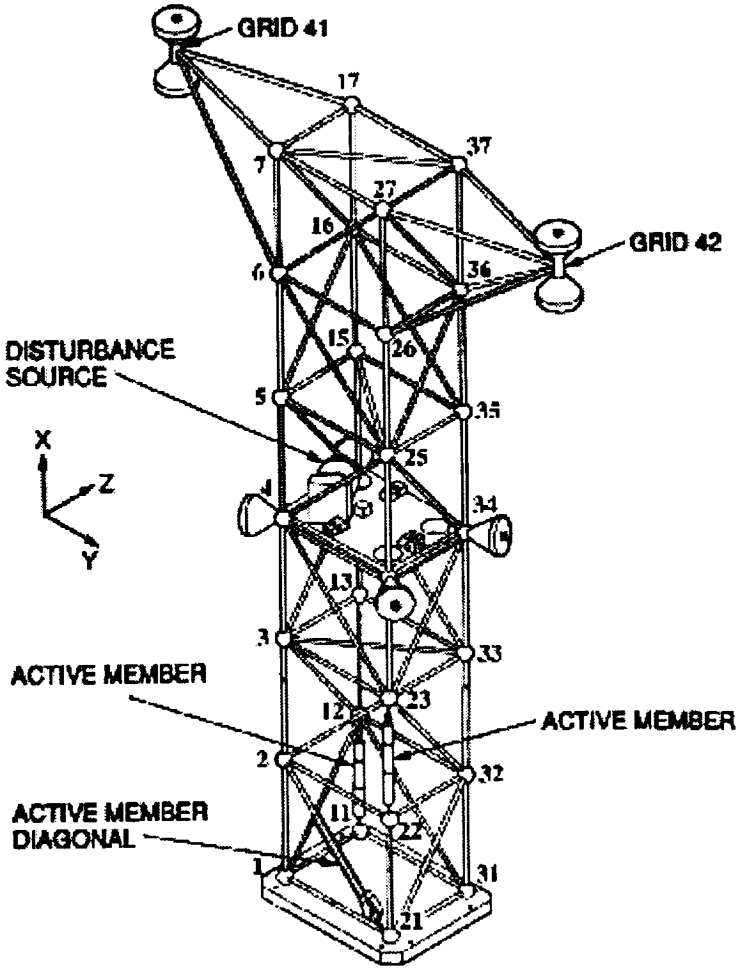

Figure 4.6: JPL precision truss.

displacements were minimized, or constrained as,

$$\begin{aligned} J_{disp} &= (\gamma^H \gamma)^{\frac{1}{2}} \,, \\ \gamma &= C_z \left(j\omega_{dist} I - A + B_u L C_y \right)^{-1} B_w \,, \end{aligned} \tag{4.6}$$

where L are the local displacement and velocity gains. Similarly, the control effort expression minimized, or constrained was,

$$\begin{aligned} J_{cont} &= (\delta^H \delta)^{\frac{1}{2}} \,, \\ \delta &= L C_y \left(j\omega_{dist} I - A + B_u L C_y \right)^{-1} B_w \,. \end{aligned} \tag{4.7}$$

Damping constraints were enforced using the real part of the closed loop poles effectively weighting the constraint by its frequency,

$$0 \geq \pm\Re(\lambda_i) \pm \zeta_{cons} |\lambda_i| \; . \tag{4.8}$$

The ± refers to respective lower or upper damping bounds, ζ_{cons}. Further stability constraints were found necessary in order to stabilize and maintain realistic authority over modeled higher modes. These constraints were not used in Sepulveda's work as only the lowest three modes were kept in his model. However, this type of sensor/actuator plant transfer function (piezo stack to displacement and displacement rate sensors) does not roll off in response at high frequencies. Poor model truncation will yield large pole-zero spacing error at lower frequencies. This leads to over prediction of dampening ability. A model of this type with correct static feed through from the actuator to the sensors will have high authority stability problems unless the rate gain is rolled off. In the proposed method high frequency roll off was added to both the position and rate feedback channels using an added mode well above the disturbance frequency. This mode was lightly damped to emulate truncated high frequency dynamics. Since no transfer functions were presented in Sepulveda's work it is not clear how well the plant was modeled.

Two runs were made for the dynamic displacement minimization objective. Run one uses fixed locations of the actuators derived from another reference and run two allows a fixed number of actuators while the locations varied. Figure 4.7 shows that the solutions for run one, *i.e.* fixed actuator locations, agree. Both in Sepulveda's method and in the gradient search (inner in the proposed method) the solution initially gets worse in order to satisfy damping constraints on the first two modes. Note that the actuator selection is fairly obvious, two longerons and a diagonal near the root providing authority over the first three modes. Comparing the gains in Tables 4.1and 4.2 shows good agreement for the fixed actuator run.

Position gains are constraint limited. The tendency for the displacement minimization case is to soften and damp the structure using the actuators. This can be seen in Fig. 4.8 where the G_{zw} transfer function shows the contribution from the three

Table 4.1: Sepulveda's final gains for precision truss dynamics displacement minimization.

Run 1			Run 2		
Element number	$h_d \times 10^3$ V/in.	$h_v \times 10^3$ V.s/in.	Element number	$h_d \times 10^3$ V/in.	$h_v \times 10^3$ V.s/in.
11-12	-200	1.1507	11-12	-200	3.5612
21-2	-200	0.1758	21-22	-200	0.0727
22-23	-200	1.1610	31-32	-200	0.0823
Object. func. in.		0.0717			0.0632
Number of analyses		7			16

modes at 12 Hz (dotted vertical line). Note how the truncation and static mode correction of the higher modes shown in the dashed-dot does not affect the performance at 12 Hz. Also note the damping constraints are met with the second constraint almost active and how the global modes have been softened to reduce the performance at 12 Hz. Transfer functions for the three independent actuators are also shown, G_{yu}, where the 45 Hz static correction, or control gain roll off, mode is apparent. The important features of these transfer functions is the narrow pole-zero spacing typical of these actuator sensor pairs. Only the diagonal strut, $21-2$, has noticeable residue of the torsion mode.

The second run in the displacement minimization case shows some differences. The first two actuators found in either method compare well, they are both root longerons, however, Sepulveda's branch and bound method comes up with a third root longeron where as the G.A. chooses a root diagonal. Some control of the torsion mode (mode 3) seems desirable (see Fig. 4.8), requiring a diagonal actuator. Tables 4.1 and 4.2 show a large difference in rate gains (again the position gains are constraint limited). Sepulveda's design essentially uses the first actuator only for damping with the other two root longerons providing very little. In contrast, the G.A. design uses two root longerons evenly and the diagonal strut lightly. Transfer functions, G_{zw} and G_{yu} shown in Fig. 4.9, for the design achieved by the G.A. are essentially the same as that shown in Fig. 4.8 with some added benefit from choosing the second longeron

Table 4.2: G.A. plus gradient search final gains for precision truss displacement minimization.

Run 1			Run 2		
Element number	$h_d \times 10^3$ V/in.	$h_v \times 10^3$ V.s/in.	Element number	$h_d \times 10^3$ V/in.	$h_v \times 10^3$ V.s/in.
11-12	-200	0.9890	11-12	-200	0.5814
21-2	-200	0.2743	21-2	-200	0.0028
22-23	-200	1.1380	31-32	-200	0.3809
Object. func. in.		0.0716			0.0654
Number of analyses		14			14
Number of generations		-			25

actuator as $31-32$ over $22-23$.

Convergence of the G.A. is shown in Fig. 4.10. In this case the search domain is rather small (24 possible locations with no actuators conjoining) and the initial population was seeded with the fixed location of run 1. Only a few improvements were made to the run 1 set as shown by four jumps in the best of generation results while the average cost showed the usual monotonic improvement.

Case two involved control effort minimization with the displacements constrained to be less than 1.0 in. Evaluation of the control effort is made at 12 Hz which is consistent with Sepulveda's method. Results for the two methods (final gradient search for the proposed method only) are compared in Fig. 4.11. Again the fixed actuator run solutions came out similar, see Tables 4.3 and 4.4, with the diagonal location $21-2$ being lightly used and the longeron actuators enforcing damping constraints. The displacement constraint is met passively so that actuation is applied to meet damping constraints only.

In G_{zw} of Fig. 4.12 it can be seen that the poles are softened less drastically than the displacement minimization case and that the damping constraints are met. Note that for a fixed rate feedback gain damping coefficient is increased by decreasing the natural frequency, seen most obviously in the first mode.

Table 4.3: Sepulveda's final gains for precision truss control effort minimization.

	Run 1			Run 2	
Element number	$h_d \times 10^3$ V/in.	$h_v \times 10^3$ V.s/in.	Element number	$h_d \times 10^3$ V/in.	$h_v \times 10^3$ V.s/in.
11-12	-200	1.9424	31-32	-188	1.5873
21-2	-13.6	0.2434	2-3	-30.0	2.6943
22-23	-106	1.1435			
Object. func. lb.		25.11			19.14
Number of analyses		16			15

Table 4.4: G.A. plus gradient-search final gains for precision truss control effort minimization.

	Run 1			Run 2	
Element number	$h_d \times 10^3$ V/in.	$h_v \times 10^3$ V.s/in.	Element number	$h_d \times 10^3$ V/in.	$h_v \times 10^3$ V.s/in.
11-12	-167	1.8676	2-3	-198	0.9182
21-2	-32	0.0003	21-22	-4.4	0.0234
22-23	-37	0.3510	33-34	-1.5	0.0068
Object. func. lb.		20.10			1.10
Number of analyses		15			15
Number of generations		-			20

In the second run the results are drastically different. Sepulveda's method came up with two actuators, one longeron at the root, $31-32$, and one longeron one-bay-removed from the root, $2-3$. The G.A. also converged to longeron $2-3$ but came up with a different root longeron, $21-22$. Also the G.A. method came up with lightly used longeron $33-34$ with virtually ignorable added control effort. The gains shown in Tables 4.3 and 4.4 are different in that Sepulveda's method uses the root actuator for the majority of control where as the G.A. result uses longeron $2-3$ resulting in far less total control effort. This result reemphasizes the differences between Sepulveda's intermediate variables and the G.A.'s completely modeled actuator impedances. Transfer functions G_{yu} of Fig. 4.13 show the improved authority of the selected actuator locations over that shown in Fig. 4.8 for the previous case. Actuator location 2–3 provides good authority over mode 1 and the root longeron, 21–22 (with noticeably less static gain), aides dampening of the second mode.

Convergence for the G.A. is again rapid, with the best actuators almost found by random seed, *i.e.* the location 2–3 came up in the seeding round with a root longeron actuator and dominated the best of generation results. With this sort of domination the average fitness of each generation converged in approximately 10 generations.

The structural mass minimization, of case three, involved structural member variation as well as actuator placement. Here displacements were constrained to be less than .01 in. and .03 in. for the y and z directions respectively, with control effort constrained to be less than 20 lb. Passive cross section areas were bounded as $0.001 \leq A_p \leq 0.8\,\mathrm{in}^2$.. When using the proposed method a feasibility projection was performed at the initial seeding stage of each run, *i.e.* combinations of member geometries and actuator locations were randomly supplied until a fully feasible population of 30 was found. Infeasible solutions that resulted from model propagation were penalized in the fitness function.

The first two runs were for fixed locations, $\{11-12, 21-2, 22-23\}$ and $\{11-12, 21-2, 31-32\}$. Figure 4.14 shows the comparison between Sepulveda's results and those achieved by the G.A., however, in this plot the G.A. convergence plot is shown rather than the inner loop gradient search. The inner loop is only being used to check that motion error and control effort constraints are satisfied.

For locations $\{11-12, 21-2, 22-23\}$ approximately the same optimum mass is achieved, 2.2 lb. Sepulveda introduced the second fixed set of locations $\{11-12, 21-2, 31-32\}$, two root longerons and one root diagonal because he thought this set would achieve a better optimum mass. In his method he did not achieve this result but the G.A. did, arriving at $\approx$ 2.07 lb. optimum.

Transfer functions for the first run are shown in Fig. 4.15. The disturbance to performance plot shows how drastic structural softening has been used to achieve the stringent displacement requirements. Under closed loop the structure is further softened and dampened to meet the damping constraints. Comparing with Fig. 4.8 the dashed-dot transfer that includes higher modes shows how the structural variations compromise the high frequency dynamics to achieve performance. This shows that that further structural discretization may be needed to bring out the local dynamic effects on the closed loop optimization problem (possible with the proposed method).

Exaggerated structural softening resulted in improved authority of the fixed locations, shown in G_{yu} of Fig. 4.15, with the torsional mode now almost completely un-observable/disturbable/controllable.

Sepulveda's best set of three actuators was found to be $\{11-12, 31-32, 33-34\}$. These three locations gave a marginally better result than the fixed location of run 1. In contrast, the G.A. achieved a better result than its run 2 yielding locations $\{11-12, 21-32, 33-34\}$, where the locations compare except for the root diagonal $21-32$ in contrast to the root longeron $31-32$. Figure 4.16 shows yet more softening over the fixed actuator case and closer modal spacing. The damping constraint on mode two is only barely met due to reduced authority over that mode seen in G_{yu} transfer functions.

Run four allowed a minimum of two actuators allowing the design to cast out an actuator if two were sufficient to meet constraints and thus save structural mass (0.556 lb. per actuator). Sepulveda's method yielded two actuators located at $11-12$ and 31–32 with optimal weight of 1.59 lb., while the G.A. came up with two actuators located at $11-12$ and $2-3$ and optimal weight 1.83 lb.. Viewing G_{zw} in Fig. 4.17 we can see that the torsion mode is, as in the fixed location mass minimization, again barely noticeable. Two actuators with good authority (see G_{yu}) are all that is needed to meet constraints.

A further run was produced by Sepulveda that showed in his method he could meet all constraints with just a single root longeron actuator at $11-12$. After a long feasibility search this was not the case with the G.A., again highlighting the differences between the accurate modeling of the proposed method and the simplified modeling presented by Sepulveda.

4.3 Summary

In whole the G.A. outer loop was found to perform well and even though it is criticized as being inefficient it was found to be fairly robust in application.

The G.A. was adapted to solve implicit problems where the structural eigenvalues depend implicitly on control gains. Results for Onoda's example were generally the same shape and actuator location. Onoda's results are dominated by rigid body control. The G.A. designs use more control of flexibility in order to reduce the system mass objective. In general the G.A. designs out performed their published counterparts.

Validation on a three dimensional example such as Sepulveda's showed the importance of sensor actuator modeling in realizing good solutions. In these cases actuator stiffness was incorporated directly into each design. The displacement minimization (pure placement) solutions compared well, while the control effort minimization solutions differed in distribution and authority of the actuators. The G.A. was found to do better than Sepulveda's method when minimizing control effort. Mass minimization solutions compared well, with structural softening and root actuator authority figuring strongly in the solutions. In the mass minimization case the actuator mass dominated the total structural mass so that the minimum number of actuators required to fulfill constraints was desirable.

Now that the method has been shown to solve both one and three dimensional examples from the literature it will be exercised on a design application current in aerospace technical needs.

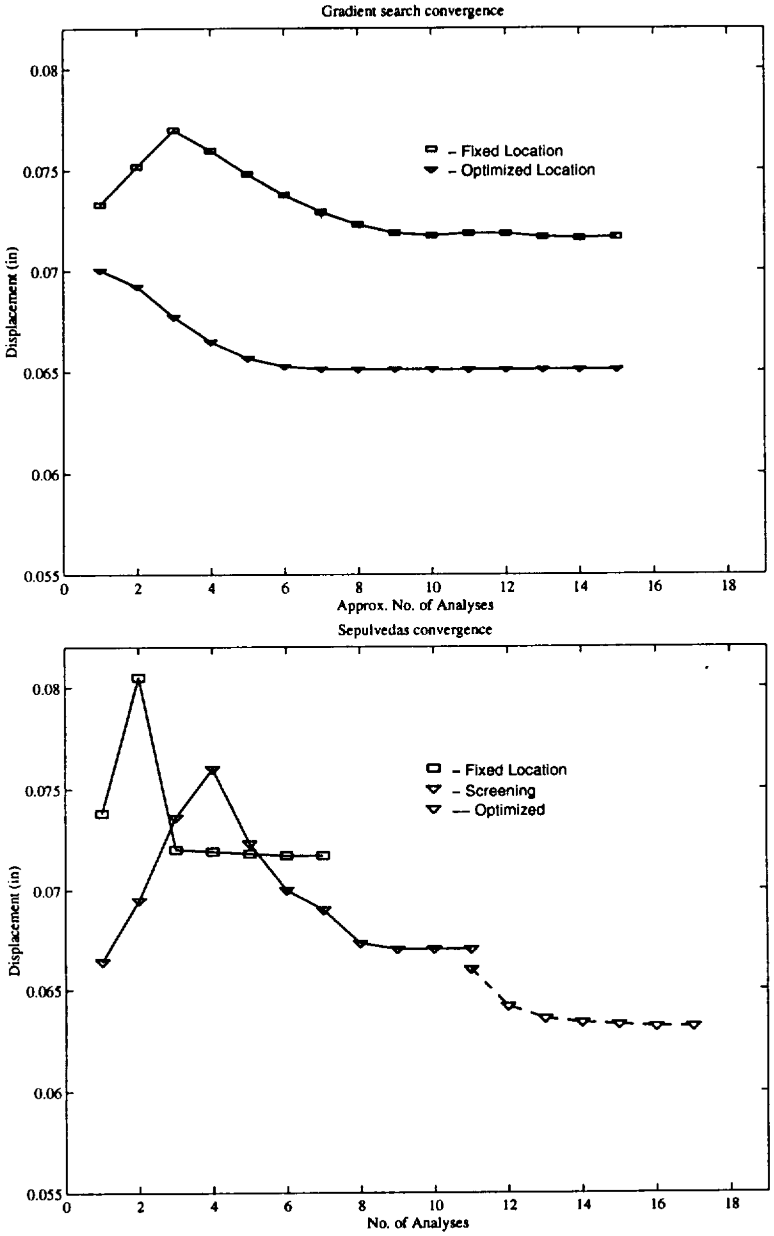

Figure 4.7: Displacement minimization comparison.

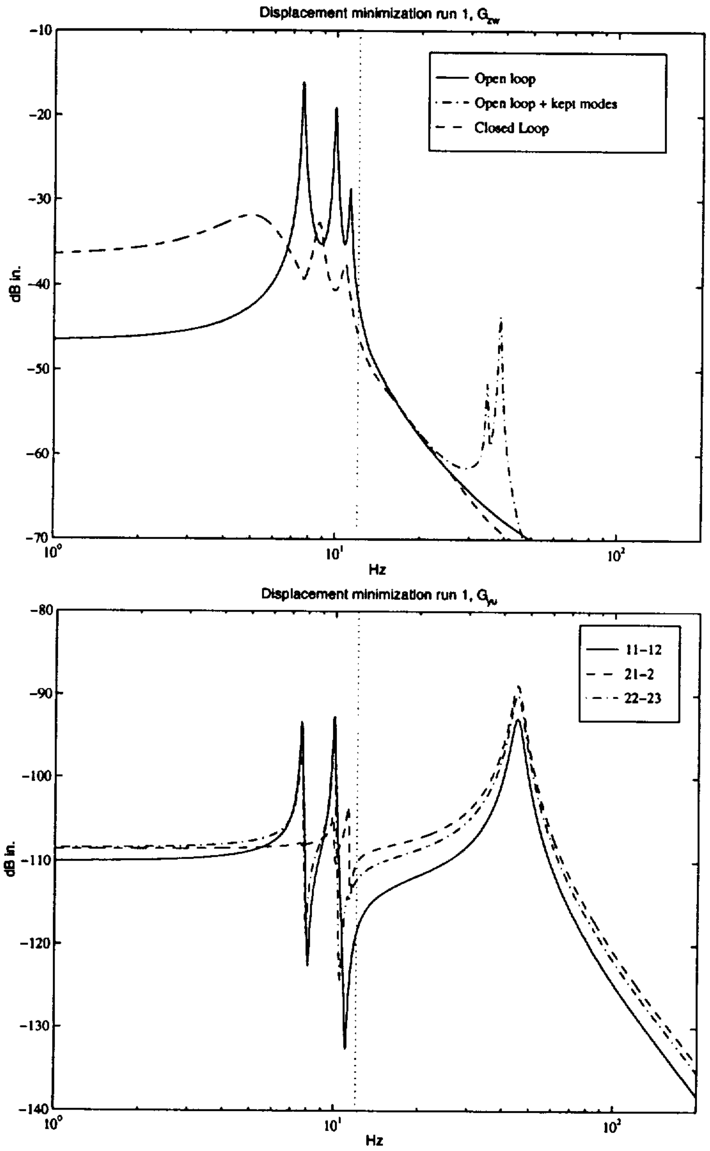

Figure 4.8: Displacement minimization disturbance to performance and control to sensor transfer functions for fixed actuator locations. The vertical dotted line at 12 Hz is the harmonic disturbance frequency, the frequency at which the optimization is performed.

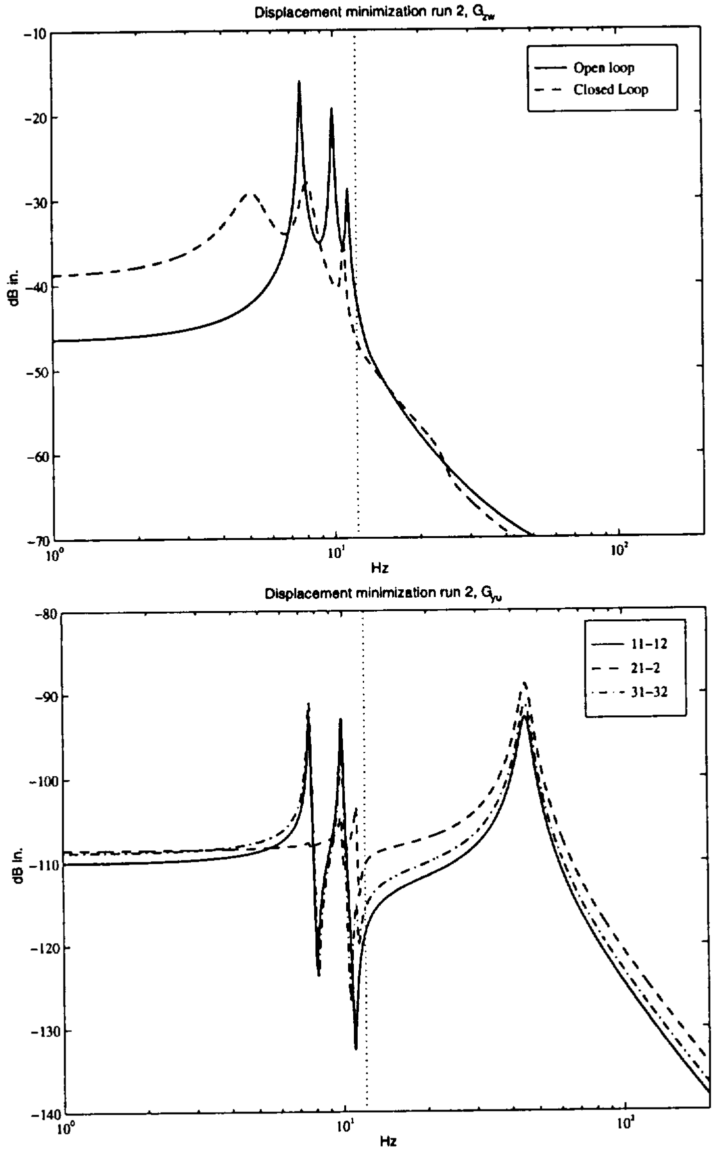

Figure 4.9: Displacement minimization disturbance to performance and control to sensor transfer functions for optimized actuator locations.

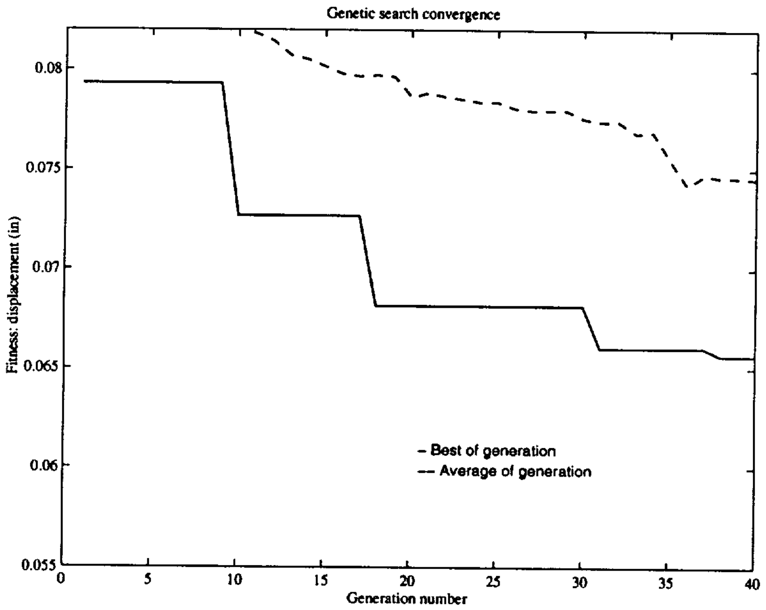

Figure 4.10: Displacement minimization genetic convergence for two trials

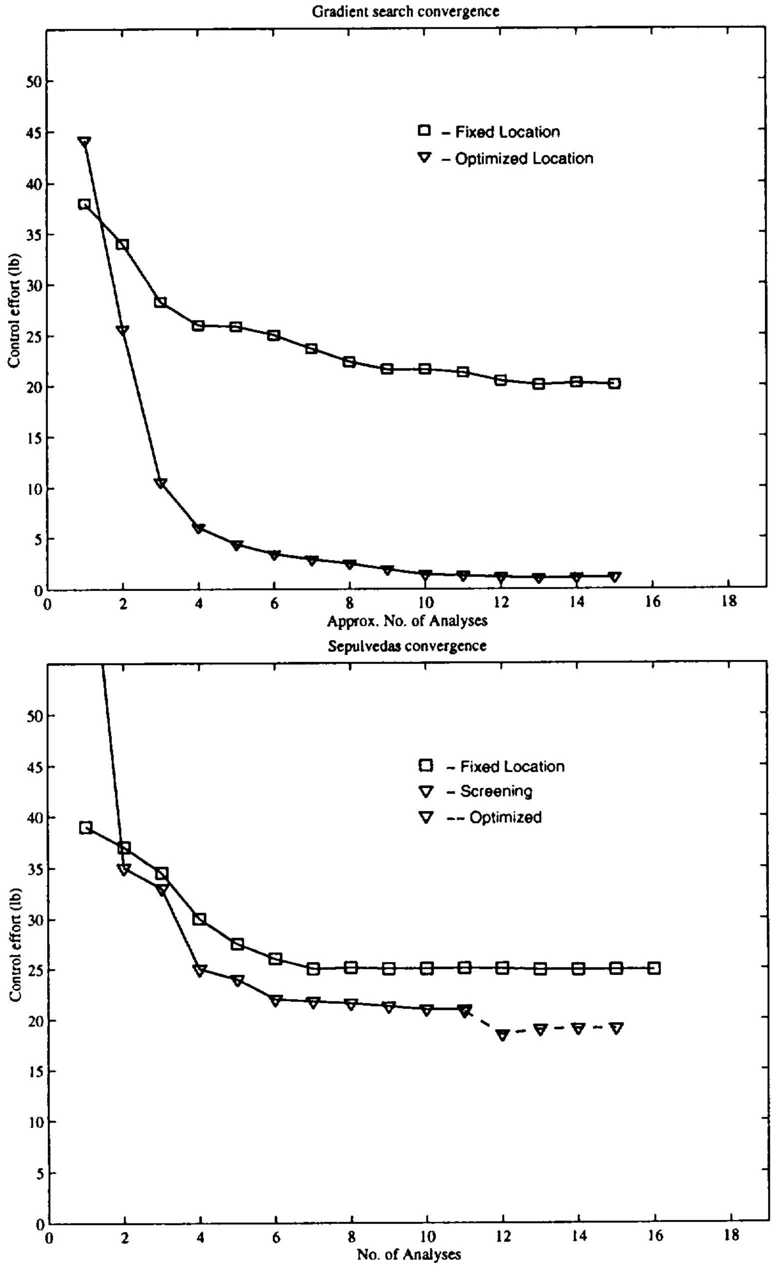

Figure 4.11: Control effort minimization comparison

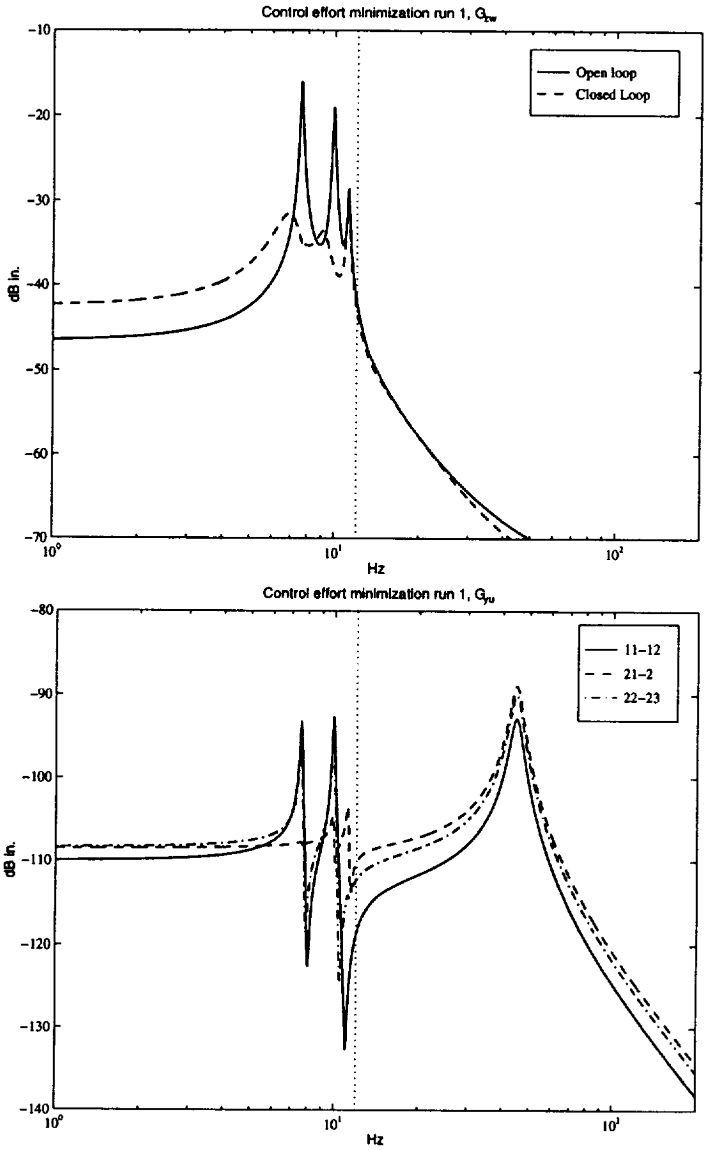

Figure 4.12: Control effort disturbance to performance and control to sensor transfer functions for fixed actuator locations.

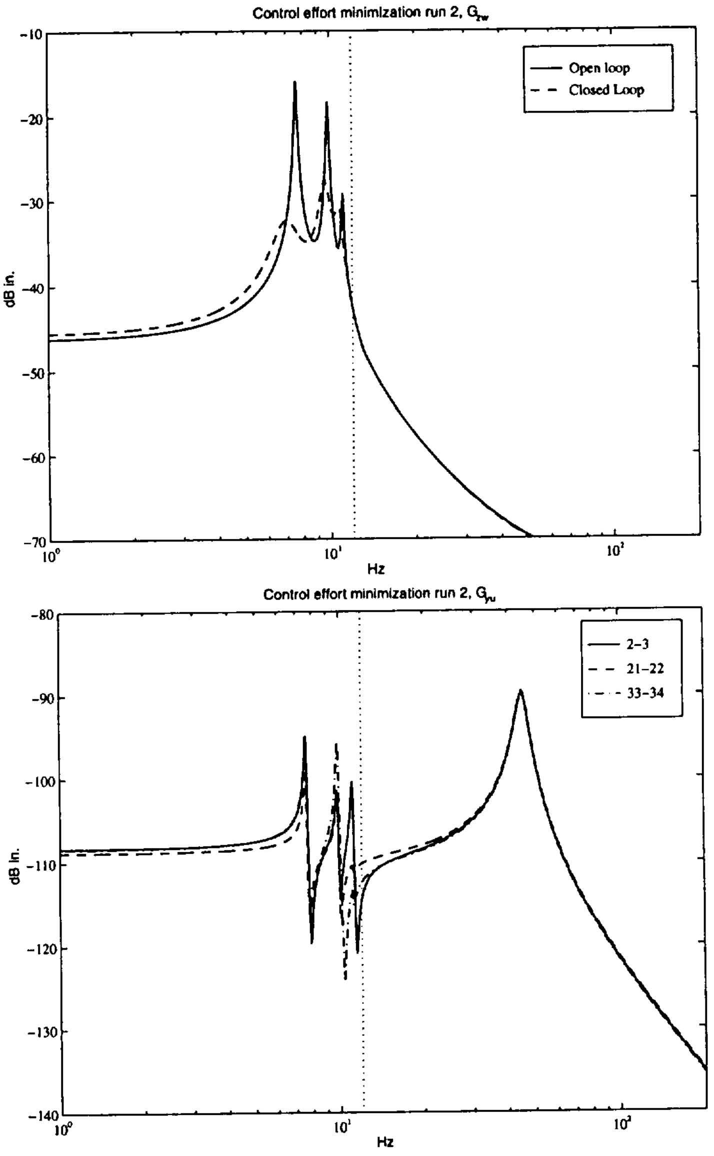

Figure 4.13: Control effort disturbance to performance and control to sensor transfer functions for optimized actuator locations.

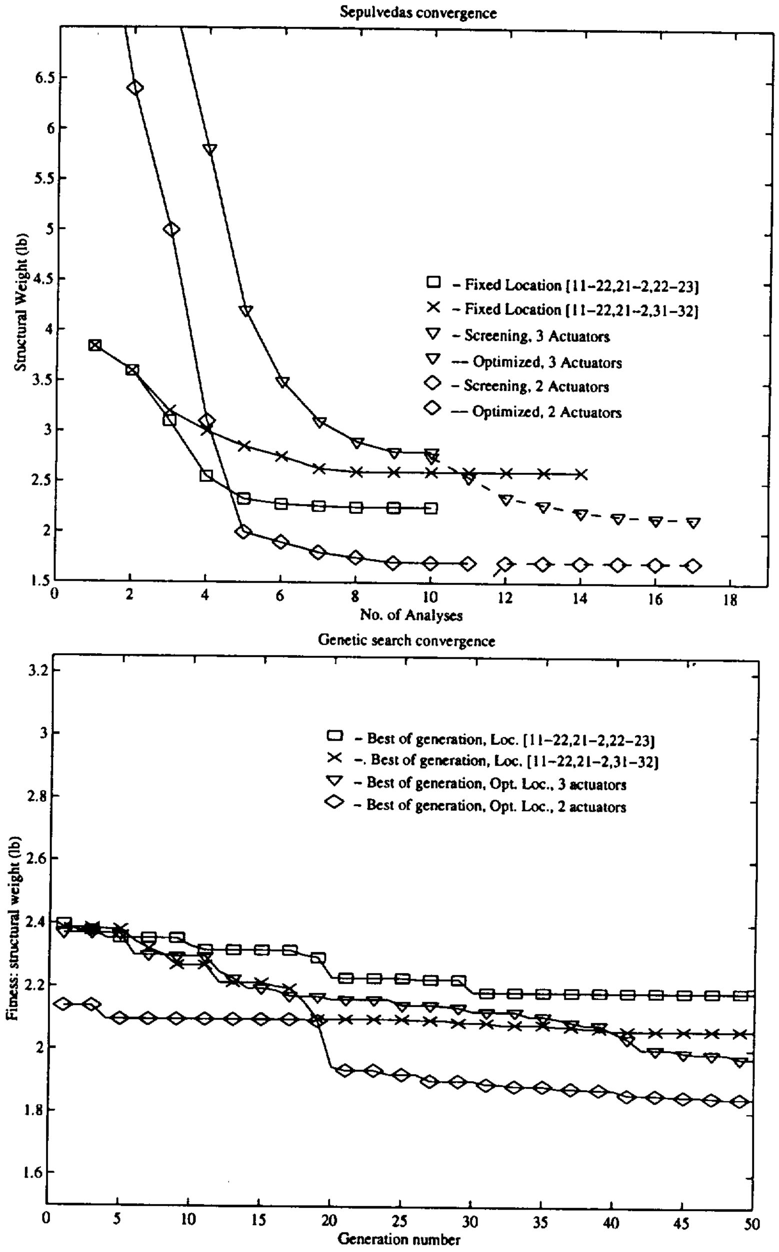

Figure 4.14: Structural mass minimization comparison.

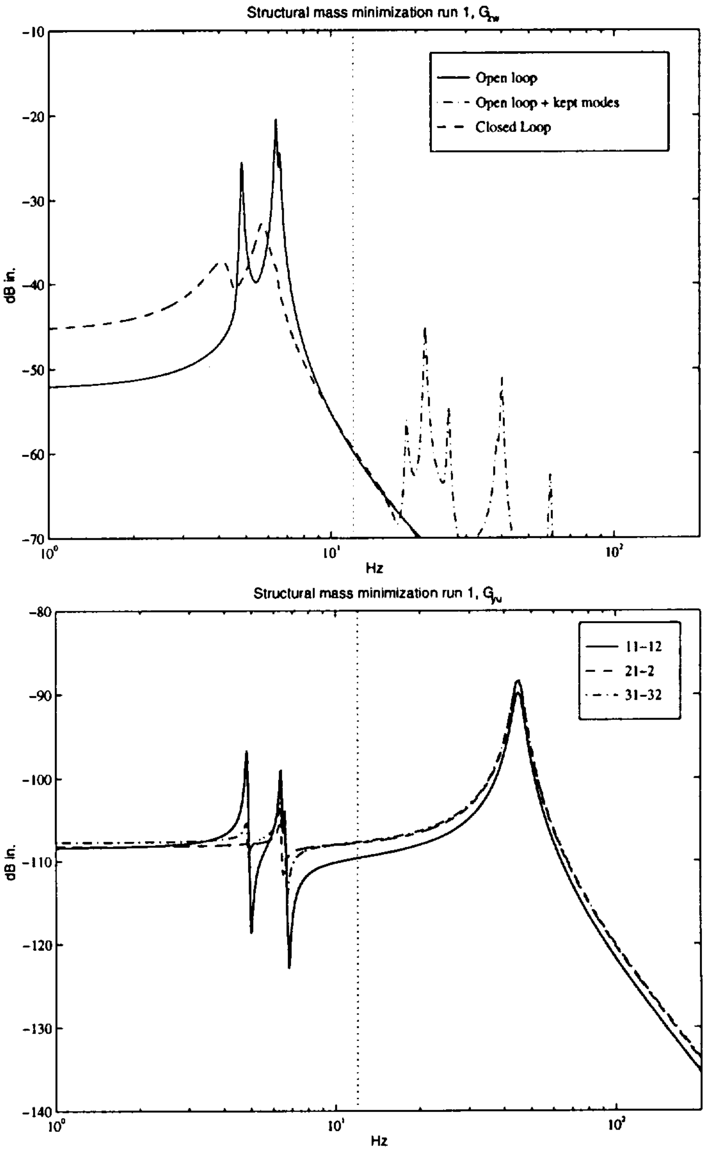

Figure 4.15: Structural mass minimization disturbance to performance and control to sensor transfer functions for fixed locations $\{11-12, 21-2, 22-23\}$.

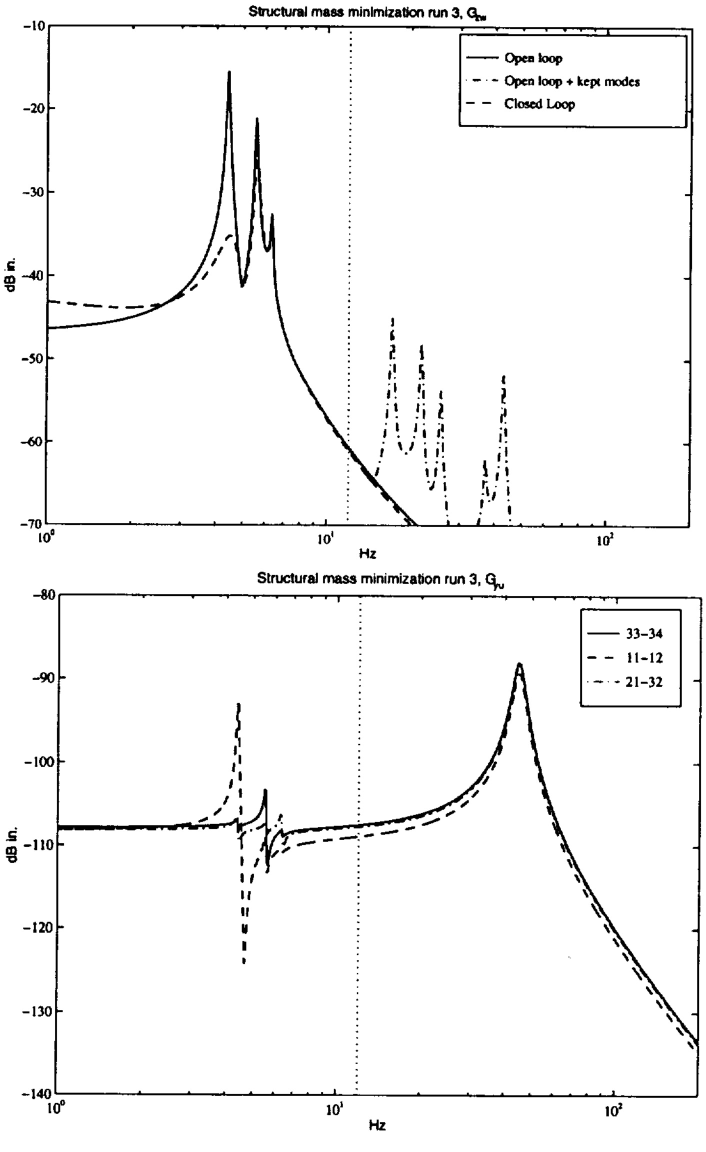

Figure 4.16: Structural mass minimization disturbance to performance and control to sensor transfer functions for optimized locations $\{11-12, 21-32, 33-34\}$.

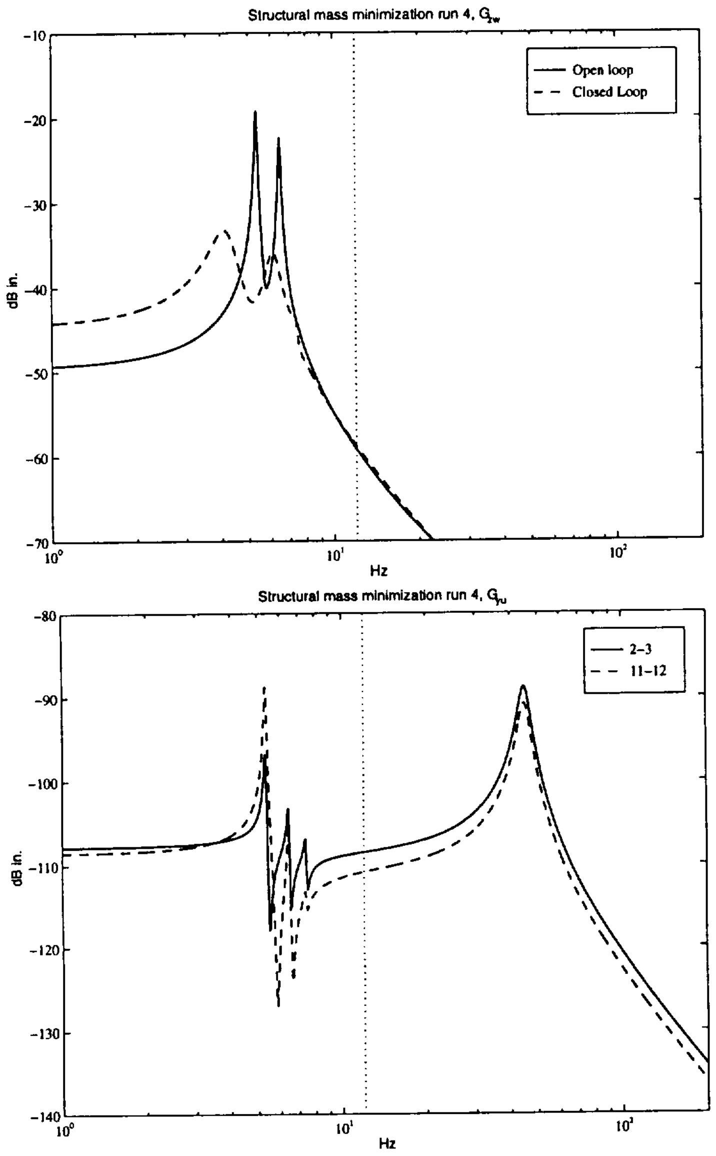

Figure 4.17: Structural mass minimization disturbance to performance and control to sensor transfer functions for optimized locations $\{2-3, 11-12\}$.

Chapter 5

Application

Both of the validation example cases shown in Chapter 4 minimized structural mass, one with an appended control effort penalty function and motion error constraint, the other with constraints on motion error and control effort. In this chapter an application was found to test the method on a structure with true motion error objective. The design application is a separated aperture, space based telescope. Here, structural mass and control effort are to be treated as weak constraints, *i.e.* mass is constrained through member sizing and control effort through control penalty weighting in the H_2 dynamic controller design.

Two examples will be investigated in this chapter. The first example explores designs of a one-dimensional beam-like structure under two different spectra of inertial forcing disturbance. A brief background of stellar interferometry is given with the setup of the one-dimensional problem. Results from the G.A. searches are given for the two different cases of disturbance spectrum. These results are investigated via scaled truss experiments in Chapter 6. The second example is a three dimensional box truss that is disturbed by a single spectrum of prescribed motions. The three dimensional example is posed and solved to show the power of the proposed method when dealing with topological variations and to show that the solutions are similar to the beam case.

Traditional mathematical-like statements specifying the search problems are given at the end of each setup section after the ground-work. In each example a description of performances, disturbances, structural discretization, actuators and sensors will be given before the statements.

5.1 Interferometry Background & One-Dimensional Example

Next generation orbiting stellar observatories require high angular resolution to meet their objectives; extra-solar planet detection, resolution of close binaries, imaging cores of galaxies, and direct measurement of parallax of extra-galactic stars. Current earth orbiting telescopes operating in the ultraviolet to near infrared band employ passive monolithic primary mirrors and secondary optics. These optics need be manufactured to accuracies on the order of fractions of the measured wavelength. Alignment of passive measurement systems need also be on the order of fractions of the measured wavelength.

Orbiting filled aperture telescopes larger than Hubble Space Telescope would be prohibitively expensive. Monetary costs is realizing such a telescope would be incurred obtaining surface accuracy, integrating to a sizable launch vehicle, and maintaining passive alignment throughout ground handling and launch. As a result space based interferometers were conceptualized that used several discrete apertures for improved resolution at lower cost. In one concept the discrete apertures are structurally connected with active collecting optics at the spacecraft hub.

A representation of a structure to host such an interferometer is shown in Fig. 5.1. This structure is simplified to a beam and will serve as the first precision structures design example. The interferometer concept shown is the result of a systems design performed at MIT for NASA's Jet Propulsion Laboratory interferometry group [50, 51]. The structure is a long truss boom mounted on a spacecraft bus hub. Collectors are located at the tips of the boom and are relatively massive compared to the structure, $m_{col} \approx 3m_s$. The hub houses attitude control actuators and sensors as well as collecting optics, $m_{hub} \approx 50m_s$.

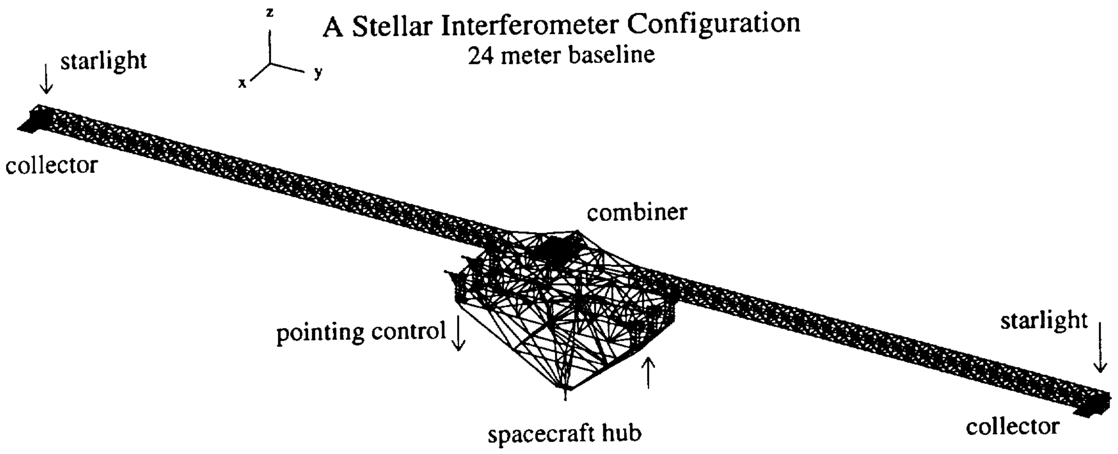

Figure 5.1: Line drawing of an interferometric spacecraft

The essence of operation of these interferometers is the pairwise combination of light paths, from a common wavefront, incident on the separated apertures. The left schematic in Fig. 5.2 shows incident light steered from separated apertures through compensation optics onto detectors. Target star light from the combined apertures need be held spatially correlated, over a coherent integration time, to yield interference fringes (right schematic) that provide intensity and spatial phase information relative to a guide star. This information collected from a number of different baselines (resolutions), through a rotated orientation, measures a spatial Fourier transform in what is known as the image plane. Inversion of the transform information yields a reconstructed image. In a fixed orientation, a line in the image plane, accurate parallax is measured between two stars by measuring the spatial phase between fringes to within fractions of a wavelength. Referenced to many starlight fringes, a single star may be observed for inertial motion, indicating orbiting celestial bodies.

Coherent fringe integration time is set roughly by the magnitude of the target star and the spatial correlation is usually over a few wavelengths. Desired accuracy requires that each star light path be controlled to the same length within nanometer levels. Pathlengths are equilibrated using optical delay lines (ODL) that are integral to the light paths. Figure 5.2 shows an ODL in one path only, where in actuality an optically equivalent ODL should be in the other path for good fringe visibility.

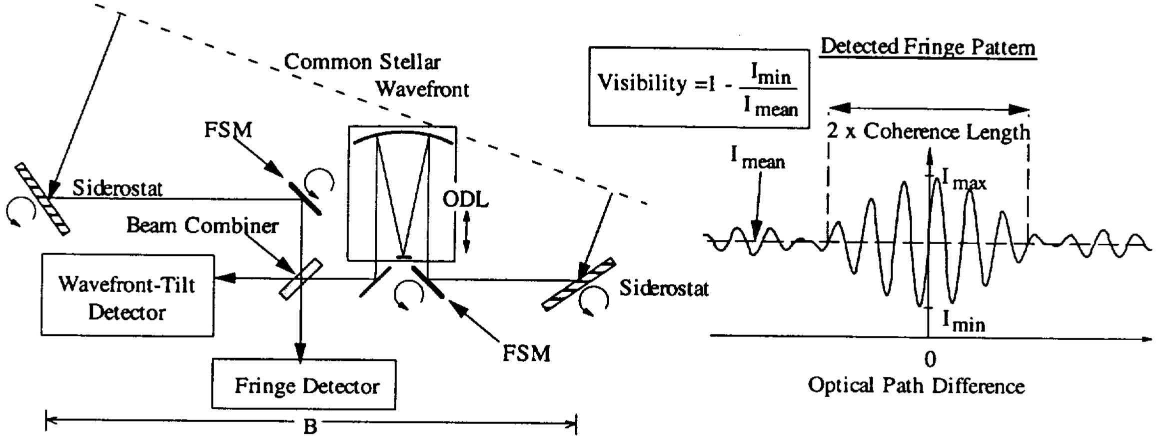

Figure 5.2: Schematic of interferometric stellar light combination

Under dynamic control action the ODL's induce pathlength to compensate for measured system pathlength error [52]. An ODL consists of staged actuators, position table-voice coil-piezo stack, that maneuver focal and reflecting optics based metered position error commands. Angular error between incident paths may also be metered and compensated for using steering optics, shown in Fig. 5.2 as tilt detector error that would drive the Siderostats and Fast Steering Mirrors.

When all the optical loops are closed, and the interferometer is in a fixed orientation, the pathlength error performance is approximately the high pass filtered, differential, tip displacement. The high pass filter comes about by assuming that for fringe feedback the optics u is collocated with the measure y of z (the external pathlength). This analogy between the inputs and outputs yields,

$$G_{zw}^{cl} = S_{yu}^{opt} G_{zw}^{ol} \tag{5.1}$$

where S_{yu}^{opt} is the sensitivity of the optical control loop and *cl* and *ol* refer to the closed loop and open loop respectively. This optical control approximation ignores the second order effects of steering misalignment. In the application example the **performance** is measured as the difference of collector vertical displacements and is weighted with a high pass filter that represents the fringe tracking closed loop delay line compensation [1].

---

[1] The high pass filter is depicted as the dashed curve in Fig. 5.3

Ground based interferometers mitigate wind and seismic pathlength disturbances by affixing to massive concrete pilings and compensate for earth's rotation using the ODL's. In the space environment disturbances are more prevalent due to the flexible structure on which the interferometer is mounted. Disturbances emanate from such sources as the spacecraft attitude control, diurnal heating and cooling, and reactions from the optical compensation system. Structural control is sought to enhance the image taking capability of a space based interferometer that uses relatively bright guide stars. When using dim guide stars structural control may enable operation. In some cases the resonance dampening structural control may also enable extended bandwidth of the optical control.

Dynamic **disturbances** that cause pathlength jitter may come from a variety of sources such as coarse pointing at the target sky, diurnal heating and cooling cycles and reaction forces from optical compensation devices. For the design problem disturbances will enter as torques about the sensitive axis, shown as the x-axis in Fig. 5.1, acting on the hub.

These disturbances may be classified roughly as low frequency or high frequency in content. For example, cold gas attitude control thrusters generate fairly low frequency step-like pulsed inputs, whereas reaction wheels generate high frequency harmonics set by the wheel size and speed. Both low and high frequency disturbance cases are investigated as bounded disturbance weights, or filtered white noise. The low frequency shaping filter is a constant gain that rolls off at $1/\omega$ above a 1 Hz corner frequency, see the solid curve in Fig. 5.3. The gain is set so that the rms disturbance input is equivalent to that of a 0.1 Hz bandwidth attitude control system. The high frequency disturbance, dashed dot in Fig. 5.3, rolls up like ω^2, corners to a constant gain at 30 Hz and rolls off like $1/\omega^4$ beyond 50 Hz. For this filter the gain is set by expected energy from reaction wheel harmonics for a 600 rpm Hubble sized wheel.

The structure shown in Fig. 5.1 was statically condensed into twelve elements a side. Fifteen different types of beam elements resulted that represented 3 different truss work topologies (varying bay depths) each with five different member designs. Nonstructural mass varied with the topology. Static condensation illuminated the

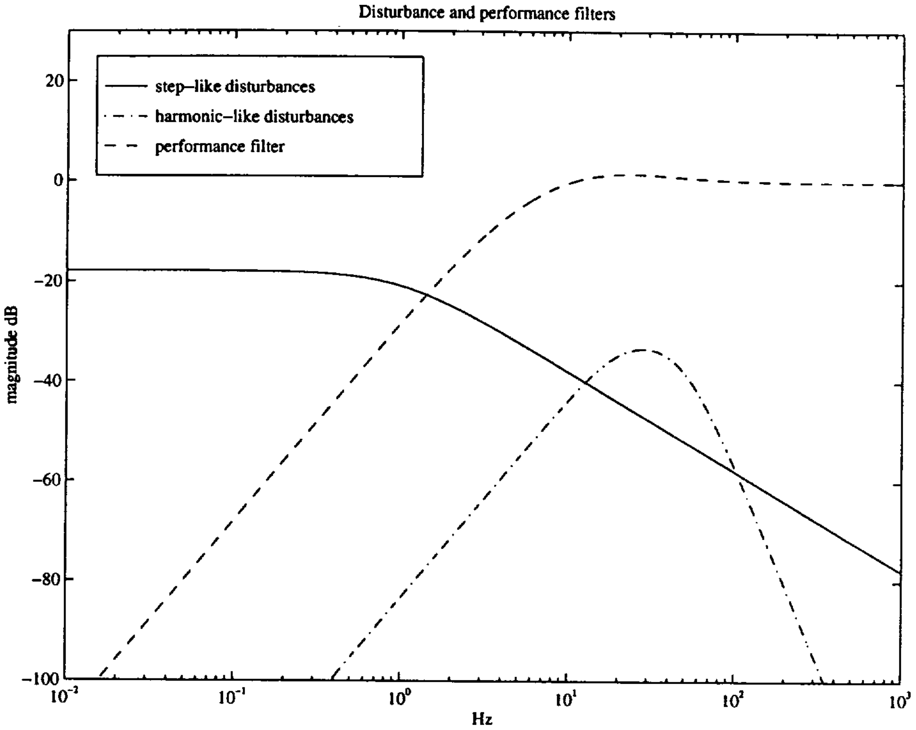

Figure 5.3: Design example disturbance weights.

necessity of component mode synthesis during the G.A. runs in this example. The two center most elements of the model structure were constrained to have very stiff properties. Fixed concentrated masses and inertias were added for the spacecraft hub and optical payload.

Structural **actuators** are included to improve pathlength compensation beyond that of the optical loops. The actuators are symmetrically placed local moment pairs that act differentially, and may be placed in elements 3–11 in the available 12 counted from the center. Note that a fixed stiffness actuator was not chosen. The optimal designs will imply the desired stiffness.

Sensor suites used for low frequency disturbances all use a hub angle sensor plus a structural sensor. The hub sensor nearly spatially collocated with the disturbance. Structural sensor choices are differential tip motion (performance feedback), collocated differential angle, and collocated differential load, where in the later two collocation refers to the structural actuation. A series of runs was made for each structural sensor choice. The collocated load sensor represents an interesting choice because the sensed signal depends on the stiffness of the local cross-section (see Section 2.1 in Chapter 2).

In the case of high frequency disturbances the sensor suite is limited to be the hub angle sensor and the collocated load sensor. The hub angle sensor is weighted so that it is barely used in the important bandwidth.

With the disturbance and the performance completely specified, the free parameters in an H_2 control design are control penalty weighting and sensor noise specification. For this design example control weightings were designed to limit the actuator authority and roll off the control at high frequencies (examples of which will be shown with the design solutions), where unmodeled dynamics are suspected in an actual interferometer instrument. Sensor noise specification is broadband with magnitude set at 1/30 th the magnitude of the control penalty. This allows the estimator dynamics to be sufficiently above the regulation dynamics. In practice this is a reasonable assumption for control design, but the reality is that poor sensor quality will cause the true performance to be swamped by sensor noise.

The sensors specified for this application are assumed to be extremely good quality. For example, the measured fringe information that is used to track a guide star is of nanometer quality [2]. Another pertinent sensor quality to mention is that of a hub angle measurement. A couple of references that publish Hubble Space Telescope Rate Gyro Assembly measurement data are by Vadlamudi *et al.* and Sharkey *et al.* [53, 54]. In science mode the RGA's resolution is ≈ 0.00012 arc-sec which translates to ≈ 10 nm resolution for a 20 m baseline interferometer instrument.

---

[2] depending on the visibility of the fringe, with well fabricated optics this nanometer quality is possible

Formally, the discrete evolutionary design problem can be stated as,

$$\begin{array}{rcll}
\min J & = & \left\|G^{cl}_{zw}\right\|_2^2 , & \\
\text{subj. to} & & \text{variables} & prop_i \in \{\text{possible beams}\} \\
 & & & u_{loc} \in \{\text{possible locations}\} \\
 & & \text{implicit} & H_2 \text{ constraint equations} \\
 & & \text{specified} & \text{frequency weightings} \\
 & & & \quad \text{disturbance} \\
 & & & \quad \text{performance (active optics)} \\
 & & & \quad \text{sensor dynamics} \\
 & & & \quad \text{control penalty} \\
 & & \text{specified} & \text{sensor suite}.
\end{array} \tag{5.2}$$

where z is the pathlength motion error, w is a selected spectrum of disturbance augmented with broadband sensor noises, $prop_i$ is the property attributes of a selected beam element i and u_{loc} is the selected actuator locations (symmetric).

Genetic algorithm parameters were set for propagation of 30 designs over 80 generations. Separate design information strings of beam type and actuator location were used. This has the effect of splitting up the design into schemata according to attribute. The splitting is detrimental to convergence if a good scheme includes the two different attributes, see Eqn. 3.48, since crossover now has two chances of separating the string. However, unnecessary "hitchhiking" of bad values within an attribute to the good values within the other attribute has been eliminated. Crossover occurred with probability $p_c = 0.8$ and mutation occurred with probability $p_m = 0.05$. Diversity was enforced during propagation so that no two copies of the same design proceeded. For each sensor suite and disturbance type several runs were made using purely random selection of initial designs. In each respective case a final run (seeded) was made that used the best designs found in earlier runs along with random initial designs. This final run represents a punctuated equilibrium where the best results from random seeds are compared and propagated with further random information.

5.2 One Dimensional Low Frequency Disturbance Results

Results from several different G.A. runs for three different low frequency disturbance cases are shown in Fig. 5.4 with the actuator location denoted by x's. The nominal structure, with best actuator location, is shown for each case in the first column of the figure. The middle two columns are samples of G.A. runs for each case that started from a random initial population. Rightmost is the final seeded G.A. run. Rows are cases for the performance z, collocated angle θ_l and collocated load f structural sensors respectively. All use the hub angle sensor θ_h. Performance improvements over the nominal open loop, *i.e.* structural controller off, are listed in dB in the bottom right hand corner of each design. Control efforts are listed in the bottom right hand corners of the nominal and seeded designs.

A couple of key characteristics are evident in the solutions of Fig. 5.4. All runs have tended to the maximum stiffness constraint increasing the overall structural mass by just 12 %. Local stiffness at each actuator location has been reduced resulting in an active hinge. Intuitively, if the trusswork either side of the hub is considered as arms, then the actuation can be considered as elbows or wrists that have fine control over the tip positioning. It is natural that there is a trade between the leverage that the actuation has over the tips and the delay that exists because of the flexible links that connect the tips to the actuators. A particular characteristic of the performance and local angle structural sensor solutions is softening near the root. The solutions are not particularly sensitive to this softening, however, the added softening near the root has the effect of isolating the disturbance forces from the sensitive payloads.

Rows of G.A. designs show the perils of the design space. On close inspection, different designs show similar performance. Exploration of the sensitivity of the optimal designs to minor structural changes revealed that the design space was shallow and bumpy near these solutions. Sensitivity to local variations in the location of the active hinge was also found to be small, until the hinges neared the end of the structure. Hinge authority was seen to vary greatly with location when near the truss

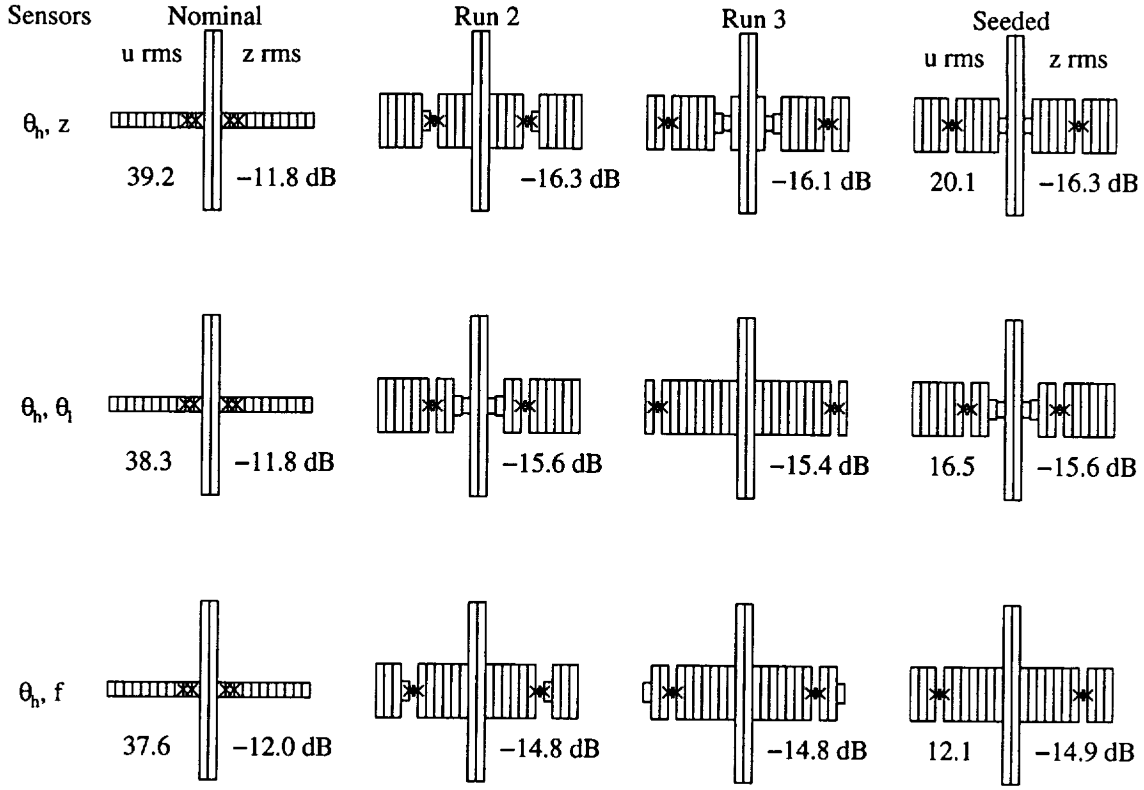

Figure 5.4: Optimized structures stiffness distributions for low frequency disturbances; columns are differing runs; rows are differing structural sensor choice; paired x's mark actuator locations. Performance/open loop nominal in bottom right-hand corner of designs. Root-mean-square control effort in bottom left hand corner of nominal and seeded designs.

tips.

For the performance sensor the optimal actuator location is near the tips so as to locate the actuator near the performance, yet removed from the tips so as to allow authority over them. Solutions similar to that using the performance sensor are found using the local angle sensor. The best local angle solution has more softening at the root and the active hinge is further inboard. The total performance is slightly worse than that of the performance sensor. The collocated load sensor apparently does worse than the performance and angle sensors in the relative numbers. This is due to load sensor impedance trade off. The optimal design is driving towards a hinge, while reducing the local stiffness reduces the overall sensor gain relative to it's noise

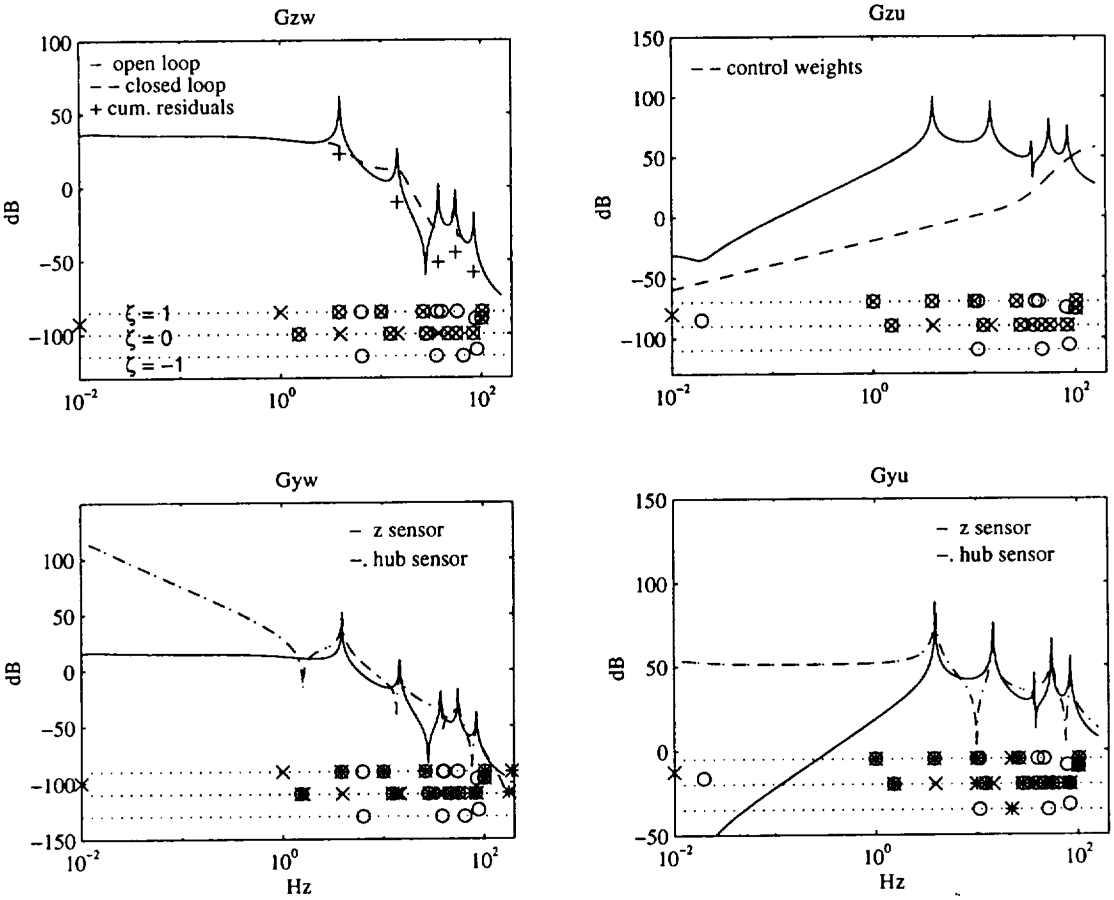

Figure 5.5: Nominal structure block transfer functions for low frequency disturbances using the performance structural sensor; x's are open loop system poles, o's are zeros to the structural sensor $\approx z$, and *'s are zeros to the hub sensor θ_h.

quality. Note that the load sensor designs in Fig. 5.4 are slightly thicker at the hinge.

In general the active hinging isolates and allows authority over the performance. Just how this is done can be seen by viewing the optimized system block transfer functions versus that of the nominal system using the same sensor suite.

The nominal system transfer function matrix is shown in Fig. 5.5. Modes that are visible in the response are antisymmetric modes of the system. Note how the plant transfer functions G_{zw} and G_{zu}, solid curves, are affected by the closed loop optics weighting. Without the weighting the low frequency response in G_{zw} would roll down at $1/\omega^2$ and would dominate the motion error cost. Low frequency disturbance weighting contributes to the roll off seen in G_{zw} and G_{yw}. Dashdot curves in G_{yw} and

G_{yu} represent the hub sensor transfer functions. Control weights are plotted on the regulator transfer function, G_{zu}. They show that the control is rolled off near 100 Hz and that more control is available at low frequencies.

On each transfer function a pole-zero frequency *vs* damping plot ($p/z-\zeta$) is provided where the x's are system poles, the o's are zeros to the structural sensor, and the *'s are zeros to the hub sensor. On the $p/z-\zeta$ plots the lower most dotted line represents real right half s-plane (RHP) and the upper most dotted line represents real left half s-plane (LHP). Poles and zeros not on the $\zeta = 1$ or $\zeta = -1$ lines are duplicate, *i.e.* they at least occur in conjugate pairs.

The slightly stiffened pseudo rigid body mode is evident at 0.01 Hz. Stable weighting poles can be seen on the $\zeta = 1$ line. The disturbance weighting pole is at 1 Hz. Performance weighting poles appear to be cancelled by zeros. These poles are duplicated, since the performance is used as a sensor. Therefore in transfer functions involving z, or y as a measure of z, one set of zeros cancels one set of these weighting poles with the duplicate set of poles remaining. Symmetric mode pole-zero cancellations are depicted on the $\zeta = 0$ line with increasing high frequency density.

As is characteristic in beam problems, real minimum-nonminimum phase zero pairs occur in transfer functions with noncollocated inputs and outputs. The pairs become less damped and gradually misaligned in frequency as their frequency increases due to discretization. When in effect it is the nonminimum phase zero of these pairs that limits the controller performance [21]. These pairs of zeros tend to raise the average transfer function gain for no phase increase. This impedes compensator roll off since the plant continues to lose phase with the occurrence of modes.

Closed loop G_{zw} is plotted as dashed in Fig. 5.5. The first antisymmetric mode is heavily damped and the second only slightly. Modes from the second onward contribute little to the total closed loop performance. Loop and sensitivity transfer functions are illustrated for the structural control in Fig. 5.6. From this figure it is clear that the hub sensor is predominantly used to control the first antisymmetric mode with the performance sensor lightly mixed in.

The control design can be thought of as separate regulator and estimator steps

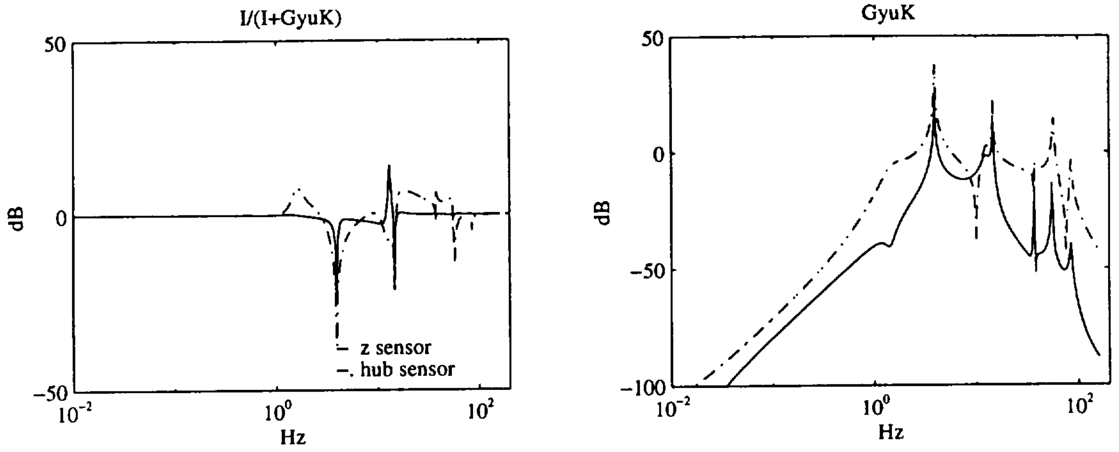

Figure 5.6: Sensitivity and loop transfer functions for structural control of the nominal system with performance structural sensor.

with the combined compensator acting on the G_{yu} transfer. In the nominal design the regulator is clearly limited by the irrational structural behavior indicated by the nonminimum phase zero at 10 Hz. The estimator primarily uses the hub sensor which is close to collocated with the disturbance in the necessary bandwidth. There are no *'s below the $\zeta = 0$ line in the bandwidth shown. The performance sensor is mixed in near the zeros of the hub sensor transfer function. Even though u is near the root, it is not collocated with the hub sensor beyond the second antisymmetric mode, shown by the zero (*) at 25 Hz in the G_{yu} loop. Since the control is focussed on the first antisymmetric mode it is really the regulator that limits performance when combined with G_{yu} loop nonminimum phase behavior.

Weighted cumulative residuals are plotted in G_{zw} of Fig. 5.5 under each pole, ω_p. They are computed as,

$$M(\omega_p)\sum R_i/\omega_i^2 \quad \omega_i \geq \omega_p\,, \tag{5.3}$$

where the weights are $M(\omega_p)$, the modal frequency of the ith mode is ω_i, and the modal residue of the ith mode is R_i. The weights $M(\omega_p)$ scale the structural residuals by the disturbance and performance spectral filters. These residuals indicate where the open loop transfer function is held up by residual static stiffness and where it is held up by the close spacing of the modes. For example, the average G_{zw} transfer function gain follows just above the first two +'s and well above the last three. The result is that the average response near the first two modes is dominated by asymptotic inertia and stiffness. Here the asymptotic effects of the real nonminimum phase zeros is important. Near the last three modes plotted the average response is dominated by the resonant nature of the modes and how closely they are spaced. See Chapter 2 for more details on simpler systems. For this spectrum of disturbance the performance is not sensitive to these closely spaced modes until extremely high bandwidth control is attempted.

When optimizing this system the objective is to lower the dashed curve in G_{zw}. This means lowering the average transfer function gain in a controllable fashion. Since the area under the curve is primarily at low frequencies, and is scaled by the total system inertia, moving the average transfer function gain via structural change alone is a difficult task.

Block transfer functions for the optimized structure shown in the right most column of the first row in Fig. 5.4 are depicted in Fig. 5.7. Comparing the G_{zw} transfer functions of the nominal and the optimized structures shows softening of the first and second modes and stiffening of the higher modes. The hinging has improved the average gain in the G_{zu} transfer function through the softening. Locating the actuator near the tip yields good pole-zero structure out to near 100 Hz in G_{zu} (alternating poles and zeros until the real zero pair near 100 Hz). Moving the hinged actuator towards the tip hasn't compromised estimator phase since again the hub sensor is primarily used. Estimator pole-zero structure to the performance sensor is worse. This sensor is lightly used. Important nonminimum phase behavior for the optimized system is now in the G_{yu} transfer function. In general, the improved authority over the first two modes can be seen by comparing the closed loop disturbance to performance plots.

The optimized design shows mass dominated transfer functions, *i.e.* zeros occurring close to the left of the poles in G_{zu} and G_{yu}, suggesting that trend is to structurally isolate the tip payloads. This isolation type solution is further aided by the high pass nature of the performance weights and the low pass nature of the disturbance weights.

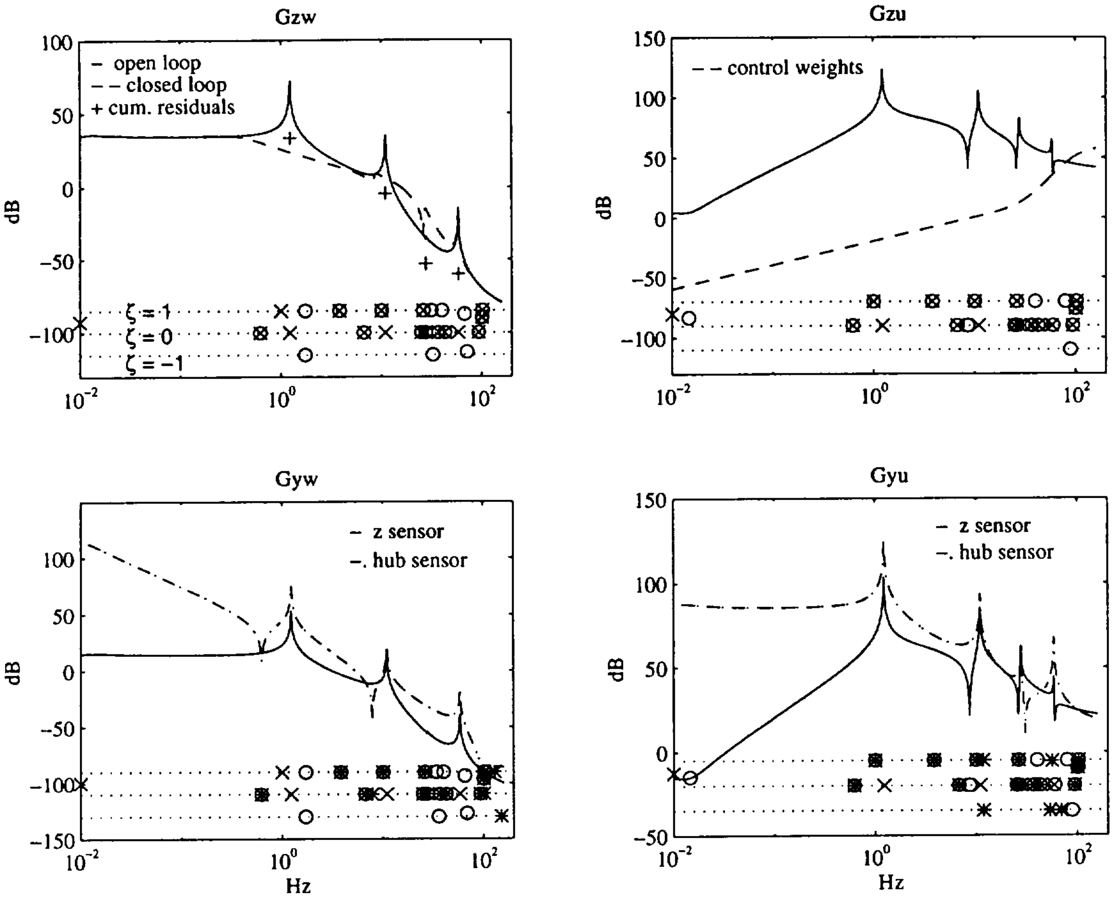

Figure 5.7: Optimized structure block transfer functions for low frequency disturbances using the performance sensor.

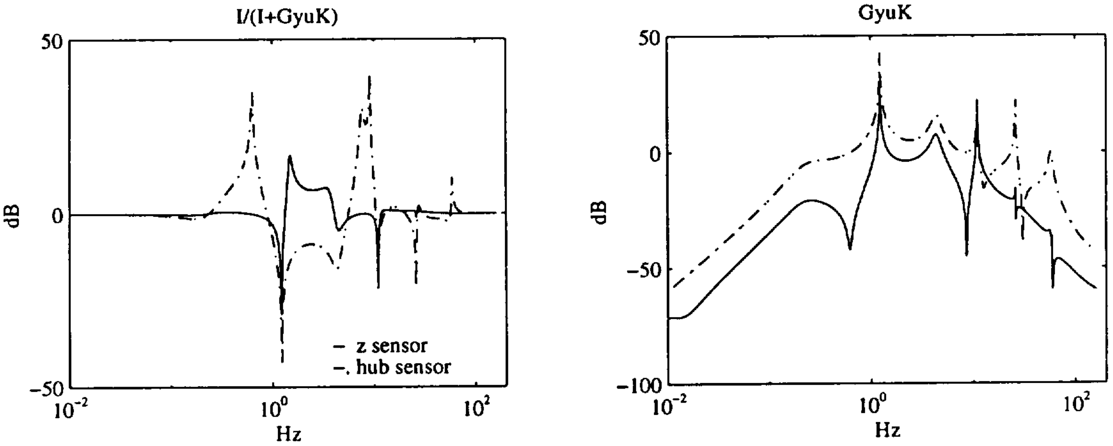

Figure 5.8: Sensitivity and loop transfer functions for structural control of the optimized system with performance structural sensor.

Authority of the controller is seen to be quite different than the nominal when comparing Fig.s 5.8 and 5.6. The sensitivity of the optimized system shows regions of strong amplification in order to achieve performance in the $1-7$ Hz band. Again the performance sensor is only lightly used, and is seen to make the performance worse in the $1-7$ band at the expense of dampening the modes.

The cumulative residuals in Fig. 5.7 show how the average transfer function gain is improved by softening the fundamental mode. A corner of the performance transfer function is shaved off. The higher frequency modes have been stiffened so that the average gain in this region is no longer dominated by the modal spacing. These improvements are minor compared to that incurred through increased authority over the fundamental.

Results from optimizing the system are limited. Improvement over the nominal system is just 4 dB in the closed loop. The reason is that performance is dominated by the system rigid body inertia, as can be seen in the low frequency region of the G_{zw} transfer functions. Optimizing the structural system for a given payload mass can only have limited effect on this response. However, it is possible to demand higher gain from the closed loop optical systems at these low frequencies (if the guide star is bright enough) attenuating more response. This effect would further emphasize the G.A. design results and will be shown in the experimental results in Chapter 6.

Of the two collocated structural sensors the load sensor will be presented here because of sensor impedance effects. The block transfer function for low frequency disturbances using the structural load sensor is shown in Fig. 5.9. The optimal design for the load sensor shows similar trends to the performance sensor. However, the fundamental antisymmetric mode is actually stiffened when compared to the nominal, even with the passive softening of the hinge. The global stiffening of the system has countered the softening due to the hinge, because the hinge is not completely destiffened. The second mode has remained unchanged while higher modes are stiffened.

Outward placement of the actuator/sensor again results in good pole-zero structure from actuator to performance, as seen by no real RHP zeros in the G_{zu} $p/z-\zeta$ plot. Again the structural sensor G_{yw} transfer function shows the effect of structural

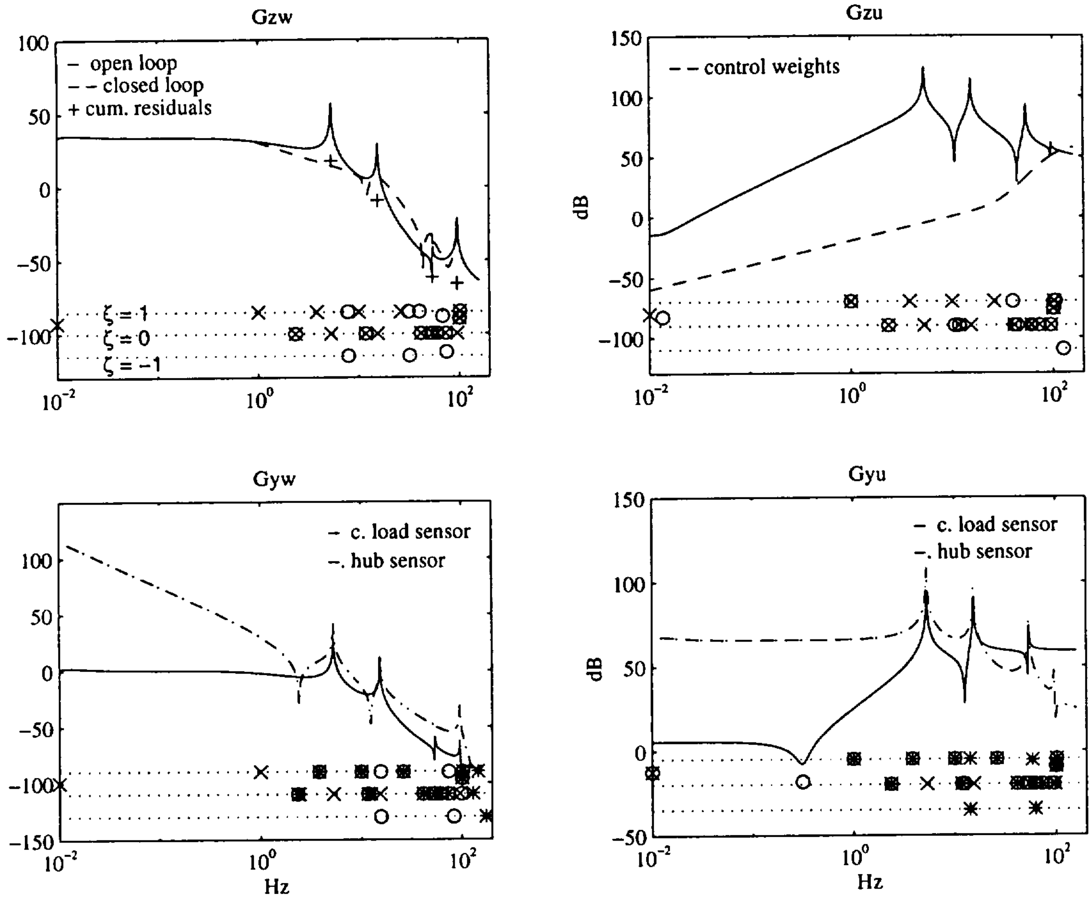

Figure 5.9: Optimized structure block transfer functions for low frequency disturbances using the collocated load sensor.

delay with real zero pairs occurring at relatively low frequencies in the bandwidth. Unique features of the load sensor transfer functions, are a strong feed through term and disappearing residues of high frequency modes in the G_{yu} transfer functions, and that the first nonminumum phase zero occurs near the second mode in the G_{yw} loop. The best load sensor design, as with the other designs shown in the last row in Fig. 5.4 shows less structural variation than the other two sensor types yet the trend is again to globally stiffen and structurally isolate the payload.

The control loop sensitivity and loop transfer functions are similar to the optimized performance sensor design in that they show a band of attenuation with some amplification at the band edges. Overall the controller is narrower in its rejection band and generally shows less authority.

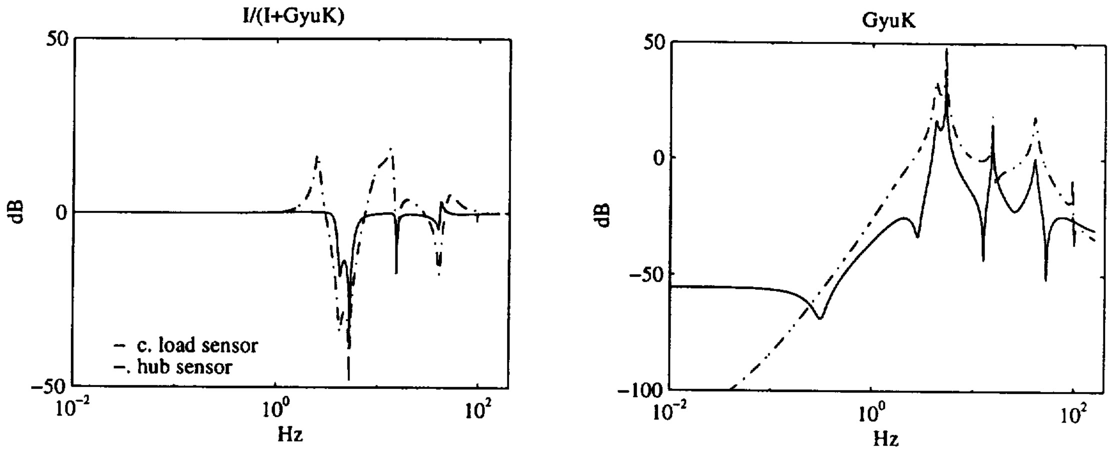

Figure 5.10: Sensitivity and loop transfer functions for structural control of the optimized system with collocated load structural sensor.

When comparing the controllers from the optimized solutions to that of the nominal it appears that they are working much harder to achieve better performance and that not allowing the nominal designs a lessor control penalty has biased the results. This is not the case. Control efforts are compared in the lower left hand corners of the nominal and best designs in Fig. 5.4. In every case the optimized designs use less control effort because of the effect hinging has on the influence coefficients. On average the reduction in control effort from this impedance effect is $\approx$ 8 dB rms, while the performance is also improved. This shows that for the same control effort the motion error performance improvement would be more dramatic, mainly because of undamped resonances in the nominal designs.

5.3 One Dimensional High Frequency Disturbance Results

Under high frequency disturbances, see Fig. 5.3 for the shape of the assumed filter, the search finds designs that are structurally discontinuous, illustrated in Fig. 5.11. In this case the collocated load sensor is predominantly used. The hub sensor is included but is rolled off at low frequencies so that its influence is small in the controlled bandwidth. Disturbance emphasis on the higher frequency modes has resulted in

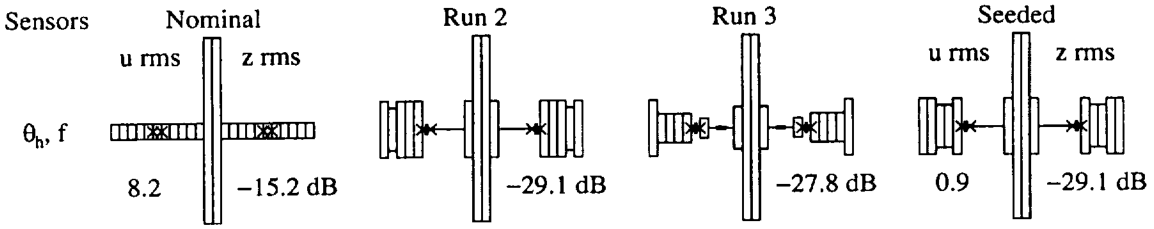

Figure 5.11: Optimized structures for high frequency disturbances and structural load sensor. Performance/open loop nominal in bottom right-hand corner of designs. Root-mean-square control effort in bottom left hand corner of nominal and seeded designs.

a complicated structural filter producing a design with actuator/sensor pair at the midspan, reduced cross section inboard and stiffened cross section outboard. The best nominal actuator location is also at the midspan, see the first column in Fig. 5.11. Again in the optimized designs the cross section at the actuator/sensor location is soft but, again, not so soft as to overly reduce the sensor gain. Overall the optimized solutions are $\approx$ 83 % of the nominal structural weight.

Physically the optimized designs shown in Fig. 5.11 are localizing the disturbance energy inboard of the actuator locations at frequencies below the peak disturbance frequency. The outboard sections have been stiffened so as to provide good leverage over the performance sensitive tips. The stiffened sections act like softly restrained pseudo rigid bodies at low frequencies. At frequencies above these pseudo rigid body modes the actuators react against the outboard section inertias to damp the localized flexible section modes that are observable in the performance.

The disturbance now serves to excite a higher frequency range of the G_{zw} transfer function. Figure 5.12 shows this as an incorporated weighting for the nominal structure. The nominal system shows that moving the actuator from the root to the midspan has improved the pole-zero structure in the regulator transfer function G_{zu}, where the first nonminimum phase zero is real and occurs at $\approx$ 40 Hz. The first nonminimum phase zero in the estimator, to the structural sensor, is real and occurs near 12 Hz. The pole spacing is good near these nonminimum phase zeros so that their effect on the average gain is important. Reasonable control is achieved over

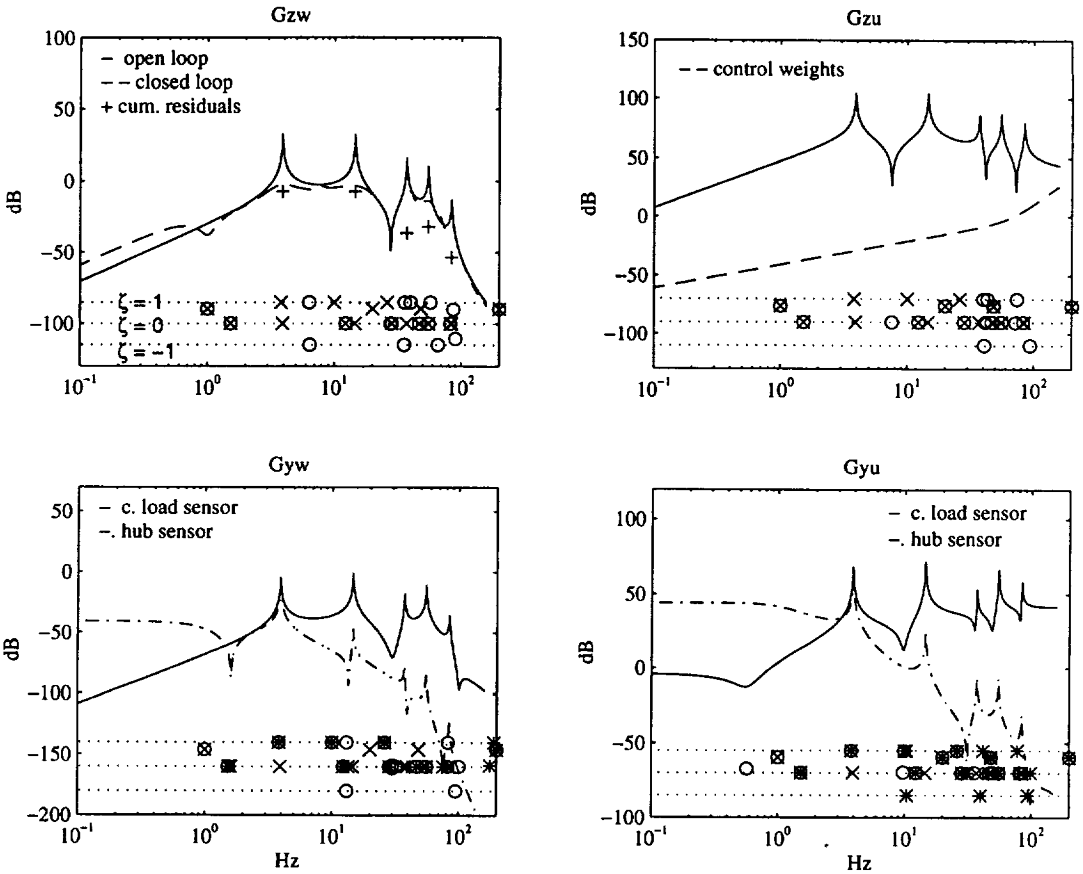

Figure 5.12: Nominal structure block transfer functions for high frequency disturbances using the collocated load structural sensor; x's are open loop system poles, o's are zeros to the structural sensor $\approx f$, and *'s are zeros to the hub sensor θ_h.

the first two modes with some dampening of the later three modes realized. As in the low frequency case the G_{zw} cumulative residuals show that the average transfer function tracks the cumulative stiffness for the first two modes and rides on near resonance effects beyond the second mode. Close pole spacing of the third and fourth antisymmetric modes is now an important contributor to the performance.

Controller sensitivity and loop transfer functions, see Fig. 5.13, show that the primary sensor used is the collocated load sensor. Narrow bands of attenuation that encompass the modes are seen in the sensitivity, with fairly good authority over the higher frequency modes. Note that because the load cell measurement has a strong feed through term the controller barely rolls off within the plotted 200 Hz band.

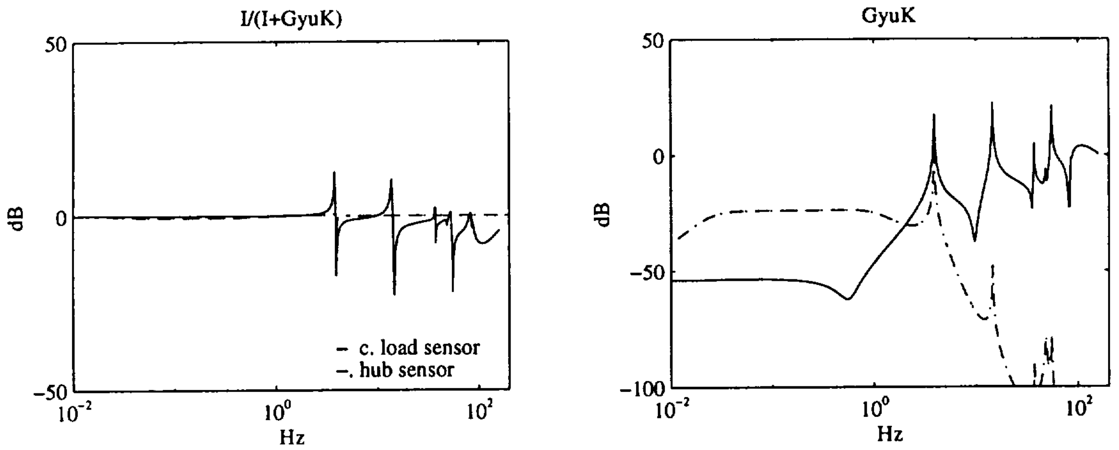

Figure 5.13: Sensitivity and loop transfer functions for structural control of the nominal high frequency disturbance system with collocated load structural sensor.

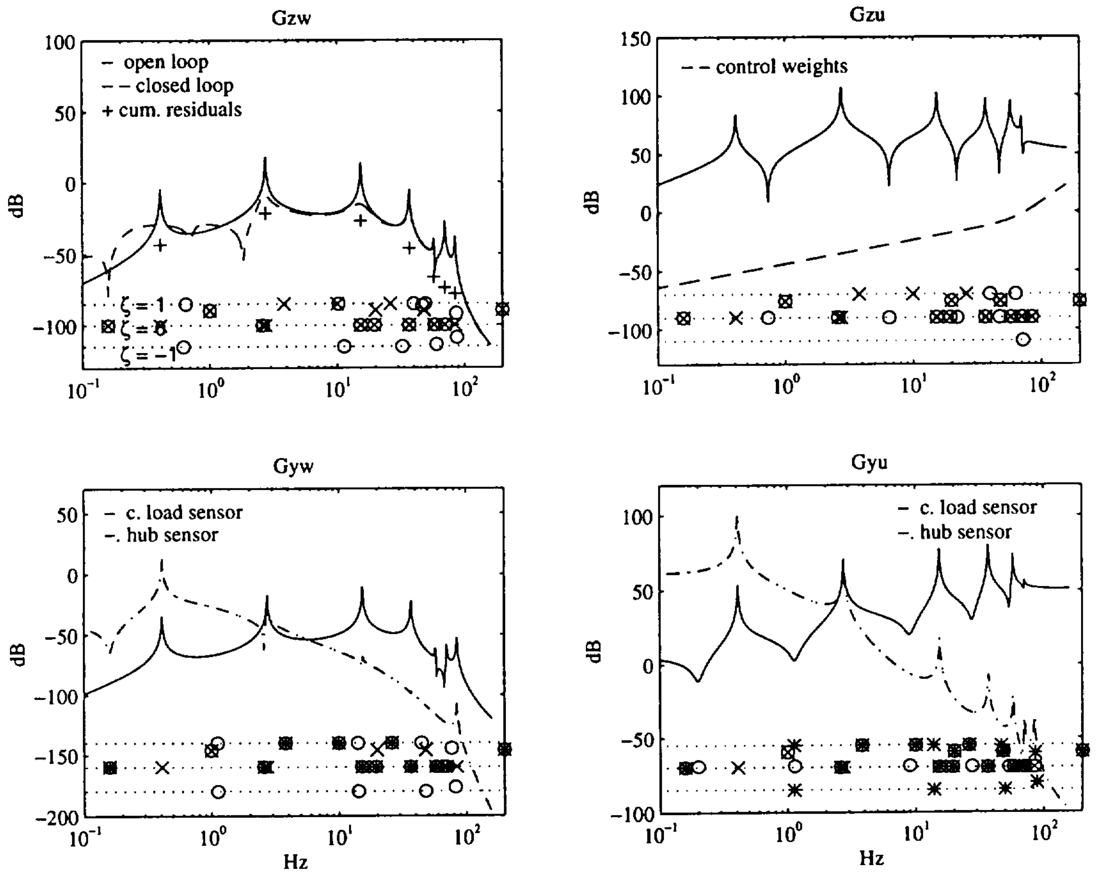

Figure 5.14: Optimized structure block transfer functions for high frequency disturbances using the collocated load structural sensor.

The system block transfer functions for the best design under high frequency disturbances are shown in Fig. 5.14. Disturbance emphasis, seen in the average gain of G_{zw}, has resulted in tailoring of the dynamics to achieve yet further improved regulator pole-zero structure. There is good authority over the emphasized bandwidth, shown in the gain and the pole zero spacing in G_{yu}. Poor estimator pole-zero structure, real zero pairs in the load G_{yw}, has resulted from the very flexible inboard portion of the structure. This limits the control to dampening of the first, second and third modes. The dampening is enough to improve performance.

Major improvements over the closed loop nominal system are realized because the overall average transfer function gain in the important frequency band has been reduced by 10-15 dB. The effect of the structural tailoring has been to stretch out the modal spacing so that beyond the second mode the average transfer function gain follows the asymptotic cumulative residues for a few more modes. The control merely dampens the system to this average gain. At these high frequencies the average gain is dominated by the flexible properties of the system. Evidently structural system optimization has greater impact here where the assumed optical control has less.

Further evidence that the control has less to do with this solution than the structural tailoring is seen in Fig. 5.15. The attenuation shown in the sensitivity plot is on the same order as that in the nominal design, however, control effort, compared in Fig. 5.11, is an order of magnitude less for the optimized system.

5.4 Three Dimensional Box Truss Example

A three dimensional example was generated that serves the same interferometry application with a low aspect ratio structure. Rather than being a free flyer spacecraft, this design is intended to be mounted to the Multi-Payload Experiment Support Structure (MPESS) in the Shuttle cargo bay. This interferometer has a much shorter baseline, due to cargo bay and MPESS geometric constraints, and is therefore limited in its scientific resolution.

A schematic of this design example is shown in Fig. 5.16 as the instrument. The

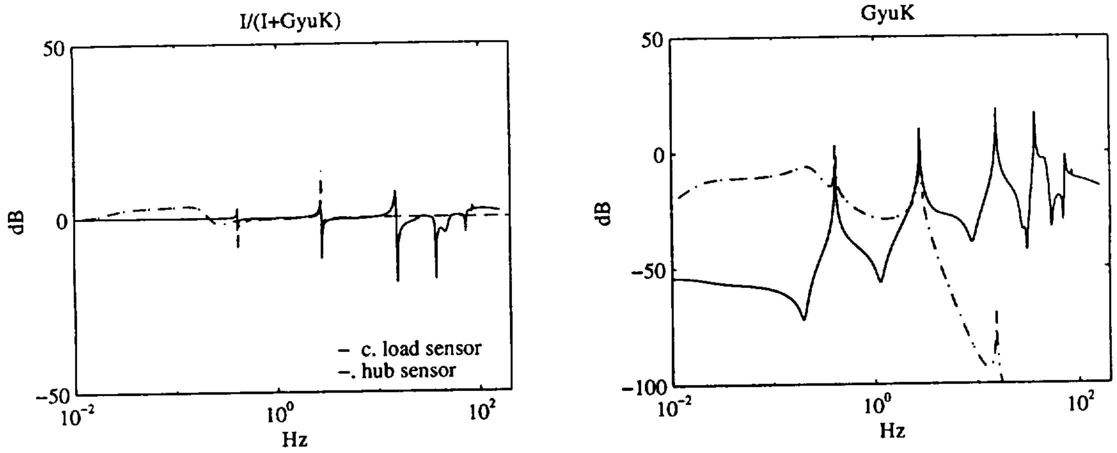

Figure 5.15: Sensitivity and loop transfer functions for structural control of the optimized high frequency disturbance system with collocated load structural sensor.

instrument was realized as a truss, see the nominal design in Fig. 5.17. The topology of this truss was searched over along with actuator/sensor placement and member cross-sections. Structural topology variables were truss bay node locations and diagonal member connectivities. Each member of the truss work was represented by two beams joined at the midpoint. Including midpoint dof increased the fidelity of the model, since for this aspect ratio local dynamics were more likely to factor in the optimized designs.

The truss was discretized into six components, each bay being a component. Components were condensed and assembled using the suggested Component Mode Synthesis since a full truss model consisted of $\approx$ 700 dof, which was too large to decompose for each design during the Genetic search. The interface dof used were three translational dof at each of the truss corner nodes that join two neighboring bays. Twelve internal modes were kept for each component along with the constraint modes.

Performance in this example is similar to the previous application example in that the pathlength error is modeled as the difference in vertical motions of the end bay optics (the left most and right most spheres in Fig. 5.17). Again a high pass filter is used that represents closed loop optics. For this example the target star is assumed brighter resulting in a higher bandwidth filter. The filter is depicted in Fig. 5.18.

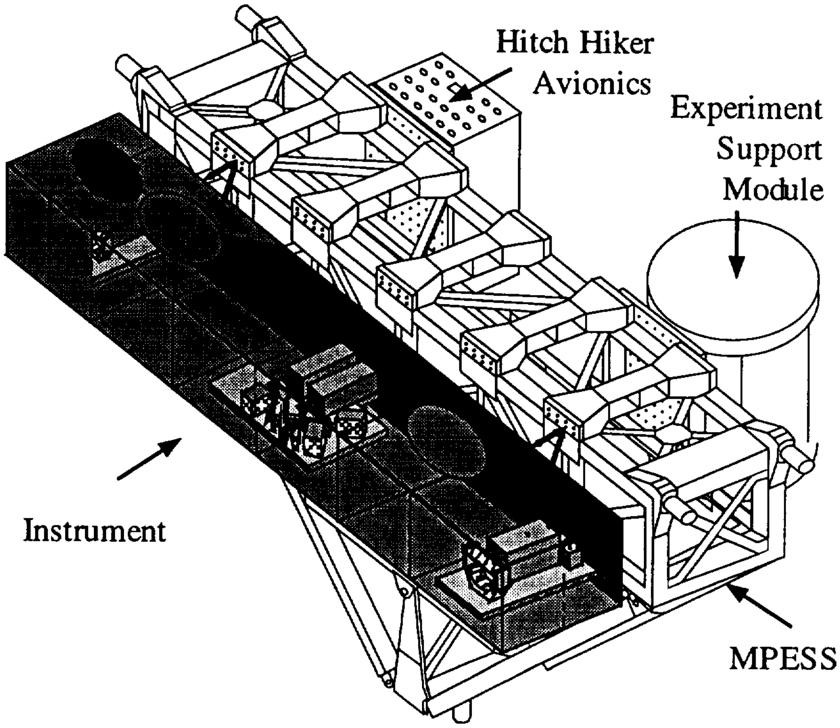

Figure 5.16: Schematic of the payload bay configuration for the three dimensional box example.

Disturbance enters as a broadband prescribed motion of the mounting interface. In reality the MPESS has flexibility which would couple to the dynamics of the box near 80 Hz. This is not modeled here. The sense of the disturbance is shown by the arrows in the bottom right of Fig. 5.17. Specifics of how the motion mathematically enters the system is given as an example in Eqn.s 2.5 and 2.6 of Chapter 2. The spectral bound on the disturbing motion is shown in Fig. 5.18. The motion is seen to roll down at $1/\omega^2$ at low frequencies, representing the shuttle deadband in pointing control. At $\approx$ 10 Hz the motion filter decreases the roll off rate to $1/\omega$ representing added motion due to the shuttle flexibility disturbed by the vernier attitude control and onboard noisey mechanisms.

Two independent actuators are placed in the structure. Possible locations are the longerons and diagonals of the truss structure, the left and right end optics mounting struts and the semi-vertical interface mounting struts. The actuators are assumed to be active struts. Again, the active strut stiffness is variable. In the nominal design the

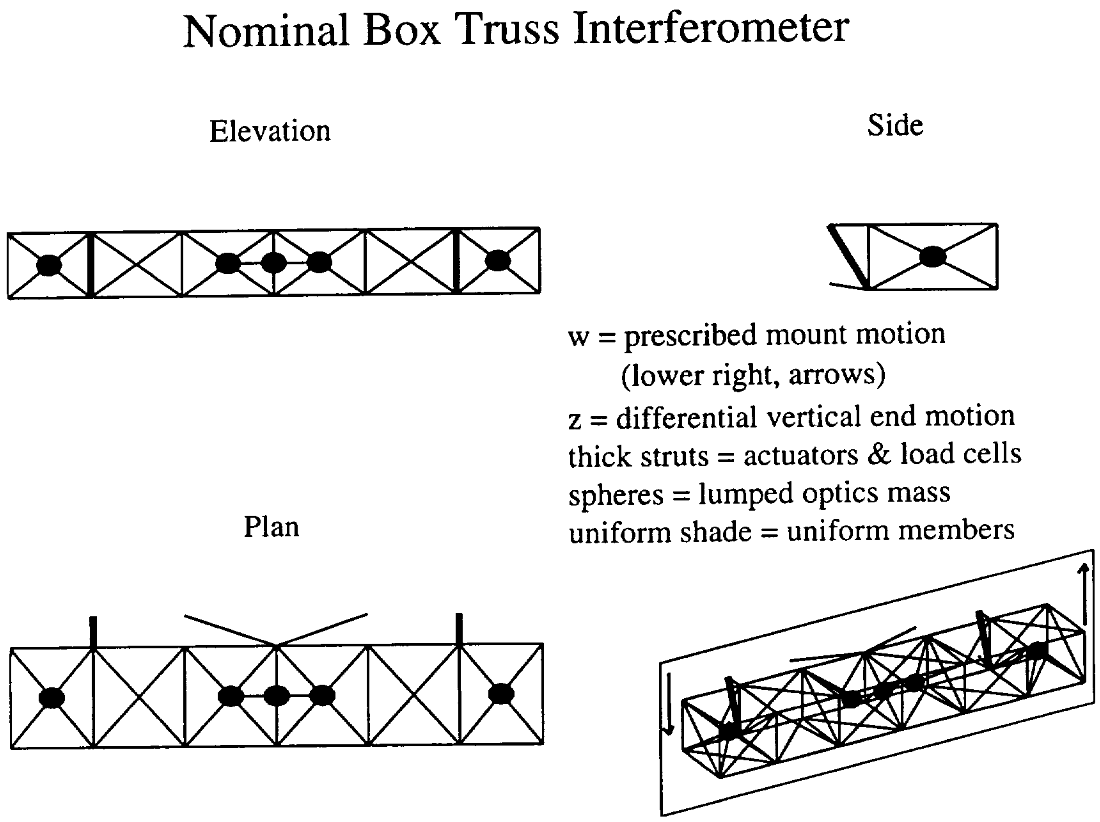

Figure 5.17: Four view of the nominal box truss structure.

active struts are both in the semi-vertical mounting positions, see the thick struts in Fig. 5.17. Control penalty frequency weighting for each of the actuators, in all designs, is assumed to be the same and is shown in Fig. 5.18. This weight again favors more actuation at low frequencies (for softer modes) and rolls off the compensator at high frequencies where unmodeled dynamics are inevitable.

The sensor suite used for structural control is comprised of a measurement of the filtered performance and two relative load measurements. Relative load measurements are collocated with the active struts and, as before, depend on the local stiffnesses of the struts.

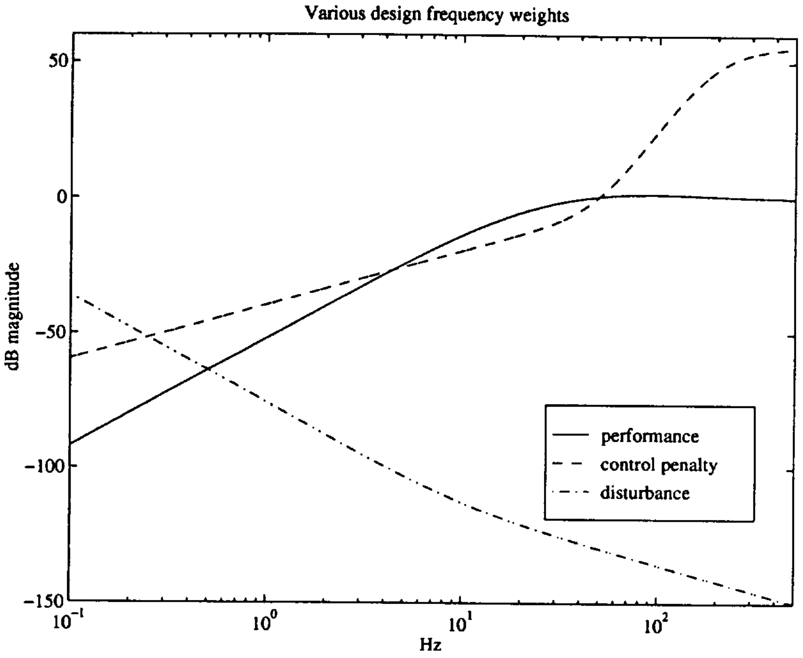

Figure 5.18: Disturbance, performance and control penalty weights used in the box truss design example.

Formally, this discrete evolutionary design problem can be stated as,

$$
\begin{array}{rcll}
\min J & = & \left\|G^{cl}_{zw}\right\|_2^2 \,, & \\
\text{subj. to} & & \text{variables} & prop_i \in \{\text{possible beams}\} \\
 & & & grid_j \in \{\text{allowable locations}\} \\
 & & & conn_k \in \{0,1\} \\
 & & & u_{loc} \in \{\text{possible locations}\} \\
 & & \text{implicit} & H_2 \text{ constraint equations} \\
 & & \text{specified} & \text{frequency weightings} \\
 & & & \quad \text{disturbance} \\
 & & & \quad \text{performance (active optics)} \\
 & & & \quad \text{sensor dynamics} \\
 & & & \quad \text{control penalty} \\
 & & \text{specified} & \text{sensor suite}\,,
\end{array}
\qquad (5.4)
$$

where z is the pathlength motion error, w is a prescribed motion disturbance augmented with sensor noises, $prop_i$ is the property attributes of a selected truss strut i,

$grid_j$ is the perturbation to the nominal grid point location for the jth grid, $conn_k$ is the connectivity selection of the kth diagonal, and u_{loc} is the selected actuator locations (two independent selections). The grid perturbation set represents 512 choices bounded to be $\pm .15$ meters in all directions. The choice of connectivity of a diagonal is posed as a $\{0, 1\}$ problem where 1 is the nominal orientation and 0 is its complement within the same truss bay face.

Genetic algorithm parameters were set for propagation of 40 designs over 80 generations. The separate design information strings were strut properties, grid point locations, diagonal connectivities and actuator locations. Crossover occurred with probability $p_c = 0.8$ and mutation occurred with probability $p_m = 0.05$. Diversity was enforced during propagation so that no two copies of the same design proceeded. Several runs were made to explore the design space and the best presented here.

5.5 Nominal Three Dimensional System

The nominal truss shown in Fig. 5.17 has uniform member properties. They are the stiffest allowable and are therefore black (softer struts will be grey shaded). Block transfer functions for the nominal system are plotted in Fig. 5.19. This system represents the condensed, reduced model.

Since the actuators replace the interface mounting struts, which are symmetrically placed with respect to the performance and each load sensor, see Fig. 5.17, the transfer functions involving both actuators overlay. That is, in G_{zu} both transfer functions to the single performance z are equivalent to numerical precision. Transfer functions from disturbance to individual load sensors also overlay due to symmetry. Here, G_{yw} is meant to be a 3×1 set of transfer functions. Since there are three sensors and two actuators the singular values of G_{yu} should really be presented. However, often in the singular values directional information is lost, so here, individual transfer functions from each strut to its collocated load sensor are shown. Transfer functions from the actuators to the performance sensor are the same as those shown in G_{zu}.

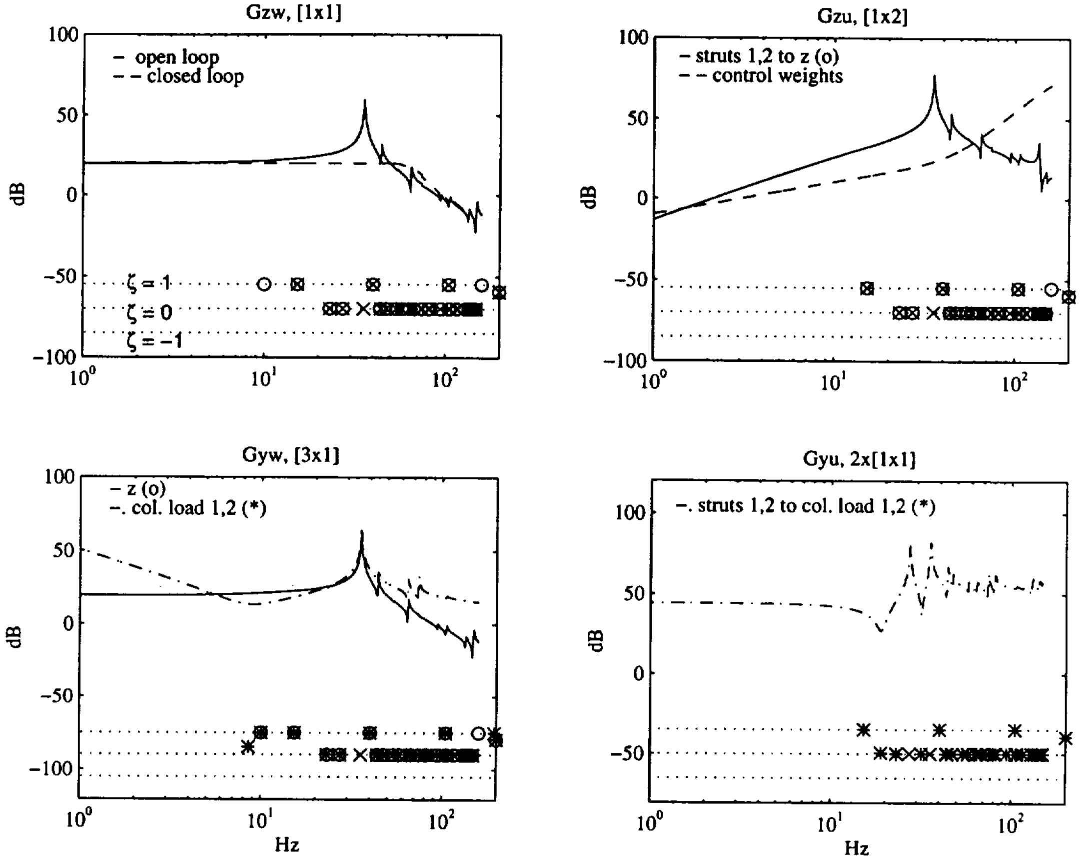

Figure 5.19: Nominal condensed system block transfer functions. The closed loop rms performance is 110 nm with 68 N rms control effort.

Cross transfer functions from each actuator to the other actuator's load sensor are not plotted.

As with the beam example, the effect of the performance filter is seen to flatten out the low frequency gain of the weighted G_{zw} transfer function. In this example the low frequency response is dominated by the interface stiffness, unlike the beam example where the inertia dominated. The responses look similar in the frequency domain because in this case the disturbance rolls down at low frequency like $1/\omega^2$. The collocated load sensor shows measurement of the low frequency prescribed displacement disturbance. This is because the mounting struts do not form a determinant mount, they are slightly indeterminant shown by the sensitivity of the load sensor to low frequency motion. Again, the collocated load sensor impedance can be seen in the G_{yu} transfer functions with the zeros (*) cancelling the weighting poles.

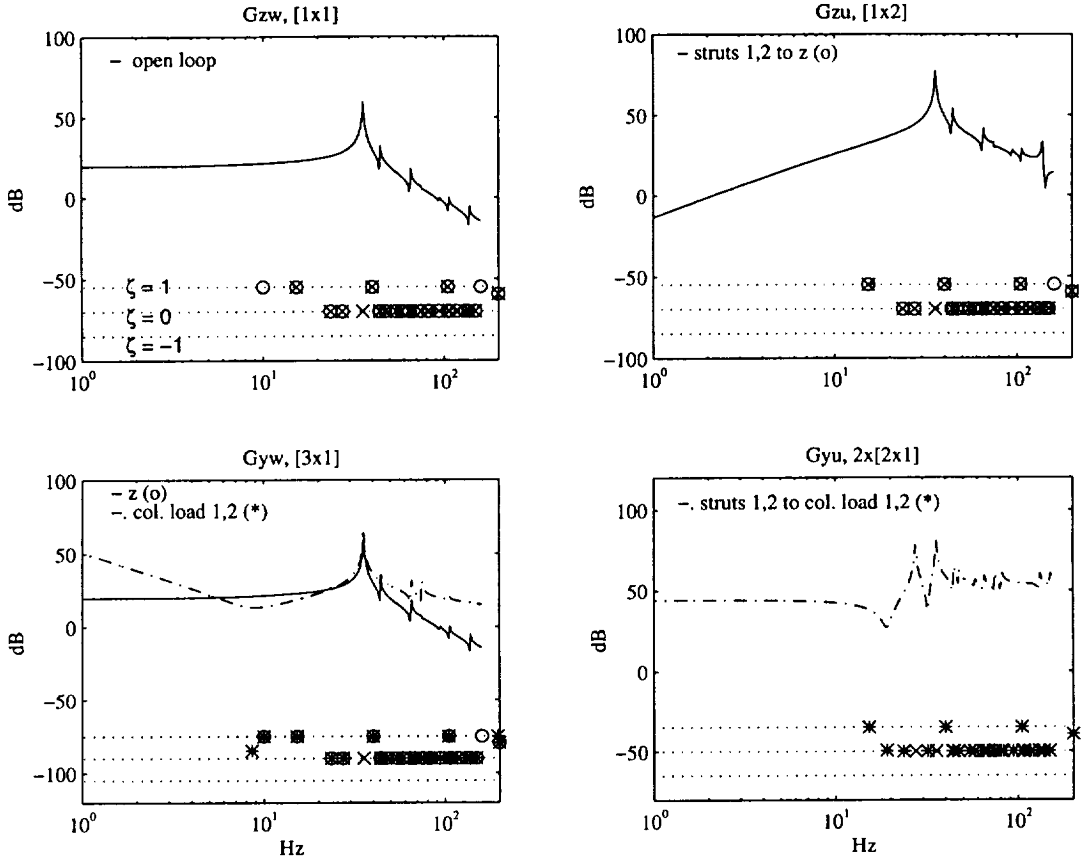

Figure 5.20: Nominal full system block transfer functions.

Pole/zero-ζ plots show the system is collocated in the bandwidth plotted. In this case performance is limited by the allowed authority of the actuators since they have to be rolled off before high frequency unmodeled dynamics. The closed loop G_{zw} shows that the performance is dominated by the rocking mode of the truss on the mounting struts. The truss appears excessively stiff as other modes appear as excursions on the transfer function. An order of magnitude of closed loop performance improvement comes about due to the dampening of the fundamental mode. The open loop performance is 1000 nm rms and the closed loop performance is 110 nm rms.

To show that the CMS condensed structure is sufficient to predict the dynamics the full 700 dof model is assembled. One hundred modes of this model are kept and transfer functions computed. The full nominal model block transfer functions are shown in Fig. 5.20. They compare extremely well with Fig. 5.19 showing that the kept internal modes are sufficient to describe this system. The full and condensed nominal models should compare since the system is very stiff, so that localized dynamics have small effect on the solutions. The G.A. solutions will be more flexible and more susceptible to condensation error.

5.6 Evolutionary Three Dimensional Design

Typically the G.A. searches took on the order of three days to run. The best result from one of the searches is presented in this section. Results from the others are similar. Performance in the nominal design is limited by structural actuation authority. For the same level of authority the G.A. design is expected to make the system more flexible to improve regulation and estimation gain at the expense of collocation.

Unusual geometries result from the G.A. search. The best result is illustrated in Fig. 5.21. Member properties are denoted by grey shading where darker shades are stiffer members. This truss is lighter weight than the nominal which is comprised of all stiff members. Note that the spheres are in constrained locations, the optics mounting bars do change length in keeping with the truss node positions. Through varying nodal locations and diagonal connectivities the G.A. has arrived at a truly unusual geometry.

The actuators are in the left hand end semi-vertical interface mounting strut and the right hand end bay outermost face diagonal. They are softer than those of the nominal and are not symmetrically placed. One is located near the disturbance entry points while the other is near a sensitive performance point.

Diagonal connectivities are such that the bottom-most truss nodes that are mounted to the interface have been destiffened. Mounting struts to the performance points have remained relatively stiff. In general, the structure appears to have been softened.

The transfer functions in Fig 5.22 confirm the softening. The fundamental mode has been softened from 36 Hz to near 22 Hz. Considerably more gain is evident in the G_{zu} loops. Note since the actuators are no longer symmetrically placed in a symmetric structure, separate transfer functions are plotted for each. Strut 1 is the

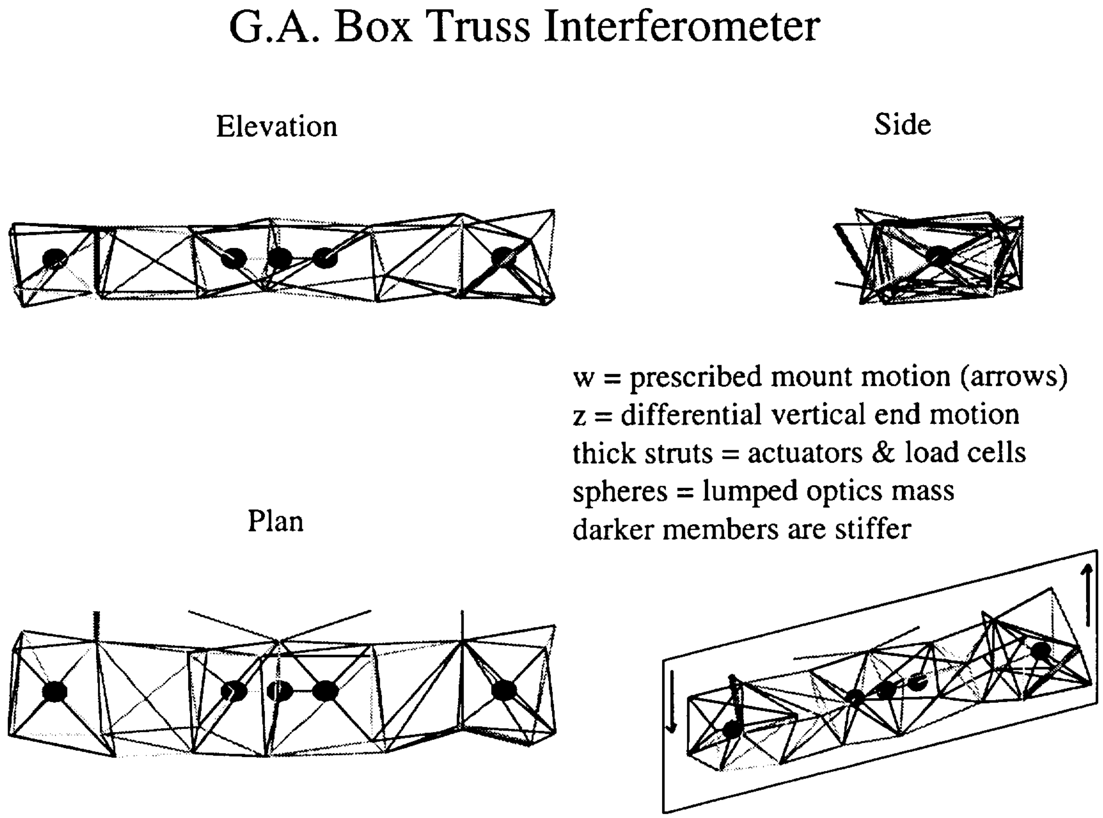

Figure 5.21: Four view of the optimized box truss structure.

actuator in the right hand end bay and strut 2 is the actuator in the left hand end interface mounting. Strut 1 has more gain in its G_{yu} transfer function to its load cell since the surrounding structure is stiffer than the interface mounting arrangement. Both load sensors measure more disturbance (see G_{yw}) since the topological variations have reduced the freedom of the interface mounting.

Subtle differences between this result and that of the nominal truss are in the existence of lightly damped nonminimum phase zeros. For example, there exists a lightly damped nominimum phase zero in the G_{zu} transfer function for strut 1 near 30 Hz. Strut 2 doesn't show this behavior in G_{zu}. The collocated load measure in strut 1 also shows nonminimum phase behavior in G_{yw} where in this case there is a zero on the real axis at near 30 Hz. The load measure in strut 2 remains collocated in G_{yu}. Evolutionary manipulation of the truss topology has not destroyed the pole-zero structure of the interface mounted active strut.

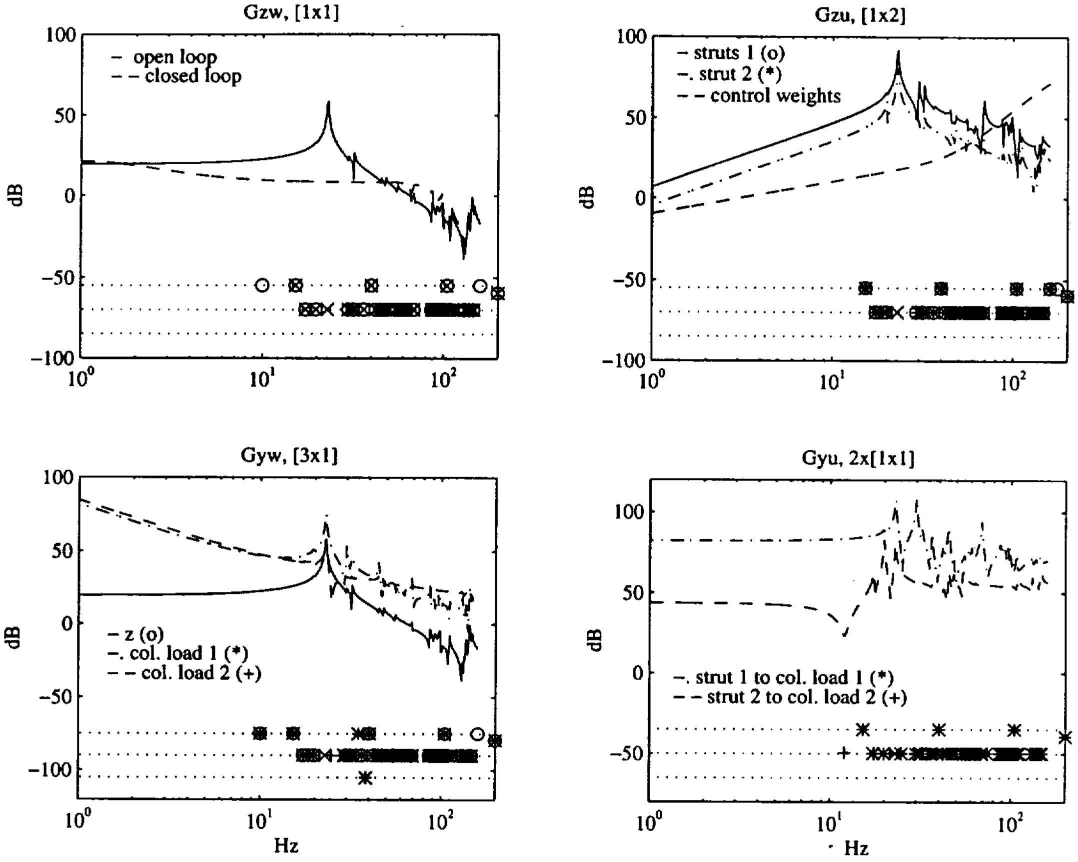

Figure 5.22: Condensed model block transfer functions for the best G.A. design. The closed loop rms performance is 33 nm with 75 N rms control effort.

Performance of the closed loop system appears much improved over the nominal system, ≈ 9 dB rms. The dashed curve shown in the G.A. G_{zw} achieves more attenuation primarily because there is more relative spacing between the control weights and the regulation transfer functions. This would occur even if the control weights were level at low frequencies. The rms control effort in the optimized case is 10 % larger than that of the nominal. The result is coupled disturbance and performance isolation. Strut 1 provides the performance isolation while strut 2 provides the disturbance isolation. The fundamental mode is softened by a decade in the closed loop and is easier to control for a given actuator forcing capability because it is passively soft. In practice this solution will be limited by the actuator stroke capability at low frequencies.

It is worth comparing this three dimensional interferometer design to the low frequency disturbance solution of the one dimensional beam example. Both tend to isolate by softening and dampening the fundamental mode. In the beam design the beam generally stiffened while the payload was isolated via active hinging. Overall the performance was difficult to improve because the low frequency response was dominated by system inertia. The three dimensional box truss case has showed similar softening and dampening effects where the right hand end is pinned at the mounting node and at the left hand end an actuator acts on the disturbing interface. A second actuator in this case allows compensation of the left hand end performance point through the end bay structural frame. The controlled truss result is more effective because the low frequency response depends on the stiffness which is being directly manipulated by the search algorithm.

5.7 Summary

An application was explored that clearly shows the benefit of considering controls and structural topology changes simultaneously when optimizing motion error performances. Both one dimensional and three dimensional structures were designed that included assumed optical control of the performance through frequency weights. Differing types of disturbance were investigated that ranged from low frequency broad band to high frequency narrow band bounds on input spectra. Structural actuators were included as active units within the structures and a variety of sensors were included for feedback to the model based compensators. In the one dimensional designs punctuated equilibrium was used to further compare the best of each run while allowing more randomized genetic information to be incorporated.

The results are topologically complex, there would be no hope of finding these solutions through gradient search techniques. Inspection of the designs in terms of system transfer functions shows, for a fixed control penalty, that the trend is to structurally isolate the performance from the disturbance. For low frequency broadband disturbances this occurs by softening and dampening the fundamental structural modes. Softening the mode coupled with good actuator/sensor placement renders the actuator with more authority over it, *i.e.* there is more relative gain in the regulation loop.

High frequency narrow band disturbance designs for the beam example have primarily improved performance by manipulating the average transfer function gain. In these high frequency ranges system collocation is difficult to achieve. The best one can expect from model based control design in these ranges is dampening of key structural modes.

Results form the motion disturbed three dimensional box truss are similar to the one dimensional beam in that structural regulation has been improved. This occurs at the expense of estimation, since good sensors were assumed. In this example larger performance improvements for a broadband input were realized because the system low frequency response is dominated by the system stiffness. Here, topological structural variations have more influence over the response.

These analytical results need to be verified experimentally before systems level conclusions are drawn about their effectiveness. Since the method was developed with an eye to implementation it is expected that these results will be verified by a scaled experiment.

Chapter 6

Experimental Results

Experiments were constructed that validate and explore the limits of the interferometer one dimensional design example. The experiments are a scaled version of the one dimensional example. Through these experiments insight into the quantitative effects of a system redesign of a closed loop system is provided. Simple arguments are given in terms of the fundamental physics of the designed structural filtering. The arguments describe how the average structural transfer gain and structural delay limit the closed loop performance.

In this chapter five different configurations are used (four of which are shown in Figures 6.1 and 6.2) when comparing six cases of closed loop performance. Both low and high frequency disturbance solutions are investigated over several sensor choices. Further cases are presented in Appendix C. As in the design example, the low frequency disturbance was assumed impulsive/step-like and broadband in nature. This disturbance serves mainly to excite the system rigid body behavior which is partially compensated by the active optics. Structurally and optically controlled performance improvements of the optimized system are expected to be limited. The high frequency disturbances are harmonic-like and narrow band in nature. They tend to excite both the structural stiffness and distributed mass. Impressive performance improvements over a simple regular truss design are expected.

The chapter is initiated with description of the hardware followed by an input/output system description and discussion of the data taking procedure. Within the input/output description a subsection on closed loop optics is given that details how the optical outputs of the system, both metrology and stellar, are implemented and emulated. A section on data realizations and control design technique provides the necessary background to the cases that follow. Selected results from the low and high frequency disturbance cases are presented.

6.1 Testbed Description

Three major constituents make up the spacecraft-like testbed; the hub, the truss boom and the optics benches. Physical properties for the testbed are listed in Table 6.1.

The truss is 24 bays of square-based pyramids connected at the apex by longerons, as shown in Figures 6.1 and 6.3 with square faces up. At any given cross section the truss is internally determinant, which is a good architectural choice for incorporating active struts as base longerons. This allows the structural actuators to have a direct effect on the sensitive axis of the interferometer. Indeterminant truss work is used to mount the truss to a mount plate that is inset in the hub concrete block shown in Fig. 6.4. The hub block is mounted on soft air-pucks to the floor that are near-under the CG of the block.

Optics benches are mounted at the tips and at the center of the truss on the upper face. The outer benches are 0.5 in. thick aluminum plate and are mounted on 1/4 in. standoffs to a slightly enlarged truss bay. The middle bench is 0.75 in. thick aluminum plate and is mounted directly (with some shimming) to the truss face. Mass is added to the tip benches to simulate the appropriate mass distribution for this scale truss.

Suspension springs are used to offload the truss tips so that the structurally softened design solutions were implementable in the gravity field, and also, to prevent piezo strut actuators from being crushed (due to stack imperfection) when inserted at the hub root.

In whole the system is $\approx 1/4$ the design space craft length, with $\approx 1/5$ the tip and hub mass, and $\approx 1/3$ the EI. These scalings render the natural frequencies a

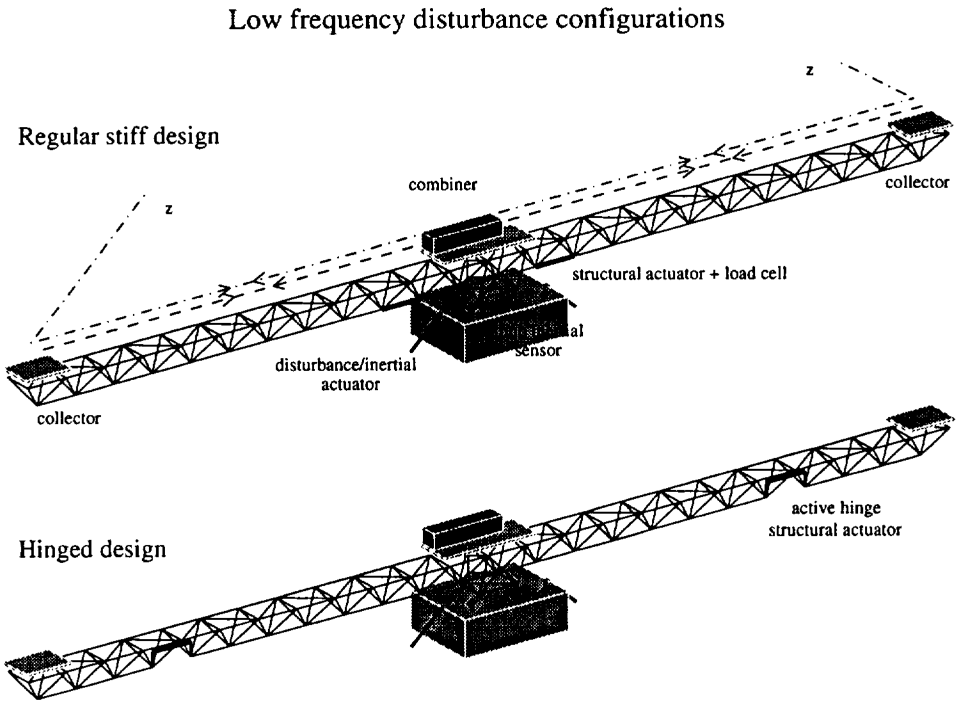

Figure 6.1: Regular and Hinged design configurations for low frequency disturbances.

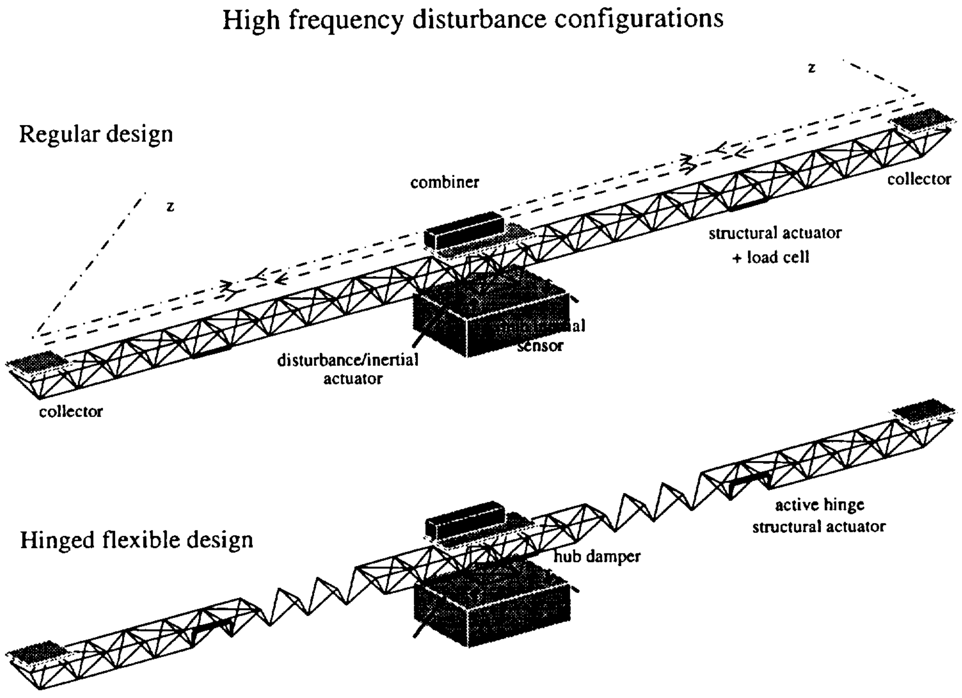

Figure 6.2: Regular and Hinged Flexible design configurations for high frequency disturbances.

Table 6.1: Physical properties for the imaging interferometer testbed.

Aspect	Property	Value
Hub	total mass	146.6 kg
	size	0.69 x 0.69 x 0.22 m
	mount plate	0.41 m sq. inset
		3/4" hole spacing
Truss	total mass	8.68 kg
	size	.25 x 6.0 x .18 m
	geometry	.25 m sq. base pyramid
		(sq. face up)
		long. connect apex
		(triangular x-section)
	members	3/8 in. OD, 0.058 in. wall
	node mass	35.5 g + 11.2 g/strut
Benches		
collector	total mass	6.37 kg
	size	0.3 x 0.3 x 0.013 m
	lump mass	2.68 kg
	optics mass	0.61 kg
combiner	total mass	17.58 kg
	size	0.3 x 0.61 x 0.019 m
	laser mass	3.4 kg
	laser size	0.11 x 0.33 x 0.13 m
	voice coil mass	1.1 kg
	voice coil size	0.09 x .11 x .11 m
	optics mass	approx. 1.5 kg

decade higher with compressed modal spacing in the ensuing decade, $\approx 10 - 100$ Hz. With the correct disturbance scaling, quantitative results can be projected for the 25 m baseline design example. The suspended pseudo rigid body rocking mode of this system is at around 1 Hz and the vertical bounce pseudo rigid body mode is at ≈ 5 Hz. Other pseudo rigid body modes fall in the $1 - 5$ Hz band and are not coupled to the design performance.

A heterodyne He-Ne laser optical system is used to measure the internal truss motions as well as emulate collected starlight. Both legs originate from the central combiner and operate as differential Michelson interferometers. In a differential Michelson interferometer both target and reference polarizations are used. A rough

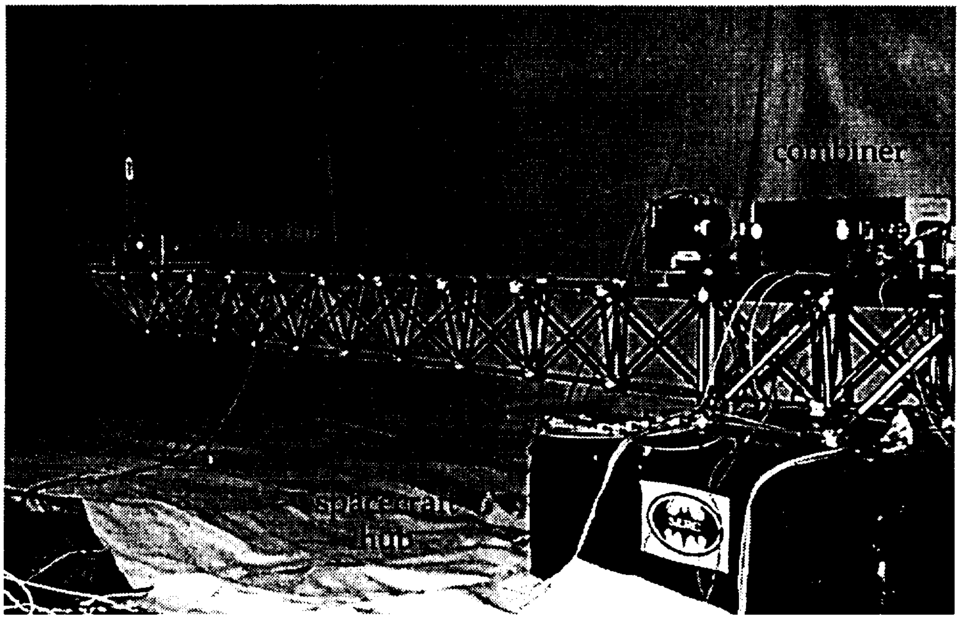

Figure 6.3: Left side oblique view of the testbed with collector optics mounted at the tip on the upper face of the truss.

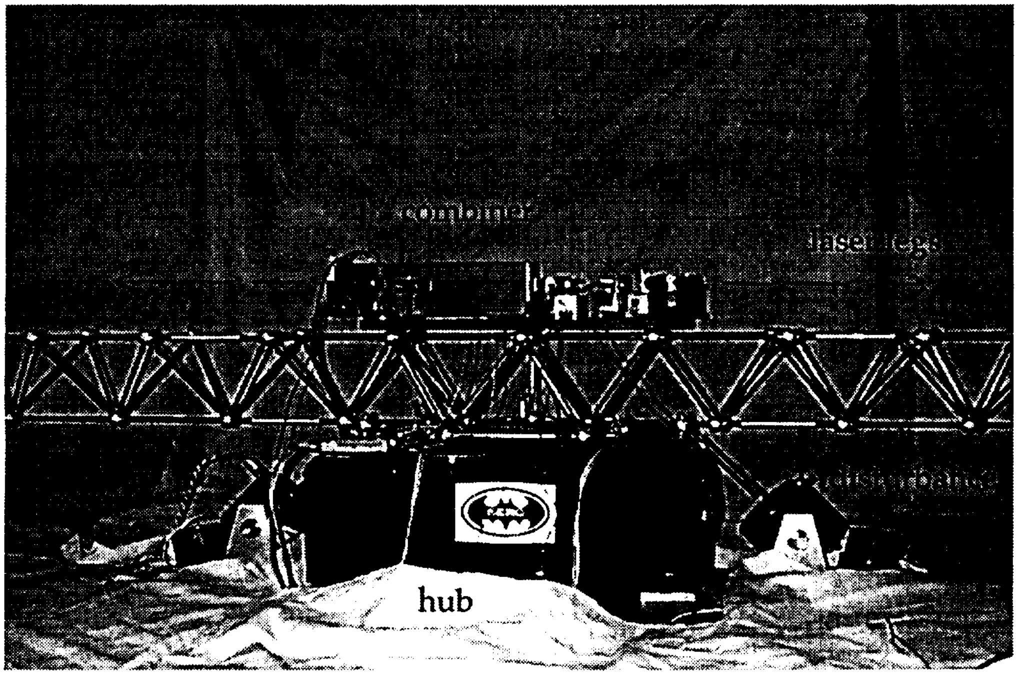

Figure 6.4: Front view of the testbed hub with combining optics mounted on the top plane of the truss.

Table 6.2: Description of optics used in the imaging interferometer testbed.

Quantity	Description
1	power splitter, 1.0 in. cube
2	polarizing splitter, 0.5 in. cube
7	fold mirrors, 1.0 in. ϕ
2	fold mirrors, 2.0 in. ϕ
8	1/4 wave plates, 0.5 in. ϕ
	(paired for 1/2 wave)
2	fiber fed HP receivers
2	retro-reflectors, 1.0 in.
1	custom cats-eye optic, 120 deg. fov,
	hemispherical focusing retro.

sketch of the legs can be seen in the upper configuration in Fig. 6.1 where the dashed line represents the internal measure and the dashed dot line represents the external measure. In the figure the z labeled external legs are reflected from the collectors upwards to a cats-eye optic "retro-reflector" directly above the combiner.

Figure 6.5 shows a plan view of the optical layout. A listing of the optical elements is given in Tables 6.2 and 6.4. The laser beam that originates from the top left of the combiner is power split into two legs. Each leg is split by polarization and each polarization is directed to the right and left ends respectively. The leftward legs pass through a zig-zag of delay line optics and fold mirrors before traversing the truss to the collector. On returning from the collectors the leftward legs rebound through the delay line optics before being combined with the rightward legs on receivers. The receivers are fed to the modulating transducers via fiber optics. Signals from the transducers are sampled and made available as digital output in the control computer VME setup. This is somewhat restrictive as the available laser output will have delay proportional to the system sampling rate (that may be limited by the size of the system required for structural control).

At each collector, shown in Fig. 6.6, the internal leg is retro-reflected while the external leg is reflected from a fold mirror towards a custom built cats-eye optic. The cats-eye optic is mounted in the ceiling $\approx$ 3 m directly above the combiner. Light

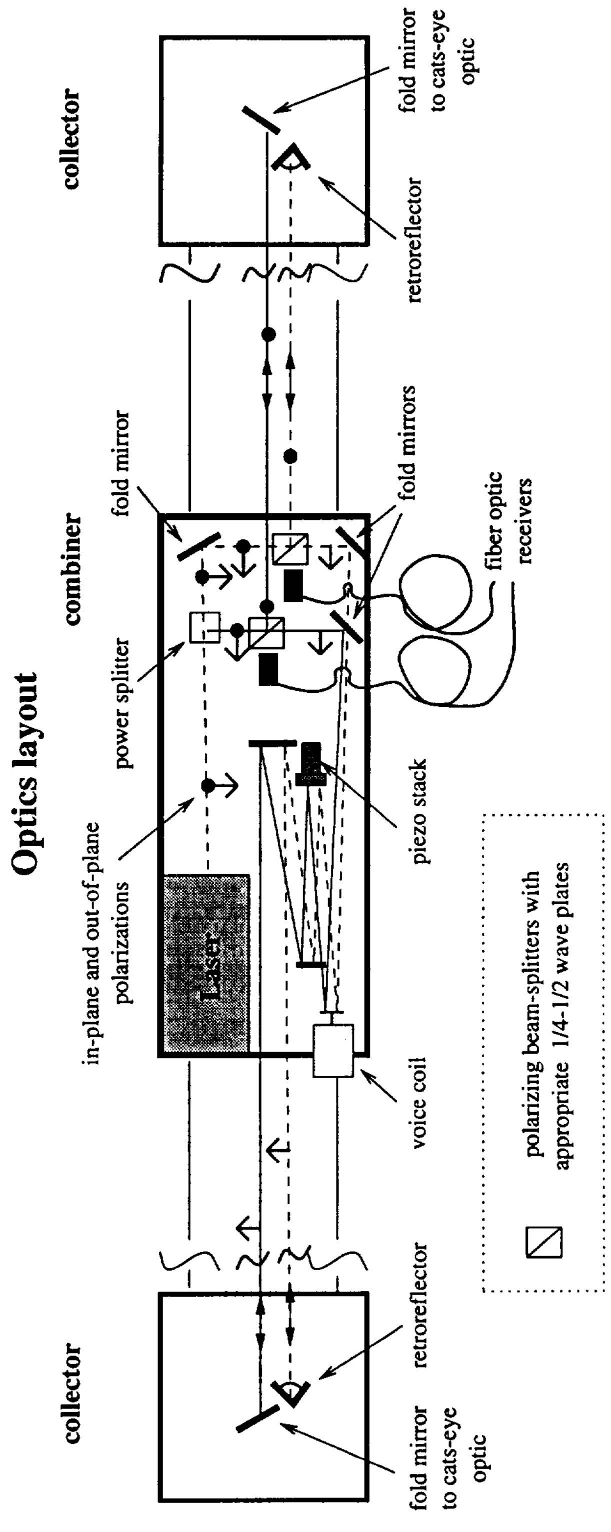

Figure 6.5: Plan view of the optical layout with arrows and dots representing in and out-of-plane polarizations

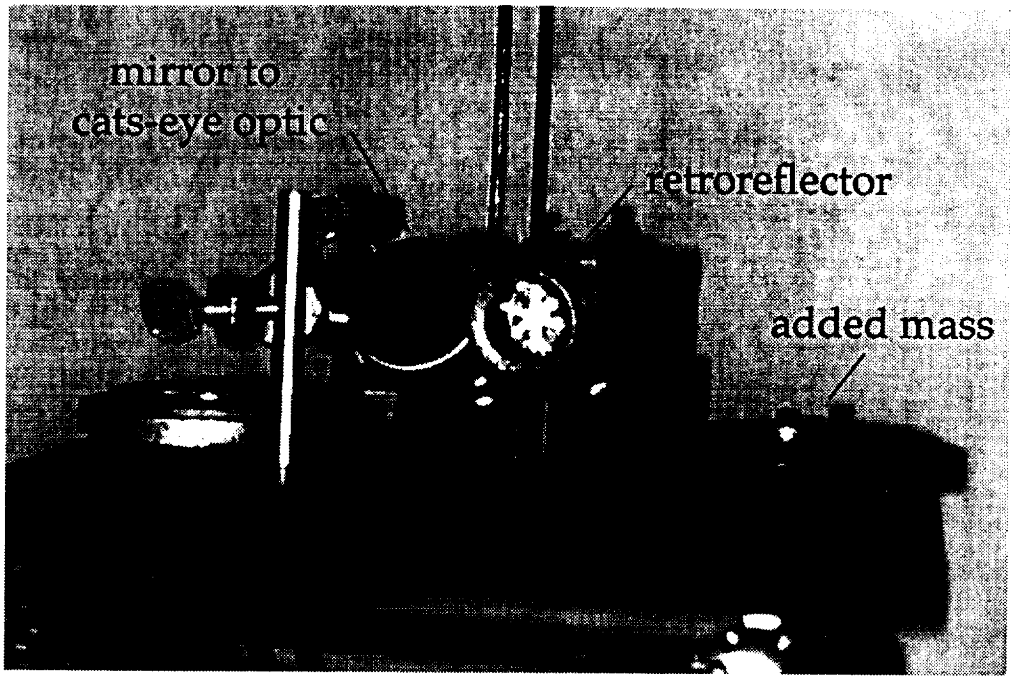

Figure 6.6: Right hand end collector. One leg is retro-reflected while the other is reflected to and received from the cats-eye optic.

incident on the cats-eye optic, shown in Fig. 6.7, from any direction in the field-of-view, is focussed through a central point and reflected back in the direction of the incident beam. This allows the emulation of a star by referencing the left and right ends of the truss through a common point in space. The effective measure obtained at the receiver is a differential pathlength proportional to the internal measure plus the laboratory referenced differential tip motion of the structure.

Hardware on the combination bench consists of a fold mirror mounted on a voice coil and a fold mirror mounted on a reactuated piezo stack. Reactuation involves an equivalent mass loaded piezo stack that is mounted on the back of the active optic. The voice coil provides large stroke capability while the piezo provides fine positioning and phase stabilization of the voice coil. A discussion of the optical control loops is deferred to the input/output description section. This delay line emulates an imaging spacecraft delay line in that it provides optical compensation of pathlength; however, an actual delay line design [52], has sizable focusing optics (f# of ≈ 3) for starlight pathlength compensation. In the actual device efforts are made

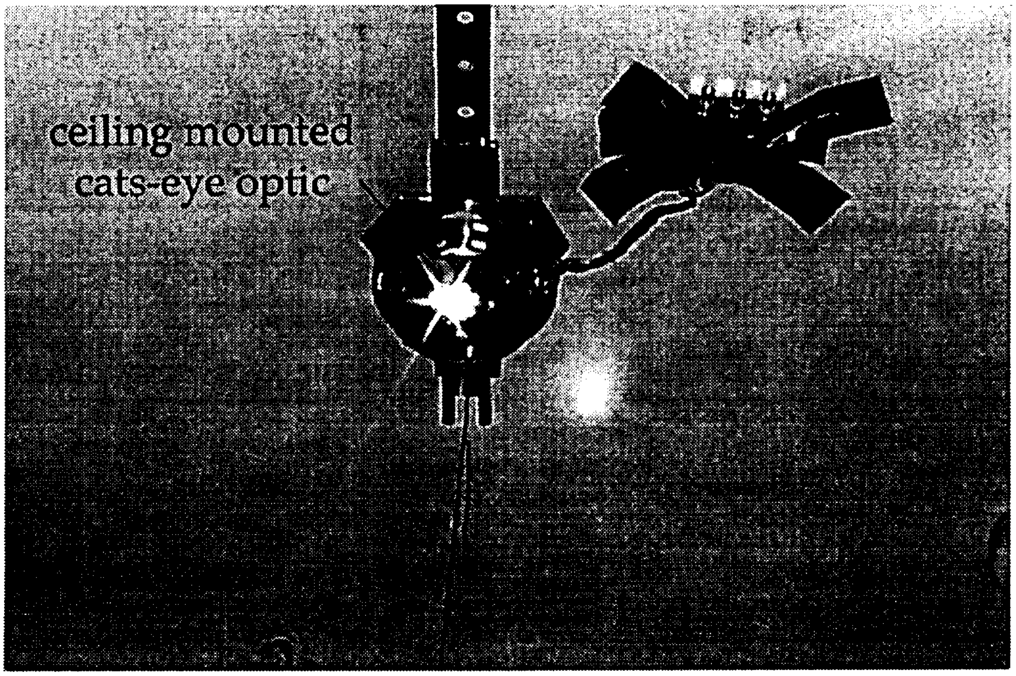

Figure 6.7: Cats-eye optic mounted in the ceiling $\approx$ 3 meters above the testbed hub. The cats-eye has a 120 degree field of view, note the camera flash visible in the glass.

to render the metrology beam coaxial with the starlight. Notice in Fig. 6.5 that the laser legs are nearly coaxial. It is sufficient to be nearly coaxial for coherent light. This will become evident in the discussion of the optical loops.

6.2 Input/output description

Detailed knowledge of the system inputs and outputs is required since the system that was optimized includes fixed bandwidth optical control. Signals are listed in Table 6.3. In general the system is four-in four-out with the optical and structural control acting independently. Figure 6.8 shows the wiring of the control computer to the hardware and the connect points of the data acquisition system to the setup. This section will outline the connectivity in Fig. 6.8 by discussing the disturbance, performance, actuators and sensors respectively. Throughout the discussion reference will be made to equipment listed in Table 6.4. A description of the data acquisition procedure will also be given.

Table 6.3: Description of effective 4 input and 9 output signals of the testbed.

Inputs	hub shaker
	delay line voice coil
	reactuated delay line piezo
	diff. PI piezo struts, left and right ends
Outputs	hub accelerometers
	strut load cells (collocated)
	internal laser leg
	external laser leg (starlight)

Table 6.4: Description of equipment used in the imaging interferometer testbed.

Equipment	Type	Gain/capability
Sensors:		
Laser	HP5517B	heterodyne, $\lambda = 632$ nm
		1 mWatt, 6mm beam ϕ
receiver	HP10780F	range .163 mm
Accelerometers	Sundstrand QA-1400	13.6 V/g
Load cells	PCB 208B	0.5 V/lb
Actuators:		
Hub shaker	B&K Type 4809	10 lb
amp.	Crown DC300A II	300 W
Optic voice coil	B&K Type 4810	2 lb
amp.	Crown DC300A II	300 W
Optic piezo	TS18-H5-202	10 μ m (free)
amp.	Crown DC150A II	150 W
Piezo strut	P-843.60	90 μ m (free)
		130 N (blocked force)
amp.	in-house	0-100 V offset
		+ gain of 10
Data acq.:		
	Tektronix 2630	4 sensors, 1 source
Control comp:	VME based	4 in 4 out, 4 kHz 60 states
	dual TIc40's	2 in 2 out, 2 kHz 200 states

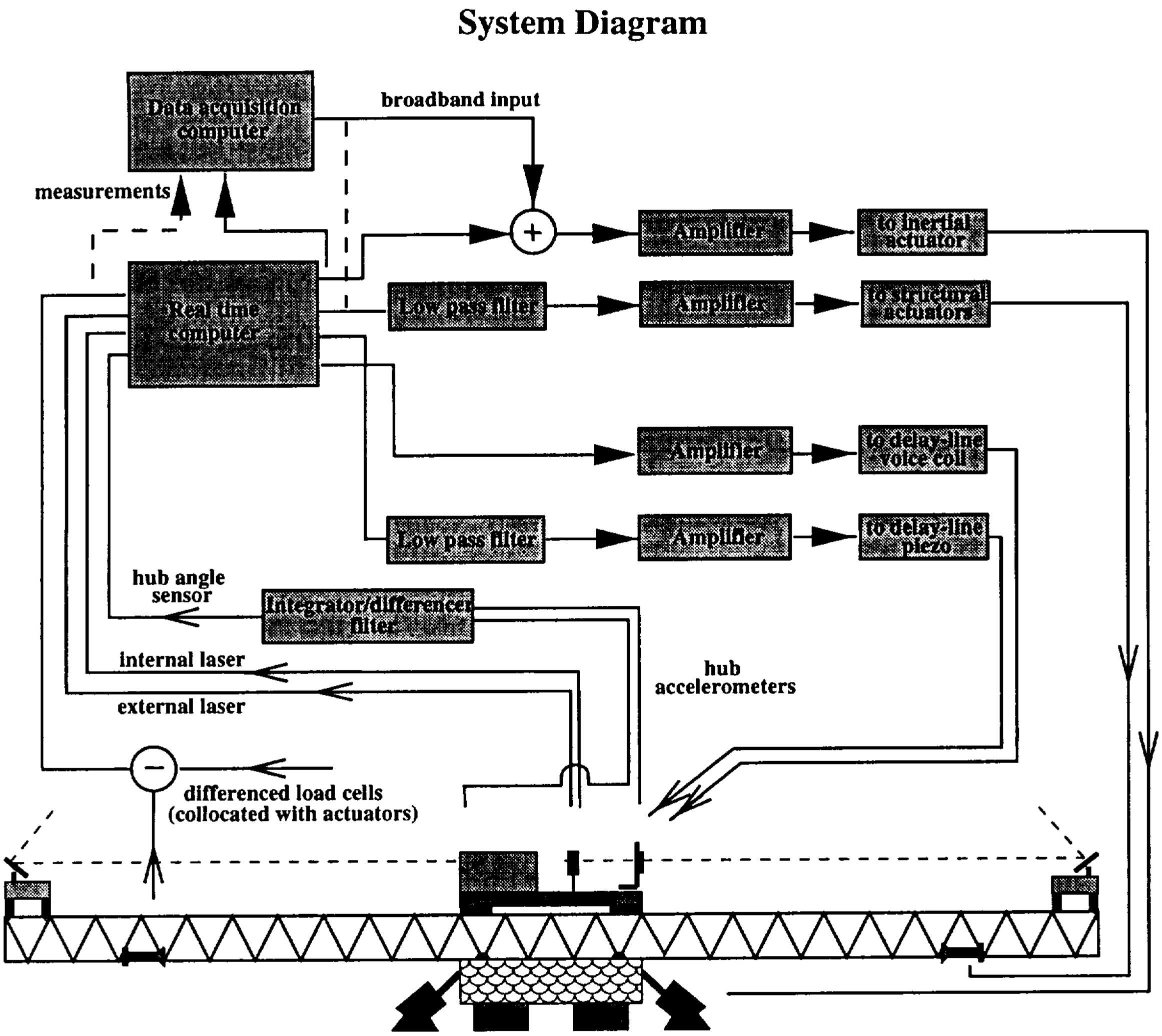

Figure 6.8: System schematic showing origination and destination of measurement and control signals. Note that data is primarily taken through the real time computer incorporating sampling delay in the measurements.

Disturbances are injected at the hub of the testbed using shakers. The disturbances are broadband, for the sake of experimentation, and are generated by the data acquisition system. Typically these inputs are generated over three broadband bandwidths, $\{0-20, 0-100, 0-500\}$ for the intended low frequency shape, and $\{0-50, 0-200, 0-500\}$ for the intended high frequency shape. Data are then appropriately concatenated. The disturbance input levels were noted for each bandwidth and input voltage level and roughly correspond to 0.25 N rms on average. This information is combined with measurements of the performance rms values in order to apply the correct magnitude shaped disturbance to the measured closed loop transfer functions.

Experiments performed involve closing sequential control loops. The first set of loops closed are the optical system, requiring measurements from the metrology system and control signals to the delay line actuators. These loops are closed in a specific order to mimic the operation of an imaging interferometric device. The actual imaging device involves some feedback of the measured **performance**, (spatial phase information from the interfered guide star fringe) so it is important to do this within the constraints of operation of the actual device.

Optical loops are closed sequentially. First the measured internal motions are compensated for in a 350 Hz bandwidth loop, well into the high modal density region of the structural response. A block diagram of the manner in which the delay line piezo and voice coil actuators are used together is shown in the dashed box in Fig. 6.9. Since the piezo stack transfer function is essentially a constant, with sampling delay, out to beyond 1 kHz, the piezo controller is designed as a high bandwidth loop with mediocre gain at low frequencies. The voice coil loop with appropriate controller is added to desaturate the piezo and provide large motion at low frequencies. This can be seen in the individual transfer functions and loop transfer functions plotted in Appendix B. The net result is shown in the combined loop transfer function in Fig. 6.10. Without the piezo in the loop, $G_p(s) = 0$, the voice coil alone is unstable with high gain out to beyond 100 Hz. An alternate interpretation of the piezo is as a fine positioner that phase stabilizes the high gain voice coil loop.

Closing the internal laser loop nullifies the internal contribution to the external measure. In this setup this is not exact nullification because the internal and external legs are not coaxial. However, since in this setup the external signal is to be fed back (tracked by the delay line), and is now a coherent measure of the differential tip displacement plus some small internal residual, this is not an issue. In the actual device, where starlight is combined, coaxial alignment is needed when imaging a target star.

The closed loop complimentary sensitivity of the delay line is shown in Fig. 6.11.

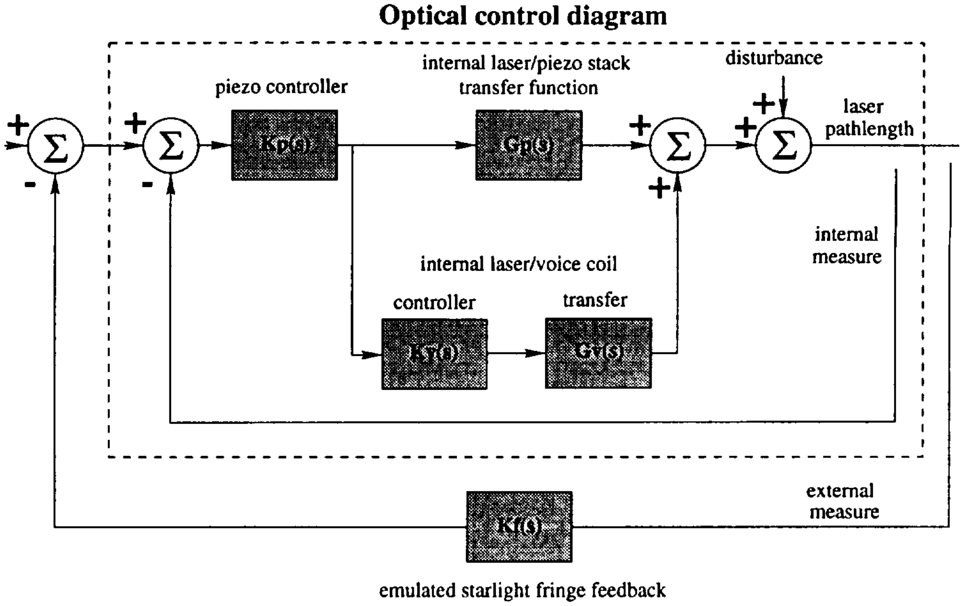

Figure 6.9: Optical control block diagram. The dashed box represents internal control that is closed first. The outer loop is the emulated fringe feedback using the external laser signal.

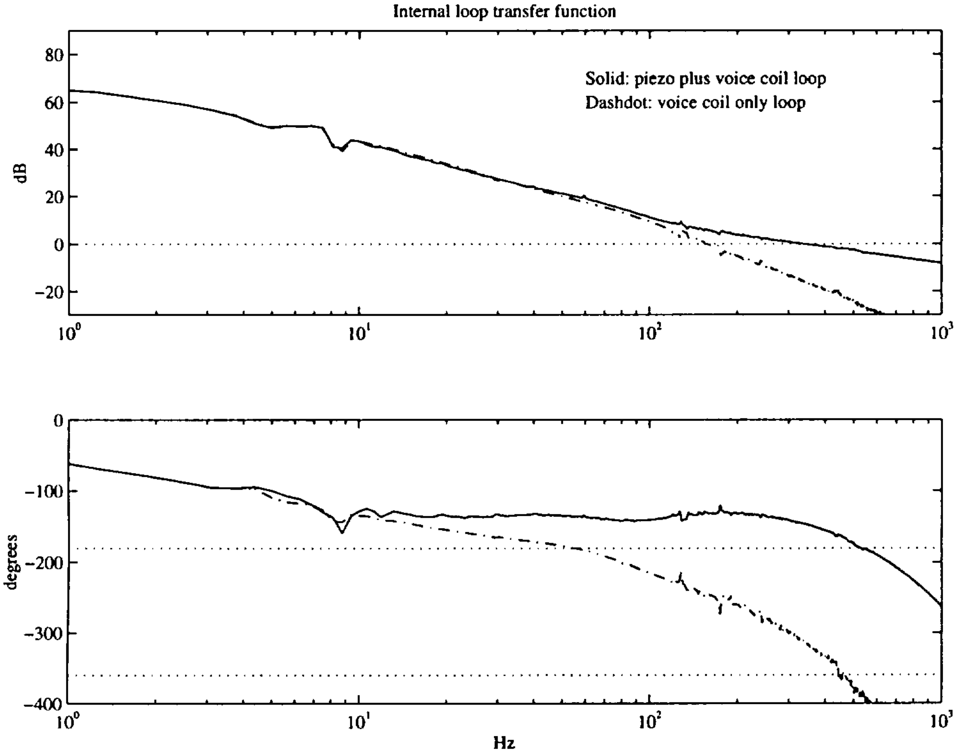

Figure 6.10: Internal loop transfer function. Also shown is the loop as if $G_p(s) = 0$.

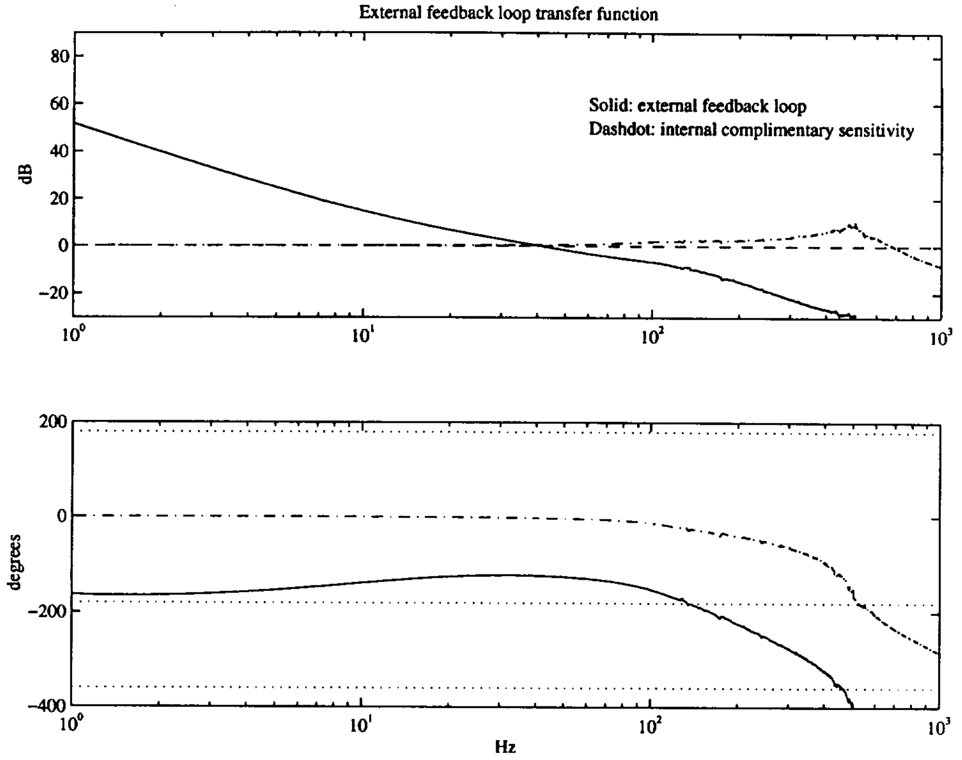

Figure 6.11: External loop transfer function, $C_{odl}K_f$ solid, where C_{odl} is the complimentary sensitivity of the closed internal loop.

As a servo on the external feedback command the delay line is ≈ 1 to beyond 100 Hz. Loop gain on the emulated fringe rolls down at a slope of -2 at low frequencies and crosses over with a slope of -1 at 40 Hz. Choice of crossover frequency was determined by the scale of modal frequencies in the experiment *vs.* the design example and is consistent with a magnitude 8 guide star fringe information rate for this scale. The shown loop is the feedback used for all structural closed loop experimental results. No modifications to the optical loops were necessary when changing the structural configuration.

Experimental transfer functions from a broadband hub disturbance to the optical outputs from the upper regular truss in Fig. 6.1 are shown in Fig. 6.12. The figure shows the transfer functions under three different conditions, open loop, closed internal loop and closed external loop (with internal already closed). The solid curve in the external measure shows the predominant pseudo rigid body motion (testbed rocking 0.9 Hz mode). Considerably less internal motion, G_{yw}, is evidenced since the internal measure is insensitive to pseudo rigid body motion. Under 0.23 N rms input level the external output is .064 mm rms. Strong flexible beam-like modes are evident at 15, 48 and 76 Hz in both outputs. These represent the first three antisymmetric modes of the beam like truss. Modes occurring above 100 Hz are coupled three dimensional modes and become very dense and local in nature. A mode that appears in the internal transfer functions at 5 Hz is a rigid body/first symmetric mode coupling. Pole-zero excursions that appear in the transfer functions below 70 Hz are either slightly disturbable/observable symmetric modes or suspension modes.

When the internal loop is closed the internal motion drops to less than 20 nm rms as shown by the dashed curve in G_{yw}. The external transfer function with the internal loop closed overlays the open loop at frequencies below the first antisymmetric mode. At frequencies above there is notable difference between the curves showing that a portion of the high frequency pathlength error is due to internal motion. Closing the external loop reduces the external pathlength to about 430 nm shown by the dashed dot curve in G_{zw}. The servo nature of the delay line can be seen in G_{yw} which is now a good approximate of the open loop external motion at frequencies below the external loop bandwidth.

It is possible to provide more gain at low frequencies in the external feedback loop, *i.e.* roll down with a slope of -3 before crossing over with a slope of -1, compensating for more external motion by cancelling it with delay line stroke. Results for this higher loop gain are shown for the regular truss in Fig. 6.13. The difference is further rejection at frequencies below the fundamental antisymmetric mode. This higher gain compensator is not implemented with the structural controllers. Performance weighting is used to project the effect of the higher loop gain onto the experimental results. Note that this is not entirely a good measure because closing the loop on the performance essentially modifies its impedance when being measured, and, some of the structural closed loop results use the performance as a sensor. It will be shown that the performance sensor is not the primary sensor in the low frequency disturbance control configurations so that the performance weighting approach is a fair indicator.

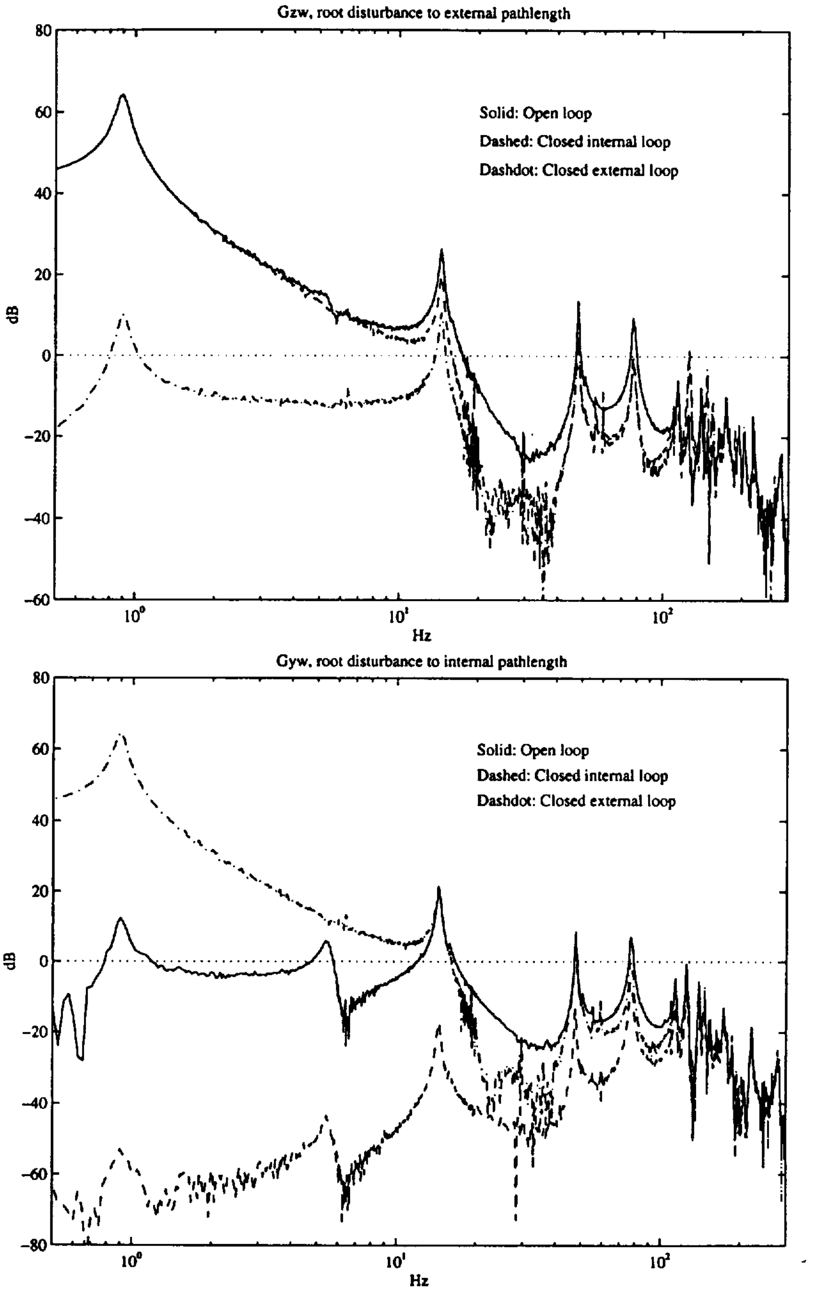

Figure 6.12: Transfer functions from the hub disturbance to internal and external laser outputs for the regular truss configuration.

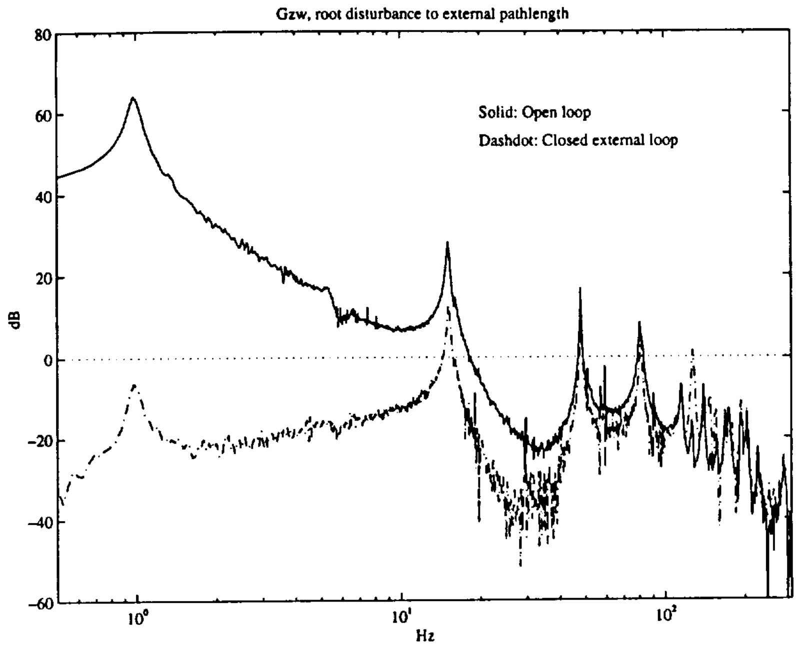

Figure 6.13: Transfer functions from the hub disturbance to external laser output for the regular truss configuration with high gain fringe feedback.

Structural **actuators** are placed symmetrically by the design algorithm and act differentially when in the structure. Configuration line drawings in Figures 6.1 and 6.2 show the actuators as thick longerons placed in the truss. Electronic images of the actuators in the actual hardware are provided at the beginning of each experiment configuration result.

The strut actuators are (repaired) Physic Instruments P-843.6 with more than enough bandwidth, blocked force and stroke necessary for this application. Their axial stiffness is comparable to that of an aluminum longeron, $15N/\mu m$ *vs.* $13N/\mu m$. When placed in the truss along the bottom stringer (see Fig. 6.15) the result is close to that in the nominal design example where the actuator stiffness is modeled as matched to the structure.

Two different realizations of the active hinge designs are made. The first uses the extra stoke capability of the actuators by placing them in series with a soft flexure. Effectively the truss is passively hinged and higher levels of voltage are used to force across the hinge. The second uses high gain collocated integral force feedback to realize the hinge and damp the structural modes at the same time. Note that neither of these are the passively very-soft hinge with differential moment actuator that the optimized results showed, however they are both reasonable approximations. The high gain active hinge is limited by ability to achieve high gain and still roll off the control in a modally dense region. The passively hinged strut is limited by coupling to the pseudo rigid body mode of the testbed at 5 Hz.

Figure 6.8 shows that the structural control signal is filtered before being split, amplified and then passed to the structure. The filter rolls off the control signal to the actuator attenuating the 4 kHz zero-order-hold through-put to the piezo. When being split the individual strut gains are adjusted so that the transfer functions from each strut to the performance match at ≈ 55 Hz.

Four **sensors** were available for the structural control designs, both the internal and external laser measurements under closed loop optical control, integrated and differenced accelerometers located on the hub, and differenced load cells collocated with the strut actuators (see Fig. 6.1). In each model-based control design a pair of sensors were used that included the hub sensor, and, for the low frequency disturbance cases presented in this chapter, the performance sensor. In the non-model-based controllers the differenced collocated load sensor was used. Sensitivities for the various sensors are listed in Table 6.4.

Closing loops on an actual imager will require careful consideration of the noise in the sensor signals used. Structural control that improves the pathlength error will pump sensor noise directly into the structure. This is the cost of high gain dampening and stiffness control of the resonances. However, these broadband noises are just shaped disturbances and are also compensated for by the optical control loops to at least the closed loop optical levels of performance.

By far, the most sensitive, and lowest noise floor sensors are the laser measurements. The laser noise floor can be as low as 5 nm for the HP5517B. In these experiments variable laser output gain was used so that, under closed loop optics, both the large commanded internal signal and the much smaller controlled external signal could be sampled by the data acquisition computer. The differenced QA-1400 accelerometers have a noise floor of $\approx 1\mu$g rms which corresponds to about 50 nm rms over the observed experimental bandwidth. Better quality accelerometers such as QA-3000's are available commercially. Note that use of such a hub sensor will be an issue in the actual imager design, because, even a mix of good quality available sensors have a noise floor of $\approx$ 20 nm over the observation bandwidth [55]. Collocated PCB 208B load cells have broadband noise of $\approx$ 0.04 N, which is over 20 % of the expected low frequency disturbance level. The use of collocated load in an imager will require extremely sensitive and noise free load cells.

Data acquisition used a Tektronix 2630 system over bandwidths consistent with the disturbance. Measurements were taken in transfer function form at the output of the control computer so that the sampling delay was included.

Measured autospectrum rms values of the closed loop performance are not reported because they are dominated by laboratory disturbances on the order of 150 nm. Projected values of the closed loop performance based on the measured input autospectrum and the closed loop disturbance to performance transfer functions are presented. The experiment was particularly sensitive because of the lab reference sensing provided by the external laser leg. This sensitivity is evident in the presented transfer function data.

The maximal level of allowable broadband input was used when measuring closed loop transfer functions. Upwards of 50 averages per bandwidth were performed. The maximal level of broadband input was set by the laser range since, even in the closed loop, the system optics have to track the low frequency rigid rocking motion. Poor coherence was noted in the performance and load cell transfer functions in the bandwidth of the "rigid body" modes of the system. This was attributed to large signal cancellation in the differential sensors.

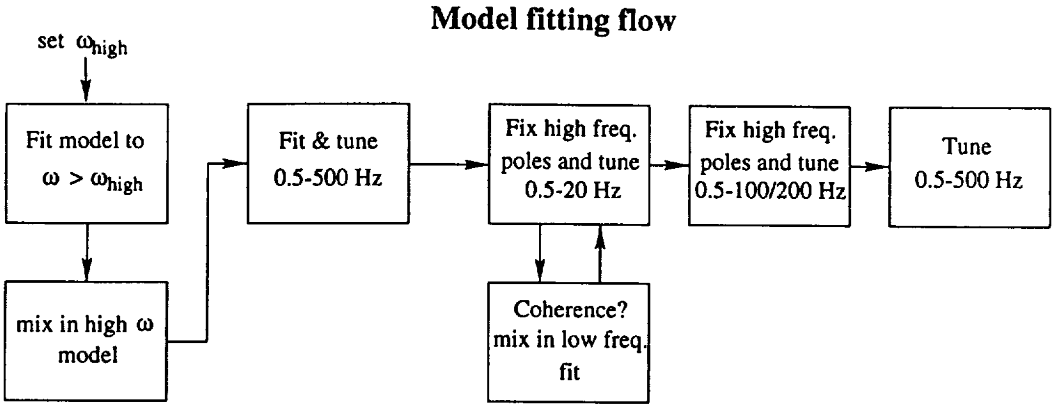

Figure 6.14: Example procedure for fitting state-space models to closed loop optical transfer function data.

6.3 Model Fitting and Control Design

Linear state-space models are fit to the closed loop optics transfer function data using Frequency Domain Observability Range Space Extraction (FORSE) for an initial guess, and logarithmic least squares tuning [56]. Equation 6.1 shows the cost that is minimized in the logarithmic tuning,

$$J(\theta) = \sum_{k=k_o}^{k_{max}} \sum_{p=1}^{n_{out}} \sum_{q=1}^{n_{in}} \left| log(\hat{G}_{pq}(j\omega_k, \theta)) - log(G_{pq}) \right|^2 \tag{6.1}$$

where θ is a vector representing the model parameters, $\hat{G}_{pq}(j\omega_k, \theta))$ is the model evaluated at discrete frequency points $j\omega_k$, and p and q are indices that enumerate the outputs and inputs respectively.

Many iterations were performed in achieving a model of control design quality. A bootstrapping technique was used that mixed data and approximate models from low to high bandwidths. A flow diagram of an example procedure is shown in Fig. 6.14. The procedure was found to eradicate unnecessary non minimum phase behavior in the fit model that often occurred in bandwidths of low coherence.

Structural control design is performed on the closed loop optics system. Weighted H_2 designs, that follow the design procedure presented in Chapter 3, were used for model-based control. Frequency weights were used that shaped the disturbance, controls and in some cases the sensors. Performance weights were not used since the system included optical control and the performance variable is directly measured. Control weights were used to roll off the structural controller before attempting to control regions of increasing modal density and increasingly poor model quality. They were also used to allow band limited dampening of the low frequency pseudo rigid body rocking mode through use of the inertial actuator at the hub. Low frequency sensor weights were used to ensure the rigid body control used only the hub sensor. Sensor weighting was not an issue in the high frequency disturbance cases since dampening of the rigid body mode was not necessary.

Robustness was introduced into the control design in two ways. The first is by using sensitivity weighting described in Chapter 3. When using sensitivity weighting under static and invariant input assumptions, extra performance and disturbance weights are added to problem modes. Using this technique works well for transfer functions that roll off as the modal residues tend to decrease on average as their modal frequency increases; however, in the closed loop this may not be the case, as shown by the weighted G_{zu} transfer functions in the design example chapter. Here, sensitivity weighting of high frequency modes renders the low frequency transfer function inaccurate. This can result in undesirable controller behavior at low frequencies.

The second method of adding robustness to the controllers was via direct manipulation of the controller parameters. In many cases, especially when the controllers were independently unstable, it was found that dampening sensitive controller modes resulted in robust designs.

In a few cases local control design was performed (non parametric model based) by integrating and appropriately notching the differential load cell sensor signal. These controllers are single-input single-output. They were designed using measured actuator to sensor transfer functions, G_{yu}. Notches were appended when instabilities were found upon implementation.

Table 6.5: Cases presented for low frequency disturbance spectrum. "rpni" abbreviates "reduced penalties, no improvement".

Configuration	Type of control	sensors	limit
regular	H_2	hub + z	rpni/margin
Opt: flexured hinge	H_2	hub + z	rpni/margin
Opt: feedback hinge	$\int F$	load	roll-off gain stab.

6.4 Low frequency disturbances

Design solutions were sought that implemented the results of the design example within the limitations of the gravity environment. The two primary configurations presented in this section are shown in Fig. 6.1 for low frequency disturbance environments. The upper configuration represents a regular design of maximal allowable stiffness. This is the optimized design without the active hinge, **not** the nominal design which was considerably less stiff. Performance improvement from a global stiffening of a truss is well understood and is predicted to be $\approx$ 1 dB rms for this system. The regular design implementation has approximately the same structural mass as the optimized design implementation.

The optimized design required a moment actuator across a soft local stiffness. Realization of the active hinge design was achieved in two ways. In the configuration shown in Fig. 6.1 the piezo strut actuators were raised towards the truss elastic axis via bending flexures. This effectively lowered the mechanical impedance of the displacement actuator by using their large stroke capability against a soft spring. Collocated designs were compromised by this flexuring since internal strain (for load measurement) at the hinge is divided into the flexures.

Active hinging was also accomplished via high gain collocated load feedback in the upper configuration shown in Fig. 6.2. This configuration also turns out to be the optimal placement for the regular configuration high frequency disturbance case. For the low frequency disturbance case a high gain feedback non parametric control design was used to achieve hinging using midspan non flexured piezo struts.

Cases presented in this section are enumerated in Table 6.5. Further cases that

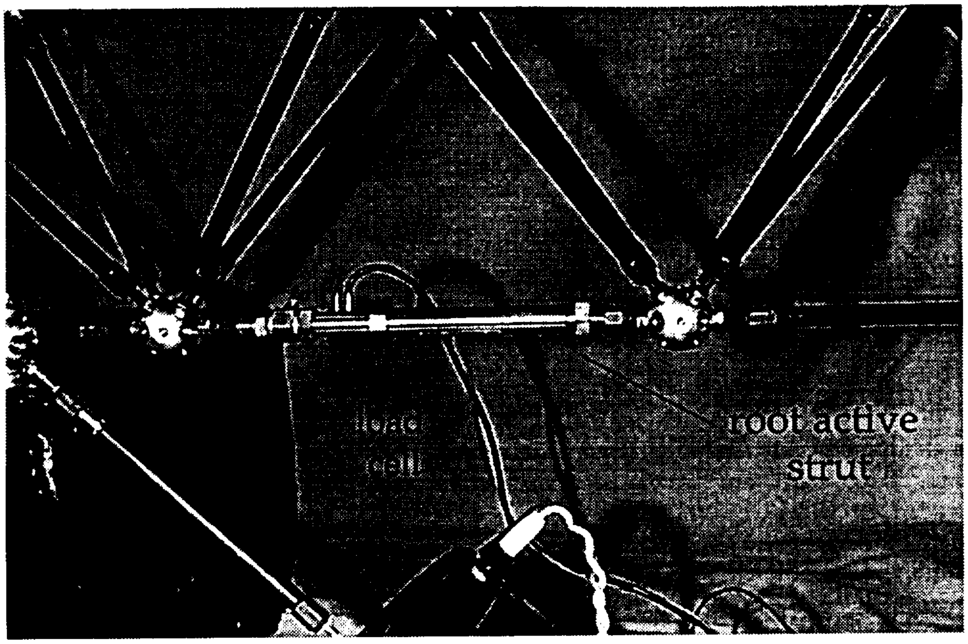

Figure 6.15: Digital image of the root active strut implementation.

investigate other sensor choices are presented in Appendix C. Results from these extra cases bring no new insight into the physics of what is happening in terms of performance, although the underlying dynamic controllers are quite different.

Implementation of the root structural actuator in the regular configuration is shown in Fig. 6.15. As in the nominal case in the design example, the root location was found to be the best by exhaustive search of the available locations. Placement at the root represents a location that would be chosen via an open loop controllability/observability metric. The root location provides a high strain location for the primary antisymmetric modes and good static leverage over tip displacement.

Transfer function data with the optics loops closed are shown in Fig. 6.16. A 59 state model was fit to the data. Modes in Fig. 6.16 can be divided into three regions, 0-10 Hz, 10-100 Hz, 100-500 Hz. Below 10 Hz the modes are predominantly pseudo rigid body modes of the hub truss system. The mode at $\approx$ 1 Hz is the rocking mode of the hub truss system. At 5 Hz there appears a coupled rigid bounce, 1st symmetric mode that appears strongly in the hub and collocated sensors and is apparently excited by the differential structural actuator. For this configuration the antisymmetric beam-like modes occur in the 10-100 Hz band. The fundamental antisymmetric mode occurs at $\approx$ 15 Hz, second antisymmetric at $\approx$ 48 Hz and third at $\approx$ 76 Hz. Close pole-zero pairs in the 10-100 Hz range are primarily due to suspension, out-of plane antisymmetric modes, and in-plane symmetric modes. In the 100-500 Hz range the modes rapidly become three dimensional and local in nature. Data above 250 Hz are purposefully smoothed to give a model that fits an average measure of the transfer function magnitude. Controllers are gain stabilized in this range.

Several notable features can be seen in the data. The first is the lack of coherent measurement in the 2-8 Hz range. This is attributed to taking data with the optics loops closed where the pseudo rigid body modes are contributing large signals that are approximately cancelling in the differential outputs. These modes are being excited through laboratory floor disturbances so that the inputs are incoherent with the provided disturbance signal.

An interesting difference between the stiffer G_{zw} shown in the data and the design model nominal case is the deep zero between the first and second antisymmetric modes (rather than between the second and third). The difference is attributable to the dynamic scaling of the experiment with respect to the design model. By itself this zero provides $\approx$ 30 dB of narrow band disturbance rejection over a bandwidth of 10 Hz.

The transfer function from the structural actuator to the performance sensor, G_{zu}, shows the impedance effects of the closed loop optical system. Phase loss in the 10-60 Hz range is over and above that of the time delay, shown in the phase of the G_{yw} hub sensor. The phase loss is due to a real pole that is introduced by the optical compensator.

Transfer functions, G_{yw} disturbance actuator to hub angle sensor (for inertial control), and G_{yu} structural actuator to load cell, appear collocated. The G_{yw} transfer exhibits some low frequency phase wrap due to the integral filtering of differenced accelerometer signals. Phase loss at high frequency is the characteristic $3T/2$ digital processing delay. The structural actuator to load cell transfer function shows noncollocated excursions at 50, 90 and 200 Hz. These are due to imperfect differencing.

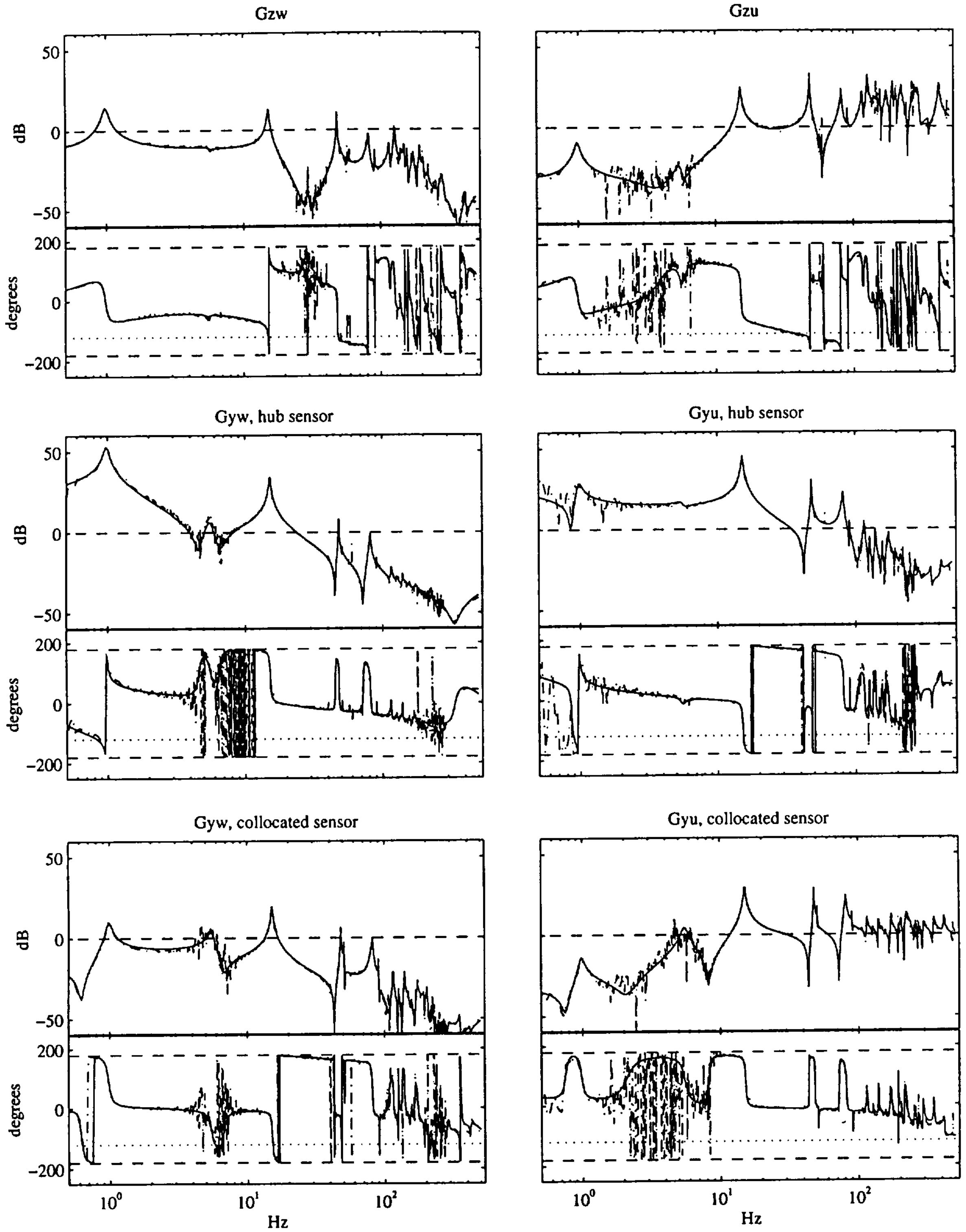

Figure 6.16: Data (dashed dot) *vs.* fit model (solid) for the regular configuration. Structural actuators at the root.

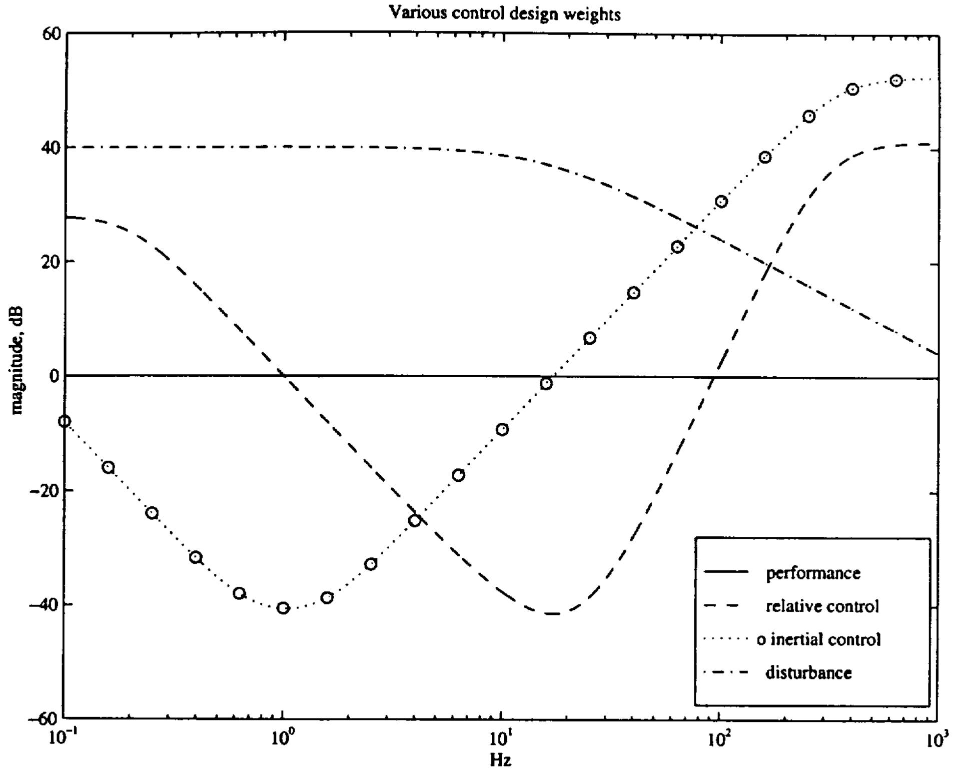

Figure 6.17: Control design weights for regular configuration, hub plus z sensors, low frequency disturbance weight.

Design weights used in the model-based control design are depicted in Fig. 6.17. There is no performance weight. Control weights are divided into weights on the inertial actuator and weights on the structural actuator. The inertial actuator weights restrict the inertial actuator (disturbance input voice coil) to dampening the fundamental rocking mode. Structural actuator weighting appears narrow band yet their effect is determined by contrast with the G_{zu} transfer function, which rolls up considerably as shown in the model block transfer functions of Fig. 6.18.

In the control design model, shown in Fig. 6.18, hub and performance sensors are used. Control designs that use the hub with collocated load sensors are in Appendix C. Disturbance and sensor weights are integrated into the control design model in Fig. 6.18 where appropriate.

Included in Fig. 6.18 are pole/zero-damping plots for each transfer function. The three dotted lines from top to bottom represent damping of 1, the $j\omega$ axis, and

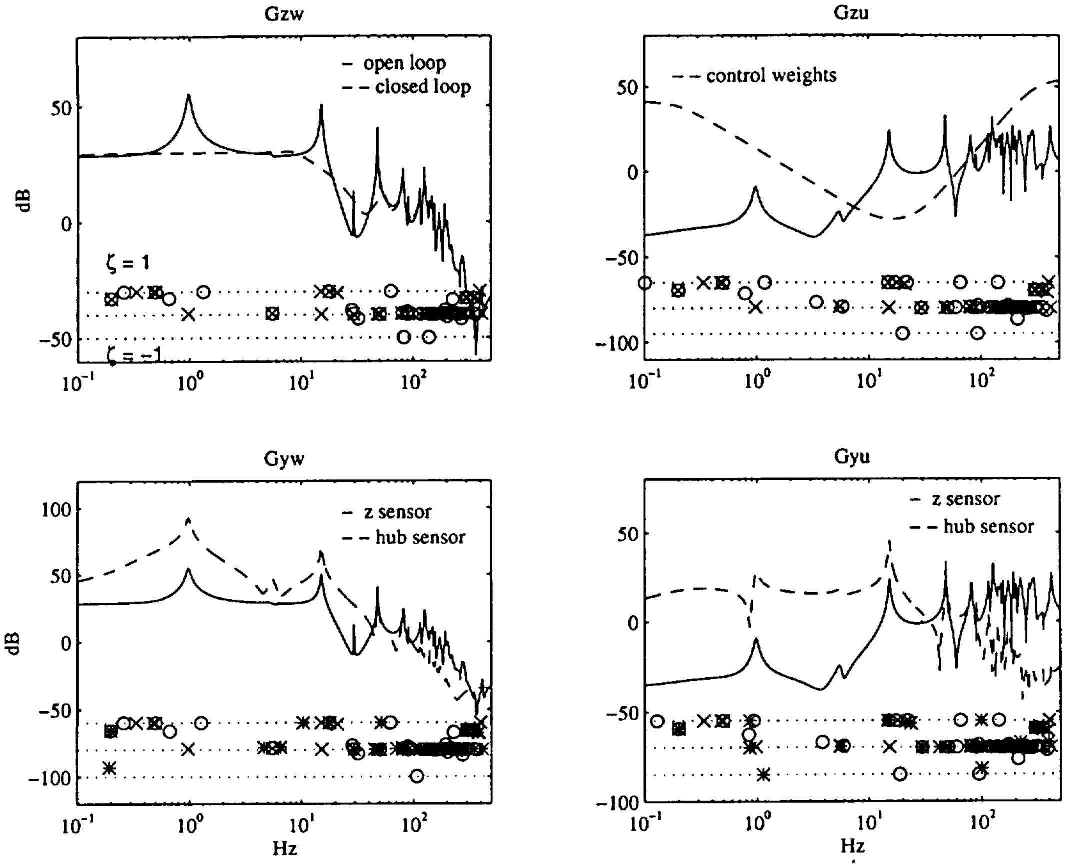

Figure 6.18: Model transfer functions with pole-zero map, hub plus z sensors, low frequency disturbance weight. 'o's correspond to the solid curve zeros, '*'s correspond to the dashed curve zeros.

damping of −1 in similar fashion to the design example and that presented for simple structures in Chapter 2. Some of the well damped and real poles and zeros shown correspond to the weights used, for example the real pole at 15 Hz in all the transfer functions involving the disturbance w. Acceleration filter poles can be found at ≈ 0.7 Hz and are cancelled by zeros in all transfer functions that do not involve the hub sensor measure.

Further well damped poles and zeros are a result of several effects. Internal compensator states add to the shaping of these transfer functions as does irrational structural delay, digital computer time delay, and discrete modeling effects. All can result in well damped zeros, or poles, or both. The later three effects are the cause of the damped nonminimum phase zeros that appear.

Sensor transfer functions for the performance sensor are plotted independent of G_{zw} and G_{zu}. Close inspection of the real nonminimum phase zeros for this sensor shows that they differ from G_{zw} to G_{yw} and from G_{zu} to G_{yu}. This is due to sensitivity weights added to the performance and disturbance which do not weight the performance sensor.

When investigating Fig. 6.18 it is instructive to refer back to the cost,

$$\begin{aligned} J_z &= \|G_{zw}\|_2^2 \\ &= 2\int_0^\infty G_{zw}^H G_{zw} d\omega\,. \end{aligned} \tag{6.2}$$

where,

$$G_{zw}^{CL} = G_{zw}^{OL} - G_{zu}K(I + G_{yu}K)^{-1}G_{yw}\,. \tag{6.3}$$

dropping the explicit dependence on s. The compensator, K, may be any stable design. Clearly, from the expansion of the closed loop transfer function, G_{zw}^{CL}, the desire is to make,

$$G_{zu}K(I + G_{yu}K)^{-1}G_{yw} = G_{zw}^{OL}\,. \tag{6.4}$$

The ability of a controller to do this depends on sensor-actuator selection, placement and impedance. For example, inertial control is used to damp the rocking "rigid body" mode by using the hub sensor (it has the best signal to noise at low frequency) and the disturbance input voice coil as the actuator, $u \approx w$. Around this mode the left hand side of Eqn. 6.4 is very close to

$$G_{zw}(K(I + G_{yw}K)^{-1}G_{yw})\,. \tag{6.5}$$

which is G_{zw}^{OL} multiplied by the complimentary sensitivity of a collocated plant that easily approximates 1 given the pole-zero structure shown. Higher bandwidth structural control design is a more convoluted task due to the relative nature of the actuator *vs.* the inertial disturbances and the nature of the performance *vs.* the sensors used. Usually, limiting structural delay occurs in the various loops in the expression.

Table 6.6 shows relevant nonminimum phase behavior extracted from the model. From the table it is clear that the hub sensor, has good G_{yw} transfer gain over the first $1\frac{1}{2}$ decades allows a relatively high gain estimator, however, spatial separation

Table 6.6: Regular truss occurrence of important nonminimum phase behavior, low frequency disturbances. Low frequency behavior due to filters is not limiting.

Transfer Function	Freq. Hz	damping %
G_{zw}	31	-0.1
G_{zu}	20	-1.0
G_{yw} (z)	31	-0.1
G_{yw} (hub)	> 400	na
G_{yu} (z)	19	-1.0
G_{yu} (hub)	100	-0.7

in the G_{zu} loop limits the ability of the regulator to achieve compensator gain. The expression in Eqn. 6.4 is therefore limited from equaling G_{zw}^{OL} over a wide bandwidth.

The multivariable Nichols plot for the best compensator designed on the plant given in Fig. 6.18 is depicted in Fig. 6.19. Good gain is noted over the first three antisymmetric modes. Phase loss between the inertial and structural control in the plot is a result of optimal concatenation of the two independent SISO controls. Further phase loss is seen in the loop design and is attributed to compensator poles being placed near the mirror images (about the $j\omega$ axis) of the real nonminimum phase zeros, primarily seen in the regulator. As a minimum phase, non minimum phase pair the zeros hold the average transfer gain high while ensuing modes cause phase loss. This unraveling is the limit on performance in that the overall curve cannot be raised without encircling critical points. Structural control weights eventually enforce roll off.

Singular values of the sensitivity transfer function matrix are plotted in Fig. 6.19 on both the model and the data. The singular values are disparate due to the ill conditioning of the transfer function matrix. Apparent huge attenuation and amplification of disturbances at the plant output are in fact not possible due to the direction of the real disturbances. The plot does indicate that the compensator performance is sensitive to the direction of the incoming disturbances. It also serves as notice of stability problems where there are large (on the order of 20 dB) narrowband excursions between the model and data predictions. The only excursions visible in Fig. 6.19 are

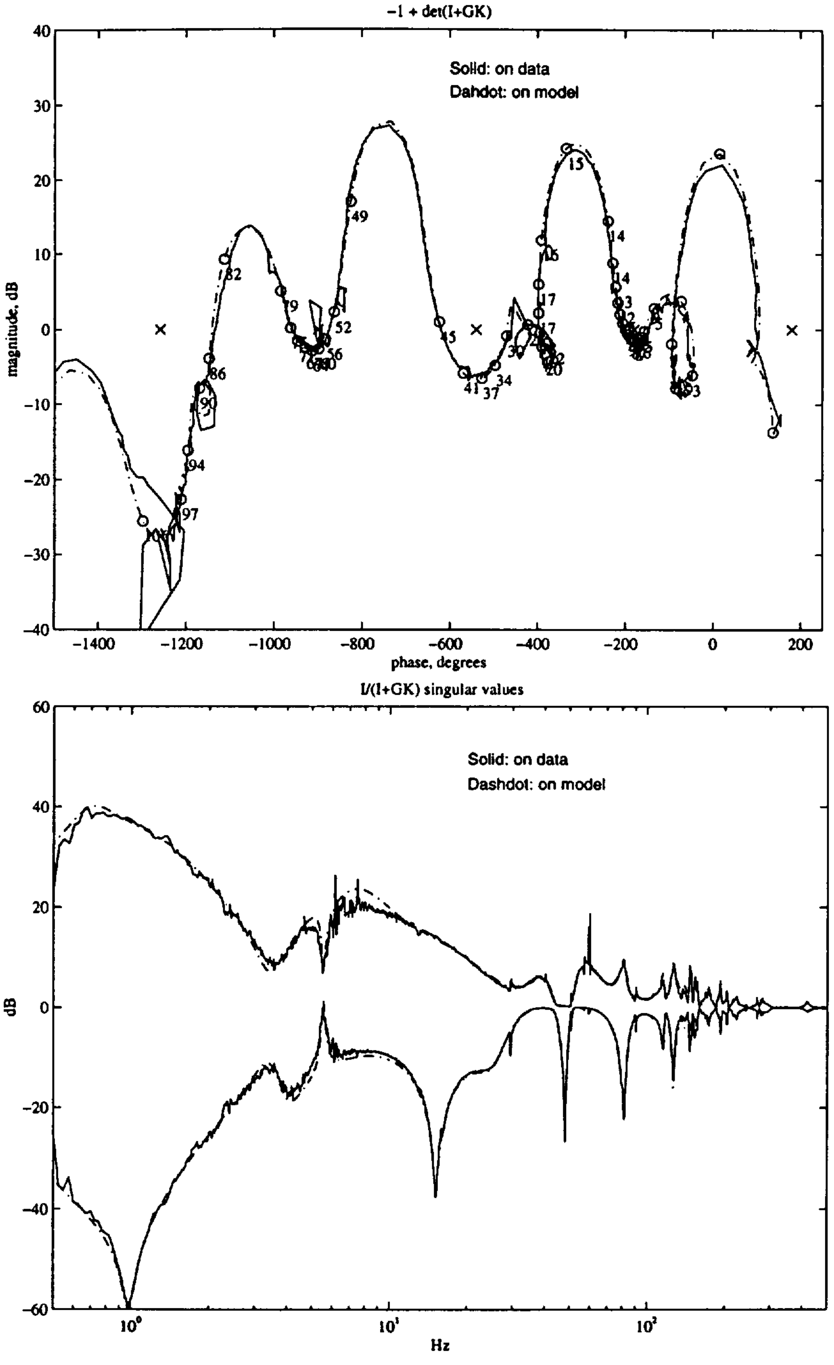

Figure 6.19: Multivariable Nichols plot and sensitivity singular values. Both plots are made on the data and the model, and are indicators of controller gain, loop phase loss, and performance limits. In the Nichols plot frequencies in Hz are marked along the curve by o's and critical points are shown as x's.

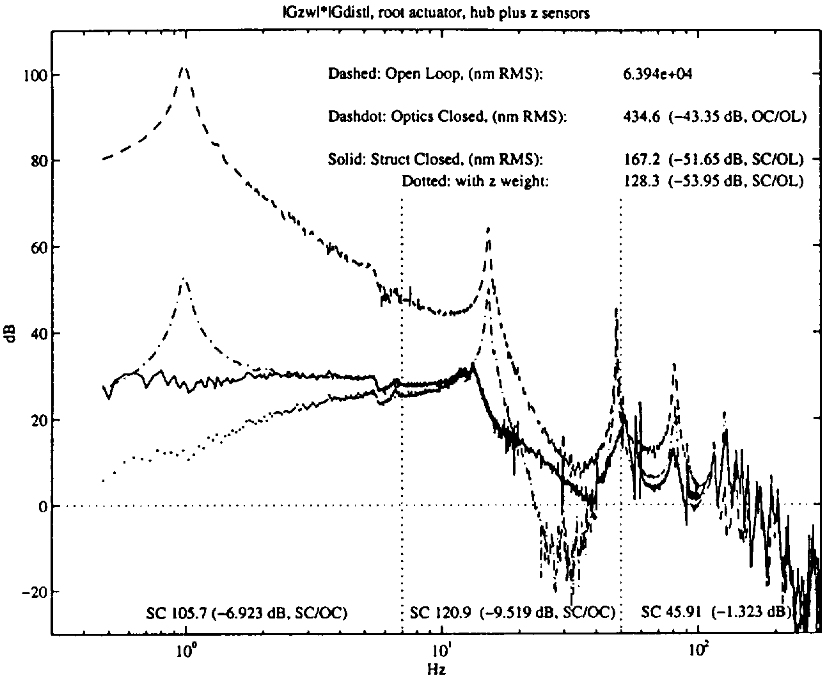

Figure 6.20: Regular truss with root actuator performance for several levels of closed loop control. OL stands for open loop, OC stands for optics loops closed, and SC stands for structural controller closed.

near 60 Hz where the data is corrupted by electrical noise and is not particularly coherent.

Performance of the various levels of control is shown in Fig. 6.20 as the shaped disturbance multiplied by the measured closed loop transfer function. Numbers quoted for performance in the figure do not therefore include sensor noise contributions. The open loop performance is .06 mm rms ($\sqrt{J_z}$), near the maximum range of the laser. Over 40 dB of improvement is achieved from the optical control most of which comes from tracking the rigid body mode. A further 10 dB of rms improvement comes from the structural control where dampening of the first, second and third antisymmetric modes is evident. Structural results seem under stated given the level of control achieved. The reason is that the first antisymmetric mode is already significantly dampened by the hub air puck mounts to 1.3 %. Typically this mode would have damping on the order of .5 % and the structural improvement would be on the order of 15 dB rms. The total closed loop result is dominated by the sub 7 Hz response. In this case level gain at low frequency is inertia dominated, as opposed to the usual stiffness dominated structural response. This is why the extra low frequency gain was sought in the optical loops.

Closed loop performance shown is the result of allowing the compensator increasing authority until the performance did not improve and inevitable instability was found. The level of control shown is not as impressive as that predicted in G_{zw} of Fig. 6.18 hinting that the limit on performance is in the fit model directional information.

An important number for comparison will be in the middle band indicated by the vertical dotted lines. This is nearly all the performance assuming the extra gain optical compensator. For the controller shown about 121 nm was achieved. This is 9.5 dB improvement over the optical control. Using collocated load along with the hub sensor achieved 117 nm closed loop performance (similar figures are in Appendix C). A root damper design that used only integral feedback on the measured differential load achieved 130 nm. The later design was not pushed further as the intent was to emulate a good damper design.

The point to note is that the above three control architectures resulted in about the same level of performance. This shows that the system behavior was limited by the underlying physics not necessarily the control architecture. A hidden caveat in using the load cell sensor is the sensor noise through put, which for these load cells corresponded to about 100 nm of broadband performance that is uncorrelated with the disturbance.

Two ways implement the hinged solution were identified. Hinging via flexuring the active struts will be shown first. Since the optimized design captures the strain of the first antisymmetric mode across the structural actuator, it is thought that the authority over this mode will be more impressive than the regular root actuator design. A digital image of one of the piezo struts in place is shown in Fig. 6.21. Location of the hinge is shown in the bottom configuration of Fig. 6.1.

A 58 state model was fit to optical closed loop transfer function data for this

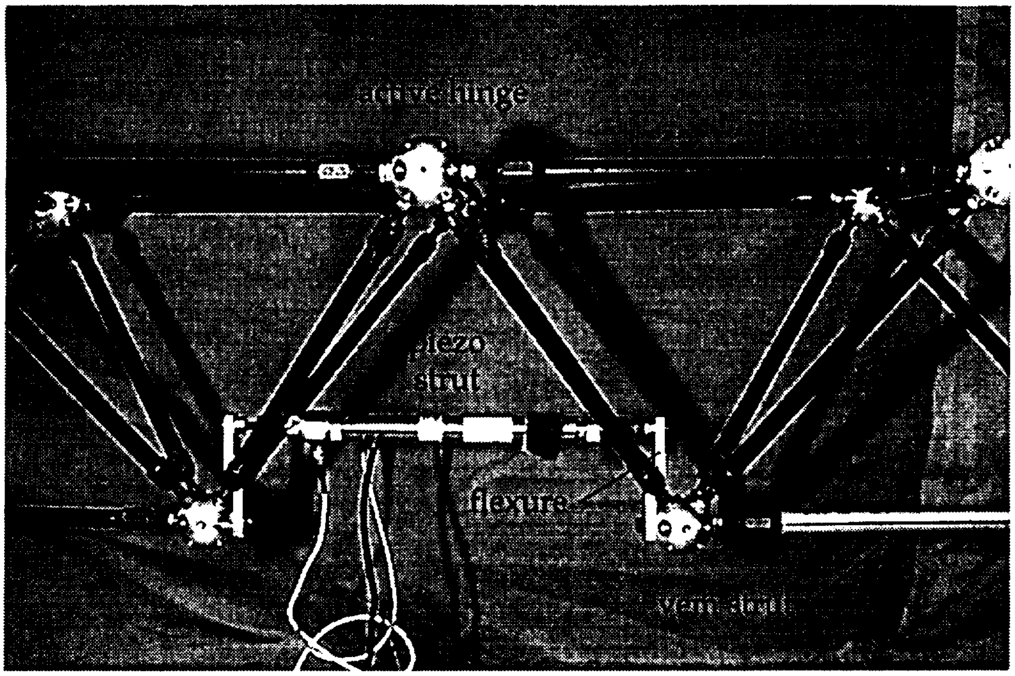

Figure 6.21: Passively hinged implementation of optimized active hinge solution.

configuration. The model *vs.* the data is shown in Fig. 6.22. Similar trends are seen in this data as in the regular configuration data. Once again a high frequency model has been mixed in to reduce the order of the overall fit. Less effort is applied to correct modeling at high frequency since the controller will be rolled off at a relatively low bandwidth. Coherence problems are again evident in the $2 - 7$ Hz range.

By hinging the actuators on flexures the first antisymmetric mode has dropped to around 8 Hz, almost a factor of 2 in frequency, or 4 in stiffness. The optimized solution actually called for this mode to be almost a decade below the fundamental nominal antisymmetric mode. It was impractical to implement this in the gravity field. Already, at 8 Hz, there is significant mode coupling with the pseudo rigid body vertical bounce mode at 5 Hz.

Flexuring the actuators has restricted the use of the collocated load sensors. Examine how the magnitude of the G_{yw} and G_{yu} load transfer function is reduced ≈ 20 dB over that in Fig. 6.16. Here, signal to noise in the data is compromised. Further restriction in using this sensor is brought about by the feed through term evident in

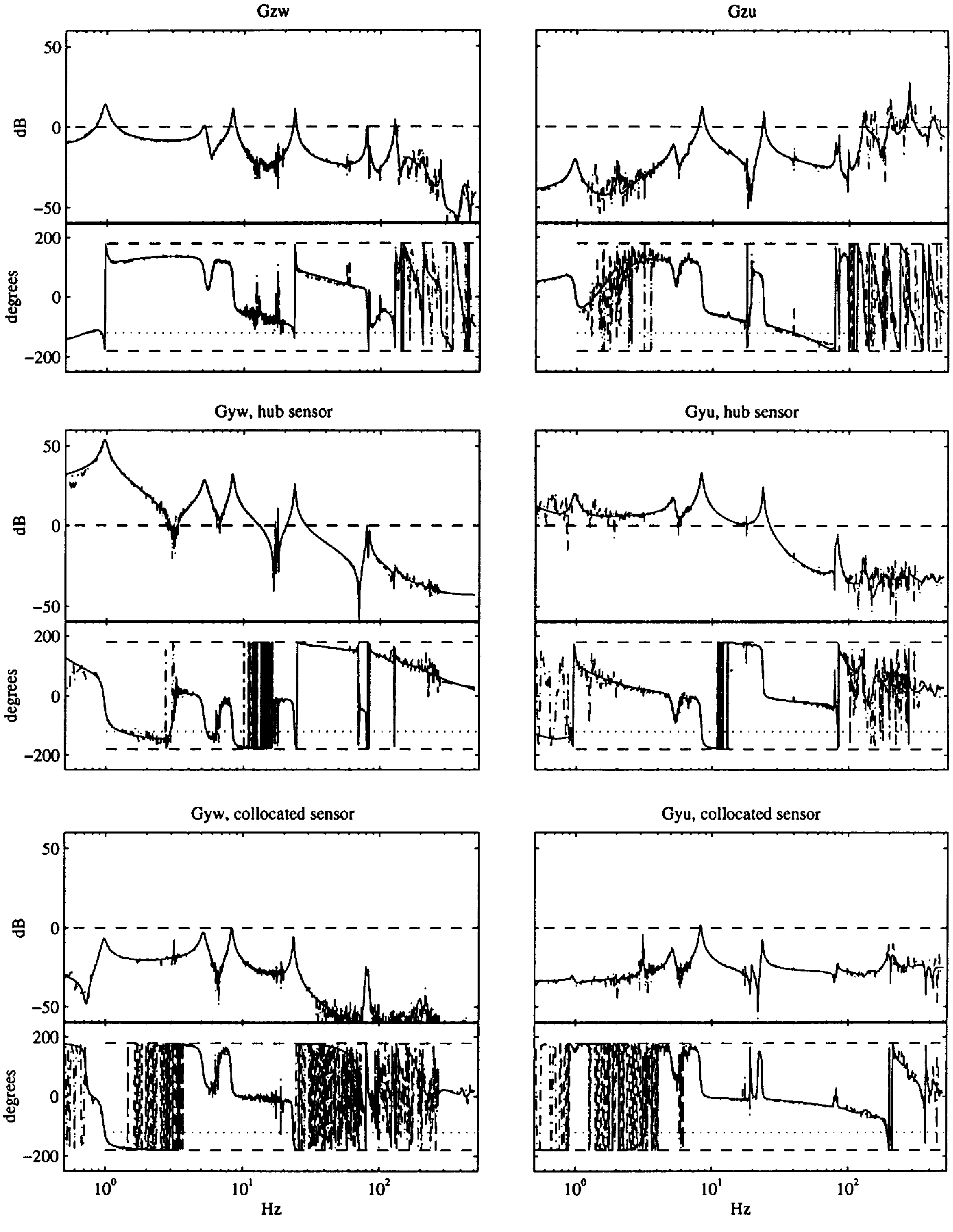

Figure 6.22: Data (dashed dot) *vs.* fit model (solid) for the optimized configuration, low frequency disturbances. Structural actuators hinged at 3/4 span.

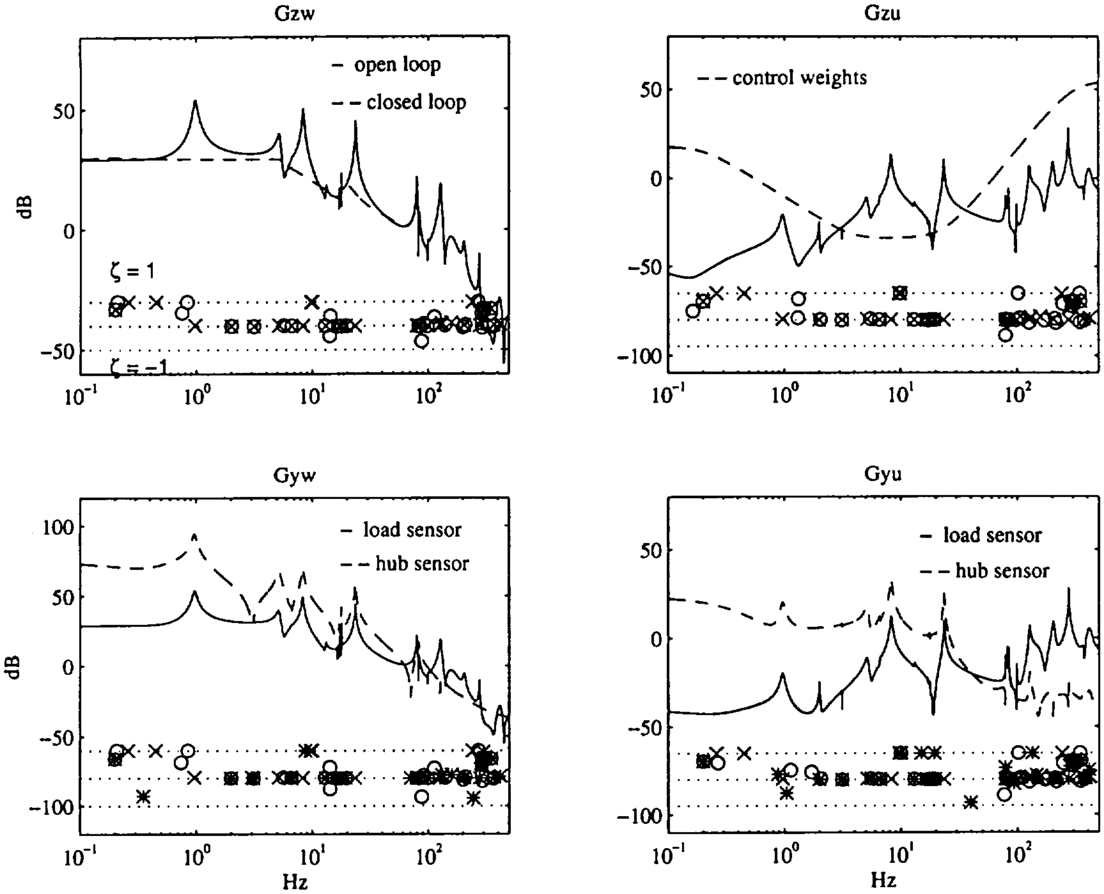

Figure 6.23: Model transfer functions with pole-zero map, hub plus z sensors, low frequency disturbance weight. 'o's correspond to the solid curve zeros, '*'s correspond to the dashed curve zeros.

the G_{yu} transfer function. A large feed through term buries the modal information in the transfer function limiting the ability to control the modes.

For reference, the design model block transfer functions are shown in Fig. 6.23. The design weights are essentially the same as shown in Fig. 6.17 (see Appendix C Fig. C.8) with some modification to the structural control weights to allow control over a lower frequency range, since the fundamental antisymmetric mode has dropped in frequency. For comparison to the regular implementation the hub and performance sensors are shown here with other cases presented in Appendix C.

An unexpected, but reasonable, feature of Fig. 6.23 is the low overall gain of the G_{zu} transfer function. In the design example this transfer function gain was increased

Table 6.7: Flexured hinge occurrence of important nonminimum phase behavior, low frequency disturbances.

Transfer Function	Freq. (Hz)	damping (%)
G_{zw}	15	-0.1
G_{zu}	80	-0.6
G_{yw} (z)	15	-0.1
G_{yw} (hub)	250	-0.7
G_{yu} (z)	78	-0.1
G_{yu} (hub)	40	-0.9

due to the hinging. The experimental implementation has reduced this effect through flexuring the piezo active struts. Gain is needed in the flexured actuator to displace the soft flexures.

The most notable feature of Fig. 6.23 is the collocated like pole-zero structure of the structural actuator with the performance. This is fundamentally different to the regular design. Table 6.7 lists the nonminimum phase behavior for the hinged configuration. The later occurrence of nonminimum behavior in the regulator G_{zu} loop allows more gain at low frequencies in the regulator. Again the estimator does the best with the hub sensor, although some nonminimum phase behavior occurs at 250 Hz possibly due to realization error. In general, as in the regular configuration control designs, the hub sensor is predominantly used with the performance sensor mixed in near the $j\omega$ axis zeros.

Similarly to the regular truss case, the Nichols plot shows the loop gain unraveling with increasing frequency. In this case, appreciable gain is noted in the first two antisymmetric modes only. Again the phase loss between the inertial and structural control is due to the optimal concatenation of the two controllers. Further phase unraveling now occurs through a different mechanism due to the actuators/sensors topology. Here, both the regulator, G_{zu}, and the estimator, using the primary hub sensor, G_{yw}, are approximately collocated in terms of pole-zero structure in the needed bandwidth. The structural delay comes about when interconnecting the system, since G_{yu} is not collocated in the needed bandwidth, y is located with the disturbance and

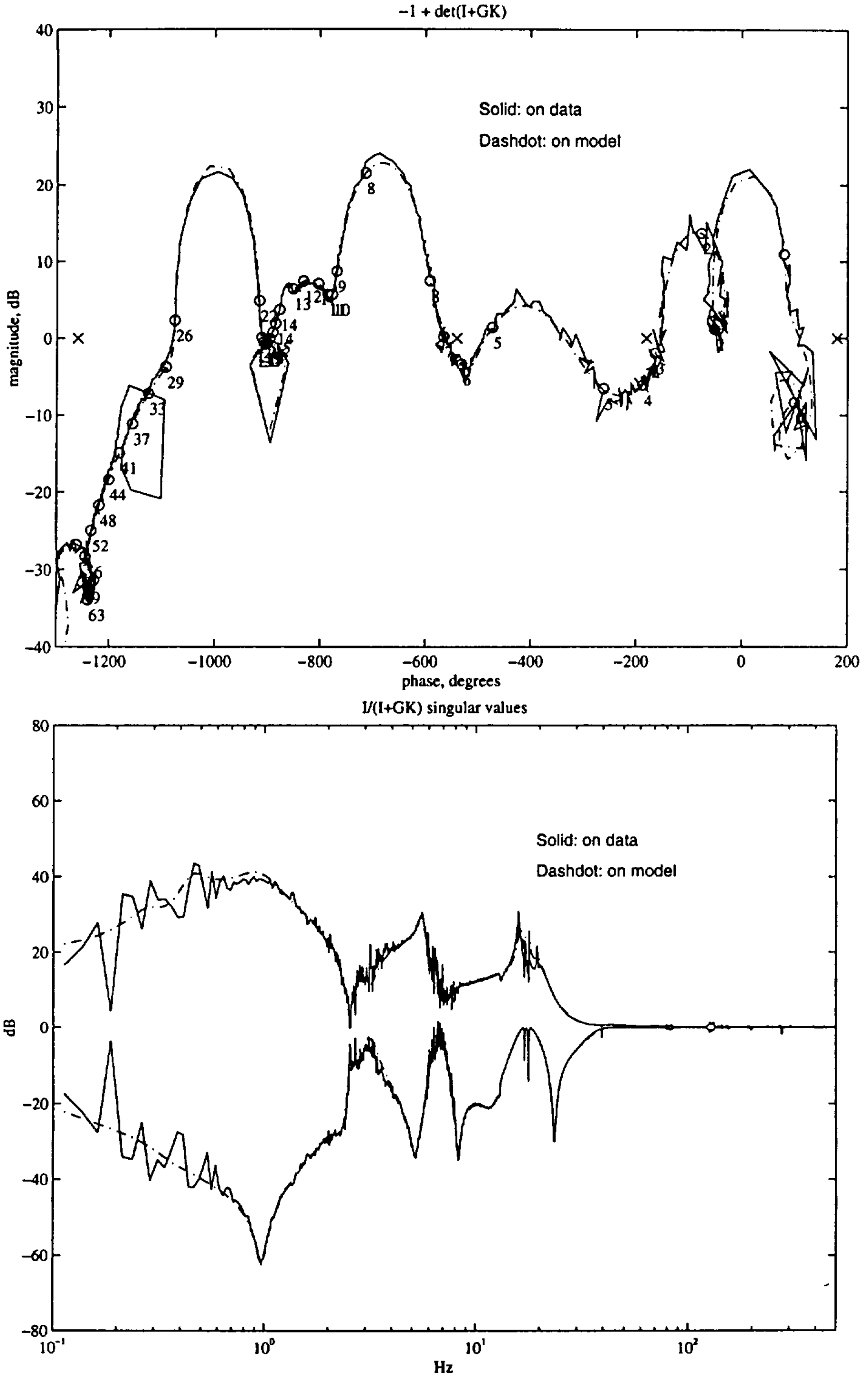

Figure 6.24: Multivariable Nichols plot and sensitivity singular values for optimized configuration with flexured active hinge.

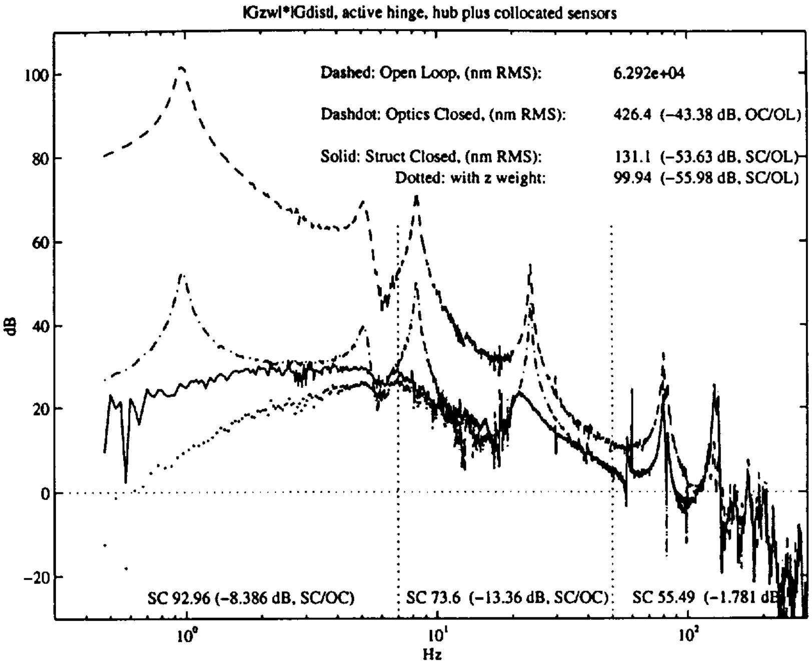

Figure 6.25: Optimized configuration with flexured active hinge performance for several levels of closed loop control.

u with the performance. The sensitivity singular values show the same ill conditioning as shown in the regular configuration case. Compensator roll off characteristics are apparently improved since no appreciable sensitivity attenuation or amplification is seen beyond 50 Hz.

Closed loop performance is shown in Fig. 6.25. Evidently, approximately the same level of improvement from optical control is realized in the hinged design as in the regular truss. Performance under optical control is reduced to 426 nm rms, showing greater than 40 dB rms improvement. Again, the structural control is responsible for over 10 dB of rms improvement, provided, for the most part, by dampening the first and second antisymmetric modes. In this case the damping of the first antisymmetric mode is 1.6 % with the optical loops closed. In the middle band the performance is reduced to 69 nm rms where the fundamental mode has been softened and dampened with more authority than in the regular truss configuration. The result using hub and collocated load sensors is similar, 68 nm rms achieved.

Figure 6.26 illustrates the comparison between fully closed loop regular *vs.* hinged designs. In general the optimized design yields 3 dB improvement over the regular with nearly 5 dB realized in the middle band. Given that the GA required a very soft active hinge in the truss this is an encouraging result. The result is extremely similar to isolation where the softening and dampening of the fundamental mode is isolating the performance from the disturbance.

A major portion of the performance improvement is in the 7-15 Hz region where the hinging has introduced a singularity into the G_{zw} average gain. The inertia of the softened fundamental mode causes an increase in the system inertia beyond this frequency until the second predominantly truss-like mode is reached. Here the response resumes with beam-like average gain, and it is not surprising that the roll off of the stiff regular truss and that of the hinged design are almost equal on average. After the hinge mode is pinned inertially, the roll off is dominated by the beam-like properties of the truss independent of the length and boundaries [16]. The hinge effectively shortens the length of the beam delaying the uniform beam-like roll off until near the second mode at which point the regular truss has already achieved a similar rate.

The active isolation behavior of the hinged design, with respect to the regular design, is evident in Fig. 6.26. Another way to achieve the hinging result experimentally is high gain integral load cell feedback to unflexured active struts. This was implemented, for low frequency disturbances, on the upper configuration in Fig. 6.2, which was also the optimal placement of structural actuators for the regular design with high frequency narrowband disturbances.

Only knowledge of the measured (non parametric) G_{yu} transfer function is needed to perform this local controller design. The ensuing design from differential actuators to differential load measurement is shown in the loop gain given in Fig. 6.27. Logarithmically even pole-zero spacing, in the region of the first and second antisymmetric modes, is an important characteristic of this loop.

Although the compensator is a basic integrator (1 state) there are six notches used to stabilize the roll off from $200-400$ Hz. These notches provide gain stability where

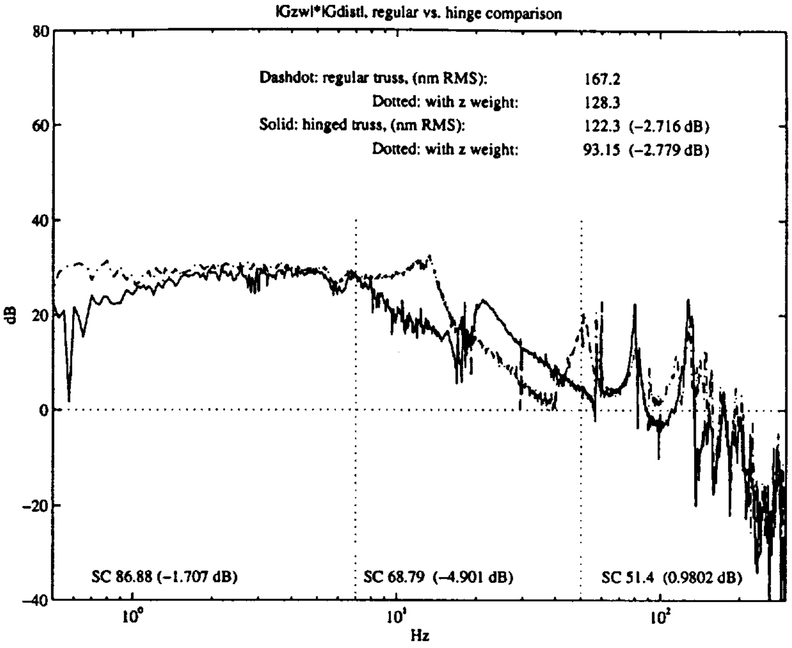

Figure 6.26: Comparison of regular *vs.* optimized (flexured structural actuator) configurations for low frequency disturbances. Performances including extra gain in the optical loops as a z weight are included.

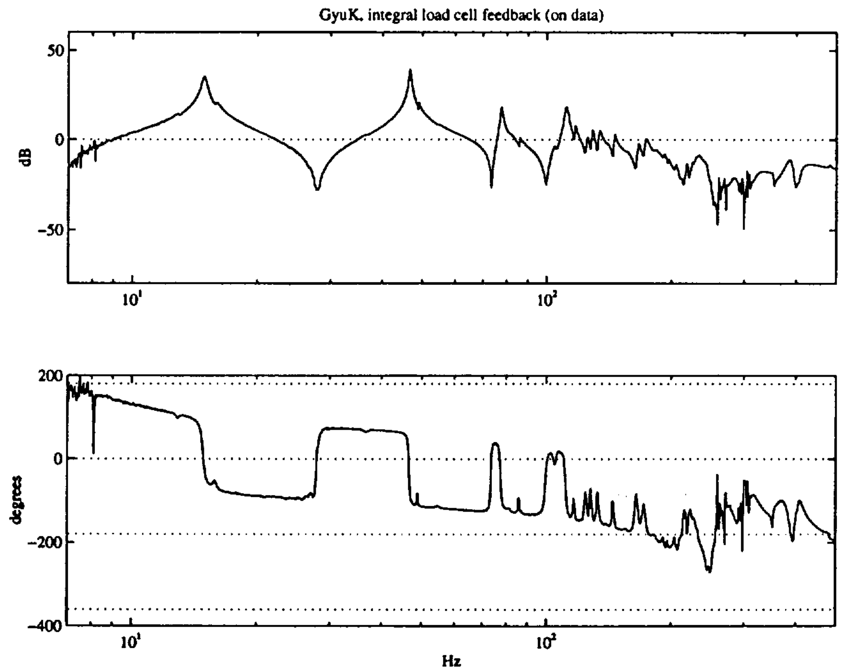

Figure 6.27: Loop gain for high gain softening of structural actuators in the regular truss midspan. Eight notches were added from 200-500 Hz.

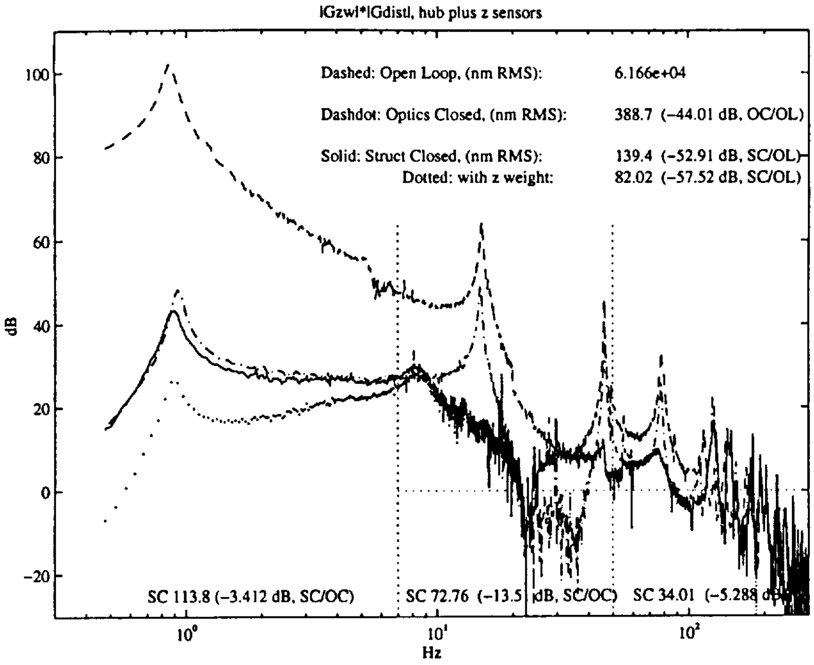

Figure 6.28: Performance for the optimized high gain hinged actuator configuration, low frequency disturbances.

the sampling delay and noncollocation effects incur phase delay.

Closed loop performance is illustrated in Fig. 6.28. No attempt has been made to apply inertial control to dampen the pseudo rigid body mode. Middle band performance is almost as good as that of the flexured hinge configuration and a net overall performance (with z weight) is 10 nm better, even with the rigid body rocking mode undampened. Most of this net gain can be seen in the second and third antisymmetric modes where good dampening has been achieved. The high band performance is improved more than 5 dB to 34 nm. Realize though, that these performance numbers exclude sensor noise and that actually the load cell sensors are too noisey to achieve this absolute level of performance.

Once again, the major achievement has been to soften and dampen the fundamental antisymmetric mode in much the same fashion as an input isolation loop would work.

6.5 High frequency disturbances

With the results from the low frequency configurations in hand the focus is now placed on high frequency disturbances. This spectrum represents that similar to reaction wheel type disturbances for the lower earth orbit imaging interferometer design example. Disturbances from such a source are harmonic in nature. Here, the harmonics are assumed to be smeared over a frequency range to represent design uncertainty in both the location of system modes as well as wheel speed and size.

The high frequency disturbances are narrowband in spectral emphasis and this leads to the postulate that a structurally redesigned system should have greater impact than in the broader-band low frequency designs. A number of implementation issues were overcome in realizing the design example solution and are fully described in the cases that follow.

In this section closed loop results of three cases are presented. For reference, a regular design was tested, as shown in the top of Fig. 6.2. Again, this design is uniformly stiffer than the equivalent nominal case, as was the case in the low frequency disturbance section. In this case the actuators are placed in the middle of the truss arms from the hub. Several experimental iterations were needed to realize the optimized result, the final of which is shown in the bottom of Fig. 6.2. Two of these iterations, the initial and the final, are presented here under structural compensation. Experimental iteration leading to the final realization is interpreted from the optics closed loop transfer function data. The initial optimized design implementation is denoted as hinged partially flexible and final optimized design implementation is denoted as hinged fully flexible. These two configurations represent differing levels of flexibility in the inboard sections of truss.

Cases for this disturbance spectrum are described in Table 6.8 by type of control design, sensor used and limits found on achievable performance. Further cases studied are presented in Appendix C. In all the cases presented the differential load cell sensor is used. When model-based control is used the hub sensor is included. The load cells are used as a collocated measure, even though they have poor noise quality, because

Table 6.8: Cases presented for high frequency disturbance spectrum. "rpni" abbreviates "reduced penalties, no improvement".

Configuration	Type of control	sensors	limit
regular	H_2	load (hub, inertial)	rpni/margin
hinged partially flexible	H_2	load	rpni/limited authority
hinged fully flexible	$\int F$ (root + hinge)	load	damps necessary modes

the emphasis on higher frequencies requires controller roll off through modes that are local in nature, and it was found that a more centralized sensor selection, such as hub plus performance sensors, were severely limited by structural delays.

Implementation of the regular configuration active struts is similar to that shown at the root in Fig. 6.15. They are placed in the midspans of the truss work (see the upper configuration of Fig. 6.2). This configuration also has symmetrically placed passive damping struts [57], one bay from the root, in the upper face diagonals of the truss. These provide some dampening of the antisymmetric torsional modes that occur near the bandwidth of the model based controllers and have little effect on the one-dimensional beam-like behavior of the system.

Design weights for this configuration are shown in Fig. 6.29. Disturbance weights consist of a second order roll up and fourth order roll off. Amplification by the disturbance occurs in the 20 – 150 Hz bandwidth. The inertial control weight is shown but is unimportant because the disturbance is attenuated by three orders of magnitude in this range. Weights on the structural control render it effective over a bandwidth from 3 – 110 Hz with compensator roll off emphasized in the higher range.

Transfer function data *vs.* the 61 state model can be found in Fig. C.14 in Appendix C. Emphasis has been placed on the model fidelity in the 100 – 150 Hz range as the controller will have to roll off here. Key characteristics of the (weighted) model are exhibited in Fig. 6.30. Examination of the pole-zero spacing in the G_{yu} load sensor transfer results in good spacing for the first few modes and collocation

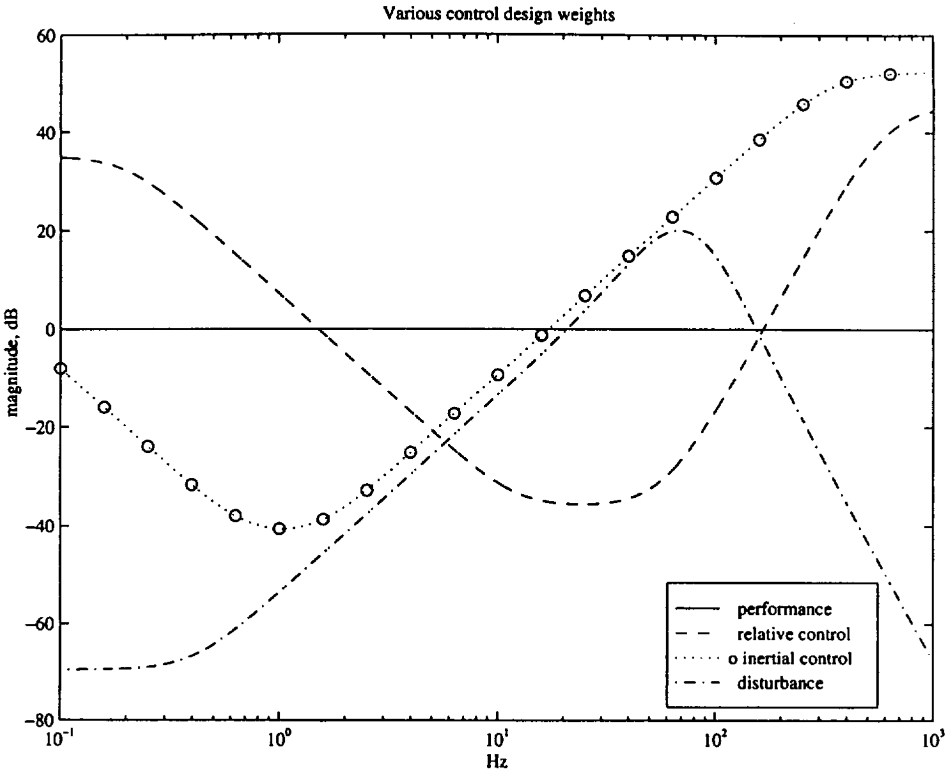

Figure 6.29: Control design weights for regular configuration, hub plus load sensors, high frequency disturbance weight.

out beyond 300 Hz. The hub sensor transfer functions show the sensor weights that enforce roll off. This ensures that the model-based compensator relies predominantly on the collocated sensor. Nonminimum phase behavior listed in Table 6.9 validates the reliance on the collocated sensor.

Control design on the given model resulted in an unstable, but implementable, compensator. The Nichols plot in Fig. 6.31 shows this as the curve passing over the top of the critical point at 900 degrees. The single compensator unstable mode is at 133 Hz, well into the roll off. In a similar fashion to the compensators in the low frequency disturbance cases, the compensator shown initially unravels. When rolling off the compensator the phase is rescued by the unstable mode, which is stabilized in the closed loop by the plant.

Tighter singular values are shown in the sensitivity plot in Fig. 6.31 than in the previous cases. The nature of the plot between 40 and 200 Hz shows impetus in the

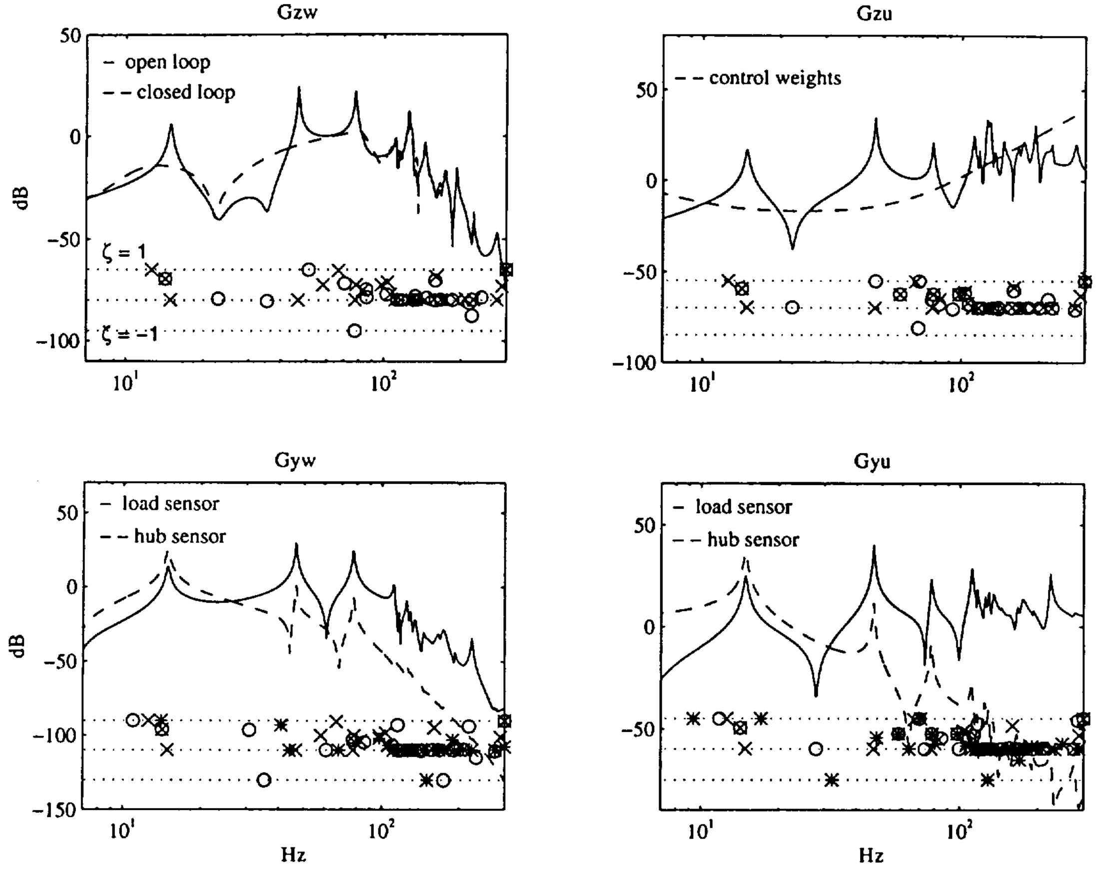

Figure 6.30: Model transfer functions with pole-zero map, hub plus load sensors, high frequency disturbance weight. 'o's correspond to the solid curve zeros, '*'s correspond to the dashed curve zeros.

Table 6.9: Regular truss occurrence of important nonminimum phase behavior, high frequency disturbances.

Transfer Function	Freq. (Hz)	damping (%)
G_{zw}	23	-0.06
G_{zu}	69	-0.8
G_{yw} (load)	35	-1.0
G_{yw} (hub)	160	-1.0
G_{yu} (load)	> 300	na
G_{yu} (hub)	31	-1.0

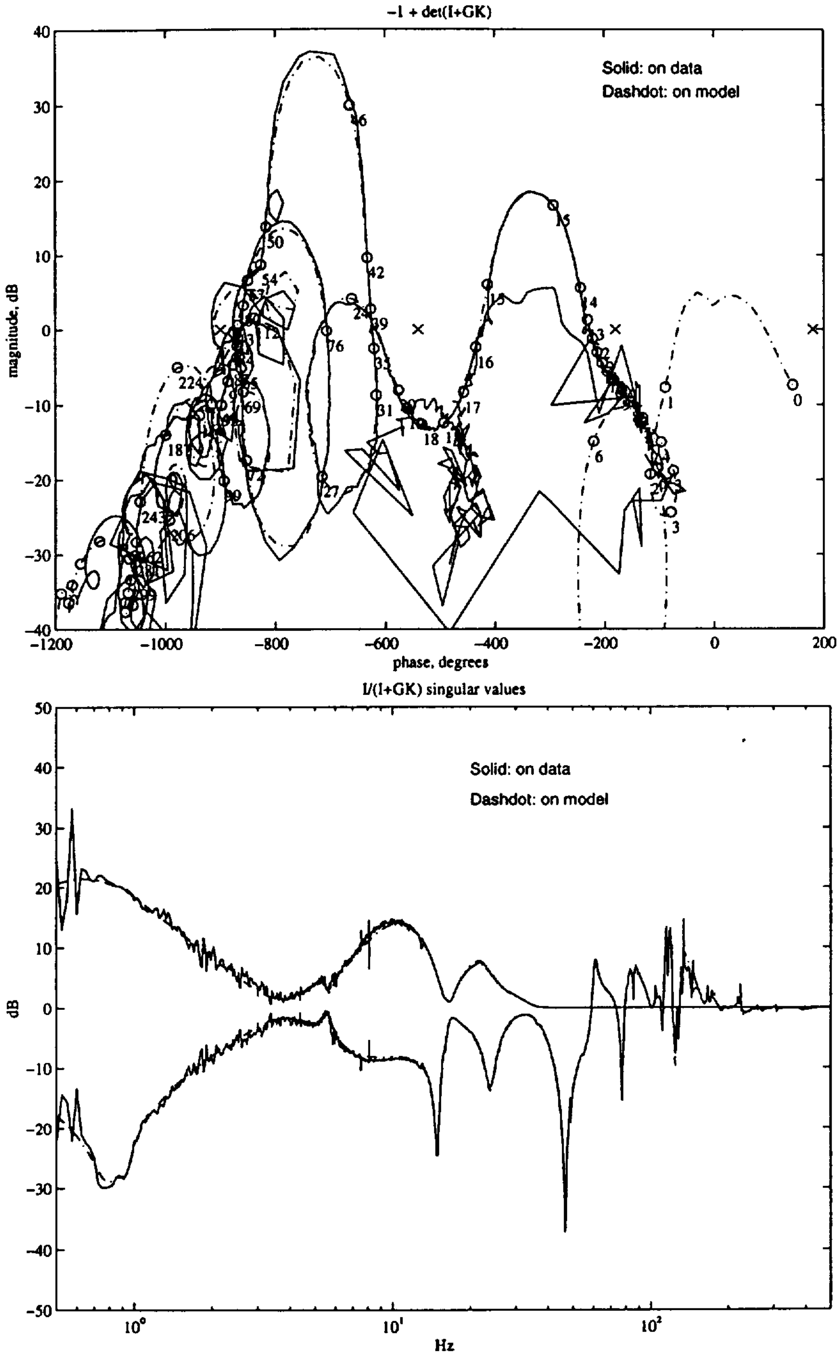

Figure 6.31: Multivariable Nichols plot and sensitivity singular values for regular configuration high frequency disturbances.

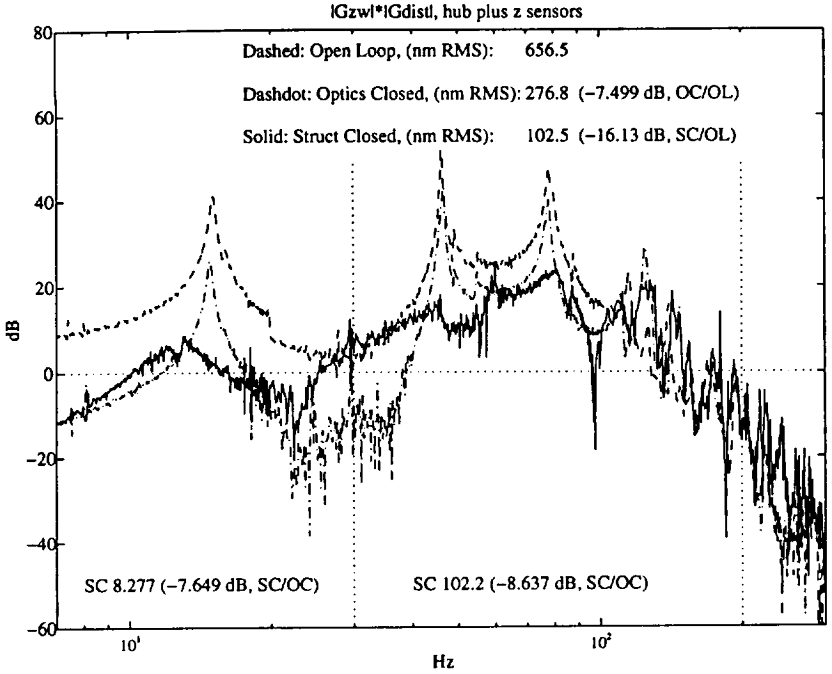

Figure 6.32: Performance for the regular configuration, high frequency disturbances.

dominant performance modes at 47, 78, and around 130 Hz. Impetus does not come without amplification which appears strong. Amplification does not happen to the shown extreme due to the measured direction of the real disturbance. Confirmation of this can be seen in the measured closed loop performance depicted in Fig. 6.32.

Now that the emphasis of the disturbances have shifted to a higher frequency range the performance can be captured, almost wholly, within the 30 – 200 Hz band. Overall the optical control is far less impressive than it was in the low frequency disturbance case achieving only 7.5 dB improvement over the open loop. Structural control improves the performance another 8.5 dB to yield a total 16 dB over the open loop. The final performance result is $\approx$ 103 nm rms and is achieved mainly through dampening of the second and third antisymmetric modes. With more authority (less control penalty) the modeled result appeared to improve but the experimental did not, reaching a fundamental limit.

The high gain damper that was applied for low frequency disturbances, in this configuration, was also applied for high frequency disturbances (since the compensator design was independent of disturbance direction knowledge) resulting in $\approx$ 98 nm rms, see Appendix C. This result shows that the model-based compensator is being limited by model breakdown, since beyond high gain damping not much more can be achieved. The performance was reduced to the average structural filter gain but not beyond.

Experimental performance results are a lot higher than would actually be incurred for reaction wheel disturbances. For this spectrum the disturbance was increased in magnitude so that the closed loop transfer functions were measured above the uncorrelated laboratory disturbances. At $\approx$ 100 nm rms the measured response is about an order of magnitude greater than that expected in the design example for a much softer system.

Figure 6.32 is important evidence that beyond 130 Hz, what looked like noise on the low frequency performance plots is actually increasing modal density. Compensator roll off is evidenced by the bunch of dampened modes underneath a dominant spike near 130 Hz. Some robustness was introduced into this compensator by increasing the damping on the unstable compensator mode, *i.e.* moving the pole closer to the $j\omega$ axis without crossing it. This enabled a larger encirclement of the critical point providing more robustness to model error while reducing performance near that particular mode.

Initially, it was thought that the optimized design solution could be implemented by one dimensional softening of the inboard sections (relative to the middle of the truss arms) of the truss, as shown in the digital image of Fig. 6.33 and upper line sketch in Fig. 6.34. Here, the structural actuators replace longerons in the midspan and are not yet flexured. Transfer function data *vs.* the 98 state model for this configuration can be found in Fig. C.17 in Appendix C. The data shows interesting coupling of the low frequency rigid modes with the softened flexible dynamics. The low frequency modes do not significantly contribute to the performance due to the limited bandwidth of the disturbances, so no effort is made to control them. In fact no further use of the hub sensor for control design is made. The hub sensor, however, does provide useful information about the softened dynamics, and will be used as

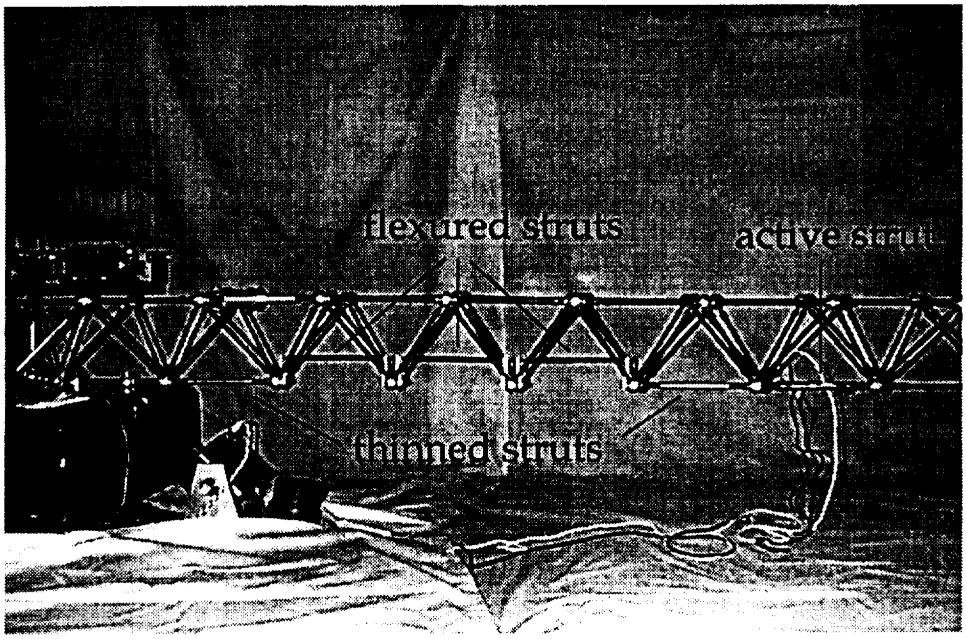

Figure 6.33: Digital image of the initial destiffened implementation. Softening in the primary bending axis is brought about by the flexured and thinned bottom longerons.

such.

Encouraging results of the structural softening are shown in the optics closed loop transfer functions in Fig. 6.35. The G_{zw} transfer function appears to have a reduced average gain when compared to the regular configuration transfer function in Fig. 6.30 over the 70 – 150 Hz range. The overall average gain reduction is offset by a strong mode at 60 Hz. This mode has a reasonable residue in the G_{yu} transfer function, but controlling it is limited by the regulator and estimator dynamics.

Customary plots of the Nichols and sensitivity singular values are given in Fig. 6.36. The controller shown required full capacity usage of the control computer, using 46 structural controller states and 12 optical controller states at a sampling rate of 4 kHz. Design weights for this structural controller are essentially the same as those shown in Fig. 6.29 with the exception that the inertial weights were set arbitrarily high resulting in no inertial control. Two unstable poles that occur in the compensator at 112 and 133 Hz are robustified by increasing the compensator damping, resulting in clear encirclements of the critical point at 540 degrees. A marginally unstable compensator

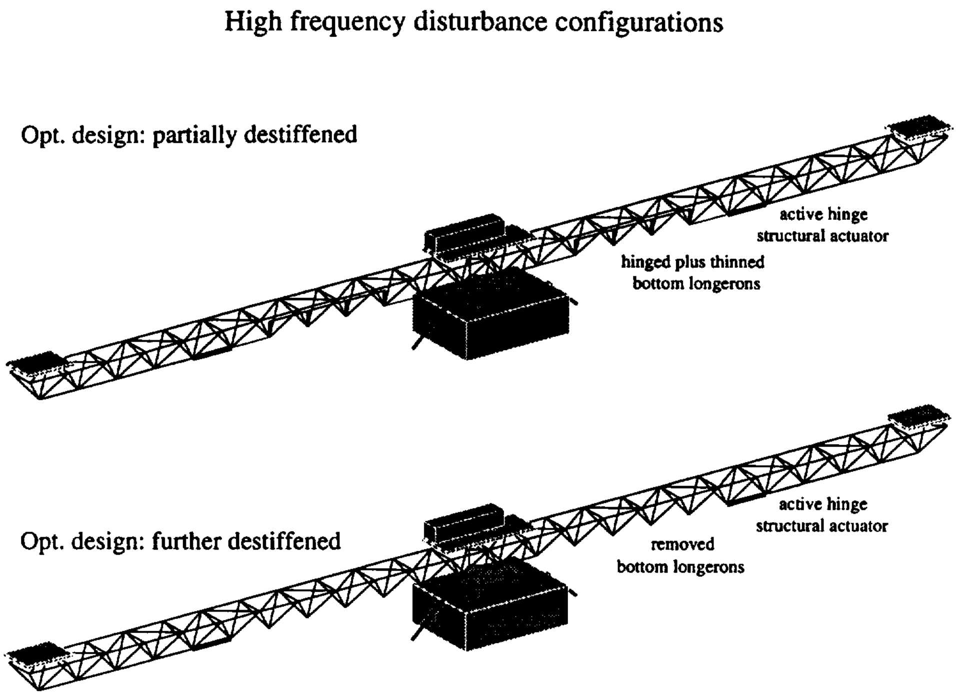

Figure 6.34: Genetic Algorithm partially flexible configurations for high frequency disturbances.

pole at 86 Hz was stabilized since no clear encirclements occur near this frequency.

The sensitivity plot is, in this case, representative of a single input single output system, structural actuator to load cell. No major excursions of model from data are exhibited in this plot so no effort to sensitivity weight this controller design was made.

Performance results are shown in Fig. 6.37. In the closed loop the result is remarkably close to that of the regular truss. Apportionment of the final result has changed, due to the softened nature of the plant. The open loop performance is larger than in the regular truss case, and the optical control achieves about the same relative level of improvement, but the structural controller acquires nearer 13 dB improvement overtaking the regular truss result. Authority over the 60 Hz dominant mode is limited as predicted by decreasing the control penalty when designing controllers on the model.

Perplexed by the inability to do any better than the regular configuration in the closed loop, but heartened by the indication that the backbone was somewhat

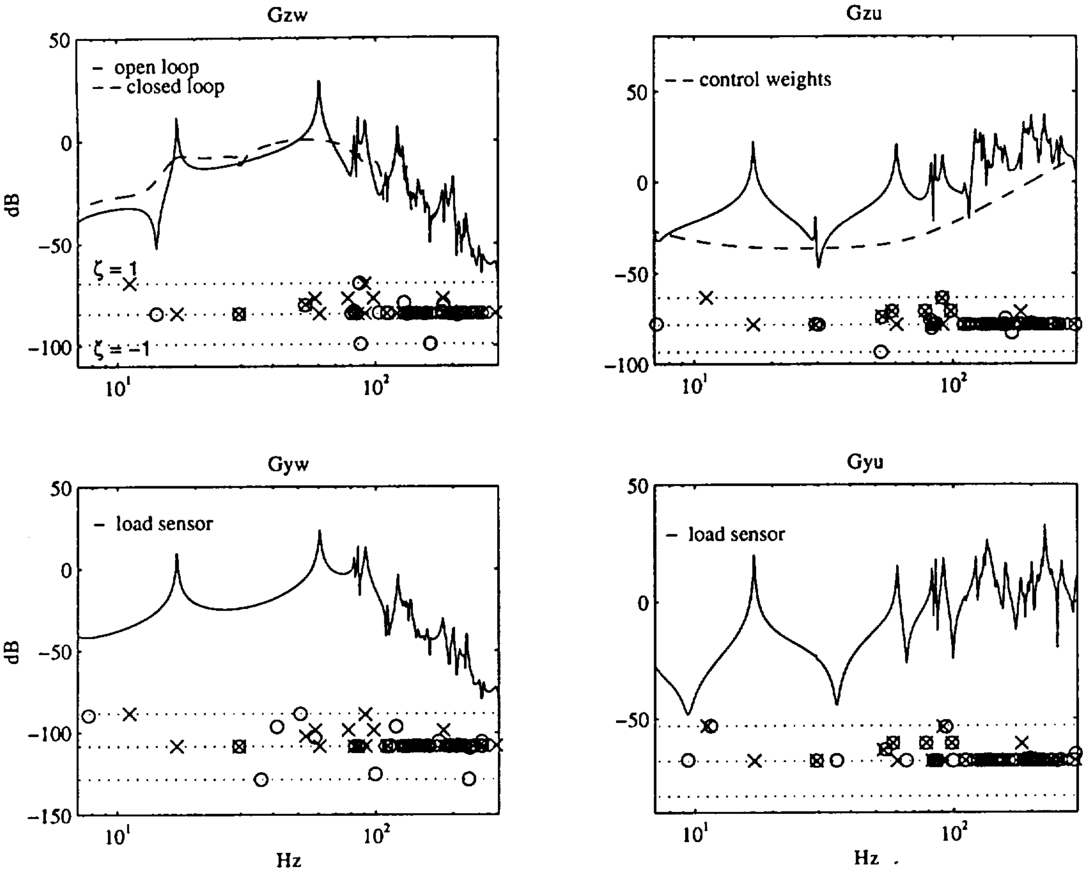

Figure 6.35: Model transfer functions with pole-zero map, load sensor only, high frequency disturbance weight.

reduced (the desired result), further measures were taken to destiffen the truss. Truss softening, in discrete steps of severity, is shown in the lower of Fig. 6.34 and the lower of Fig. 6.2 respectively. Transfer function data, with optics loops closed, are depicted for the regular, further destiffened, and fully destiffened designs respectively in Fig. 6.38. Data from disturbance to performance, hub and collocated sensors are shown. Removing only the bottom longerons does little to reduce the F_{zw} with respect to the E_{zw} transfer function average gain. A considerable number of modes with significant residue appear in the $50-150$ Hz band. The strongest appears to be a mode at $\approx$ 70 Hz. This mode is strongly apparent in the hub sensor transfer function while less so in the collocated sensor. Structural modes corresponding to modes of the softened section of the truss occur as pole-zero excursions in the F_{zw} and F_{yw} (hub)

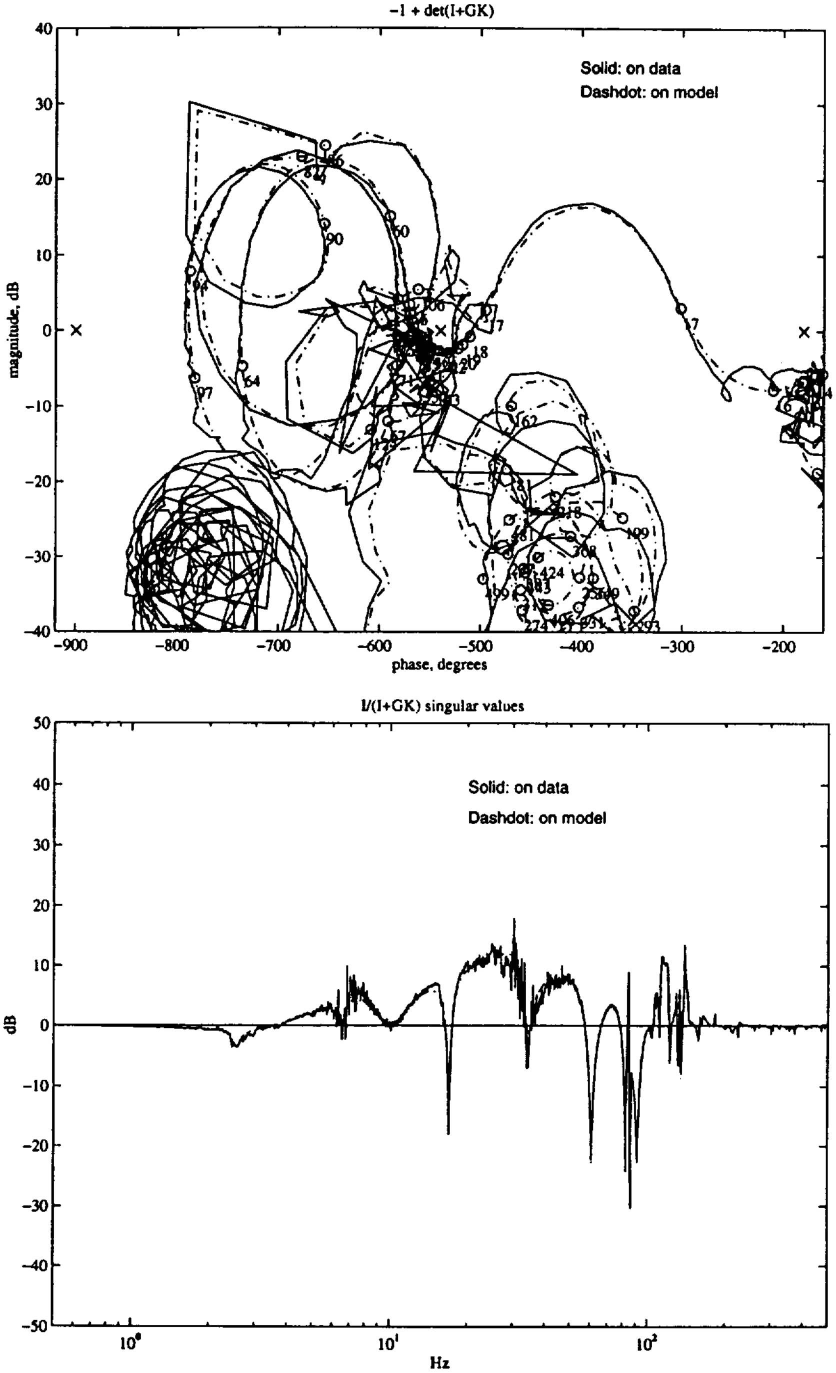

Figure 6.36: Multivariable Nichols plot and sensitivity singular values for partially destiffened configuration high frequency disturbances.

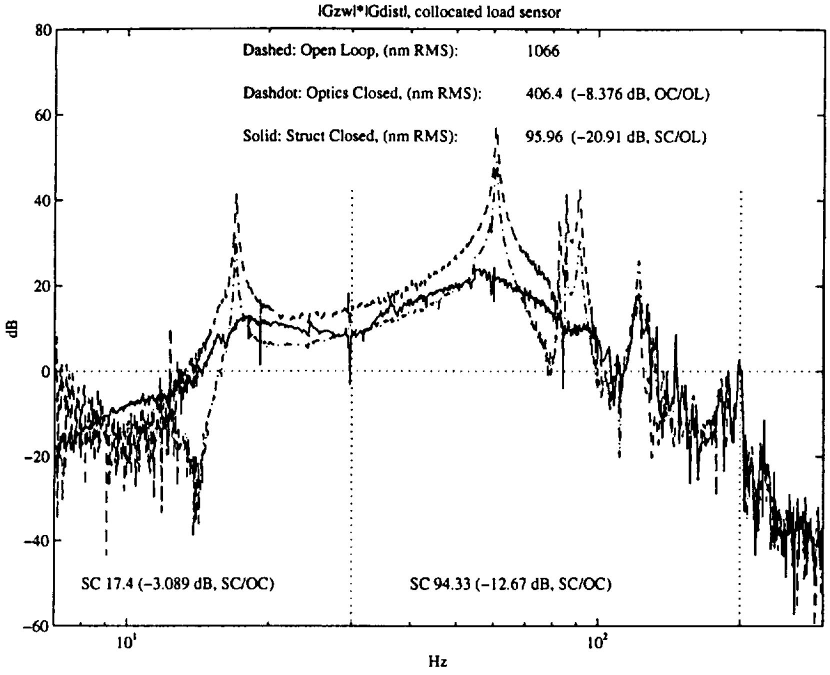

Figure 6.37: Performance for the partially destiffened configuration, high frequency disturbances.

transfer functions. These structural modes are evident in the collocated transfer and the overall gain of this transfer function is reduced.

Removal of supporting truss work in the optimized full destiffened implementation results in $\approx 10 - 15$ dB reduction in average gain, G_{zw}/E_{zw}. A strong mode is still apparent in the important bandwidth at 90 Hz. The mode is a stiffened version of the 70 Hz mode of the second destiffened configuration (60 Hz in the initial configuration), which is now spatially decoupled from the truss ends. Strong evidence of the mode in the hub sensor and not the collocated sensor confirms that it is the primary antisymmetric mode of the shortened middle truss section. Large residue of the mode in the performance transfer function shows the sensitivity of the optics design to local combiner angle. The one-sided delay line design adds small amounts of local combiner angle sensitivity which is now apparent under severe structural variations.

Another feature of the fully destiffened optimized design is the reduced complexity of the modal structure in the $100-200$ Hz range. These modes, depicted in G_{zw} are in neither the hub nor collocated sensor transfer functions. Again the collocated sensor

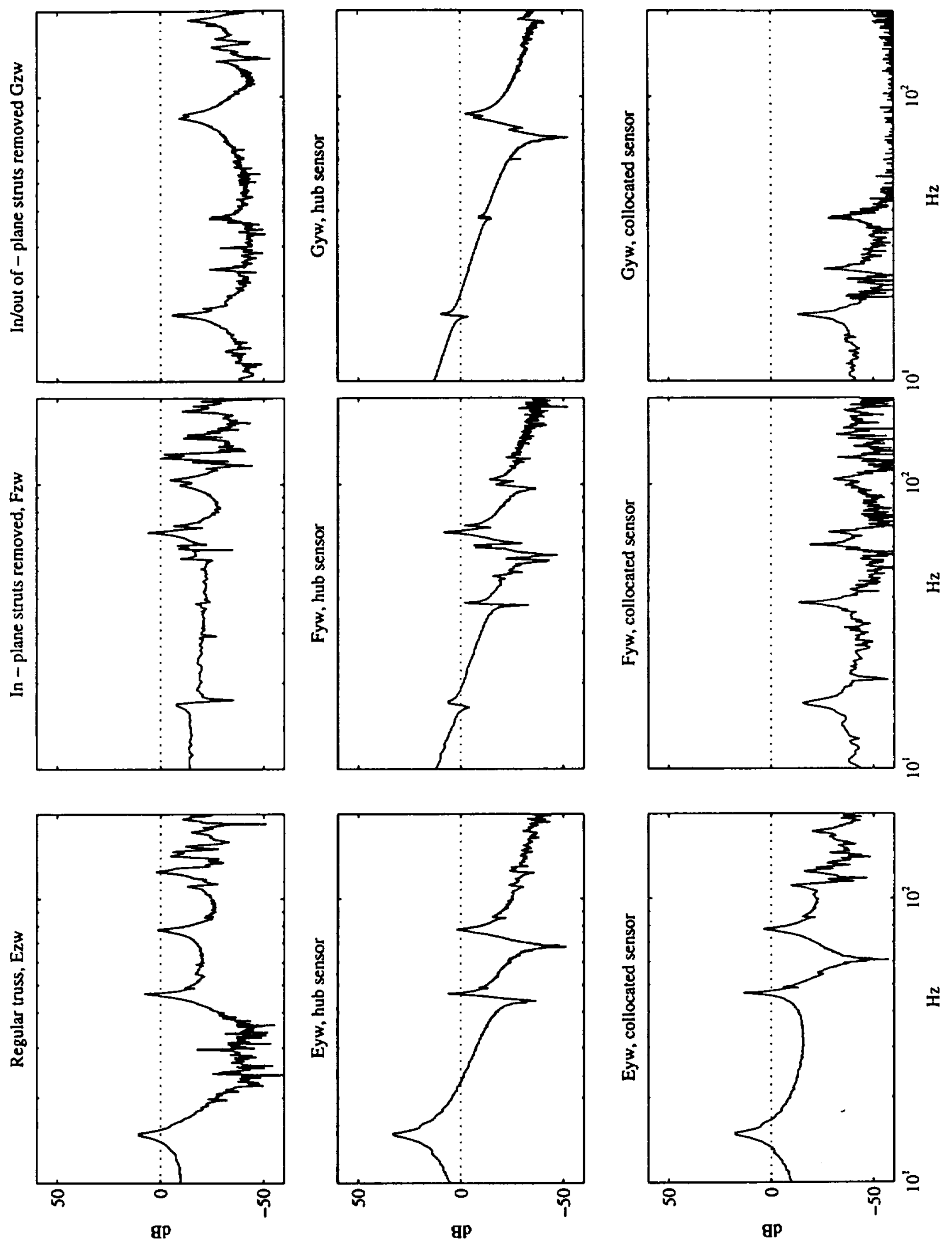

Figure 6.38: Closed loop optics transfer function comparison between regular, E, further destiffened, F, and fully destiffened, G, designs.

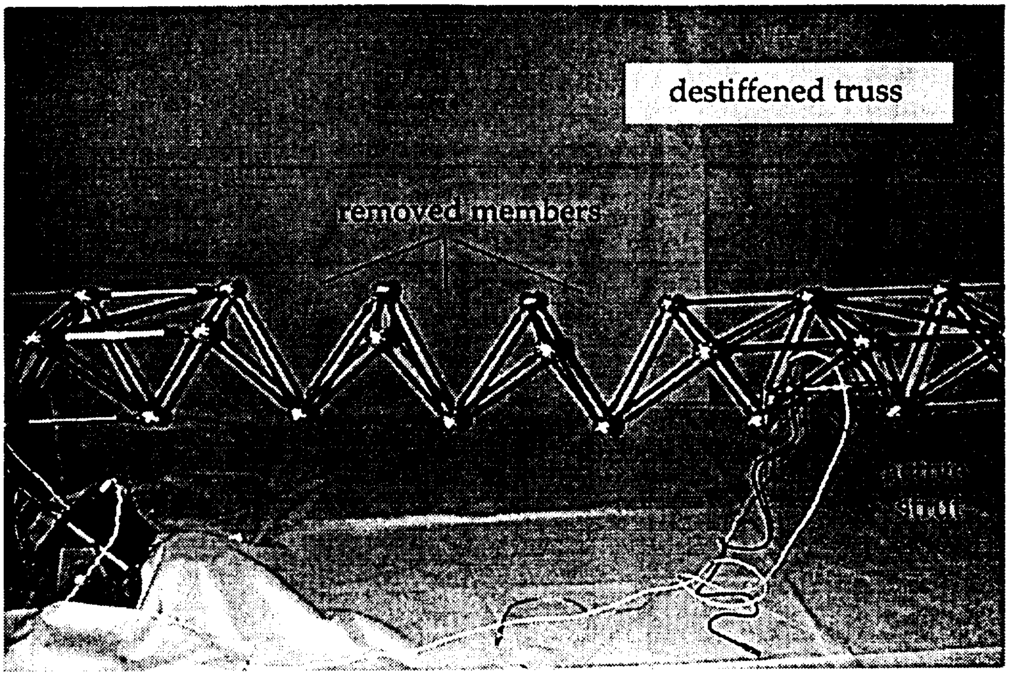

Figure 6.39: Implementation of soft inboard section of the G.A. final design. Longerons and cross members have been removed.

has reduced gain with only a few of the inboard flexural modes apparent when excited by the disturbance.

In order to study the extremely flexible final configuration (lower in Fig. 6.2) extra suspension was added at the truss tips to enable alignment. The suspension took the form of barely resting the truss tips on a highly elastic rubber pad, and served to reduce lateral truss motion while allowing alignment of the optics. Even with this modification alignment still required on the order of 30 minutes. Adding the tip constraint did not affect the dynamics above 5 Hz, where the disturbance is important. Below 5 Hz the system response is not indicative of free end conditions.

Implementation in one side of the fully flexible configuration is shown in Fig. 6.39. Bottom and upper plane longerons were removed from the truss. Connecting zig-zaged struts deform in bending when excited. Lowering the inboard truss stiffness, as such, resulted in significant static sag due to the fact that the tip suspension points were not at the CG of the remainder lengths of truss. The optics were aligned and system controlled regardless of this static sag.

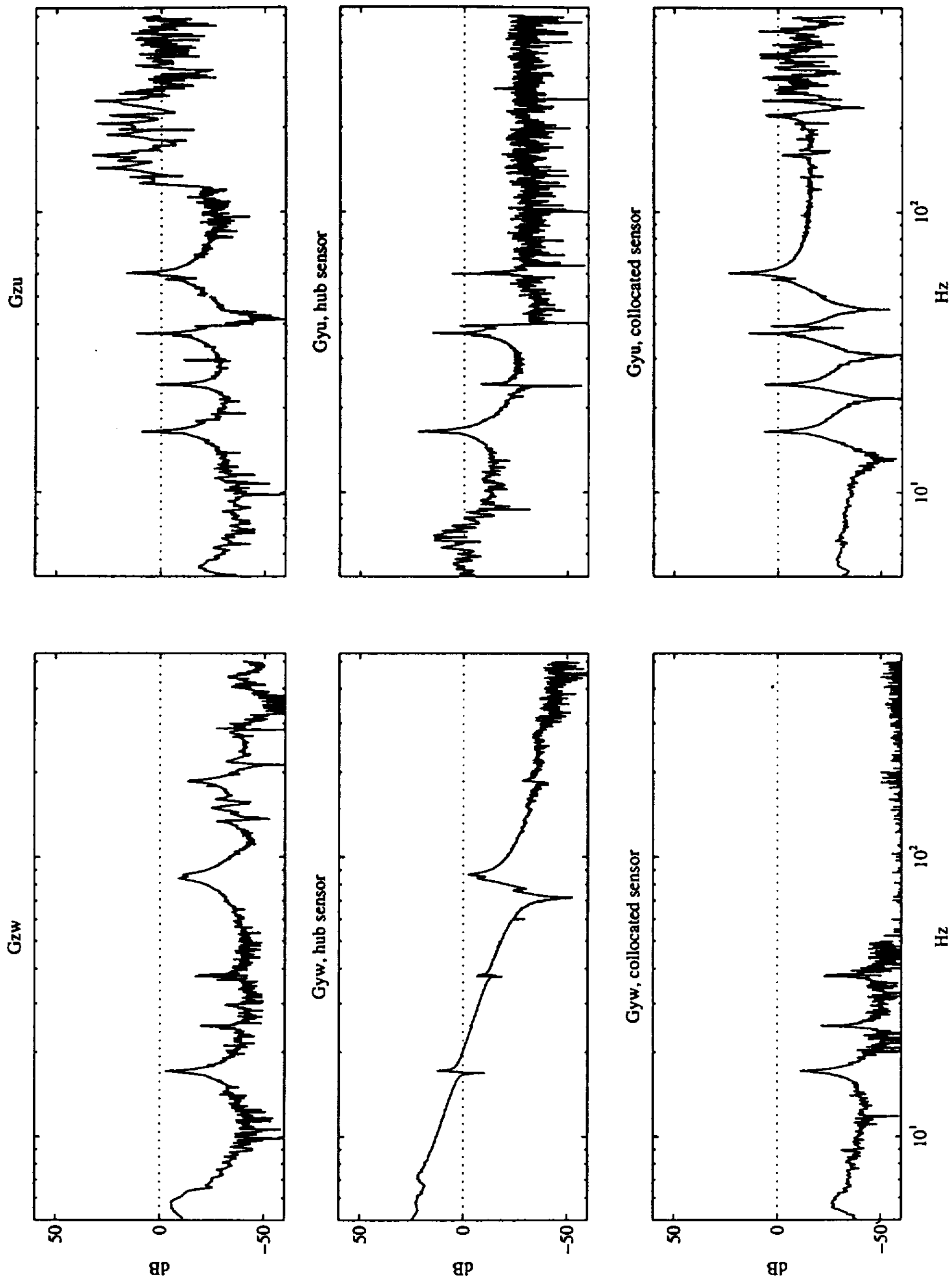

Figure 6.40: Transfer function data for the fully flexible design implementation.

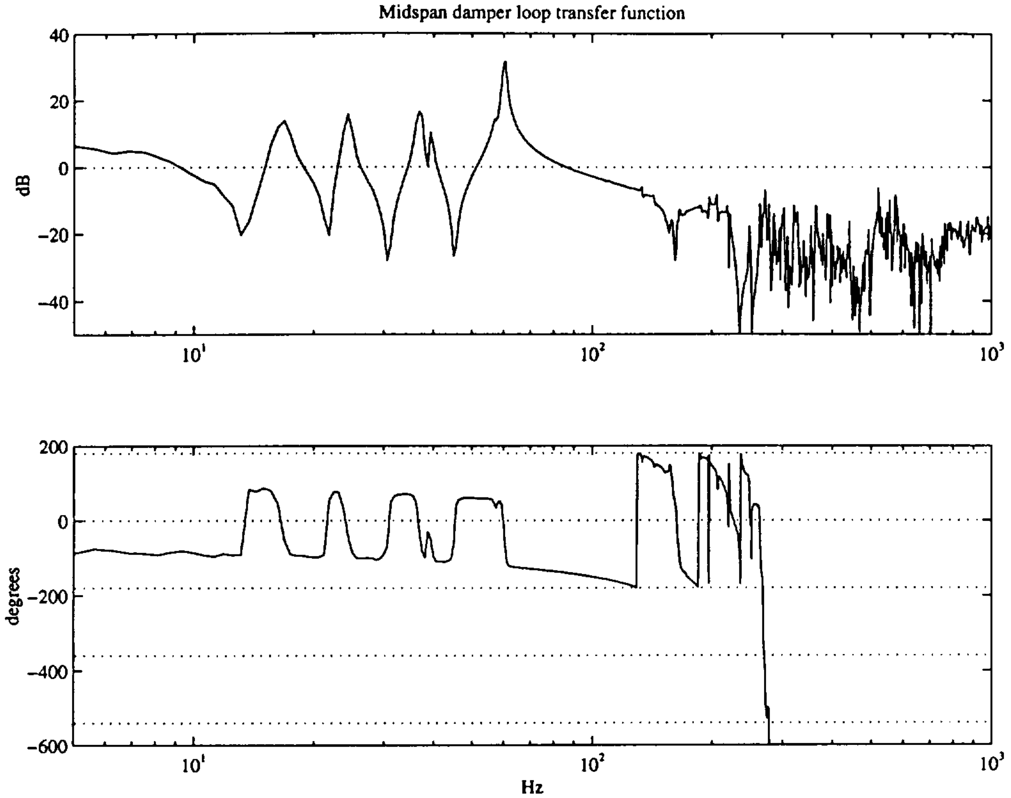

Figure 6.41: Loop gain on data for integral load feedback to the midspan flexured actuators in the fully flexible design implementation.

No model was fit to the fully destiffened configuration data illustrated in Fig. 6.40. Only non parametric control design was used for the differential structural actuator to collocated load cell pair. Transfer functions from the actuator show the softened beam-like flexural modes at $\approx$ 18, 23 and 37 Hz, a substantially stiffer beam-like flexural mode at $\approx$ 60 Hz, and outer truss local dynamics occurring beyond $\approx 130Hz$.

Hinging the actuator on flexures resulted in good coupling to the softened modes and significant separation from the localized modes, as can be seen in the load sensor G_{yu}. Such separation allowed easy implementation of an integral compensator as shown in the loop transfer function in Fig. 6.41. The modal separation allowed dampening of the first three modes without incurring roll off problems due to the local modes.

The combiner 90 Hz mode was also dampened by use of a local loop. Extra structural actuators were placed at the hub in the locations illustrated in the lower

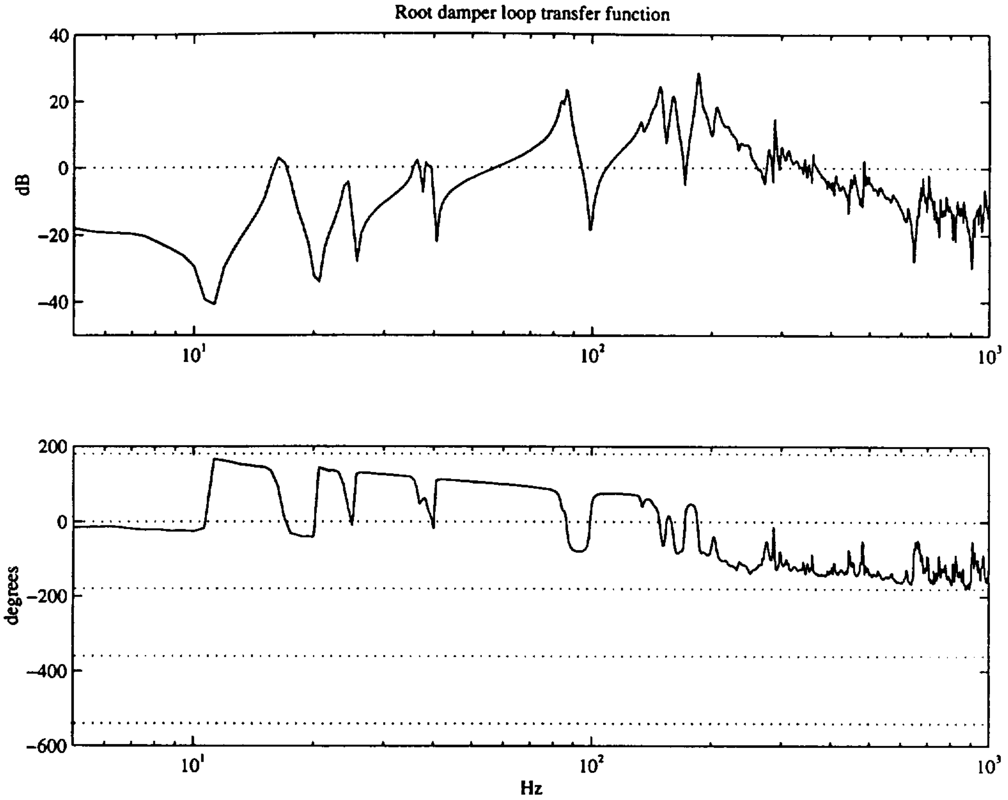

Figure 6.42: Loop gain on data for integral load feedback to the root/combiner actuators in the fully flexible design implementation.

configuration in Fig. 6.2. As before, integral (differential) load feedback was used and the loop gain shown in Fig. 6.42. As much as 20 dB of gain is attained near the problem mode, while high gain is also achieved on modes from 130 – 150 Hz, were they to be disturbed.

With the two SISO compensators closed the performance is greatly improved over the regular truss, and over the partially destiffened design, see Fig. 6.43. Open loop rms performance is $\approx$ 8 dB less than that of the regular truss, and $\approx$ 12 dB less than that of the partially destiffened truss. Closed loop optics now achieves 11 dB improvement with structural control adding a further 9 dB to yield an overall performance of 25 nm rms. The structural performance improvement is nearly all attained by dampening of the 90 Hz mode by the root actuator.

Comparison of the closed loop results for the regular and final GA configurations

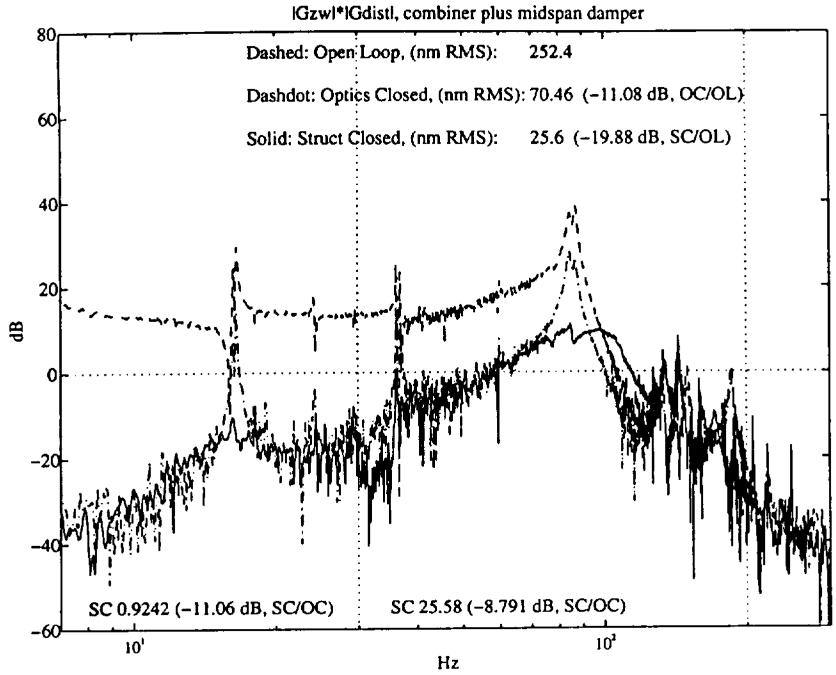

Figure 6.43: Performance for the fully flexible configuration, high frequency disturbances.

is shown in Fig. 6.44. The GA final design provides 12 dB of overall improvement. This result is consistent with the design example. They are almost entirely due to average gain reduction. In the 5 – 10 Hz range the GA result shows singularity in the average transfer function gain where the end structure rigid modes are providing isolation from the hub disturbance. That these modes cause more response below 10 Hz is of no concern for this disturbance spectrum under closed loop optics. The only concern is that the optical actuators have enough stroke to cancel the disturbed low frequency motion.

6.6 Summary

A testbed was designed and implemented that allowed investigation and validation of the (scaled) imaging interferometer design example. Closed loop optical control was used to emulate the complicated output isolation stage of such a device and thus provide the correct performance sensor impedance.

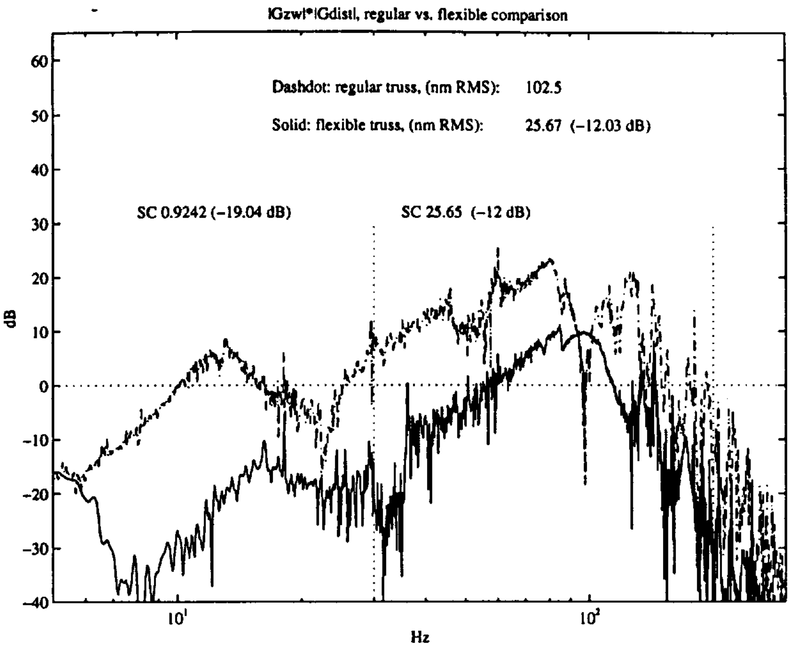

Figure 6.44: Comparison of regular *vs.* fully flexible configurations for high frequency disturbances.

Six cases, three low frequency disturbances, three high frequency disturbances, have been presented under closed loop optical and structural control. In the case of low frequency broadband disturbances the performance was dominated by the system inertia. Higher optical loop gains at low frequency alleviated some of this dominance. Implementation of the optimized hinge design was realized in two parts, a regular stiffened truss was compared to the stiffened truss including an active hinge. The active hinge (to the extent implemented) improved closed loop rms performance by $\approx$ 3 dB. This is significant when compared to a mere 1 dB improvement predicted for global stiffening of the nominal design. Even though the optimized design required further softening of the active hinge this result shows the difficulty in maneuvering the low frequency average gain which is dominated by the system inertia.

Examination of the high frequency, narrow band, disturbance results shows dramatic improvements through the implemented structural softening. This is because the disturbance emphasizes a flexibility dominated region of the G_{zw} transfer function. Several experimental iterations were required to achieve the GA design goal, each showing the impact on the G_{zw} average transfer function gain of various extremes of structural softening. Again results from a regular stiffened truss are compared to an implementation of the optimized design with the fully destiffened optimized design achieving $\approx$ 12 dB rms improvement over the regular truss. Implementation of the active structural hinge enabled dampening of the captured inboard flexural modes while a root damper reduced the combiner sensitivity to asymmetries.

Chapter 7

Conclusions, Contributions and Recommendations

The purpose of this chapter is to provide general and detailed conclusions pertinent to this thesis. Conclusions are first given that are general to controlled structures systems. Specific conclusions are then given that are based on the specific validation and application examples studied. Contributions to the controlled structures optimization field are given and recommendations for further work detailed.

The approach provided in this thesis has been from an accurate modeling perspective. Therefore the conclusions will be based on interpretation and development of structures for control.

7.1 General Systems Level Conclusions

The fundamental behavior that causes difficulty in controlling irrational structural systems is the fact that the average frequency domain system response stays high while the system phase decreases due to the occurrence of poles. This effect is the manifestation of structural delay and is realized between noncollocated input/output pairs. Discretization of noncollocated systems results in nonminimum phase zeros. These zeros are more sensitive to assumed model damping than spatial refinement.

Sensitivities of asymptotic approximations to simple collocated systems show that for truss structures topological variations affect motion-based performance more than simple member cross-section variations. For constrained structures the motion performance goes like $1/(l^2 m^2 \omega_x^3)$ where for unconstrained structures the performance is dominated by the upper or lower limit of the frequency domain performance integral. Narrow band average structural filtering from noncollocated disturbances to performances is very sensitive to damping, modal spacing and modal residues.

Good pole-zero structure is necessary for high bandwidth, high authority control. System transmission zeros are more sensitive to placement changes than to structural variations unless the later are local to relative input/output pairs. Structural variations tend to cause the zeros to track changes in the modes.

This thesis provides a general method by which to design structures for control. The method, utilizing the Genetic Algorithm, is admittedly computationally expensive in that it uses zeroth order stochastic propagation of a parallel model space, however, the method is not specialized to any one modeling or control technique and allows simultaneous discrete update of topological variables without sacrificing model accuracy. A good representative model for control is provided in the proposed method via a consistent effort that employs condensation, reduction, static mode correction and design frequency weights. The inherently discrete decisions that are integral in such a process require that a discrete search method be used. Sensitizing the method with derivatives of the performance with respect to structural parameters is too computationally intensive for realistically sized structures. The method was found to work well and provide results comparable to those published in the literature.

Physical insight, as to the capability of an active system optimization to yield useful improvements, has been provided through study of an application example. The active solutions are limited by the average transfer function gain combined with system loss of phase. Within the limits of the allowable controls topology variations, centralized controllers can only be as effective as the system noncollocation allows. Usually, for relative structural actuation compensating an externally disturbed system with inertial type performance, this means active dampening only. Combined structural optimization and actuator/sensor placement provides good direction in manipulating the average transfer gain and system loss of phase to yield performance improvements.

Under the assumption of aerospace-like sensors, which have low sensor noise specifications, optimized controls-structures topologies improve the regulation of the structure. Improving regulation entails improving the average controls to performance transfer function gain while maintaining good pole-zero structure in the important bandwidth. Delays in the estimator and the controls to sensors transfer functions are compromised in order to achieve this result which enables improved performance through regulation gain.

7.2 Specific Systems Conclusions

Adaptation can be successfully added to a Genetic Algorithm to enable the solution of problems with implicit dependencies of the variables, for example, where increased control effort requires a more massive actuator. When minimizing structural weight of a controlled free-free beam, flexibility is traded for mass when the control effort required to meet specified performance does not necessitate heavy actuators. In the three dimensional cantilevered truss example heavy actuators were removed from the design and performance constraints met through passive isolation and active damping of fundamental modes. This later example showed that accurate modeling of sensors and actuators as pairs is imperative to the ability to predict closed loop performance.

Analytical and experimental investigations of an optimized, structurally and optically controlled, space-based interferometer show the benefits of active technologies in enhancing pathlength compensation. System transfer function representations clearly show the important frequency band components of the disturbance to performance, and how the relationship with integral structural actuators and commonly available sensors affects performance.

The fundamental contribution to performance response, when disturbed by low frequency impulsive/step-like hub sources, was found to be dictated by the system inertia. For these spectra of disturbances genetically designed structural-isolation yields mild improvements over a closed loop regular system design. The active design calls for fundamental antisymmetric mode softening and dampening. This was realized under some restrictions in the experiments. A regular isolation design that separates the hub from the truss-optics system would bare better results here. However, this would require more optical capability.

A genetically optimized, active structural-isolation, design for high frequency harmonic-like disturbances was found have good performance improvements over a regular truss implementation. In the important bandwidth the average transfer function gain is reduced while the active system provides dampening of the softened beam-like flexible modes. The price of this improved performance is realized in the difficulty of the quasi-static optical alignment problem. Genetic manipulation of the stiffness under closed loop considerations has more effect where the flexibility is important in the performance.

In the later case, experimental sensitivity to the optics arrangement was found. This shows that the design of a symmetric optical layout is important in achieving low levels of pathlength error.

7.3 Contributions

- A simple representation of structural transfer functions is provided with pole-zero frequency versus damping plotted directly on the Bode magnitude plot. This plot allows interpretation of the model structure by allowing visualization of damped zeros, pole-zero cancellations and modal density characteristic in structural systems.

- Interpretation of physical limitations in basic noncollocated structural systems is developed. Structural delay is detailed in terms of system phase loss due to the occurrence of poles. Structural transmissibility is detailed in terms of high average transfer function gain. Simple structural systems are investigated from three points of view: the exact irrational transcendental transfer function, a FEM generated rational transfer function and cumulative residuals generated from a finite modal summation form of the transfer function. The noncollocated free-free rod example is given to detail the sensitivity of discretization zeros. These zeros were found to be more sensitive to assumed model damping than spatial refinement and were found not to contribute strongly to the average transfer function gain. The free-free beam example is given to show how physical nonminimum phase zeros eventually couple into discretization effects. Fundamental sensitivities of motion error performance integrated under average transfer function gain asymptotes is given for collocated input/outputs in simple structures. Noncollocated average structural transfer function magnitudes were numerically shown to be sensitive to damping, modal spacing and modal residues.

- A general method that optimizes controlled structures allowing topological variations is developed. The method is derived from a modeling perspective where accurate models were desired for controls analysis. Specifically in the method, control variables were incorporated into the condensation technique as interface dof. Performance and disturbance weights were included as weights in the model reduction step. Multiple chromosome phenotype encoding was developed for genetic algorithms that optimize controlled structures. Non simple crossover operations that act within each attribute chromosome were implemented. The Genetic Algorithm was also specialized to include adaptation for the first validation example. The adaptation allowed the solution of an optimization problem that had an implicit dependency.

- Optimizing several structures under motion error objective showed that, generally, the solution is generally to improve the regulation of the structure, where good quality sensors are assumed. To support this conclusion an imaging interferometer spacecraft application was encoded into a one dimensional design example. Punctuated equilibrium was added to the search optimization, that restarted the method with the best designs from several runs and propagated them with random designs. This enabled the best designs to be compared with each other while improving their attributes. Further support of the general conclusion is found by encoding and optimizing a true topological three dimensional problem. The results found were similar to the beam-like example. In this example variables such as nodal locations, diagonal connectivities, member properties and actuator locations were searched over simultaneously.

- Experimental investigations of topologically optimized controlled structures are provided. Experiments were scaled and designed from the systems perspective to include closed loop optical control and structural control. The broadband disturbance, active hinge solution to the application example was implemented two ways, the first using passive flexures and the second using high gain local feedback. Both were found to improve the closed loop performance, yet be limited by the overall system inertia. Experimental iteration was used to realize the narrow band disturbance result showing the effects of multiple load paths in truss structure transmissibility. Results confirm that manipulating the average disturbance to performance transfer function gain provides the expected improvements.

7.4 Recommendations

- Analytical interpretations of structural filtering of noncollocated input/output pairs is needed. With further understanding of these systems a more rigorous (non numerically based) understanding of how to effect the structural transmission paths from disturbance to performance can be found.
- Smart crossover operations that adapt to the available information provided by a generation of designs need be developed. Within each generation there is plenty of inexpensive (computationally) information in terms of statistics of the objective function with respect to specific attributes that could be used to accelerate the method, even towards multi modal solutions.
- The method should be further developed to bridge conceptual and preliminary

design stages. That is, more radical topological changes enabled in a geometrically free design space. This is where the big systems pay-off lies.

- Highly distributed damping systems should be investigated for the application example presented. Under very high frequency disturbances the system response is dominated by the packed local modes and it is here that damping was found to have a large influence in the simple examples.
- In panel-like structures such as fuselage enclosures, non geometric rib spacing should be investigated to reduce coupling to an acoustic field. As in truss structures the band pass nature of these structures can be affected by redistributing the highly packed panel modes.

References

[1] Rao, S., V. Venayya, and N. Khot, "Game Theory Approach for the Integrated Design of Structures and Controls," *AIAA Journal*, Vol. 26, No. 4, Apr. 1988, pp. 463–469.

[2] Maghami, P., S. Gupta, K. Elliot, and S. Joshi, "Experimental Validation of an Integrated Controls- Structures Design Methodology for a Class of Flexible Space Structures," in *NASA Technical Paper 3462.*

[3] Canfield, R., R. Grandhi, and V. Venkayya, "Optimum Design of Structures with Multiple Constraints," *AIAA Journal*, Vol. 26, Jan. 1988, pp. 78–85.

[4] Miller, D. and J. Shim, "Combined Structural and Control Optimization for Flexible Systems Using Gradient Based Searches," No. AIAA Paper 86-0178, Jan. 1986.

[5] Onoda, J. and R. T. Haftka, "An Approach to Structure/Control Simultaneous Optimization for Large Flexible Spacecraft," *AIAA Journal*, Vol. 25, No. 8, 1987.

[6] Sepulveda, A. E., I. M. Jin, and L. A. Schmit, "Optimal Placement of Active Elements in Control Augmented Structural Synthesis," *AIAA Journal*, Vol. 31, No. 10, 1993.

[7] Hanks, B. and R. Skelton, "Closed-form solutions for the design of optimal dynamic structures using linear quadratic regulator theory," in *Proceedings of the 32nd Structures, Structural Dynamics and Materials Conference*, (Baltimore, MD), Apr. 1991.

[8] Smith, M. J., K. M. Grigoriadis, and R. E. Skelton, "Optimal Mix of Passive and Active Control in Structures," *Journal of Guidance, Control, and Dynamics*, Vol. 15, No. 4, Aug. 1992.

[9] Skelton, R. E., B. R. Hanks, and M. J. Smith, "Structure Redesign for Improved Dynamic Response," *Journal of Guidance, Control, and Dynamics*, Vol. 15, No. 5, Sept. 1992.

[10] Skelton, R. E. and J. Lu, "Performance-oriented Optimization of Structures with Mixed Passive and Active Control," in *Proceedings of the SPIE Conference on Smart Structures and Materials*, (San Diego, Ca), Apr. 1997.

[11] Keane, A. J., "Passive Vibration Control Via Unusual Geometries: Experiments On Model Aerospace Structures," *Journal of Sound and Vibration*, Vol. 192, No. 1, 1996.

[12] Crawley, E., S. Hall, and M. Campbell, *High Performance Structures: Dynamics and Control*, T.B.D., 1999.

[13] Miller, D. W. and A. H. von Flotow, "Power Flow in Structural Networks," *Journal of Sound and Vibration*, No. 128, 1989, pp. 145–162.

[14] von Flotow, A. H., "Disturbance Propagation in Structural Networks," *Journal of Sound and Vibration*, No. 126, 1986, pp. 127–144.

[15] MacMartin, D., *A Stochastic Approach to Broadband Control of Parametrically Uncertain Structures*, Ph.D. thesis, Massachusetts Institute of Technology, June 1992. SERC Report number 5-92.

[16] McCain, A. J., *Shaped Actuators and Sensors for Local Control of Intelligent Structures*, Master's thesis, Massachusetts Institute of Technology, June 1995. MIT SERC Report number 3-95.

[17] Crawley, E. F., B. P. Masters, and T. T. Hyde, "Conceptual Design for High Performance Dynamic Structures," in *AIAA Structures, Structural Dynamics, and Materials Conference*, No. 95-2557, (New Orleans, La), Apr. 1995, pp. 2768–2787.

[18] Glaese, R. M. and D. W. Miller, "Derivation of 0-g Structural Control Models from Analysis and 1-g Experimentation," *Journal of Guidance, Control, and Dynamics*, Vol. 19, No. 4, July 1996, pp. 787–793.

[19] Davis, L., T. Hyde, and D. Carter, "Second Generation Hybrid D-strut," in *Proceedings of the SPIE Conference on Smart Structures and Intelligent Systems*, (San Diego, CA), Feb. 1995.

[20] Gevarter, W. B., "Basic Relations of Flexible Vehicles," *AIAA Journal*, Vol. 8, No. 4, 1970, pp. 666–672.

[21] Freudenberg, J. S. and D. P. Looze, "Right Half Plane Poles and Zeros, and Design Tradeoffs in Feedback Systems," *IEEE Trans. on Automatic Control*, Vol. 30, 1985.

[22] Boyd, S. and C. A. Desoer, "Subharmonic Functions and Performance Bounds on Linear Time-Invariant Feedback Systems," *IMA J. of Mathematical Control and Information*, Vol. 2, 1985, pp. 153–170.

[23] Anderson, E. H., G. H. Blackwood, and J. P. How, "Passive Damping in the MIT SERC Controlled Structures Testbed," Alexandria, VA, Nov. 1991.

[24] Keane, A. J., "Experiences With Optimizers in Structural Design," *Adaptive Computing in Engineering Design and Control*, Sept. 1994.

[25] Keane, A. J., "Passive Vibration Control Via Unusual Geometries: The Application of Genetic Algorithm Optimization to Structural Design," *Journal of Sound and Vibration*, Vol. 185, No. 3, 1995, pp. 441–453.

[26] Grocott, S. C. O., D. G. MacMartin, and D. W. Miller, "Experimental Implementation of a Multi-Model Design Technique for Robust Control of the MACE Test Article," *Proceedings, Third International Conference on Adaptive Struc-*

tures, San Diego, CA, Nov. 1992, pp. 375–387.

[27] Aubrun, J. and K. Lorell, "The Multi-Loop Control/Structure Interaction Effect: Experimental Verification Using the ASCIE Test Bed," in *Proceedings of the Fourth NASA/DOD Controls/Structures Interaction Technology Conference*, Nov. 1990.

[28] Belvin, W. *et al.*, "The LaRC CSI Phase-0 Evolutionary Model Testbed: Design and Experimental Results," in *Proceedings of the Fourth NASA/DOD Controls/Structures Interaction Technology Conference*, Nov. 1990.

[29] Grocott, S. C. O., J. P. How, and D. W. Miller, "An Experimental Comparison of Robust H_2 Control Techniques for Uncertain Structural Systems," *Journal of Guidance, Control, and Dynamics*, May 1997.

[30] Ih, C.-H., D. Bayard, A. Ahmed, and S. Wang, "Experiments in Multivariable Adaptive Control of a Large Flexible Structure," *Journal of Guidance, Control, and Dynamics*, Vol. 16, No. 1, Jan-Feb 1993, pp. 9–13.

[31] Ih, C.-H., D. Bayard, A. Ahmed, and S. Wang, "Experimental Study of Robustness in Adaptive Control for Large Flexible Structures," *Journal of Guidance, Control, and Dynamics*, Vol. 16, No. 1, Jan-Feb 1993, pp. 14–20.

[32] Jacques, R. and D. Miller, "Physical Insight into the Simultaneous Optimization of Structure and Control," in *Proceedings of the fifth NASA/DoD Conference*, (Lake Tahoe, NV), Mar. 1992.

[33] Levine, W., ed., *The Control Handbook*, CRC Press, 1996.

[34] Nelson, R., "Simplified Calculation of Eigenvector Derivatives," *AIAA Journal*, Vol. 14, No. 7, Sept. 1976.

[35] Mills-Curran, W., "Calculation of Eigenvector Derivatives for Structures with Repeated Eigenvalues," *AIAA Journal*, Vol. 26, No. 7, July 1988.

[36] Hou, G. J. and S. P. Kenny, "Eigenvalue and Eigenvector Approximate Analysis for Repeated Eigenvalue Problems," *AIAA Journal*, Vol. 30, No. 9, Sept. 1992.

[37] Luongo, A., "Eigensolutions Sensitivity for Nonsymmetric Matrices with Repeated Eigenvalues," *AIAA Journal*, Vol. 31, No. 7, July 1993.

[38] Bathe, K.-J., *Finite Element Procedures in Engineering Analysis*, Prentice-Hall Inc., 1982.

[39] Craig, R. R. and M. C. Bampton, "Coupling of Substructures for Dynamic Analyses," *AIAA Journal*, Vol. 6, No. 7, July 1968.

[40] Triller, M. J. and D. C. Kammer, "Controllability and Observability Measures for Craig-Bampton Substructure Representations," *Journal of Guidance, Control, and Dynamics*, Vol. 17, No. 6, Dec. 1994.

[41] Gregory, C. Z., "Reduction of Large Flexible Spacecraft Models Using Internal Balancing Theory," *Journal of Guidance, Control, and Dynamics*, Vol. 7, No. 6, Dec. 1984.

[42] Doyle, J. C., B. A. Francis, and A. R. Tannenbaum, *Feedback Control Theory*, The Macmillan Publishing Company, 1992.

[43] Kwakernaak, R. and R. Sivan, *Linear Optimal Control Systems*, John Wiley and Sons, Inc., 1972.

[44] Banda, S. S., H. H. Yeh, and S. Heise, "A Surrogate System Approach to Robust Control Design," Tech. Rep. 89-3492, AFWAL/FDCC, Flight Dynamics Laboratory, Wright-Patterson Air Force Base, Sept. 1989.

[45] Yeh, H. H., S. S. Banda, A. Bartlett, and S. Heise, "Robust Design of Multivariable Feedback Systems with Real Parameter Uncertainty and Unmodelled Dynamics," in *American Control Conference*, (Pittsburg, PA), June 1989.

[46] Goldberg, D. E., *Genetic Algorithms in Search, Optimization and Machine Learning*, Addison Wesley, 1989.

[47] Ackley, D. H., "An Empirical Study of Bit Vector Function Optimization," in *Genetic Algorithms and Simulated Annealing* (Davis, L., ed.), pp. 170–204, Morgan Kaufmann, Los Altos, CA, 1987.

[48] Baker, J. E., "Adaptive selection methods for genetic algorithms," *Proceedings, International Conference on Genetic Algorithms and Their Applications* (Grefenstette, J. J., ed.), Pittsburgh, PA, 1985, pp. 101–111.

[49] Fiacco, A. and G. McCormick, *Nonlinear programming: sequential unconstrained minimization techniques*, Wiley, 1968. Reprinted 1990 in the SIAM Classics in Applied Mathematics series.

[50] Shao, M., M. M. Colavita, B. Hines, and D. Staelin, "The Mark III Stellar Interferometer," *Journal of Astronomy and Astrophysics*, Vol. 193, 1988, pp. 357–371.

[51] Shao, M. and M. M. Colavita, "Long Baseline Optical and Infrared Stellar Interferometry," *Annual Review of Astronomy and Astrophysics*, Vol. 30, 1992, pp. 457–498.

[52] O'Neal, M. and J. Spanos, "Optical pathlength control in the nanometer regime on the JPL phase B interferometer testbed," in *Proceedings of the SPIE Conference on Active and Adaptive Optical Systems*, (San Diego, CA), July 1991.

[53] Vadlamudi, N., M. A. Blair, and B. R. Clapp, "Hubble Space Telescope On-Orbit Transfer Function Test," in *Lockheed Missiles and Space Company CP*, No. 92-4614-CP, (Sunnyvale, Ca), 1992.

[54] Sharkey, J. P., G. S. Nurre, G. A. Beals, and J. D. Nelson, "A Chronology of the On-Orbit Pointing Control System Changes on the Hubble Space Telescope and Associated Pointing Improvements," in *NASA Marshall SPace Flight Center and Lockheed Missiles and Space Company CP*, No. 92-4618-CP, (Hunstville, AL and Sunnyvale, Ca), 1992.

[55] Hyde, T. T., *Active Vibration Isolation for Precision Space Structures*, Ph.D. thesis, Massachusetts Institute of Technology, Jan. 1996. MIT SERC Report

number 4-96.

[56] Jacques, R. N., *On-line System Identification and Control Design for Flexible Structures*, Ph.D. thesis, Massachusetts Institute of Technology, May 1995. MIT SERC Report number 3-95.

[57] Anderson, E. H., *Robust Actuator and Damper Placement for Structural Control*, Ph.D. thesis, Massachusetts Institute of Technology, Oct. 1993. MIT SERC Report number 14-93.

Appendix A

Exact Wave Domain Solutions

The appendix gives the proceedure used to generate the exact transfer functions used for the beam example in Chapter 2. In this example the beam of length l is free-free and acted on by a moment at the center span, $x = 0$. The sensed output is the differenced tip vertical motions at $x = -l/2$ and $x = l/2$. The proceedure assumes a complex wave solution for the fourth order beam equation in uniform sections of a given beam in between singularities. For the given example this means separate solutions for the left half and right half of the beam,

$$\begin{aligned} w_l &= A_l \exp(ikx + i\omega t) + B_l \exp(kx + i\omega t) \\ &+ C_l \exp(-ikx + i\omega t) + D_l \exp(-kx + i\omega t)\,, \\ w_r &= A_r \exp(ikx + i\omega t) + B_r \exp(kx + i\omega t) \\ &+ C_r \exp(-ikx + i\omega t) + D_r \exp(-kx + i\omega t)\,, \end{aligned} \tag{A.1}$$

where the subscript l stands for the left half of the beam while subscript r stands for the right half. The coefficents A, B, C, and D are complex. The singularities represent crossections of the beam where there are jumps in the internal moment and shear distributions due to forcing inputs. The complex coefficients of the displacements are solved for by applying the boundary conditions and solving the resulting set of symbolic equations. For example, at the left beam tip, $x = -l/2$,

$$\begin{aligned} \frac{\partial^2 w_l}{\partial x^2} &= 0\,, \\ \frac{\partial^3 w_l}{\partial x^3} &= 0\,. \end{aligned} \tag{A.2}$$

In the center,

$$\begin{aligned} w_l - w_r &= 0\,, \\ \frac{\partial w_l}{\partial x} - \frac{\partial w_r}{\partial x} &= 0\,, \\ \frac{\partial^2 w_l}{\partial x^2} - \frac{\partial^2 w_r}{\partial x^2} - M\exp(i\omega t)/EI &= 0\,, \\ \frac{\partial^3 w_l}{\partial x^3} - \frac{\partial^3 w_r}{\partial x^3} &= 0\,. \end{aligned} \tag{A.3}$$

The input is assumed to be a complex exponential of positive frequency and amplitude M. The right end boundary conditions are the same as the left end but act on w_r.

Given that the coefficients are found, the general solution for the displacement everywhere along the beam is known. The sensed variables are now exactly computed from the known displacements or spatial derivatives thereof. In the example case the sensor z is,

$$z = w_l(\tfrac{l}{2}) - w_r(\tfrac{l}{2})\,, \tag{A.4}$$

and the exact transfer function, TF, is evaluated as,

$$TF = \frac{z}{M\exp(i\omega t)}\,. \tag{A.5}$$

The exact transfer function is generated by assuming a one-sided exponential input with amplitude equal to that of the applied singularity. This transfer function represents the repsonse for positive frequency and it is easy to show that since the function is purely real the negative frequency result is entirely equivalent.

Appendix B

Optical Control Transfer Functions

This appendix provides plant and control loop transfer functions for the optical control used in experiments for this thesis. All loop transfer functions are contollers evaluated on the plant data.

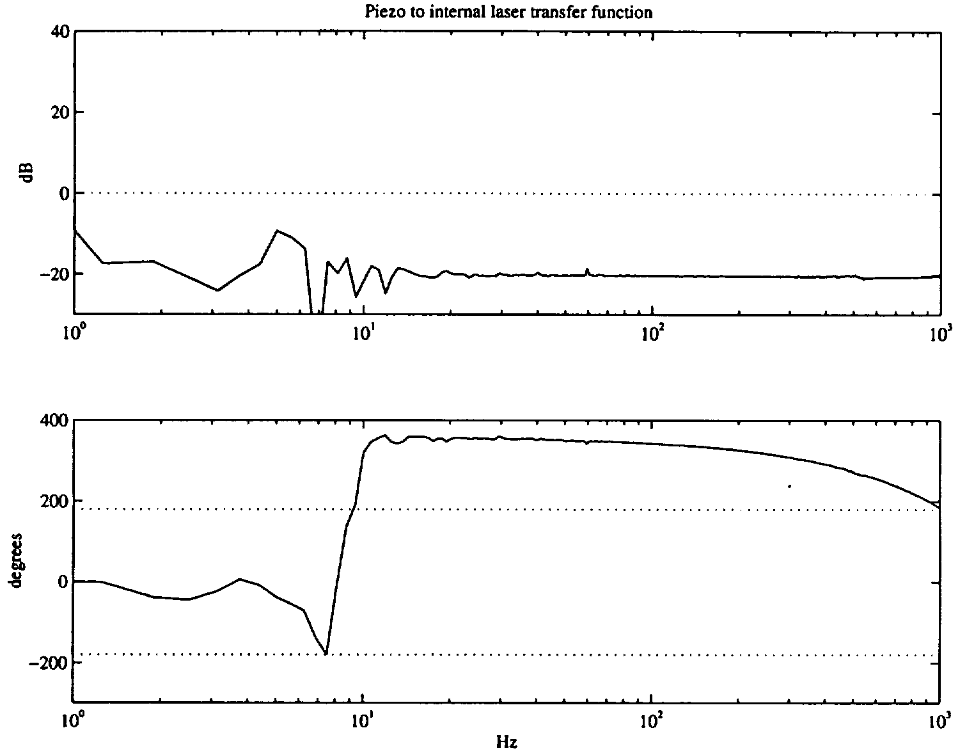

Figure B.1: Optical piezo plant transfer function, G_p. The low coherence at low frequencies is due to pole-zero cancellation of system modes and low density of data points. Note that the transfer function is of constant gain out to 1 kHz and the phase roll down is due to 4 kHz sampling delay.

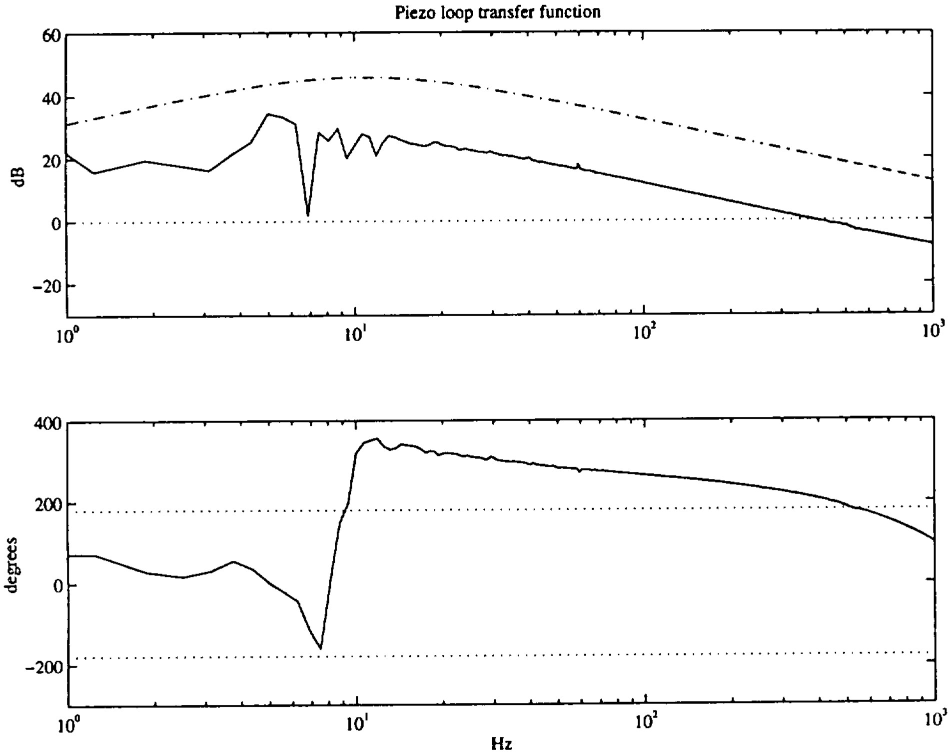

Figure B.2: Optical piezo loop transfer function, K_pG_p solid, controller, K_p dashed dot. The loop has moderate gain at low frequencies and is reduced at very low frequencies to avoid stack saturation due to laser drift.

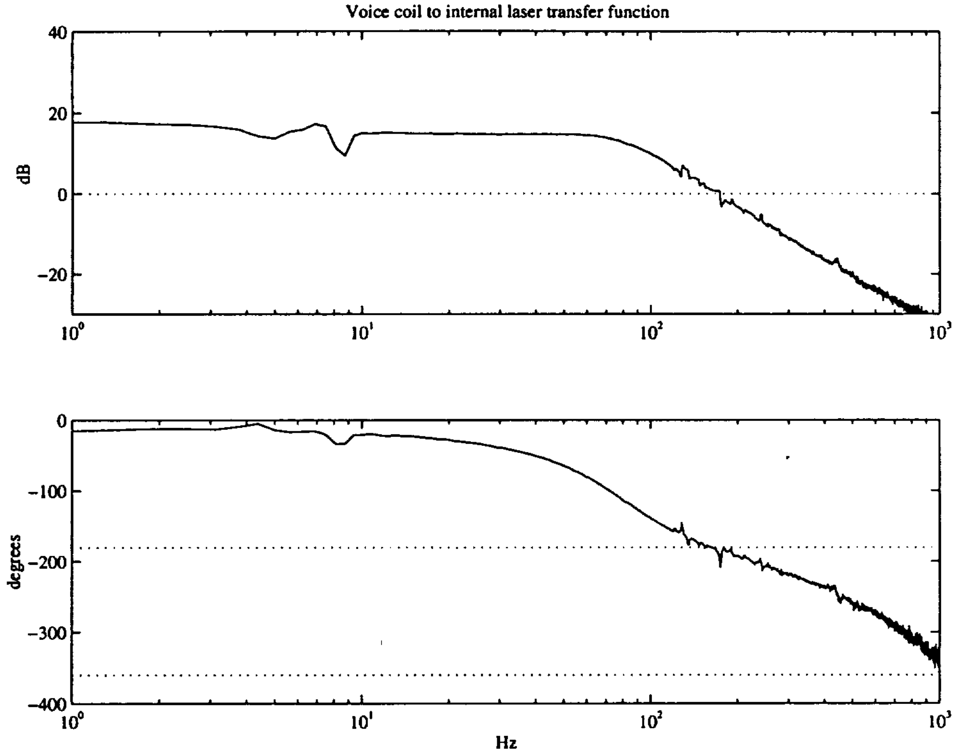

Figure B.3: Optical voice coil plant transfer function, G_v. Second order roll-off of the transfer function ocurrs after the fundamental mode of the mirror plus head mass on the flexural stiffness.

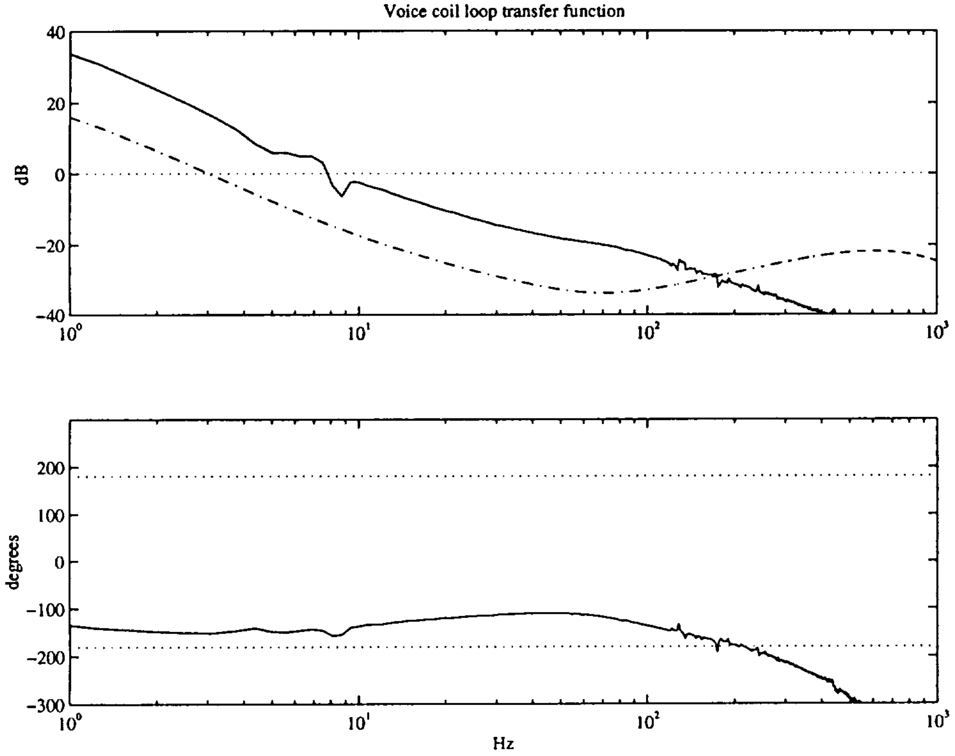

Figure B.4: Optical voice coil loop transfer function, K_vG_v solid, controller, K_v dashed dot. The loop has high gain at low frequencies to desaturate the piezo when used as a servo.

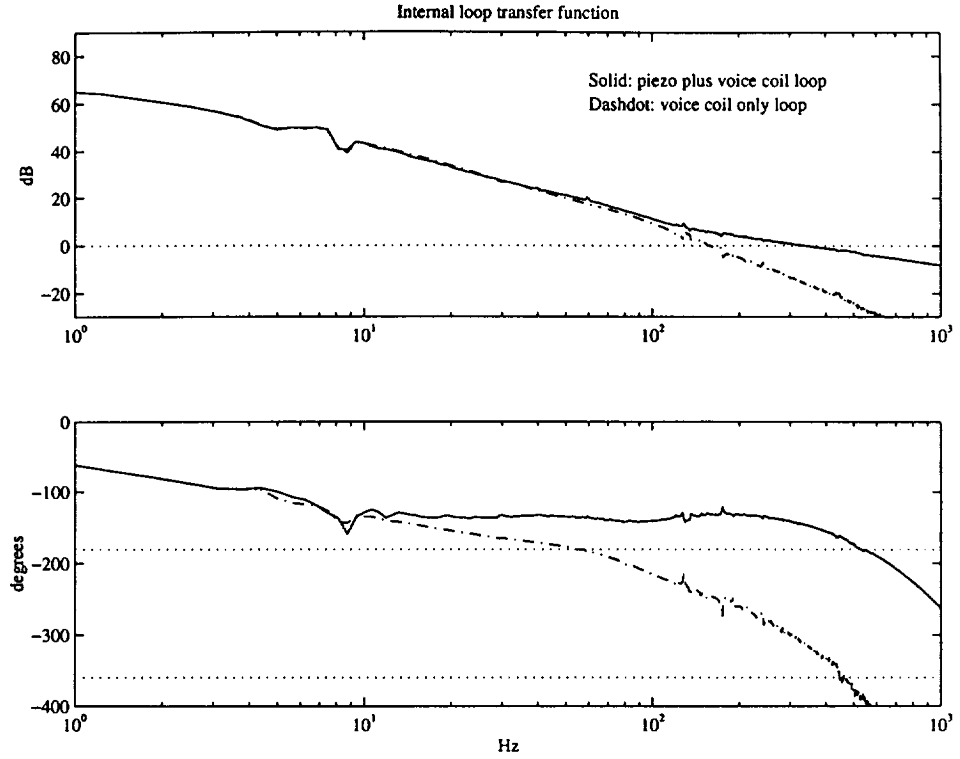

Figure B.5: Internal loop transfer function. Also shown is the loop as if $G_p = 0$. Stable crossover occurs near 350 Hz.

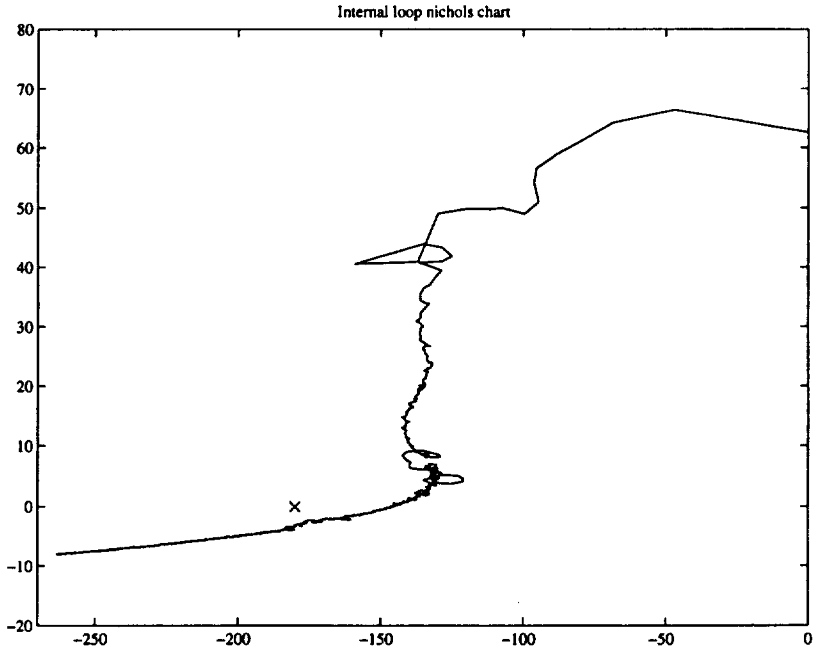

Figure B.6: Internal loop nichols chart showing about 4 dB of gain stability and about 30 degress of phase margin.

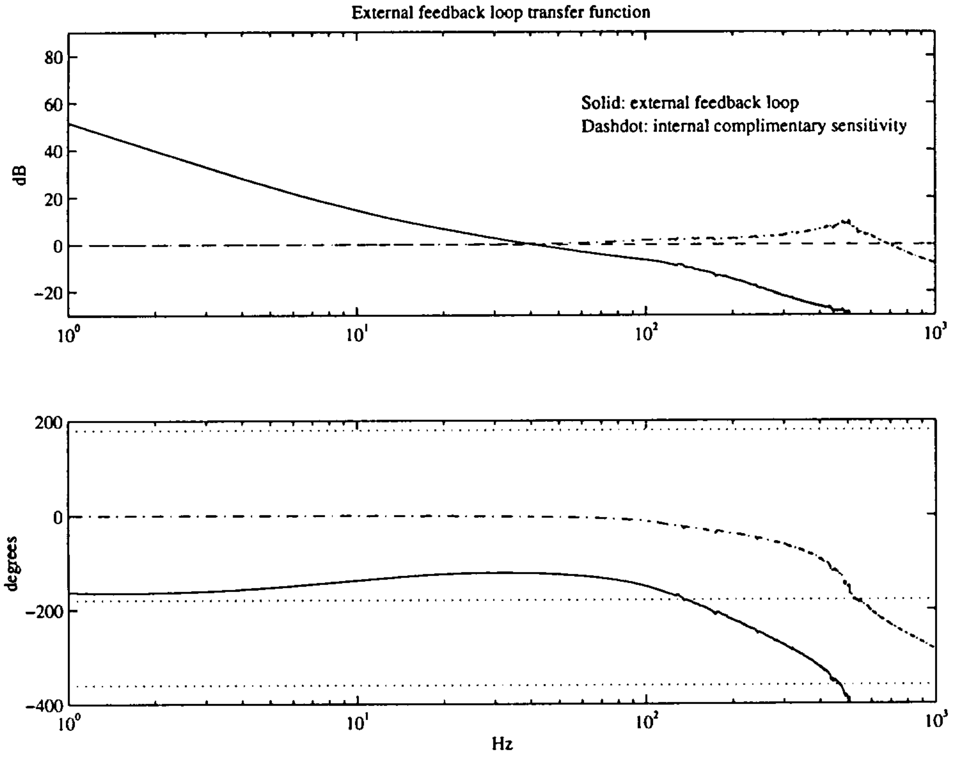

Figure B.7: External loop transfer function, $C_{odl}K_f$ solid, where C_{odl} is the complimentary sensitivity of the closed internal loop. This shows why the actuators are ganged in the internal loop in order to track the external fringe.

Appendix C

Experimental Cases

For both low and high frequency disturbance spectrum designs were implimented experimentally that spanned the usage of available sensors and local controller test matrix space. This appendix suppliments the results in Chapter 6 by presenting supporting experimental cases studied.

Presentation for each case will follow that of Chapter 6. that is, model fits, design weights, model block transfer functions, and performance results. Comparitive results are also tabulated and projected to the imaging interferometer example.

C.1 Low Frequency Disturbances

The following figures are for the straight design with root structural actuator.

C.1.1 Regular truss, H_2 design, hub and load sensors

Model versus measured transfer function data for the following controller design are shown in Fig. 6.16.

C.1.2 Regular truss, integral force design, load sensors

This section presents the control design for a damper in the straight truss located at the root of the truss. The loop gain is plotted for the structural actuator in Fig. C.5.

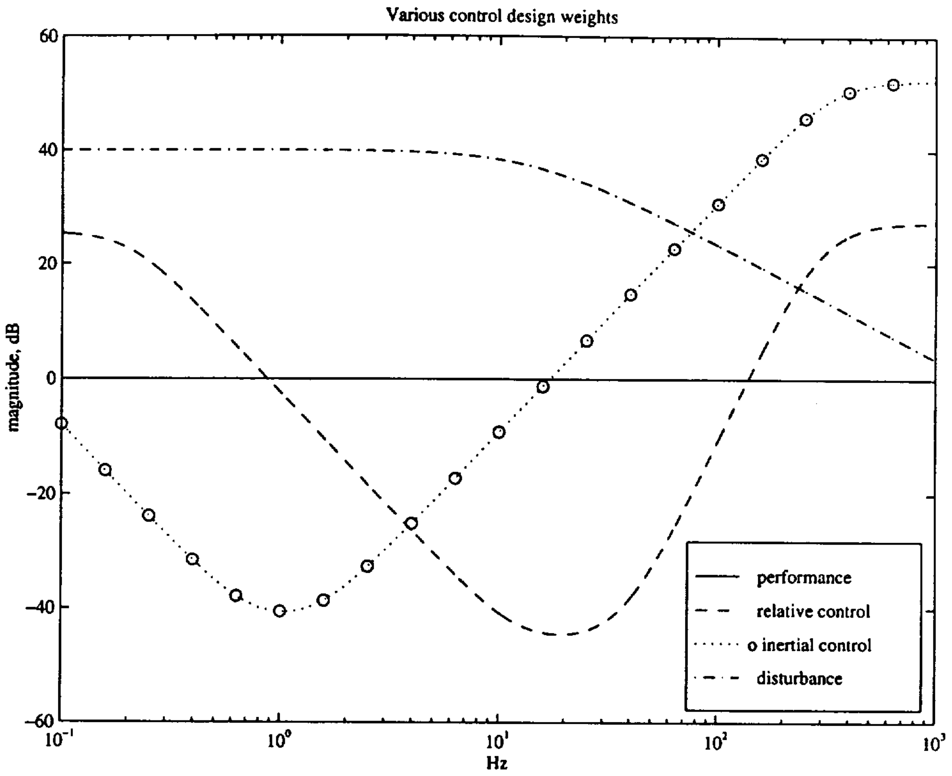

Figure C.1: Control design weights for straight configuration, hub plus load sensors, low frequency disturbance weight.

The compensator is integral with notches to gain stabilize the low frequency rigid body dynamics (see Fig. C.6). Figure C.5 also shows noncollocation excursions at 50 and 90 Hz. The gain on this controller was therefor limited, although it was only intended as a damper.

C.1.3 G.A. flexured active hinge, H_2 design, hub and load sensors

Model versus measured transfer function data for the following controller design are shown in Fig. 6.22.

Note that the transfer function for the collocated sensor in Fig. C.9 shows a well damped pair of zeros near 6 Hz, one of them nonminimum phase. These occur becuase of the attempt to improve the modal residues of the first and second antisymmetric

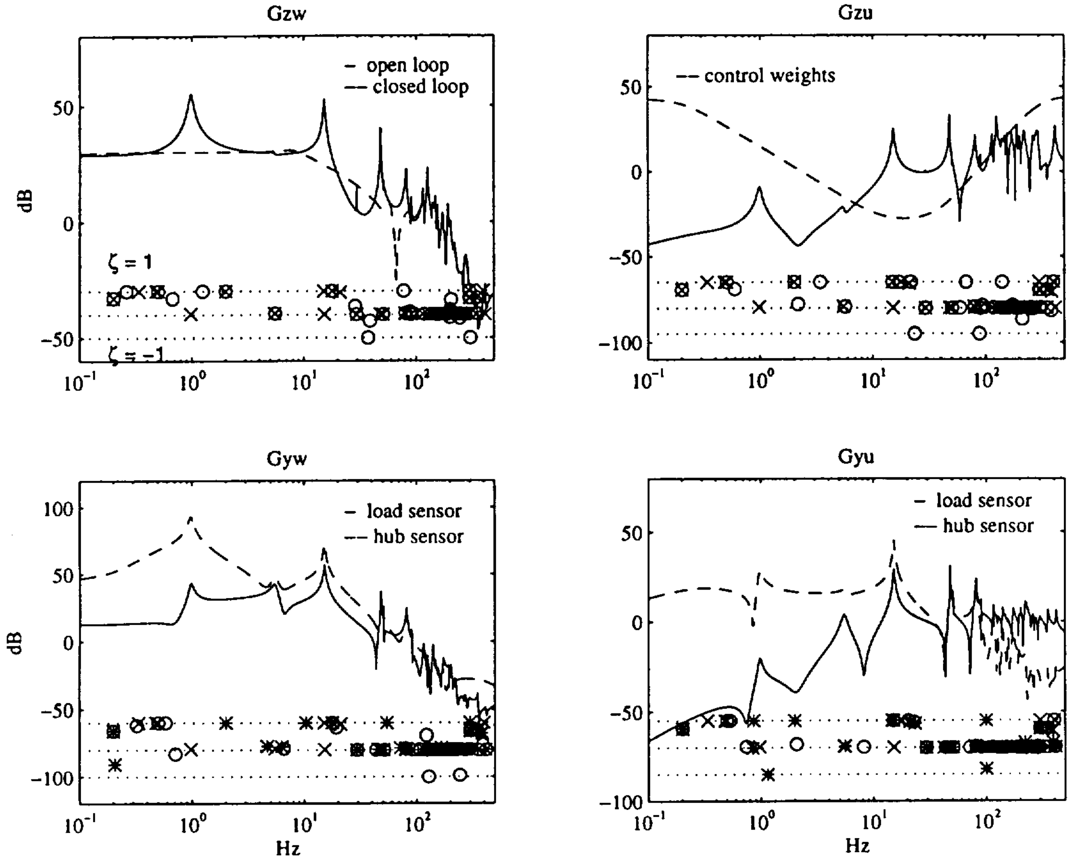

Figure C.2: Model transfer functions with pole zero map, hub plus load sensors, low frequency disturbance weight. 'o's correspond to the solid curve zeros, '*'s correspond to the dashed curve zeros.

modes by cancelling the feed through term electronically. The improved residues do not come without this cost, *i.e.* the transfer function average gain stays high with no apparent gain in phase.

C.1.4 Regular truss, stiff pivot isolator design, load sensors

A root isolator design was investigated by raising the truss connection to the hub to a three point semi-determinant connection. Piezo strut actuators were then placed in the mounting struts to the truss and acted differentially on the pivoted truss.

Loop gain on the integral compensator is shown in Fig. C.12. The compensator is still dampening modes out beyond 100 Hz.

The performance in the middle band is near that of the GA designs at 86 nm.

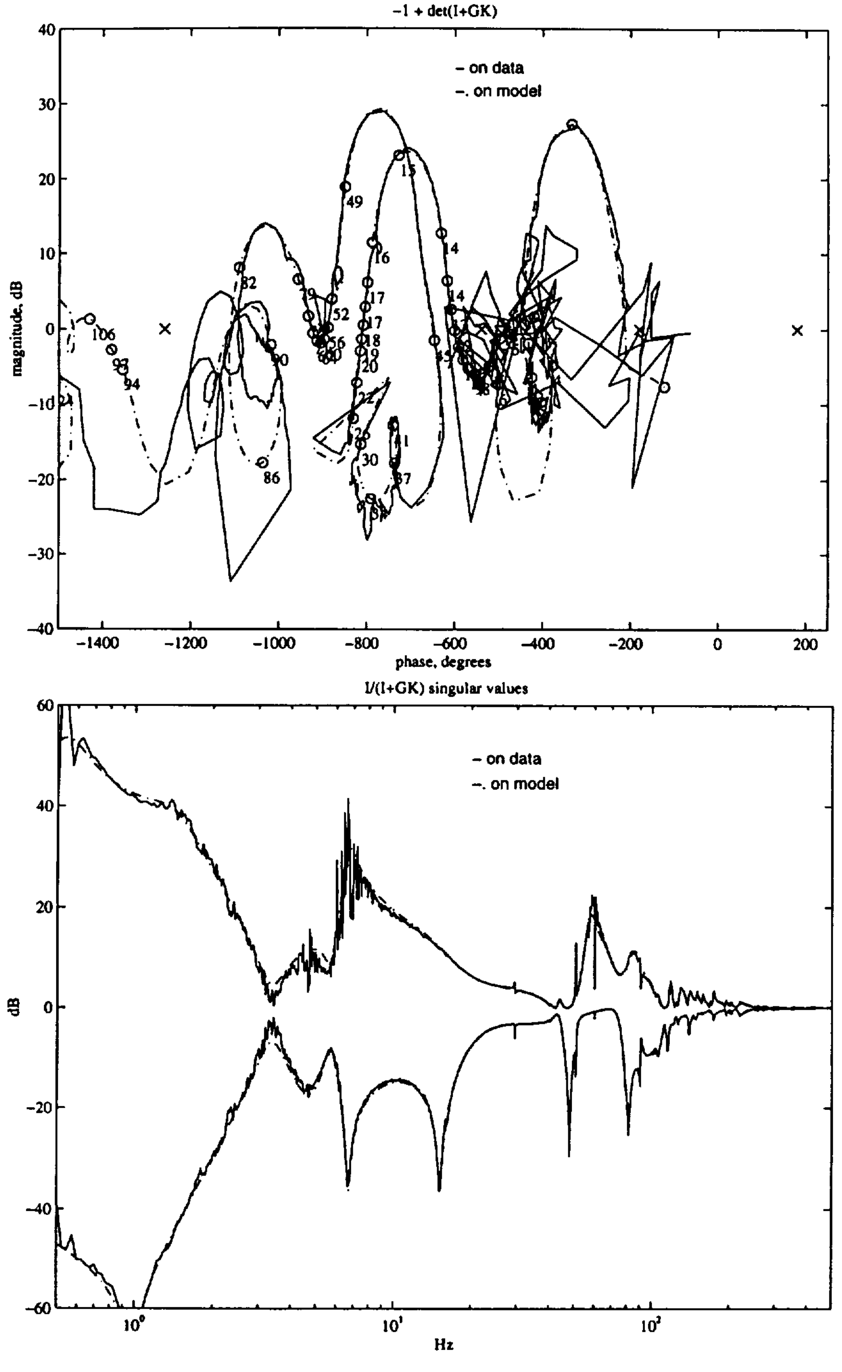

Figure C.3: Multivariable nichols plot and sensitivity singular values for hub and load sensors. In the Nichols plot frequencies in Hz are marked along the curve by o's and critical points are shown as x's.

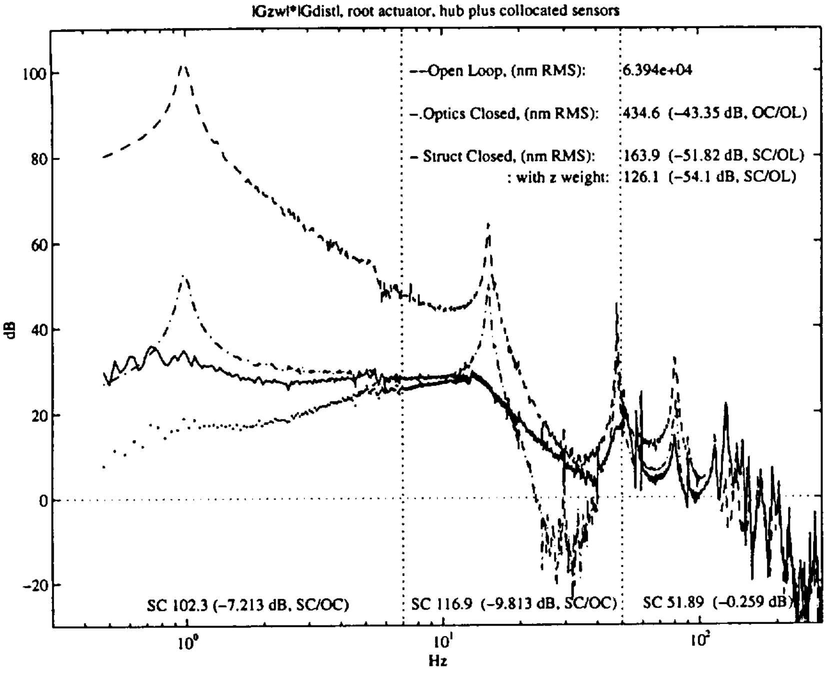

Figure C.4: Regular truss with root actuator performance for hub and load sensors.

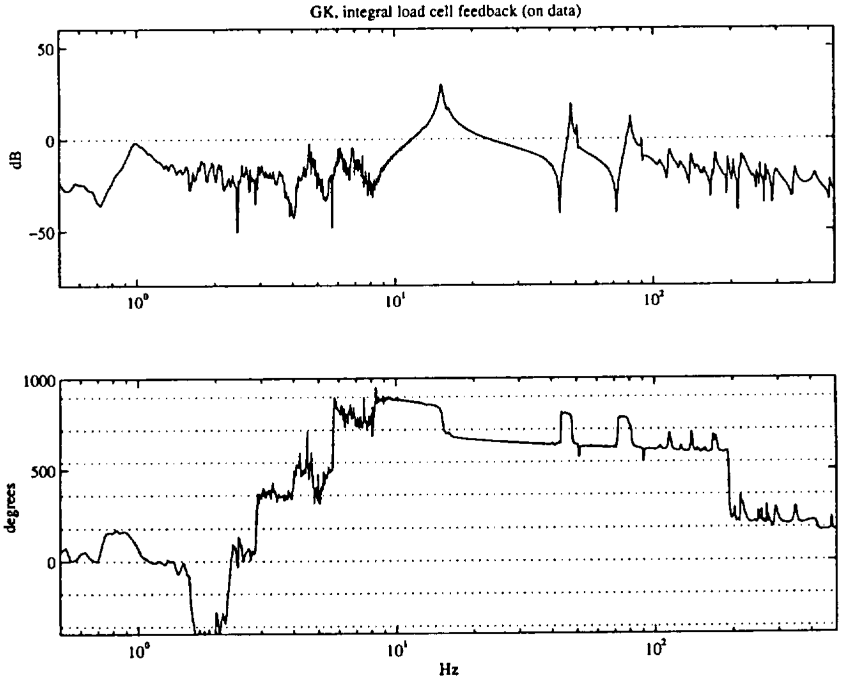

Figure C.5: Loop transfer function for structural actuator to differential load cell. Vertical dotted lines in the phase plot are spaced 180 degrees apart.

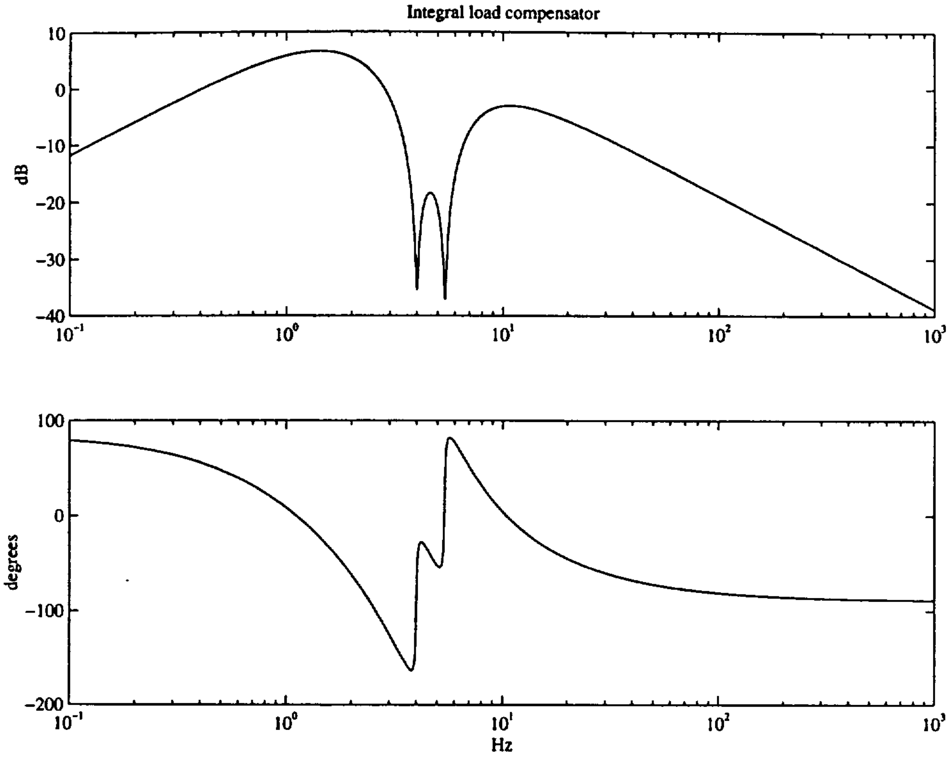

Figure C.6: Compensator for structural actuator to differential load cell. Note notching of low frequency dynamics.

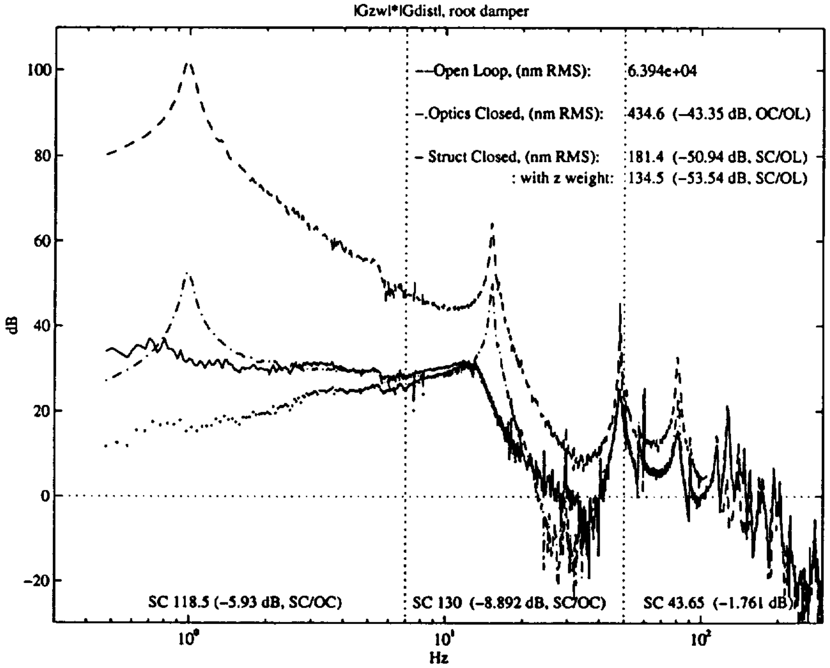

Figure C.7: Regular truss with root damper performance. Note the inertial controller was also on dampening the rigid body mode.

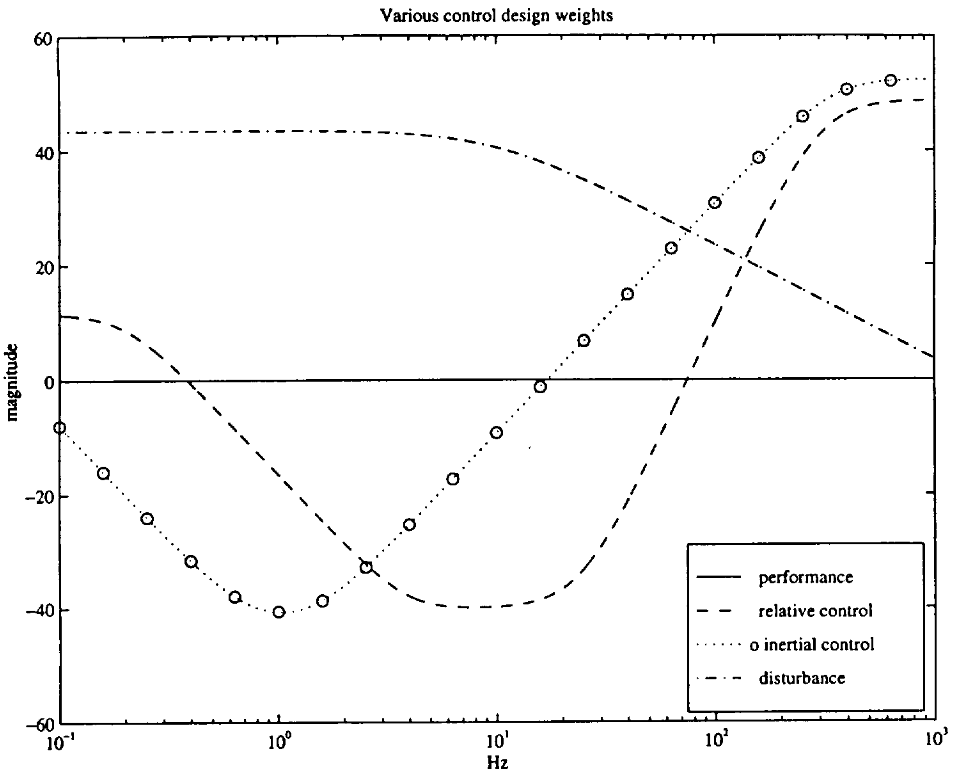

Figure C.8: Control design weights for the GA flexured active hinge configuration, low frequency disturbance weight.

Interesting behavior is depicted near the first antisymmetric mode where ther appears to be a roll down before a dampened stiffened mode. Stiffening of the antisymmetric mode is due to the active release of the mount boundary condition by the controller.

C.2 High Frequency Disturbances

Several design configurations were implimented in the case of high frequency disturbances. Each design contributed to the understanding of the average transfer function gain.

C.2.1 Regular truss with actuators as longerons in the midspan

Figure C.15 is the same figure as that presented for low frequency disturbances in Chapter 6. It is reiterated here because the same design was applied for high frequency

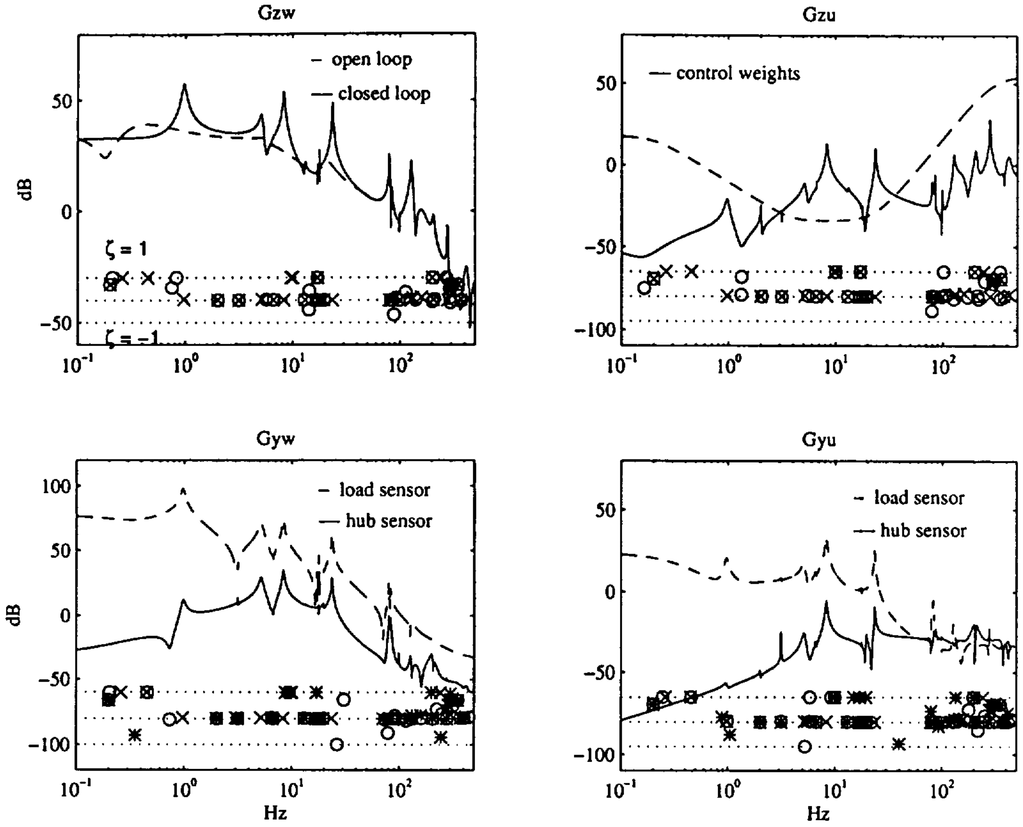

Figure C.9: Model transfer functions with pole zero map, hub plus load sensors, low frequency disturbance weight. 'o's correspond to the solid curve zeros, '*'s correspond to the dashed curve zeros.

disturbances since this design is independent of knowledge of the disturbances.

Performance achieved in Fig. C.16 is similar to that achieved by the H_2 control design. Impressive levels of dampening the first, second and third antisymmetric modes are realized in achieving ≈ 98 nm rms preformance. Modes near 120 Hz are also well dampened, while modes near 130 Hz again show resistance to control.

C.2.2 G.A. partially destiffened truss with actuators as longerons in the midspan

This configuration is shown in the upper of Fig. 6.34. This configuration is the first tried in a sequence of experimental iterations needed to realize the G.A. solution.

The model shown in Fig. C.17 represents a 98 state model. This model was the

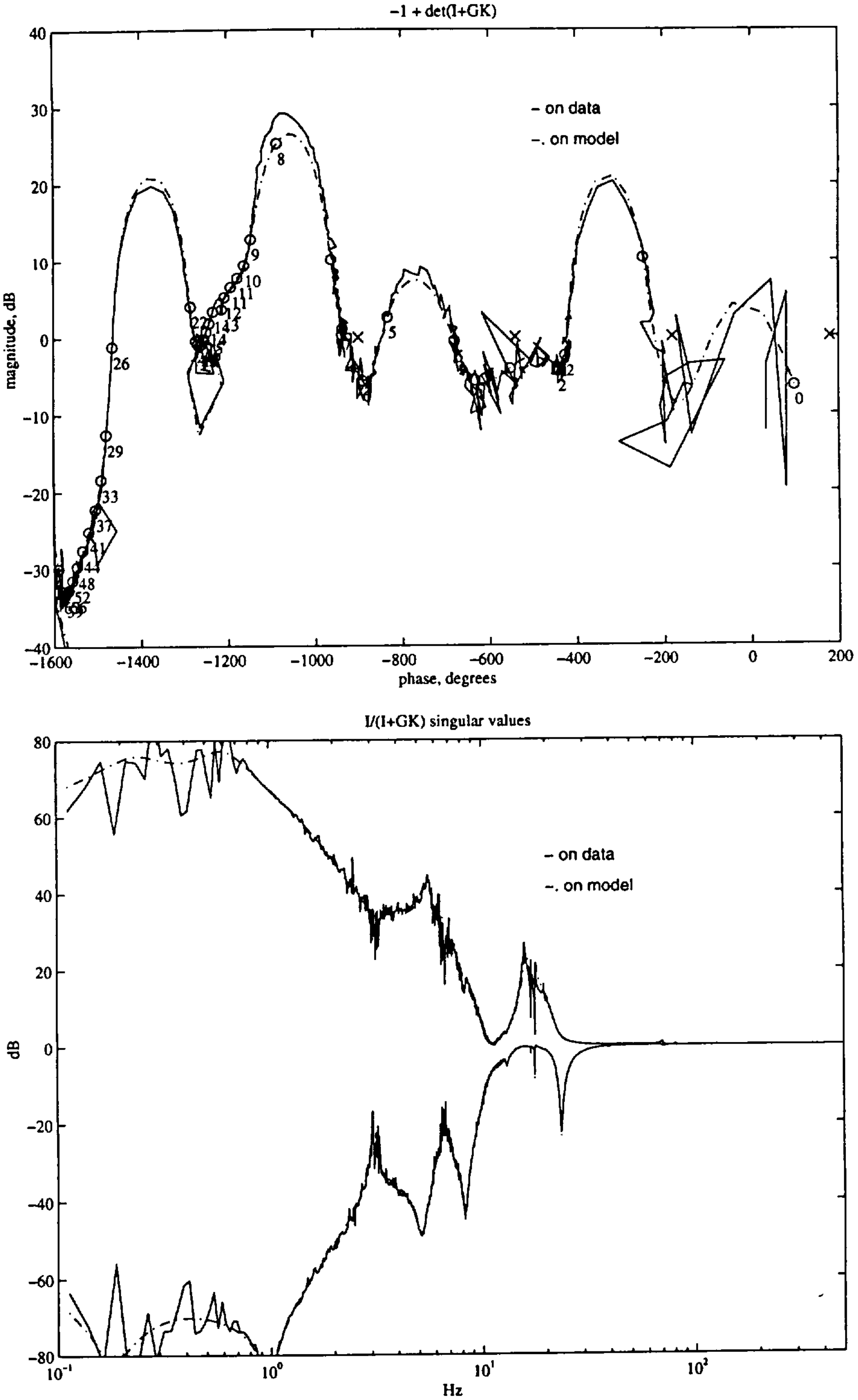

Figure C.10: Multivariable nichols plot and sensitivity singular values for hub and load sensors.

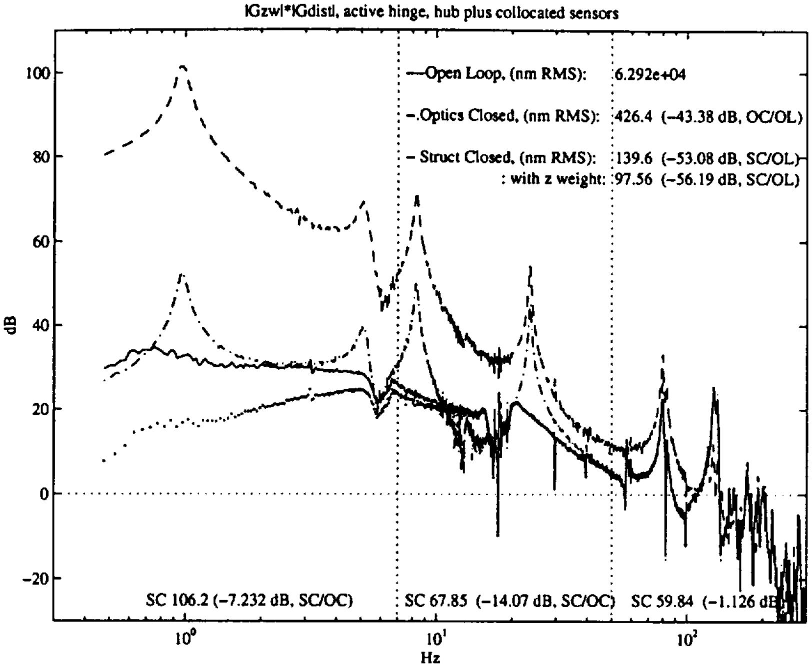

Figure C.11: GA flexured active hinge performance for hub and load sensors.

largest used to design a model based compensator. The compensator was reduced to 42 states before being appended to the 14 state optical compensator.

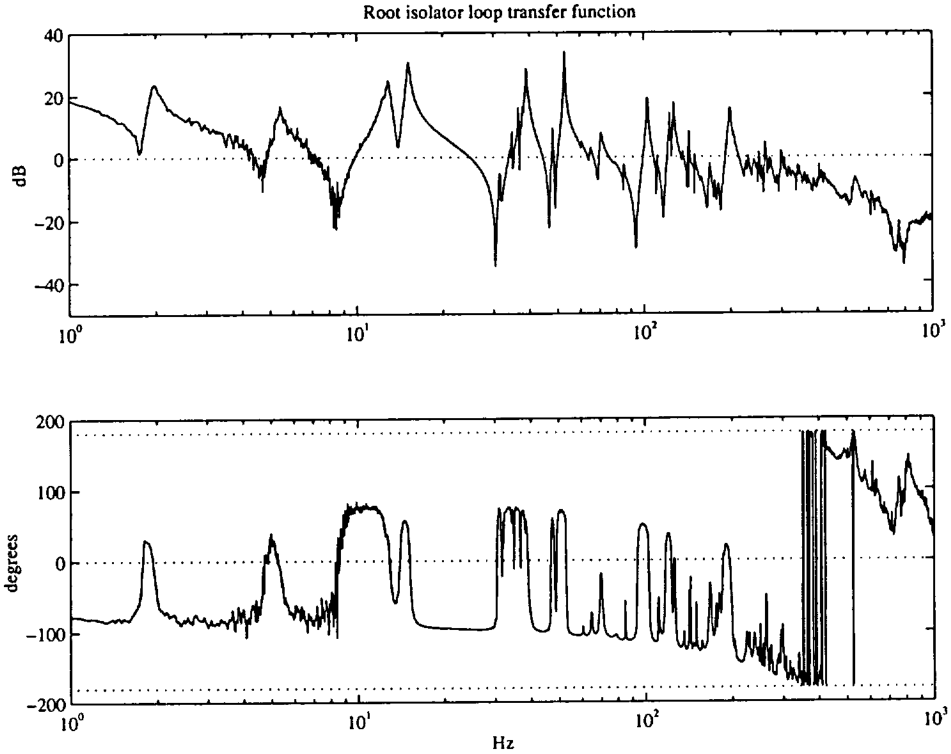

Figure C.12: Loop transfer function for the root isolator to differential load cell. Vertical dotted lines in the phase plot are spaced 180 degrees apart.

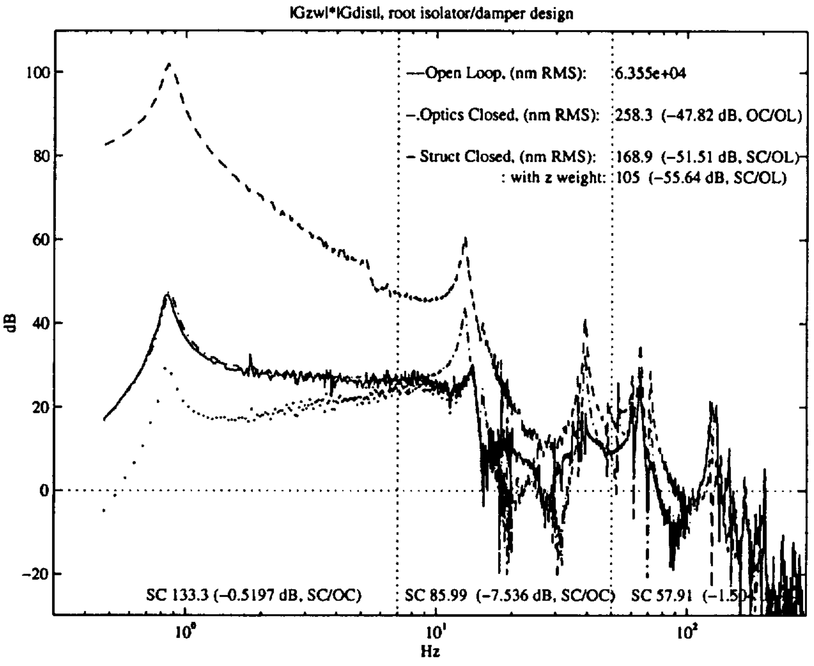

Figure C.13: Regular truss with stiff pivot isolator performance.

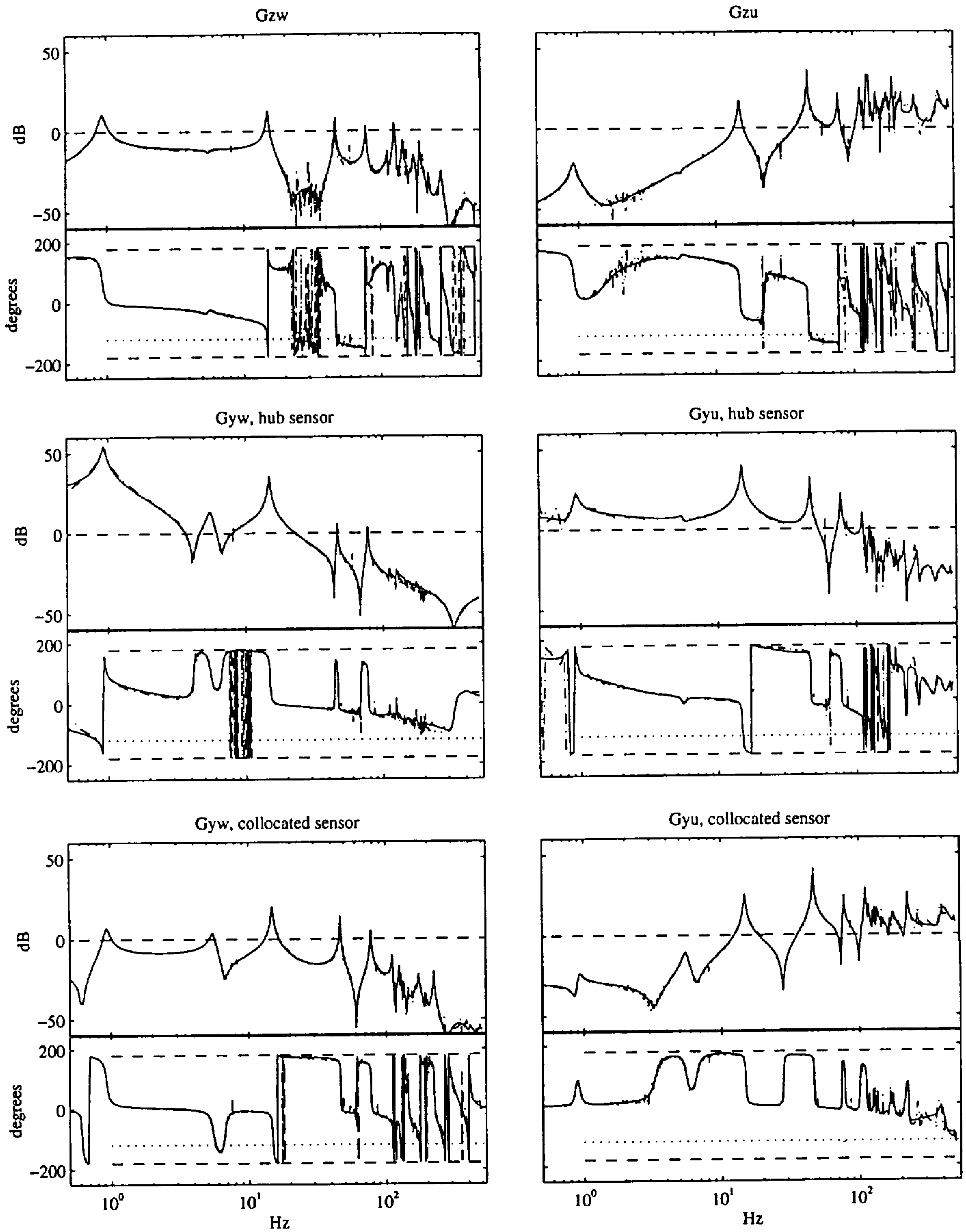

Figure C.14: Data (dashed dot) versus fit model (solid) for the regular configuration, high frequency disturbances. Structural actuators replace longerons at the midspan span.

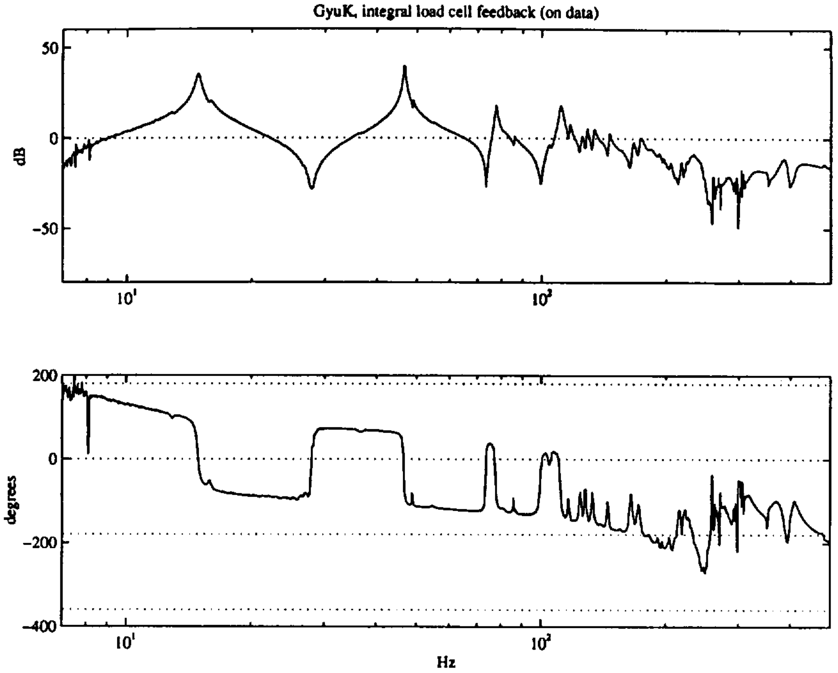

Figure C.15: Loop gain for high gain softening of structural actuators in the regular truss midspan.

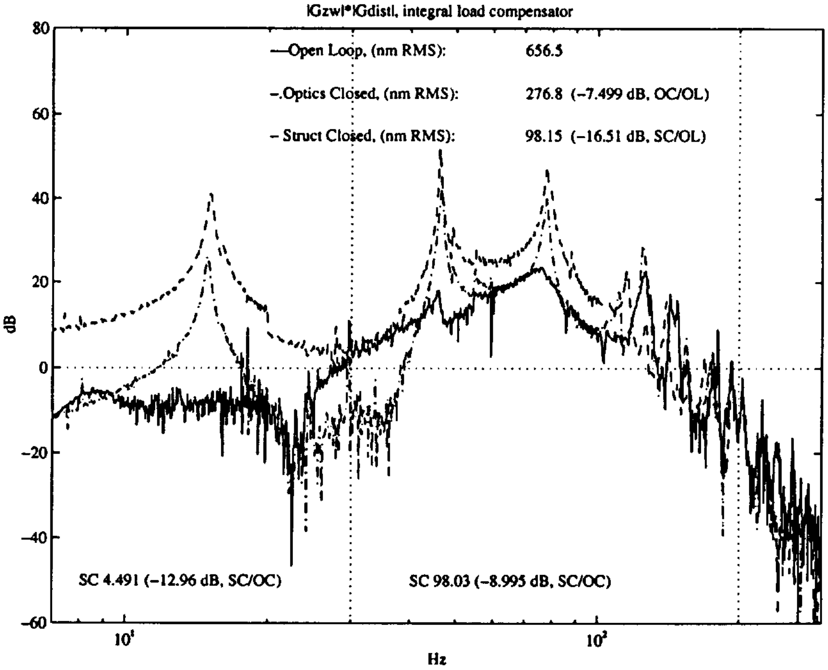

Figure C.16: Performance for the regular truss design, high frequency disturbances, high gain integral force feedback on midpsan struts.

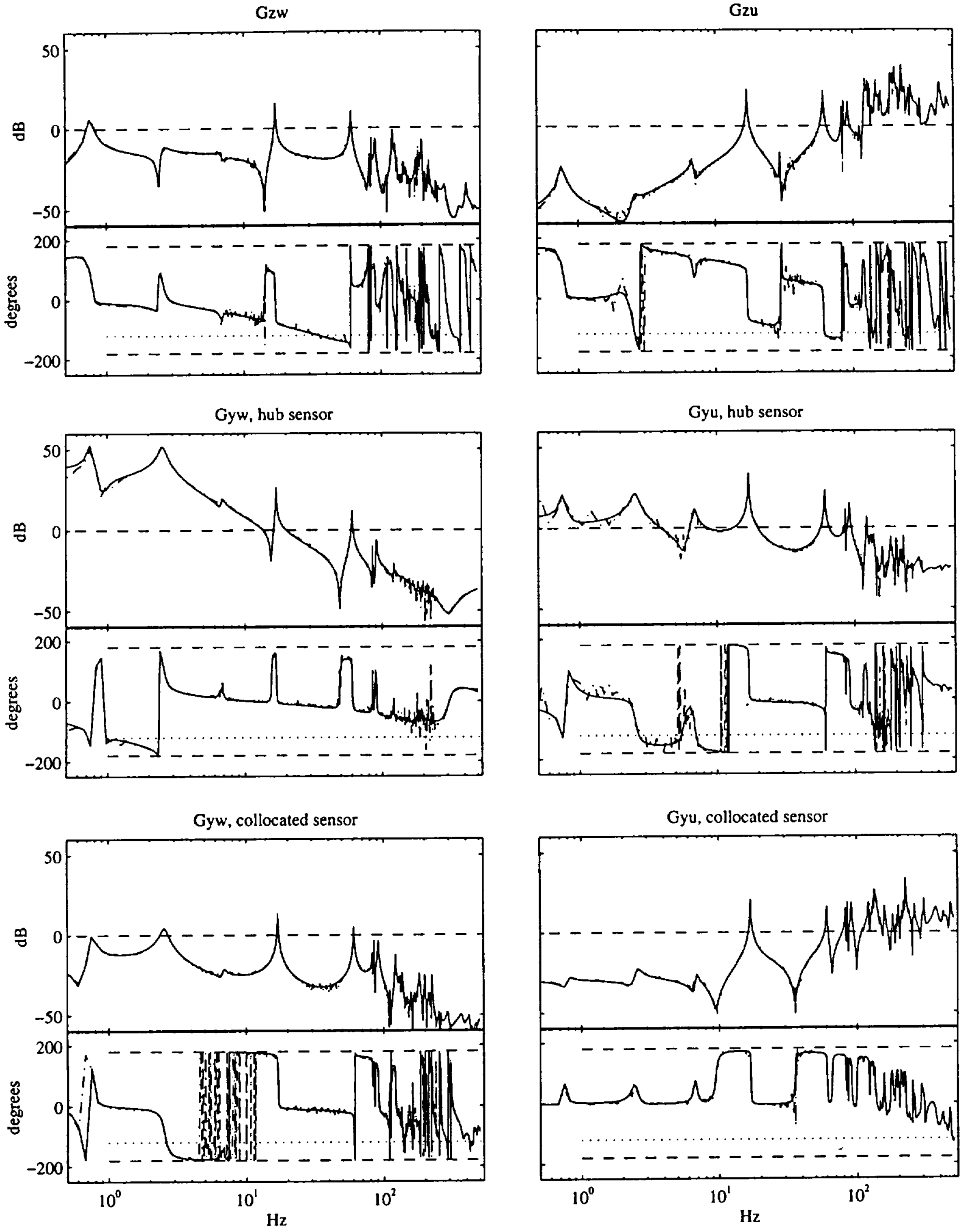

Figure C.17: Data (dashed dot) versus fit model (solid) for the optimized partially destiffened configuration, high frequency disturbances. Structural actuators replace longerons at the midspan span.